
Basis functions for residual stresses

*A thesis submitted in fulfilment of the requirements
for the degree of PhD*

by

Sankalp Tiwari



Department of Mechanical Engineering
INDIAN INSTITUTE OF TECHNOLOGY KANPUR

March 2022

CERTIFICATE

It is certified that the work contained in the thesis titled “Basis functions for residual stresses” by Sankalp Tiwari has been carried out under my/our supervision and that this work has not been submitted elsewhere for a degree.



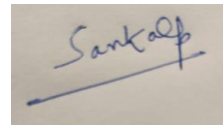
Signature of the Supervisor(s)
Name: Anindya Chatterjee
Department: Mechanical Engg
I.I.T. Kanpur

July 2021

Declaration

This is to certify that the thesis titled 'Basis functions for residual stresses' has been authored by me. It presents the research conducted by me under the supervision of Dr. Anindya Chatterjee.

To the best of my knowledge, it is an original work, both in terms of research content and narrative, and has not been submitted elsewhere, in part or in full, for a degree. Further, due credit has been attributed to the relevant state-of-the-art and collaborations (if any) with appropriate citations and acknowledgements, in line with established norms and practices.

A photograph of a handwritten signature in blue ink on a light-colored surface. The signature reads 'Sankalp' and is underlined with a single horizontal stroke.

Name: Sankalp Tiwari

Programme: PhD

Department: Mechanical Engineering
Indian Institute of Technology Kanpur
Kanpur 208016

Abstract

Name of the student: **Sankalp Tiwari**

Roll No: **14205266**

Degree for which submitted: **PhD**

Department: **Mechanical Engineering**

Thesis title: **Basis functions for residual stresses**

Thesis supervisor: **Anindya Chatterjee**

Month and year of thesis submission: **March 2022**

Self-equilibrating, traction free stresses are known as residual stresses. They are ubiquitous in solid manufactured components, and their presence may be either beneficial or harmful. In this work, we consider basis functions for residual stress fields of reasonable regularity.

Specifically, we consider arbitrary pre-existing residual stress states in arbitrarily shaped, unloaded solid bodies. Common treatments of the topic tend to focus on either the mechanical origins of the stress, or methods of stress measurement at certain locations. Here we take the stress field as given and consider the problem of approximating any such stress field, in a given body, as a linear combination of pre-determined fields which can serve as a basis. We consider planar stress states in detail, and introduce an extremization problem that leads to a linear eigenvalue problem. Eigenfunctions ϕ of that problem form an orthonormal basis for square integrable residual stress states. We outline the extension of our theory to three dimensional bodies and states of stress.

In general, the eigenvalue problem is not solvable analytically, and we use numerical methods. We compute the eigenfunctions ϕ for arbitrary planar geometries using the finite element method. We also compute them using semi-numerical methods for the following four geometries: an annulus, a circular disk, a rectangle and an annular wedge. Results

from these two independent methods agree. We then consider several different candidate residual stresses on different geometries and fit them using our eigenfunctions ϕ . We consider four candidate residual stresses with fixed circumferential wave number on an annulus: two hypothetical, one from shrink fitting of two elastic cylinders, and one from non-uniform heating of a thermoelastic annulus. We also fit three candidate residual stresses obtained from metal forming simulations of (a) rolling and (b) angular extrusion using the non-linear finite element software package Abaqus. Convergence of fits to these stresses is noted in the L^2 and the H^1 norms for continuous stress fields, and in the L^2 norm for stress fields with simple discontinuities.

Next, we modify our approach for two special classes of problems: (a) residual stresses in prismatic geometries and (b) spatially localized planar residual stresses. In the first problem, we see that the original 3D extremization problem decouples into three 2D sub-problems: one for the planar components, one for the out of plane shear components, and one for the axial component. In the second problem, we obtain spatially localized eigenfunctions by weighting the objective function and the normalization constraint in the extremization problem by appropriate functions. Finally, instead of fitting an already given residual stress, we consider solving for one using the basis functions ϕ , given a governing differential equation. In particular, we look at a non-uniformly heated thermoelastic annulus. Our aim in this part of the work is to try Galerkin projections to obtain convergent solutions. We find that a direct use of the weighted residual method, with ϕ as the weighting functions, does not work. This leads us to a study of some useful properties of harmonic functions relevant to this problem. A correct application of the weighted residual method with ϕ then yields the correct solution with much faster convergence as compared to a direct, displacement based, virtual work method.

The overall approach of this thesis can be used to describe arbitrary pre-existing residual stress states in arbitrarily shaped bodies using basis functions that are determined by the body geometry alone, independent of the physical mechanisms, the constitutive properties of the material or the prior deformation history that have produced these stresses.

Acknowledgements

I have spent a long time at IIT Kanpur (about 153 months, starting with my undergraduate studies, at the time of writing this!). No wonder, as I write the acknowledgement section, I am filled with a sense of grief at the thought of my impending eventual departure. My memories of this rather long period are filled with some noteworthy, but mostly unremarkable moments that have no reason to stick around otherwise: a late night chat with an SIS guard; the little courtesies extended to me by the CCD staff, like allowing me to put my feet up on the sofa if I felt sleepy; the barely noticeable window like opening in the beer shop that came to our rescue if our merriment went beyond the official closing time; and so on. After some contemplation, I realize that these moments probably stuck around because I felt so happy and relaxed when I was living them. Apart from serendipitous star alignments, what made them happen were the people (and sometimes dogs) around me. I would like to thank all such wonderful people making up the seldom acknowledged workforce of IIT Kanpur: the SIS guards, the washer men, the cleaning staff, the canteen workers, the autorickshaw drivers, the gardeners, people in administrative offices, etcetera.

Those who know me personally know that I am always more likely to be found in CCD than in my lab or my hostel, thanks to its wonderful ambience and the ever so sweet staff over the years: Babli, Supriya, Vaishali, Akash, Govind, Monis, Abhishek, Mridula, Shilpi, Mustakeem, and many more whose names I have now forgotten. Most of the work that makes up this thesis was done while sipping a Café Frappé (in summers) or a hot chocolate (in winters) in the CCD premises.

I am indebted to my thesis advisor Prof. Anindya Chatterjee for agreeing to take me as his student. I was so impressed by a talk he gave on rotations sometime in 2014 (I still remember how he showed that finite rotations are not commutative) that I walked straight into his office a few days later asking if I could do my PhD with him. In hindsight, I should perhaps have studied more of his earlier work before approaching him, but it is a decision I have never regretted. This PhD has been an amazing journey and I have learnt a lot from him. His clarity of thinking, his little thought experiments that bridge the seemingly disparate maths and physics worlds, his command over language (he once told me how he envisions turbulence in fluids; it was rather poetic), the impressive originality of his ideas (including the one that led to this thesis), are all excellent. I could see while writing this thesis that the long hours spent discussing things with him have undoubtedly left an imprint on my thought process, and some of his clarity of thought has apparently rubbed

off on me as well. He is a wonderful human being too, and I like to think of him more as a friend than as my advisor.

I am lucky to have Prof. Anurag Gupta's continued presence in my life since my bachelor's degree days. I have taken seven courses with him, and also worked with him on the acoustics of the Indian musical drum prior to my PhD. He is an amazing teacher and I owe a lot to him for whatever little mechanics I know. Also, all these courses with him made me very comfortable with the mathematics I used to be so scared of. Here is a case in point: in the early days of this work, we were looking for a functional that contains stress derivatives and follows objectivity. I realized one day that the functional we are after is actually the L^2 norm of the gradient of the stress tensor, which is a third order tensor. When I told this to Prof. Chatterjee, he remarked, and I quote, "Very interesting that you went up to a third order tensor, I would perhaps not have dared. Anurag's effect, for sure!" Prof. Gupta bailed us out at several crucial junctures throughout this work and I cannot thank him enough for all his help.

I thank Prof. Pritam Chakraborty for helping us with the Abaqus simulations and Prof. Sovan Das for helping us with the calculus of variations part. I also thank Prof. Pankaj Wahi, who guided me during my master's degree, for all his support.

I thank my wife Garima for being there for me, always.

Coming to my friends, the first name surely has to be Animesh. I am extremely fortunate to have had his company for the last seven years or so. He is, simply put, the most brilliant person I know, and his passion for research is contagious. He is the one stop solution to almost all my doubts, and I am not sure how am I ever going to manage without him should I continue in academics.

I would like to thank Kiran, Rishikesh and Saptarshi, who are my closest friends on campus, for their wonderful company. I would also like to thank my lab mates: Arindam, Bidhayak, Ashok (Kumar), Arnav, Santhosh, Aakash, Arunava, Ankush, Shivam, Husain, Saurabh, Tapan, Ghulam, Ritwik, Maiti; my PhD friends: Rupal, Manish, Ashok (Mandal), Santanu, Sunit, Anup, Mousumi; my musician friends: Aakash, Vipul, Pratul, Shreyan, Apoorv, Sagar (Paul), Afifa, Pushkar, Samya, Debdeep; my beer friends: Pisharody, Cherian, Ayan, Vijju, Sagar (Setu), Lavish; my Counselling Service friends: Aarush, Rupesh, Ashlesha, Prachi (Kharb), Afreen; my football friends: Sudipta, Arnab, Sayantan, Bakshi, Hari, Shubro; my family members: Prateek, Ila, Shubham, Priyanka, Curie; and other friends (who I find difficult to put in any of the above categories): Roohi, Apoorva,

Praachi (Tiwari), Shivangi, Samiksha, Mukesh, Anansh, Pranjali, Bharath, Tushar, Vidhi, Parnika, Deepa. I am so sorry if I missed out on anyone who expected to be here.

I would like to dedicate this thesis to my mother, the most important person in my life. She has had her reservations about my career choices, but she has supported me no matter what, despite all my oddities. I am not sure if she will ever read my thesis, but I would like to think that by now she has *some* idea what residual stresses are. When I tell her that if I make a cut in my skin it is because of residual stresses that it opens up, her look is one of concern.

Contents

Acknowledgements	v
1 Introduction	1
1.1 Motivation	1
1.2 Organization of the thesis	5
1.3 Notation	6
2 Extremization problem and governing PDEs	7
2.1 Problem statement	8
2.2 Solution approach <i>via</i> an extremization problem	9
2.3 Orthonormality of the eigenfunctions	11
2.4 Basis of $\bar{\mathcal{S}}$	13
2.5 Extension of the theory to three dimensions	14
2.6 A minimizer of \mathbf{J}_0 exists in the unit ball of $\mathcal{S}_{N\perp}$	16
2.7 Summary of the chapter	22
3 Computation of eigenfunctions	23
3.1 Eigenfunctions on arbitrary domains using the FEM	24
3.1.1 Formulation	24
3.1.2 Computed eigenfunctions and their stability	28
3.2 Semi-numerical methods for special domains	36
3.2.1 Annular domain	36
3.2.2 Solid circular disk	38
3.2.3 Rectangular domain	47
3.2.3.1 Orthogonal bases for ψ and η	48
3.2.3.2 A basis of variable separable residual stress fields	51
3.2.3.3 Alternative computation of residual stress eigenfunctions ϕ_i	52
3.2.4 Annular wedge	54
3.3 Summary of the chapter	56
4 Examples of fitting residual stress fields	58
4.1 Residual stress fields in an annulus	59

4.1.1	Example 1: hypothetical stress field, $m = 3$	60
4.1.2	Example 2: hypothetical stress field, $m = 3$	62
4.1.3	Example 3: shrink fitted cylinder, $m = 0$	64
4.1.4	Example 4: thermoelastic residual stress, $m = 3$	65
4.2	Residual stresses from metal forming simulations	69
4.2.1	Rolling simulation	69
4.2.1.1	Details of the simulation	69
4.2.1.2	Results	71
4.2.1.3	Rolling simulation with Johnson-Cook hardening	74
4.2.2	Angular extrusion simulation	77
4.2.2.1	Details of the simulation	77
4.2.2.2	Results	79
4.3	Summary of the chapter	83
5	Modifications of the eigenvalue problem for special purposes	84
5.1	Basis functions for residual stress fields in infinitely long prismatic bodies	85
5.1.1	Properties of residual stress fields in such bodies	85
5.1.2	Development of basis functions	86
5.2	Basis functions for localized 2D residual stress fields	104
5.2.1	Demonstration of the concept in 1D	104
5.2.2	Spatially localized basis functions in 2D	106
5.2.2.1	Extremization problem	106
5.2.2.2	Orthogonality of the eigenfunctions	108
5.2.2.3	Computation of eigenfunctions using the FEM	109
5.2.2.4	Computation of eigenfunctions on an annulus	112
5.2.2.5	Fitting a given spatially localized residual stress field	113
5.3	Summary of the chapter	117
6	Solution of a thermoelasticity problem using residual stress basis	119
6.1	Problem description	121
6.2	Approximate solution using the virtual work method	121
6.2.1	Computation of the free vibration modes	121
6.2.2	Computation of approximate residual stress	123
6.3	Approximate solution using the residual stress basis functions ϕ_i	129
6.3.1	A direct (incorrect) application of the weighted residual method	129
6.3.2	Reasons for the failure of the direct approach	131
6.3.2.1	The fit σ^F , and its derivatives	132
6.3.2.2	What role do the operator and the basis play?	132
6.3.3	A characterization of harmonic functions in terms of planar residual stresses	134
6.3.4	A correct application of the weighted residual method with ϕ_i	137
6.4	A new basis for residual stresses	141
6.4.1	Construction of the new basis	142
6.4.2	Weighted residual method with Φ_i	146

6.5	Summary of the chapter	150
7	Comments on the modified extremization problems studied in this thesis	152
7.1	An outline of the proof presented in Chapter 2	153
7.2	1D eigenfunctions f of Section 3.2.3.1	154
7.3	Axial stress eigenfunctions ϕ_{zz} of Section 5.1.2	156
7.4	Out of plane shear stress eigenfunctions v of Section 5.1.2	158
7.5	Spatially localized residual stress eigenfunctions φ of Section 5.2.2	160
7.6	Residual stress eigenfunctions Φ with zero boundary value of Section 6.4	164
7.7	Summary of the chapter	165
8	Conclusions and future work	166
8.1	Conclusions	166
8.2	Future work	167
A	Proof that the stationary points are sufficiently regular	170
B	Sufficient conditions for a stationary point	172
C	Proof of Eq. 2.14	174
D	Proof that complex conjugates of eigenvalues/eigenfunctions are themselves eigenvalues/eigenfunctions	176
E	Proof that the eigenfunctions form a basis for \mathcal{S}	178
F	Eigenfunctions ϕ form an orthogonal basis to \mathcal{S} in the H^1 norm	180
G	Proof that Eq. 5.23 is an inner product and Eq. 5.24 is a norm	182
	Bibliography	184

List of Figures

1.1	Approximation error versus number of (vibrational) modal stress fields used. Convergence to zero is not apparent and seems unlikely.	3
3.1	A sample 2×2 mesh of serendipity elements	25
3.2	First six eigenfunctions for an annular domain; $\lambda_1 = 293.34$, $\lambda_2 = \lambda_3 = 348.76$, $\lambda_4 = 1065.71$, $\lambda_5 = \lambda_6 = 1104.19$	29
3.3	First six eigenfunctions for a circular disk; $\lambda_1 = 137.54$, $\lambda_2 = \lambda_3 = 293.11$, $\lambda_4 = \lambda_5 = 472.56$, $\lambda_6 = 523.84$	30
3.4	First six eigenfunctions for a rectangular domain; $\lambda_1 = 58.54$, $\lambda_2 = 102.37$, $\lambda_3 = 103.54$, $\lambda_4 = 144.57$, $\lambda_5 = 168.03$, $\lambda_6 = 171.31$	31
3.5	First six eigenfunctions for an annular wedge subtending 45° at center; $\lambda_1 = 1966.50$, $\lambda_2 = 3200.31$, $\lambda_3 = 3529.09$, $\lambda_4 = 4840.81$, $\lambda_5 = 5191.44$, $\lambda_6 = 5519.98$	32
3.6	First six eigenfunctions for an arbitrarily shaped domain; $\lambda_1 = 131.01$, $\lambda_2 = 184.35$, $\lambda_3 = 258.56$, $\lambda_4 = 291.82$, $\lambda_5 = 339.05$, $\lambda_6 = 380.92$	33
3.7	First ten eigenvalues on a square domain meshed with $8/1$, $9/3$ and $9/4$ -c elements; left: 10×10 elements, right: 40×40 elements.	34
3.8	Convergence of eigenvalues upon mesh refinement.	35
3.9	Time (in seconds) for computation of first one hundred eigenfunctions for different mesh refinements (log-log scale). The data points are joined by straight lines for visibility alone.	35
3.10	Radial variation of the first six eigenfunctions for the annular domain, with $m = 3$. In the finite element solution, the first three of these are mode numbers (9,10), (26,27) and (55,56). The eigenvalues from the semi-numerical approach and the FEM match near-perfectly.	39
3.11	Radial variation of the first four eigenfunctions for a circular disk, with $m = 0$. In the finite element solution, these are mode numbers 1, 6, 15 and 30, respectively. The eigenvalues from the semi-numerical approach and the FEM match near-perfectly.	41
3.12	Radial variation of the first four eigenfunctions for a circular disk, with $m = 1$. In the finite element solution, these are mode numbers (2,3), (9,10), (22,23) and (37,38), respectively. The eigenvalues from the semi-numerical approach and the FEM match near-perfectly.	43

3.13	Radial variation of the first four eigenfunctions for a circular disk, with $m = 2$. In the finite element solution, these are mode numbers (4,5), (13,14), (28,29) and (47,48), respectively. The eigenvalues from the semi-numerical approach and the FEM match near-perfectly.	44
3.14	A representative Mohr's circle at the center C for the case $\sigma_{xy} = 0$	45
3.15	A representative Mohr's circle at C for $m = 0$	46
3.16	First five functions in the sequence (f_k)	51
3.17	First 100 eigenvalues for a square domain obtained using the semi-numerical approach and the FEM.	53
3.18	An annular wedge.	54
3.19	First 100 eigenvalues for the annular wedge with $r_a = 0.1, r_b = 0.3, \theta_0 = \frac{\pi}{4}$, obtained using the semi-numerical approach and the FEM.	57
4.1	Radial variation of true and fitted stress fields σ and σ_N of Example 1, with $N = 100$	61
4.2	E_N versus N , Example 1. Left: linear scale; right: log-log scale. Compare with Figure 1.1.	62
4.3	\tilde{E}_N versus N , Example 1. Left: linear scale; right: log-log scale.	62
4.4	Radial variation of true and fitted stress fields σ and σ_N of Example 2, with $N = 100$	63
4.5	E_N versus N , Example 2. Left: linear scale; right: log-log scale.	64
4.6	\tilde{E}_N versus N , Example 2. Left: linear scale; right: log-log scale.	64
4.7	Radial variation of true and fitted stress fields σ and σ_N of Example 3, with $N = 100$. Note the Gibbs oscillations in $\sigma_{N\theta\theta}$	66
4.8	E_N versus N , Example 3. Left: linear scale; right: log-log scale.	66
4.9	Radial variation of true and fitted thermoelastic stress fields σ (Eqs. 4.7 and 4.8) and σ_N of Example 4, with $N = 100$	67
4.10	E_N versus N , Example 4. Left: linear scale; right: log-log scale.	68
4.11	\tilde{E}_N versus N , Example 4. Left: linear scale; right: log-log scale.	69
4.12	Schematic of the rolling simulation (figure not to scale).	70
4.13	True and fitted stress components (GPa) for the rolling simulation with linear strain hardening (1000 eigenfunctions).	71
4.14	True and fitted stress components (GPa) for the rolling simulation with linear strain hardening (using 10, 50 and 100 eigenfunctions, respectively).	72
4.15	E_N versus N , rolling simulation with linear strain hardening. Left: linear scale; right: log-log scale.	72
4.16	\tilde{E}_N versus N , rolling simulation with linear strain hardening. Left: linear scale; right: log-log scale.	73
4.17	Time (in seconds) for computation of first one thousand eigenfunctions for different refinements of mesh used in rolling simulation (log-log scale). The data points are joined by straight lines for visibility alone.	73
4.18	True and fitted stress components (GPa) for the rolling simulation with Johnson-Cook hardening (1000 eigenfunctions).	75
4.19	E_N versus N , rolling simulation with Johnson-Cook hardening. Left: linear scale; right: log-log scale.	76

4.20	\tilde{E}_N versus N , rolling simulation with Johnson-Cook hardening. Left: linear scale; right: log-log scale.	76
4.21	Schematic of the angular extrusion process at the beginning of the simulation (figure not to scale). All dimensions are in millimetres.	77
4.22	A schematic of the angular extrusion process <i>during</i> the simulation.	78
4.23	True and fitted (using 1000 eigenfunctions) stress components for the angular extrusion simulation (in GPa). Note that x and y axes are unequally scaled for better visibility.	80
4.24	True and fitted (using 10, 50 and 100 eigenfunctions, respectively) stress components for the angular extrusion simulation (in GPa). Note that x and y axes are unequally scaled for better visibility.	81
4.25	The workpiece mesh at the end of the angular extrusion simulation. We see that the corner elements are heavily distorted.	81
4.26	E_N versus N , angular extrusion simulation. Left: linear scale; right: log-log scale.	82
4.27	\tilde{E}_N versus N , angular extrusion simulation. Left: linear scale; right: log-log scale.	82
5.1	First four eigenfunctions for σ_{zz} computed using our own FEM code on an annular domain, with eigenvalues $\lambda = 95.58, 95.58, 192.71, 192.71$, respectively.	91
5.2	A candidate σ_{zz} field (top-left), and fits obtained with the first 100 basis functions ϕ_{zzi} (top-right) and the first 100 Laplace eigenfunctions \tilde{u}_i (bottom).	92
5.3	E_N versus N with our basis ϕ_{zzi} . Left: linear scale; right: log-log scale.	92
5.4	E_N versus N with Laplace eigenfunctions \tilde{u}_i . Left: linear scale; right: log-log scale.	93
5.5	Schematic of an axially stressed rail (adapted from Figure 1.12 of [1]). We use the values of the axial stress at 10 points, marked with light yellow crosses, for interpolation.	94
5.6	The first four eigenfunctions ϕ_{zzi} on the rail geometry.	95
5.7	Interpolated axial stress (in MPa) using the first N eigenfunctions ϕ_{zzi} , with $N = 2, 4, 6$ and 8	96
5.8	Interpolated axial stress (in MPa) using the first N Laplace operator eigenfunctions with zero boundary value \tilde{u}_i , with $N = 4$ and 6	96
5.9	First three eigenfunctions for out of plane shear components computed using our own FEM code on an annular domain, with eigenvalues $\lambda = 293.41, 293.41$ and 356.19 , respectively.	100
5.10	A candidate out of plane shear stress field (top row), and fits obtained with the first 200 basis functions v_i (middle row) and the first 200 Stokes operator eigenfunctions \mathbf{v}_i (bottom row).	102
5.11	E_N versus N with our basis v_i . Left: linear scale; right: log-log scale.	103
5.12	E_N versus N with the Stokes operator eigenfunctions \mathbf{v}_i . Left: linear scale; right: log-log scale.	103
5.13	First five localized 1D eigenfunctions for $n = 10$ and $n = 20$	106

5.14	First three eigenfunctions on an arbitrarily shaped domain, localized around the origin.	111
5.15	Radial variation of the first four spatially localized eigenfunctions on an annular geometry with $n = 10$	113
5.16	Radial variation of the first four spatially localized eigenfunctions on an annular geometry with $n = 20$	114
5.17	Radial variation of the candidate localized residual stress field fitted with 10 weighted (with $n = 20$) and 10 unweighted eigenfunctions.	115
5.18	Fitting error E_N versus the number of eigenfunctions N ; left: linear scale, right: loglog scale.	116
6.1	Radial variation of the first five free vibration modes with $m = 3$ in an annulus, corresponding to free-free boundary condition.	123
6.2	Radial variation of the actual and the approximate displacements obtained using the virtual work method, with 10, 20 and 100 free vibration modes.	125
6.3	Radial variation of the actual and the approximate stresses obtained using the virtual work method, with 10, 20 and 100 free vibration modes.	126
6.4	Approximation error E_N versus N with the free vibration modes. Left: linear scale; right: log-log scale.	126
6.5	Radial variation of the actual and the approximate displacements obtained using virtual work, with 10, 20 and 100 Laplace operator eigenfunctions.	127
6.6	Radial variation of the the actual and the approximate stresses obtained using virtual work, with 10, 20 and 100 Laplace operator eigenfunctions.	127
6.7	Approximation error E_N versus N using the Laplace operator eigenfunctions. Left: linear scale; right: log-log scale.	128
6.8	Radial variation of the actual and the approximate traces $\bar{\sigma}$ and $\bar{\sigma}_N^A$ using the weighted residual method, with 10, 20 and 100 residual stress basis functions.	130
6.9	Approximation error E_N versus N using the weighted residual method with ϕ_i . Left: linear scale; right: log-log scale.	130
6.10	Radial variation of the actual and the approximate traces $\bar{\sigma}$ and $\bar{\sigma}_N^A$ using least squares approximation, with 10, 20 and 100 residual stress basis functions.	131
6.11	Approximation error E_N versus N using least squares approximation with ϕ_i . Left: linear scale; right: log-log scale.	131
6.12	Radial variation of $\bar{\sigma}$ and $\bar{\sigma}^F$, and their r -derivatives. We see that the second derivatives, and hence the Laplacians, do not match well.	133
6.13	Squared relative L^2 norm of $\Delta\bar{\sigma} - \Delta\bar{\sigma}^F$. Left: linear scale; right: log-log scale.	134
6.14	Radial variation of the actual and the approximate stresses with a correct application of the weighted residual method, using 10, 20 and 100 residual stress basis functions ϕ_i	138
6.15	Approximation error E_N versus N with a correct application of the weighted residual method using ϕ_i . Left: linear scale; right: log-log scale.	139
6.16	Radial variation of the first four residual stress eigenfunctions Φ_i for the annular domain, with $m = 3$	143

6.17	Radial variation of the thermal stress σ of Section 6.1 and its fits σ^F using 10, 20 and 50 residual stress basis functions Φ_i	144
6.18	Fitting error E_N versus N for fitting of the thermal stress σ of Section 6.1 using Φ_i . Left: linear scale; right: log-log scale.	145
6.19	Radial variation of the actual and the approximate stresses using the weighted residual method with 10, 20 and 50 residual stress basis functions Φ_i	148
6.20	Approximation error E_N versus N using residual stress basis functions Φ_i . Left: linear scale; right: log-log scale.	149

Abbreviations

FEM Finite Element Method
ODE Ordinary Differential Equation
PDE Partial Differential Equation

Chapter 1

Introduction

1.1 Motivation

Practically all solid manufactured objects have residual stress locked in them as a consequence of processing history. This thesis is primarily concerned with mathematical descriptions of general states of residual stress, rather than the specific physical history that produced a specific residual stress field. In particular, we consider basis functions for interpolating such residual stress fields in finite solid bodies. We consider bodies that are arbitrarily shaped, not subjected to body forces, in equilibrium, and with traction free boundaries, but with non-zero internal residual stresses. The physical sources of the residual stresses may be prior manufacturing processes, deformation history, thermal gradients, or other phenomena. As noted, however, here we are interested solely in mathematical ways to discuss or describe residual stress fields that already exist, independent of the physical mechanisms that have produced them.

For example, if residual stress states are experimentally determined at N points on a manufactured component, and if reasonable smoothness in residual stress variations can be assumed, how should the residual stresses be interpolated between those points in space? As another example, in a metal forming simulation, can final residual stresses in the formed component be reported using some sequence of orthogonal basis functions that is specifically constructed, *in advance*, for the domain of interest?

With the above motivation, we seek self-equilibrating traction-free fields ϕ_i defined on the finite body of interest, such that linear combinations $\sum_{i=1}^{\infty} a_i \phi_i$ can capture any sufficiently regular residual stress field.

In this work, we will construct such fields ϕ_i *via* stationary values of a suitable quadratic functional. These fields ϕ_i will serve as a basis for representing arbitrary residual stress fields in bodies of a given but arbitrary shape, without regard for the physical source of the residual stress. To the best of our knowledge, such a basis has not been presented in the mechanics literature before¹. The construction of such a basis is not obvious in advance. For example, readers familiar with vibration theory [3] may be interested to see that the stress fields induced by vibration modes *cannot* be used for such ϕ_i , because those modal stresses necessarily satisfy the strain-compatibility conditions of linear elasticity while not satisfying equilibrium, whereas residual stresses necessarily satisfy equilibrium and violate strain-compatibility equations of linear elasticity². To see the latter easily, we can use the result that for a linearly elastic body subjected to given tractions and body forces, the displacement is unique up to a rigid motion (see page 45, theorem 4.3.1 of [4]). The solution to zero traction and zero body force is therefore zero stress and zero displacement, unique up to rigid body motions, by the above result. But the stress corresponding to rigid body motions is zero. Hence, non-zero residual stresses cannot be caused by compatible strains in linear elasticity.

As motivation for the development that is to follow, in order to demonstrate that vibration mode-induced (or modal) stresses *cannot* be used to construct a basis for residual stresses, we choose a candidate residual stress field in an annular domain of inner radius 0.1 and outer radius 0.3, with components

$$\begin{aligned}\sigma_{rr}(r, \theta) &= \left(-\frac{0.067}{r^2} + \frac{1.6}{r} - 12.833 + 40r - 41.667r^2 \right) \cos 3\theta, \\ \sigma_{r\theta}(r, \theta) &= \left(-\frac{0.022}{r^2} + 5.5 - 40r + 75r^2 \right) \sin 3\theta, \\ \sigma_{\theta\theta}(r, \theta) &= (3.667 - 40r + 100r^2) \cos 3\theta.\end{aligned}\tag{1.1}$$

We will properly motivate and use this stress field later in the thesis, after presenting our theory. Here we merely attempt to *numerically* approximate the above stress field with the first N modal stresses on this domain, with $1 \leq N \leq 50$. An approximation error E_N (which will be described fully in due course) is plotted against N in Figure 1.1. We see that the error does not seem to be converging to zero. The implications of Figure 1.1, which is given here only for motivation, will be clear as we present our theory in subsequent sections.

¹We have published the work presented in Chapters 2 - 4 in [2].

²Equilibrium, zero tractions *and* compatibility lead to zero stresses as a unique solution.

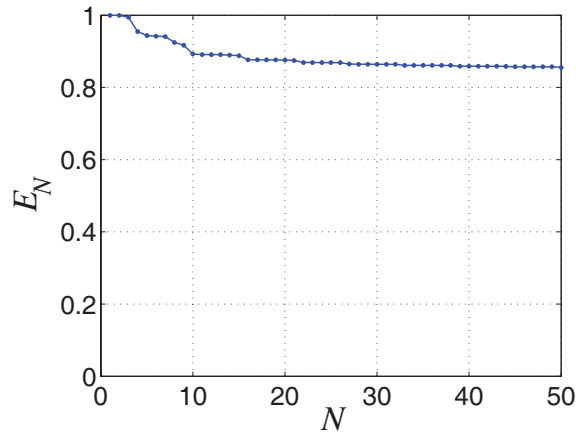


FIGURE 1.1: Approximation error versus number of (vibrational) modal stress fields used. Convergence to zero is not apparent and seems unlikely.

Readers may note that residual stresses in a component can be either beneficial or harmful, depending on the application. For example, they can impede the growth of surface micro-cracks and extend fatigue life, or cause warping in manufactured components, respectively. In either case, it is important to characterize a body’s residual stress state with sufficient accuracy, both in the bulk and at the surface. Readers may refer to [1, 5, 6] for comprehensive discussions on the origin and measurement of residual stresses from differing sources and at different length scales. Broadly, some common sources of residual stresses are thermal effects [7, 8], inclusions and defects [9–14], and biological growth [15–18], in addition to prior inelastic deformation.

A substantial amount of literature on residual stresses pays explicit attention to incompatibility, e.g., through equations of the form $\nabla^4\phi = \eta$, where nonzero η is the source of incompatibility [13, 14, 16]. As mentioned above, we directly seek a basis for expanding and interpolating the stress components without approaching the problem through specific choices of η , i.e., through specific sources or types of incompatibility. We acknowledge here the work of Hoger [19, 20], who discussed the general residual stress fields possible in an elastic cylinder, but did not seek to develop a basis for interpolation on arbitrary geometries as we do here. Her papers led to interesting subsequent work on elastic bodies with residual stress, in which the strain energy density is considered to be a function of both the deformation gradient tensor and the initial residual stress. These works, like ours, make no assumptions about the origin of the prescribed residual stress [19–26]. These works, especially those concerned with calculating the optimal residual stress that results in a targeted Cauchy stress (e.g. [27]), deviate almost immediately from our approach in that they focus on elastic bodies.

We also distinguish our approach from a more restricted interpolation employed in some destructive measurement techniques for residual stresses. In those techniques, elasticity-based relationships between the measured strain data [28–31], and the tractions that *were* acting on surfaces that have since been exposed by cutting [32], are the key considerations. In such measurements, the stress is often interpolated along a single spatial coordinate (like depth of cut), using splines, polynomials, Fourier series, etc. Unlike those interpolants defined on specific line segments, here we will develop self-equilibrating, traction free, tensor valued interpolants for the entire body without appeal to any underlying material constitutive relations. We also acknowledge the challenging problem of inversion of boundary data (displacements, strains) to estimate the residual stress in a three dimensional body [32–35]. The orthonormal basis we develop here, in such applications, may ease the need for statistical regularization [36, 37]. Such potential applications provide yet another motivation for our work.

Finally we distinguish our approach from stress-based formulations derived in linear elasticity using variations of a positive definite functional of the stress gradient [38–41], an example of which is the Beltrami-Michell equation [42]. These formulations, too, refer specifically to linearly elastic materials, and do *not* construct basis functions. Our aims are quite different, as explained above. In particular, we will consider variations of a functional involving the stress gradient, which leads to an eigenvalue problem, which in turn yields a basis we can use. In the applied mathematics literature, there are similar issues studied using the somewhat simpler Stokes operator from incompressible fluid mechanics (see e.g., [43]; we will discuss these similarities later). In those works, to prove that the eigenfunctions of the Stokes operator span the space of divergence-free velocity fields with zero boundary value, the spectral theorem is used. Readers wishing to read a general discussion of the spectral theorem may see, e.g., [44]. However, our discussion is less formal, accessible to a broader audience, and resembles the development of classical vibration theory [3].

Our basic formulation, though first developed for two dimensions, is easily extended to three dimensions.

Having developed a basis, we first compute it numerically on planar bodies. The computed basis functions are then used to fit given, but arbitrary, candidate residual stress fields. Subsequently, for fitting residual stress of certain special types, such as those which are axially invariant or spatially localized, we develop new eigenfunctions with these same characteristics by appropriately modifying our original extremization problem. Finally,

we demonstrate yet another application of our basis by using it to *compute* approximate residual stresses using the weighted residual method.

1.2 Organization of the thesis

This thesis is organized as follows. In Chapter 2, we pose an extremization problem in 2D that leads to an eigenvalue problem. We show that the solutions of this eigenvalue problem exist, and that they span the space of all residual stresses of interest to us. Extension of the theory to 3D is presented at the end of the chapter.

In general, the eigenvalue problem of Chapter 2, which involves a system of partial differential equations (PDEs), is not solvable analytically. Chapter 3 is devoted to numerical solutions of the eigenvalue problem in 2D. The numerical methods used are broadly divided into two categories: finite element method (FEM), and semi-numerical methods. The former can be used to compute the eigenfunctions in bodies of arbitrary shapes, and the latter exploit symmetries of some special geometries to convert the PDE system into a system of ordinary differential equations (ODEs) or algebraic equations. We consider four such special geometries: an annulus, a circular disk, a rectangle and an annular wedge. We observe that the solutions from FEM and semi-numerical methods agree in all cases.

In Chapter 4, we consider some candidate residual stress fields, and fit them using the eigenfunctions developed in the previous chapters. In the first part of the chapter, we consider residual stress fields on an annular geometry, and fit them using the eigenfunctions computed semi-numerically in Chapter 3. Four such residual stresses are considered: two hypothetically made up, one from shrink fitting of two concentric elastic cylinders, and one from non-uniform heating of an elastic annulus. In the second part of the chapter, we consider three residual stress fields obtained by simulating 2D metal forming processes of rolling and angular extrusion in the FEM software Abaqus, and fit them using eigenfunctions computed using the FEM formulation of Chapter 3. We demonstrate the convergence of the fits to the actual fields in both L^2 and H^1 norms.

In Chapter 5, we show that the eigenvalue problem of Chapter 2 is amenable to modifications for special purposes. In the first part of the chapter, we consider long (in the z -direction) prismatic geometries, and show that the eigenvalue problem of Chapter 2 decouples into three separate eigenvalue problems for such bodies: one for the planar stress components $(\sigma_{xx}, \sigma_{yy}, \sigma_{xy})$, one for the out of plane shear stress components $(\sigma_{xz}, \sigma_{yz})$ and one for the axial stress (σ_{zz}) . In the second part of the chapter, we modify our eigenvalue

problem to obtain eigenfunctions that are localized in a small 2D region, and decay rapidly away from it. Such eigenfunctions are more suitable for residual stresses that are localized, such as that near a crack tip, or near the surface in a shot peened body.

In Chapter 6, we solve a ‘forward’ problem using our residual stress basis functions, in the sense that instead of fitting an already given residual stress field, we *solve* for a residual stress given its physical governing differential equation. For this purpose, we take up the problem of non-uniform heating of a thermoelastic annulus. We solve for the resulting residual stress using the weighted residual method with both free vibration displacement modes and our stress eigenfunctions as the weighting functions; and observe that the latter give much faster convergence. We discuss in detail some unexpected issues of convergence and boundary conditions, and present some interesting new results necessary for developing a correct weighted residual approximation.

In Chapter 7, we discuss how the proof presented in Chapter 2 of eigenfunctions forming a basis could be adapted for the modified extremization problems considered in the subsequent chapters.

In Chapter 8, we present conclusions and discuss possible future work.

1.3 Notation

We close this introduction with a brief description of the notation used in this thesis. The dot product ‘ \cdot ’ between two tensors of the same order represents total tensor contraction. Using Einstein’s summation convention,

$$\mathbf{A} \cdot \mathbf{B} = \begin{cases} A_i B_i & \text{if } \mathbf{A} \text{ and } \mathbf{B} \text{ are vectors,} \\ A_{ij} B_{ij} & \text{if } \mathbf{A} \text{ and } \mathbf{B} \text{ are second order tensors,} \\ A_{ijk} B_{ijk} & \text{if } \mathbf{A} \text{ and } \mathbf{B} \text{ are third order tensors,} \end{cases}$$

where A_i, A_{ij}, A_{ijk} etc. are the Cartesian components of the tensor \mathbf{A} (likewise for \mathbf{B}). For a second order tensor \mathbf{A} , $\text{div}\mathbf{A}$ represents $A_{ij,j}\mathbf{e}_i$, where a subscript following a comma denotes a partial derivative and \mathbf{e}_i are the unit Cartesian basis vectors. For a vector \mathbf{v} , $\mathbf{A}\mathbf{v}$ represents $A_{ij}v_j\mathbf{e}_i$. The dyadic product $\mathbf{u} \otimes \mathbf{v}$ for vectors \mathbf{u} and \mathbf{v} is defined by its action on a vector \mathbf{w} as $(\mathbf{u} \otimes \mathbf{v})\mathbf{w} = (\mathbf{v} \cdot \mathbf{w})\mathbf{u}$. The cross product $\mathbf{u} \times \mathbf{v}$ is defined as $\epsilon_{ijk}u_iv_j\mathbf{e}_k$, where ϵ is the permutation tensor.

Chapter 2

Extremization problem and governing PDEs

In this chapter, we pose an extremization problem that leads to an eigenvalue problem. We show that the solutions to this eigenvalue problem form an orthogonal basis for the set of all residual stress fields of interest to us.

The chapter is arranged as follows. Sections 2.1 through 2.4 are for 2D bodies. In Section 2.1, we define the set of residual stress fields that are of interest to us, and formally state the problem we will address. In Section 2.2, we propose a quadratic functional involving the gradient of an input stress field, and derive necessary and sufficient conditions satisfied by stationary points of this functional using the calculus of variations. These conditions are in the form of an eigenvalue problem. In Section 2.3, we show that the eigenfunctions ϕ_i satisfying this eigenvalue problem form an orthogonal sequence, with real and positive eigenvalues. In Section 2.4, we show that ϕ_i , assuming that they exist, span the space of residual stresses in L^2 and H^1 norms. In Section 2.5 we extend our theory to three dimensions, and derive the corresponding eigenvalue problem and boundary conditions. Finally, in Section 2.6, we prove the existence of ϕ_i , something which was assumed in Section 2.4. Due to its heavier mathematical content, we have kept this section at the end of the chapter.

2.1 Problem statement

Let Ω be an open, bounded, sufficiently regular domain in \mathbb{R}^2 with area $|\Omega|$ (the extension to \mathbb{R}^3 is discussed towards the end of this chapter). The unit outward normal \mathbf{n} at each point on the boundary $\partial\Omega$ is assumed well defined¹.

Let us denote the set of symmetric second order tensor fields defined over Ω by “Sym”. We define:

$$\mathcal{S} = \left\{ \boldsymbol{\sigma} \mid \boldsymbol{\sigma} \in \text{Sym}, \operatorname{div} \boldsymbol{\sigma} = \mathbf{0}, \boldsymbol{\sigma} \mathbf{n}|_{\partial\Omega} = \mathbf{0}, \int_{\Omega} \boldsymbol{\sigma} \cdot \boldsymbol{\sigma} dA < \infty, \int_{\Omega} \nabla \boldsymbol{\sigma} \cdot \nabla \boldsymbol{\sigma} dA < \infty \right\}, \quad (2.1)$$

where the five conditions included imply symmetry, equilibrium, zero tractions, square integrability of stresses, and square integrability of stress gradients respectively; and dA is an infinitesimal area element of the domain Ω ².

The inner product between two elements $\boldsymbol{\sigma}_1$ and $\boldsymbol{\sigma}_2$ of \mathcal{S} is taken to be

$$(\boldsymbol{\sigma}_1, \boldsymbol{\sigma}_2) = \int_{\Omega} \boldsymbol{\sigma}_1 \cdot \boldsymbol{\sigma}_2 dA,$$

and accordingly, the norm of any $\boldsymbol{\sigma} \in \mathcal{S}$ is

$$\|\boldsymbol{\sigma}\| = (\boldsymbol{\sigma}, \boldsymbol{\sigma})^{\frac{1}{2}} = \left(\int_{\Omega} \boldsymbol{\sigma} \cdot \boldsymbol{\sigma} dA \right)^{\frac{1}{2}}. \quad (2.2)$$

Let $\bar{\mathcal{S}}$ be the closure of \mathcal{S} . All residual stresses of interest to us are elements of $\bar{\mathcal{S}}$ ³. We seek a sequence of functions ϕ_i that span $\bar{\mathcal{S}}$.

¹Isolated corners can be rounded out using tiny radii, for simplicity. In finite element approximations, the weak formulation allows a piecewise C^1 boundary. For the definition of C^n continuity, please see page 50 of [45].

²It is easy to check that \mathcal{S} is a real vector space. For instance, it satisfies linearity: if $\boldsymbol{\sigma}_1$ and $\boldsymbol{\sigma}_2$ are elements of \mathcal{S} and α is a real number, then the function $\boldsymbol{\sigma} = \boldsymbol{\sigma}_1 + \alpha\boldsymbol{\sigma}_2$ satisfies $\operatorname{div} \boldsymbol{\sigma} = \mathbf{0}$, $\boldsymbol{\sigma} \mathbf{n} = \mathbf{0}$, $\int_{\Omega} \boldsymbol{\sigma} \cdot \boldsymbol{\sigma} dA < \infty$ and $\int_{\Omega} \nabla \boldsymbol{\sigma} \cdot \nabla \boldsymbol{\sigma} dA < \infty$; so, $\boldsymbol{\sigma}$ belongs to \mathcal{S} . Similarly, it can be shown that \mathcal{S} also satisfies commutativity, associativity, distributivity, and has an additive identity and a multiplicative identity.

³Residual stresses are either (a) elements of \mathcal{S} , or (b) have simple *internal* discontinuities in addition. These are both elements of $\bar{\mathcal{S}}$. Stresses in category (b) are not elements of \mathcal{S} because their gradients are not square-integrable. Note however that not all elements of $\bar{\mathcal{S}}$ are residual stress fields. For example, there could be elements of $\bar{\mathcal{S}}$ which may have discontinuities at the boundary. For such fields, $\boldsymbol{\sigma} \mathbf{n} = \mathbf{0}$ on the boundary may not be physically meaningful; but such fields are not of physical interest to us.

2.2 Solution approach *via* an extremization problem

Let us seek stationary points of the functional

$$J_0(\tilde{\boldsymbol{\sigma}}) = \frac{1}{2} \int_{\Omega} \nabla \tilde{\boldsymbol{\sigma}} \cdot \nabla \tilde{\boldsymbol{\sigma}} \, dA \quad (2.3)$$

in \mathcal{S} , subject to the normalization constraint $\int_{\Omega} \tilde{\boldsymbol{\sigma}} \cdot \tilde{\boldsymbol{\sigma}} \, dA = 1$.

We note that for any nonzero residual stress field, the quantity J_0 must be nonzero (see e.g., [19]).

We will use the calculus of variations [46]. Since the constraint $\operatorname{div} \tilde{\boldsymbol{\sigma}} = \mathbf{0}$ is defined pointwise in Ω , we introduce a spatially varying Lagrange multiplier $\boldsymbol{\mu}$ for it. Since $\int_{\Omega} \tilde{\boldsymbol{\sigma}} \cdot \tilde{\boldsymbol{\sigma}} \, dA = 1$ is a scalar integral constraint, we use a constant scalar Lagrange multiplier $\frac{\lambda}{2}$ for it. We then consider variations of

$$J(\hat{\boldsymbol{\sigma}}) = \int_{\Omega} \left\{ \frac{1}{2} \nabla \hat{\boldsymbol{\sigma}} \cdot \nabla \hat{\boldsymbol{\sigma}} - \frac{\lambda}{2} \left(\hat{\boldsymbol{\sigma}} \cdot \hat{\boldsymbol{\sigma}} - \frac{1}{|\Omega|} \right) - \boldsymbol{\mu} \cdot (\operatorname{div} \hat{\boldsymbol{\sigma}}) \right\} \, dA, \quad (2.4)$$

where we have used a “hat” instead of a “tilde” on $\hat{\boldsymbol{\sigma}}$ because it belongs to the larger, or less restricted, set

$$\mathcal{R} = \left\{ \hat{\boldsymbol{\sigma}} \mid \hat{\boldsymbol{\sigma}} \in \operatorname{Sym}, \hat{\boldsymbol{\sigma}} \mathbf{n}|_{\partial\Omega} = \mathbf{0}, \int_{\Omega} \hat{\boldsymbol{\sigma}} \cdot \hat{\boldsymbol{\sigma}} \, dA < \infty, \int_{\Omega} \nabla \hat{\boldsymbol{\sigma}} \cdot \nabla \hat{\boldsymbol{\sigma}} \, dA < \infty \right\}. \quad (2.5)$$

If a stationary point of Eq. 2.4 is $\boldsymbol{\sigma}$ then, for arbitrary infinitesimal variations $\boldsymbol{\zeta} \in \mathcal{R}$, we must have

$$\int_{\Omega} \{ \nabla \boldsymbol{\sigma} \cdot \nabla \boldsymbol{\zeta} - \lambda \boldsymbol{\sigma} \cdot \boldsymbol{\zeta} - \boldsymbol{\mu} \cdot (\operatorname{div} \boldsymbol{\zeta}) \} \, dA = 0. \quad (2.6)$$

Assuming that $\boldsymbol{\sigma}$ is sufficiently regular, and using integration by parts and the divergence theorem⁴, we obtain

$$\int_{\partial\Omega} \{ \nabla_n \boldsymbol{\sigma} \cdot \boldsymbol{\zeta} - \boldsymbol{\mu} \cdot (\boldsymbol{\zeta} \mathbf{n}) \} \, ds - \int_{\Omega} \{ \Delta \boldsymbol{\sigma} - \nabla \boldsymbol{\mu} + \lambda \boldsymbol{\sigma} \} \cdot \boldsymbol{\zeta} \, dA = 0, \quad (2.7)$$

where $\nabla_n \boldsymbol{\sigma}$ is the normal gradient of $\boldsymbol{\sigma}$ at $\partial\Omega$. In Cartesian coordinates, $\nabla_n \boldsymbol{\sigma} = \sigma_{ij,k} n_k$.

⁴We need more regularity on $\boldsymbol{\sigma}$ than what is afforded to elements of \mathcal{S} . We show in Appendix A that (a) this regularity requirement is that $\Delta \boldsymbol{\sigma}$ should be square-integrable, and (b) $\boldsymbol{\sigma}$, on account of being a stationary point, meets this requirement.

In Eq. 2.7, since $\zeta \in \mathcal{R}$, $\zeta \mathbf{n}$ on $\partial\Omega$ is zero, yielding

$$\int_{\partial\Omega} \nabla_n \boldsymbol{\sigma} \cdot \boldsymbol{\zeta} ds - \int_{\Omega} \{\Delta \boldsymbol{\sigma} - \nabla \boldsymbol{\mu} + \lambda \boldsymbol{\sigma}\} \cdot \boldsymbol{\zeta} dA = 0. \quad (2.8)$$

By considering the set of $\boldsymbol{\zeta}$ which are zero on $\partial\Omega$, we conclude that⁵

$$-\Delta \boldsymbol{\sigma} + \nabla \boldsymbol{\mu} - \lambda \boldsymbol{\sigma} = \mathbf{R} \quad \text{in } \Omega,$$

where \mathbf{R} is some skew symmetric second order tensor field; and where the scalar eigenvalue λ and the vector field $\boldsymbol{\mu}$ need to be determined along with $\boldsymbol{\sigma}$. Adding the above equation to its transpose and dividing by two,

$$-\Delta \boldsymbol{\sigma} + \nabla_s \boldsymbol{\mu} - \lambda \boldsymbol{\sigma} = \mathbf{0} \quad \text{in } \Omega, \quad (2.9)$$

where

$$\nabla_s \boldsymbol{\mu} = \frac{\nabla \boldsymbol{\mu} + (\nabla \boldsymbol{\mu})^T}{2}.$$

Equation 2.8 reduces to the line integral alone, i.e.,

$$\int_{\partial\Omega} \nabla_n \boldsymbol{\sigma} \cdot \boldsymbol{\zeta} ds = 0. \quad (2.10)$$

Considering $\boldsymbol{\zeta}$ on the boundary, at each point we have $\boldsymbol{\zeta} \mathbf{n} = \mathbf{0}$, so \mathbf{n} is an eigenvector of $\boldsymbol{\zeta}$. Since $\boldsymbol{\zeta}$ is symmetric, the local tangent vector \mathbf{t} must be the other eigenvector (we are in two dimensions). It follows that we can consider $\boldsymbol{\zeta} = \kappa(s) \mathbf{t} \otimes \mathbf{t}$ for any scalar $\kappa(s)$ varying arbitrarily along the boundary. The arbitrariness of $\kappa(s)$ implies that

$$\nabla_n \boldsymbol{\sigma} \cdot (\mathbf{t} \otimes \mathbf{t}) = 0 \quad (2.11)$$

everywhere on the boundary $\partial\Omega$. Less formally, this conditions means that the normal gradient of the circumferential stress is zero at the boundary. If the domain is circular, this circumferential stress is the hoop stress.

Finally, variation of the Lagrange multiplier $\boldsymbol{\mu}$ gives the equilibrium condition

$$\text{div } \boldsymbol{\sigma} = \mathbf{0},$$

⁵Since $\boldsymbol{\zeta}$ is symmetric, by localizing it near any $\mathbf{x} \in \Omega$ we conclude that the integrand at \mathbf{x} is skew symmetric.

and variation of the Lagrange multiplier $\frac{\lambda}{2}$ gives

$$\int_{\Omega} \boldsymbol{\sigma} \cdot \boldsymbol{\sigma} \, dA = 1.$$

To summarize, any sufficiently regular unit-norm stationary point of J_0 in \mathcal{S} , assuming for simplicity that one exists, is a solution to the following eigenvalue problem⁶:

$$\begin{aligned} -\Delta \boldsymbol{\sigma} + \nabla_s \boldsymbol{\mu} &= \lambda \boldsymbol{\sigma} & \text{and} & & \operatorname{div} \boldsymbol{\sigma} &= \mathbf{0} & \text{in } \Omega, \\ \boldsymbol{\sigma} \mathbf{n} &= \mathbf{0} & \text{and} & & \nabla_n \boldsymbol{\sigma} \cdot (\mathbf{t} \otimes \mathbf{t}) &= 0 & \text{on } \partial\Omega. \end{aligned} \quad (2.12)$$

The eigenvalue problem in Eqs. 2.12 can be solved on arbitrary domains using the FEM, and we will present some such solutions later in this thesis. For the simple case of an annular domain, it can also be solved as a two-point boundary value problem using ODE solvers after separation of variables, and we will present such solutions as well, obtaining complete agreement with finite element solutions.

Proceeding now with our theoretical development, our primary claim is that the sequence of eigenfunctions $\boldsymbol{\sigma}_k$, computed for a given domain Ω , forms a basis for $\bar{\mathcal{S}}$ defined on Ω . Any state of residual stress in $\bar{\mathcal{S}}$ can be expressed as a linear combination of these basis functions. We shall henceforth denote these stress-eigenfunctions as $\boldsymbol{\phi}$ throughout this thesis.

2.3 Orthonormality of the eigenfunctions

Let λ be an eigenvalue, and $\boldsymbol{\phi}$ and $\boldsymbol{\mu}$ represent the corresponding eigenfunction. Let $\boldsymbol{\sigma}$ be any element of \mathcal{S} (recall Eq. 2.1). Consider the inner product of the first equation in 2.12 with $\boldsymbol{\sigma}$, i.e.,

$$\int_{\Omega} (-\Delta \boldsymbol{\phi} + \nabla_s \boldsymbol{\mu} - \lambda \boldsymbol{\phi}) \cdot \boldsymbol{\sigma} \, dA = 0, \quad (2.13)$$

which reduces to (see Appendix C)

$$\int_{\Omega} (\nabla \boldsymbol{\phi} \cdot \nabla \boldsymbol{\sigma} - \lambda \boldsymbol{\phi} \cdot \boldsymbol{\sigma}) \, dA = 0 \quad (2.14)$$

for any eigenvalue-eigenfunction pair $(\lambda, \boldsymbol{\phi})$ and any $\boldsymbol{\sigma} \in \mathcal{S}$.

⁶These conditions are also *sufficient* for stationarity, i.e., if $\boldsymbol{\sigma}$ is a solution to this eigenvalue problem, it must be a stationary point. See Appendix B.

Now let (λ_p, ϕ_p) and (λ_q, ϕ_q) be two distinct eigenvalue-eigenvector sets of Eq. 2.12, with μ_p and μ_q the corresponding Lagrange multipliers. By Eq. 2.14,

$$\begin{aligned} \int_{\Omega} \nabla \phi_p \cdot \nabla \phi_q dA &= \lambda_p \int_{\Omega} \phi_p \cdot \phi_q dA, \\ \int_{\Omega} \nabla \phi_q \cdot \nabla \phi_p dA &= \lambda_q \int_{\Omega} \phi_q \cdot \phi_p dA, \end{aligned} \quad (2.15)$$

and if $\lambda_p \neq \lambda_q$, then

$$\int_{\Omega} \phi_p \cdot \phi_q dA = 0 \text{ and } \int_{\Omega} \nabla \phi_p \cdot \nabla \phi_q dA = 0. \quad (2.16)$$

If $\lambda_p = \lambda_q$ but $\phi_p \neq \phi_q$, then we can choose ϕ_p and ϕ_q to be orthogonal, and Eq. 2.16 still holds. Finally, if $\lambda_p = \lambda_q$ and $\phi_p = \phi_q$ but $\mu_p \neq \mu_q$, then $\nabla_s \mu_p = \nabla_s \mu_q$, and there is no distinction between these two cases.

Following arguments used by Rayleigh [3], we note that the eigenvalues λ are real and positive. To obtain a contradiction, if λ_p is complex with corresponding complex eigenfunction ϕ_p , then by the linearity of Eq. 2.12 (for details, please see Appendix D) it follows that their complex conjugates $\overline{\lambda_p} = \lambda_q$ and $\overline{\phi_p} = \phi_q$ give another solution pair. Using these two eigenfunctions in either of Eqs. 2.15, we obtain a contradiction; so λ is real. The eigenfunctions are real as well. Next, using the same ϕ twice (i.e., $p = q$), we conclude that $\lambda > 0$ because the left hand side is strictly positive for any nonzero residual stress.

We thus have an orthogonal sequence of eigenfunctions, satisfying Eq. 2.16 whenever $p \neq q$. The orthogonal sequence of stress eigenfunctions ϕ_p is assumed to be normalized such that

$$\int_{\Omega} \phi_p \cdot \phi_p dA = 1, \quad p = 1, 2, 3, \dots$$

to obtain an *orthonormal* sequence, with

$$\int_{\Omega} \nabla \phi_p \cdot \nabla \phi_p dA = \lambda_p.$$

We can arrange this sequence⁷ simply in order of increasing λ_p .

⁷ In some cases we may restrict attention to a subset of eigenfunctions. For an annular domain, for example, we may sometimes consider only eigenfunctions with a fixed circumferential wave number (e.g., $m = 3$).

2.4 Basis of $\bar{\mathcal{S}}$

Consider the sequence $(\lambda_p, \phi_p, \mu_p)$, $p = 1, 2, \dots$. There are infinitely many such eigenvalue-eigenfunction pairs, i.e., the sequence is not finite. For proof, we argue by contradiction.

Assume that only a finite number N of such eigenvalue-eigenfunction pairs exist.

Let \mathcal{S}_N be the subspace of \mathcal{S} spanned by the finite sequence $\{\phi_p\}$, $p = 1, 2, \dots, N$. Let $\mathcal{S}_{N\perp}$ be the orthogonal complement of \mathcal{S}_N in \mathcal{S} . Let us now extremize J_0 (recall Eq. 2.3) within $\mathcal{S}_{N\perp}$. To the extremizer σ , restriction to $\mathcal{S}_{N\perp}$ adds N integral constraints to the previous extremization problem, namely

$$\int_{\Omega} \phi_p \cdot \sigma \, dA = 0, \quad p = 1, 2, \dots, N, \quad (2.17)$$

for which we introduce N new scalar Lagrange multipliers, $\nu_1, \nu_2, \dots, \nu_N$, and obtain the new equations (recall Eq. 2.12)

$$\begin{aligned} -\Delta \sigma + \nabla_s \mu &= \lambda \sigma + \sum_{p=1}^N \nu_p \phi_p & \text{and} & \quad \operatorname{div} \sigma = \mathbf{0} & \quad \text{in } \Omega, \\ \sigma n &= \mathbf{0} & \text{and} & \quad \nabla_n \sigma \cdot (\mathbf{t} \otimes \mathbf{t}) = 0 & \quad \text{on } \partial\Omega, \end{aligned} \quad (2.18)$$

along with Eq. 2.17. We assume that at least one solution $\tilde{\sigma} \in \mathcal{S}_{N\perp}$, with associated $\tilde{\mu}$, $\tilde{\lambda}$ and $\tilde{\nu}_p$, to the above eigenvalue problem exists. Accordingly,

$$-\Delta \tilde{\sigma} + \nabla_s \tilde{\mu} = \tilde{\lambda} \tilde{\sigma} + \sum_{p=1}^N \tilde{\nu}_p \phi_p. \quad (2.19)$$

The proof of existence of an extremizer in $\mathcal{S}_{N\perp}$ is technical and is presented in Section 2.6.

Consider any eigenfunction ϕ_k , $1 \leq k \leq N$. Compute the inner product of Eq. 2.19 with ϕ_k . By the reasoning in Appendix C, the $\nabla_s \tilde{\mu}$ term drops out. By Eq. 2.17, the $\tilde{\lambda} \tilde{\sigma}$ term drops out. By orthonormality of the eigenfunctions obtained so far, $\sum_{p=1}^N \tilde{\nu}_p \phi_p$ contributes just $\tilde{\nu}_k$. By the manipulations that led to Eq. 2.14, the inner product thus becomes

$$\int_{\Omega} \nabla \tilde{\sigma} \cdot \nabla \phi_k \, dA = \tilde{\nu}_k. \quad (2.20)$$

However, since $\tilde{\sigma}$ is an element of \mathcal{S} and also orthogonal to ϕ_k , Eq. 2.14 shows that

$$\int_{\Omega} \nabla \phi_k \cdot \nabla \tilde{\sigma} \, dA = 0. \quad (2.21)$$

Thus $\tilde{v}_k = 0$ for $1 \leq k \leq N$. Inserting these zeros in Eq. 2.18 we obtain exactly Eq. 2.12, which shows that the new solution merely adds another element to the existing sequence. We conclude that there are infinitely many eigenfunctions.

It can now be shown that these eigenfunctions form a basis for $\bar{\mathcal{S}}$, as follows. Let \mathcal{S}_∞ be the subspace spanned by the infinite sequence $\{\phi_p\}$, $p = 1, 2, \dots$, with all eigenfunctions included. If indeed there is an element of \mathcal{S} that is not in \mathcal{S}_∞ , then arguments in the same spirit as above establish that this element merely adds one more eigenfunction to the sequence, giving a contradiction (for details, see Appendix E). Finally, since every element of \mathcal{S} can be expressed to arbitrary closeness in the L^2 norm as a linear combination of our basis functions, so can every element of the closure $\bar{\mathcal{S}}$ ⁸. We conclude that our eigenfunctions provide a basis for residual stress states, as claimed⁹. Numerical examples presented later will provide ample empirical evidence of the same.

Recalling footnote 3, we emphasize that $\bar{\mathcal{S}}$ includes some elements which are not physically meaningful, for example, those with discontinuities right at the boundary. However, all physically meaningful residual stress fields will be elements of $\bar{\mathcal{S}}$.

2.5 Extension of the theory to three dimensions

Our derivation of the eigenvalue problem in Eq. 2.12 was for a two-dimensional domain. The extension of the theory to three dimensions is straightforward, and is now presented for completeness. Computations, which will require finite element formulations in 3D, are left for future work.

Most of the development of the 2D theory is directly applicable to three dimensions if we interpret the “ dA ” in the domain integrals to be volume elements. While obtaining Eq. 2.12, the two-dimensionality of the domain Ω was used only to derive the point-wise natural boundary condition of Eq. 2.11 from the integral condition of Eq. 2.10. As a result, in three dimensions, only the fourth of Eqs. 2.12 changes.

Equation 2.10 in three dimensions is

$$\int_{\partial\Omega} \nabla_n \boldsymbol{\sigma} \cdot \boldsymbol{\zeta} dS = 0, \quad (2.22)$$

⁸The eigenfunctions ϕ also form a basis to the set \mathcal{S} in the H^1 norm. See Appendix F.

⁹One might, in some cases, consider self-equilibrating stresses under prescribed non-zero boundary tractions. In such cases, the total stress $\boldsymbol{\sigma}$ can be written as the sum of a general traction free residual stress $\boldsymbol{\sigma}_h$ and *any* particular self-equilibrating $\boldsymbol{\sigma}_p$, consistent with the applied tractions, and computed in any way we like. Our basis can then be used to represent $\boldsymbol{\sigma}_h$.

where “ dS ” is now interpreted as an infinitesimal area element on the surface $\partial\Omega$ of the three-dimensional domain Ω .

Consider an arbitrarily small portion ΔS including any point P on $\partial\Omega$. Restricting attention to ζ that is nonzero only on ΔS , Eq. 2.22 becomes

$$\int_{\Delta S} \nabla_n \boldsymbol{\sigma} \cdot \boldsymbol{\zeta} dS = 0. \quad (2.23)$$

Since ΔS is arbitrarily small, and $\nabla_n \boldsymbol{\sigma}$, $\boldsymbol{\zeta}$ are continuous, we can use localization to conclude that

$$\nabla_n \boldsymbol{\sigma} \cdot \boldsymbol{\zeta} = 0 \text{ on } \partial\Omega.$$

We choose a pair of convenient orthonormal vectors \mathbf{t}_1 and \mathbf{t}_2 in the tangent plane passing through P . This can be done, e.g., using the Cartesian unit vector \mathbf{e}_1 as

$$\mathbf{t}_1 = \frac{\mathbf{e}_1 \times \mathbf{n}}{\|\mathbf{e}_1 \times \mathbf{n}\|} \text{ and } \mathbf{t}_2 = \mathbf{n} \times \mathbf{t}_1,$$

where ‘ \times ’ represents the vector cross product; $(\mathbf{t}_1, \mathbf{t}_2, \mathbf{n})$ form a right handed orthonormal triad. If \mathbf{n} is parallel, or almost parallel to \mathbf{e}_1 , then \mathbf{e}_1 can be replaced by \mathbf{e}_2 in the subsequent discussion.

Since $\boldsymbol{\zeta}$ is symmetric and satisfies $\boldsymbol{\zeta} \mathbf{n} = \mathbf{0}$, it must be expressible as

$$\boldsymbol{\zeta} = \kappa_1 \mathbf{t}_1 \otimes \mathbf{t}_1 + \kappa_2 \mathbf{t}_2 \otimes \mathbf{t}_2 + \kappa_3 (\mathbf{t}_1 \otimes \mathbf{t}_2 + \mathbf{t}_2 \otimes \mathbf{t}_1)$$

for arbitrary $\kappa_1, \kappa_2, \kappa_3$. First choosing $\kappa_2 = \kappa_3 = 0$ and $\kappa_1 \neq 0$, we obtain the natural boundary condition (compare with Eq. 2.11)

$$\nabla_n \boldsymbol{\sigma} \cdot (\mathbf{t}_1 \otimes \mathbf{t}_1) = 0.$$

Similarly, we obtain two more natural boundary conditions:

$$\nabla_n \boldsymbol{\sigma} \cdot (\mathbf{t}_2 \otimes \mathbf{t}_2) = 0 \quad \text{and} \quad \nabla_n \boldsymbol{\sigma} \cdot (\mathbf{t}_1 \otimes \mathbf{t}_2 + \mathbf{t}_2 \otimes \mathbf{t}_1) = 0.$$

The last condition can be simplified, because $\nabla_n \boldsymbol{\sigma}$ is symmetric, to

$$\nabla_n \boldsymbol{\sigma} \cdot (\mathbf{t}_1 \otimes \mathbf{t}_2) = 0.$$

Since $\boldsymbol{\sigma}$ has six components, the essential boundary conditions $\boldsymbol{\sigma} \mathbf{n} = \mathbf{0}$ along with these natural boundary conditions present a total of six boundary conditions as needed.

To summarize, the eigenvalue problem developed earlier for two dimensions is extended in principle to three dimensions as follows:

$$\begin{aligned} -\Delta\boldsymbol{\sigma} + \nabla_s\boldsymbol{\mu} &= \lambda\boldsymbol{\sigma} \quad \text{and} \quad \text{div}\boldsymbol{\sigma} = \mathbf{0} && \text{in } \Omega, \\ \boldsymbol{\sigma}\mathbf{n} &= \mathbf{0} && \text{on } \partial\Omega, \\ \nabla_n\boldsymbol{\sigma} \cdot (\mathbf{t}_1 \otimes \mathbf{t}_1) &= 0, \quad \nabla_n\boldsymbol{\sigma} \cdot (\mathbf{t}_2 \otimes \mathbf{t}_2) = 0 \quad \text{and} \quad \nabla_n\boldsymbol{\sigma} \cdot (\mathbf{t}_1 \otimes \mathbf{t}_2) = 0 && \text{on } \partial\Omega, \end{aligned}$$

for any two orthonormal unit vectors \mathbf{t}_1 and \mathbf{t}_2 tangential to the surface at the point of interest.

In the above, $\boldsymbol{\sigma}$ is a symmetric three dimensional second order tensor field and $\boldsymbol{\mu}$ is a three dimensional vector.

The proof of orthogonality of eigenfunctions, and the fact that they form a basis, proceeds along lines identical to the two dimensional case, and is omitted.

2.6 A minimizer of J_0 exists in the unit ball of $\mathcal{S}_{N\perp}$

Showing the existence of minimizers in infinite dimensional spaces is tricky and filled with traps. In the early stages of this work, we had incorrectly guessed from the non-emptiness of $\mathcal{S}_{N\perp}$ that it *must* contain a minimizer of J_0 ¹⁰. Such ideas generally make sense for a finite dimensional space, because the minimizing sequence is forced to converge eventually. But the sequence need not converge in a space with infinitely many dimensions as there are infinitely many directions in which it can go. Consequently, the minimizing sequence may keep hopping about in orthogonal directions and never converge. This lack of compactness can sometimes be compensated by the convexity of the space. However, the unit ball of $\mathcal{S}_{N\perp}$ is not convex because of the constraint

$$\int_{\Omega} \boldsymbol{\sigma} \cdot \boldsymbol{\sigma} dA = 1.$$

However, this lack of convexity is compensated by two other important structural elements: compactness of L^2 in H^1 , and convexity of the functional J_0 itself.

¹⁰Riemann made the same mistake, although he did it at a time when the notions of compactness were not well established. See [47] for a nice discussion. For an interesting account of a somewhat bitter exchange between Riemann and Weierstrass on this matter, see [48].

We now present the proof of existence. Firstly, we note that the unit ball in $\mathcal{S}_{N\perp}$ is understood to be the set

$$\mathcal{P} = \left\{ \boldsymbol{\sigma} \mid \boldsymbol{\sigma} \in \mathcal{S}_{N\perp}, \left(\int_{\Omega} \boldsymbol{\sigma} \cdot \boldsymbol{\sigma} \, dA \right)^{\frac{1}{2}} = 1 \right\}.$$

In this section, we show that \mathcal{P} contains a minimizer of $J_0(\boldsymbol{\sigma}) = \frac{1}{2} \int_{\Omega} \nabla \boldsymbol{\sigma} \cdot \nabla \boldsymbol{\sigma} \, dA$.

When we wish to include the elements in $\mathcal{S}_{N\perp}$ which have norm less than 1 as well, we will use the symbol $\bar{\mathcal{P}}$, as in

$$\bar{\mathcal{P}} = \left\{ \boldsymbol{\sigma} \mid \boldsymbol{\sigma} \in \mathcal{S}_{N\perp}, \left(\int_{\Omega} \boldsymbol{\sigma} \cdot \boldsymbol{\sigma} \, dA \right)^{\frac{1}{2}} \leq 1 \right\}.$$

We note that the problems of minimizing $J_0(\boldsymbol{\sigma})$ and minimizing

$$\hat{J}(\boldsymbol{\sigma}) = (2J_0(\boldsymbol{\sigma}))^{\frac{1}{2}} = \left(\int_{\Omega} \nabla \boldsymbol{\sigma} \cdot \nabla \boldsymbol{\sigma} \, dA \right)^{\frac{1}{2}}$$

are equivalent. The values of \hat{J} evaluated in \mathcal{P} have a greatest lower bound ψ_0 . Thus, there exists a sequence $(\boldsymbol{\sigma}_n)$ in \mathcal{P} such that

$$\lim_{n \rightarrow \infty} \hat{J}(\boldsymbol{\sigma}_n) = \psi_0.$$

We must show that the limit of $(\boldsymbol{\sigma}_n)$ is in \mathcal{P} , and \hat{J} evaluated at that limit is ψ_0 .

We will use the L^2 and H^1 norms of a function $\boldsymbol{\sigma} \in \mathcal{S}$, as in

$$\|\boldsymbol{\sigma}\|_{L^2} = \left(\int_{\Omega} \boldsymbol{\sigma} \cdot \boldsymbol{\sigma} \, dA \right)^{\frac{1}{2}},$$

$$\|\boldsymbol{\sigma}\|_{H^1} = \left(\int_{\Omega} \boldsymbol{\sigma} \cdot \boldsymbol{\sigma} \, dA + \int_{\Omega} \nabla \boldsymbol{\sigma} \cdot \nabla \boldsymbol{\sigma} \, dA \right)^{\frac{1}{2}}.$$

Our proof will proceed using the following steps. First we will show that the sequence $(\boldsymbol{\sigma}_n)$ is bounded in the H^1 norm, and thus has a subsequence that converges weakly in the H^1 norm, and strongly in the L^2 norm, to some $\boldsymbol{\sigma}_0$. We will then show that $\boldsymbol{\sigma}_0$ belongs to \mathcal{P} . Finally, we will show that although \hat{J} is not continuous, it is lower semi-continuous, a property which implies that \hat{J} achieves ψ_0 at $\boldsymbol{\sigma}_0$.

Proposition 2.1. *$(\boldsymbol{\sigma}_n)$ is bounded in the H^1 norm.*

Proof. Since residual stresses have zero mean [19], by Poincaré's inequality [49] there exists a positive real number C that depends only on Ω such that

$$\left(\int_{\Omega} \boldsymbol{\sigma} \cdot \boldsymbol{\sigma} \, dA \right)^{\frac{1}{2}} \leq C \left(\int_{\Omega} \nabla \boldsymbol{\sigma} \cdot \nabla \boldsymbol{\sigma} \, dA \right)^{\frac{1}{2}} \quad \forall \boldsymbol{\sigma} \in \mathcal{S}.$$

This implies that

$$\|\boldsymbol{\sigma}\|_{H^1} \leq \sqrt{C^2 + 1} \hat{J}(\boldsymbol{\sigma}). \quad (2.24)$$

By definition, all the elements in the sequence $(\boldsymbol{\sigma}_n) \in \mathcal{P}$ yield finite \hat{J} (Eq. 2.1). We then conclude from the above equation that $(\boldsymbol{\sigma}_n)$ is bounded in the H^1 norm. \square

Proposition 2.2. $(\boldsymbol{\sigma}_n)$ has a subsequence that converges to some $\boldsymbol{\sigma}_0$ weakly in the H^1 norm, and strongly in the L^2 norm.

Proof. It is well known in the theory of functional analysis that H^1 (set of $\boldsymbol{\sigma}$ with finite H^1 norm) is a Banach space. Every bounded sequence in a Banach space has a weakly convergent subsequence (see corollary A.60, page 506 of [49]). It follows that there is a subsequence $(\boldsymbol{\sigma}_{n_k})$ of $(\boldsymbol{\sigma}_n)$ that converges weakly to some $\boldsymbol{\sigma}_0 \in H^1$. By the Rellich-Kondrachov theorem [49], H^1 is compactly embedded in L^2 (set of $\boldsymbol{\sigma}$ with finite L^2 norm)¹¹, and therefore $(\boldsymbol{\sigma}_{n_k})$ converges strongly to $\boldsymbol{\sigma}_0$ in the L^2 norm¹² (e.g., see exercise 3.5, page 80 of [50]). \square

Proposition 2.3. $\boldsymbol{\sigma}_0 \in \mathcal{P}$.

Proof. Recall that \mathcal{P} consists of elements $\boldsymbol{\sigma}$ that

- (i) are divergence free,
- (ii) are traction free,
- (iii) have $\int_{\Omega} \nabla \boldsymbol{\sigma} \cdot \nabla \boldsymbol{\sigma} \, dA < \infty$, and
- (iv) are orthogonal to \mathcal{S}_N , and

¹¹If a set S_1 with norm $\|\cdot\|_{S_1}$ is compactly embedded in a set S_2 with norm $\|\cdot\|_{S_2}$, then for a sequence (a_n) bounded in S_1 , there is a subsequence (a_{n_k}) that is a Cauchy sequence in S_2 [49].

¹²Since the sequence $\boldsymbol{\sigma}_{n_k}$ is bounded in the H^1 norm, by definition of compact embedding, there is a subsequence $\boldsymbol{\sigma}_{n_{k_l}}$ that is a Cauchy sequence in the L^2 norm. That is, $\boldsymbol{\sigma}_{n_{k_l}}$ converges strongly in the L^2 norm to some $\tilde{\boldsymbol{\sigma}}_0$. Since weak convergence is weaker than strong convergence, $\boldsymbol{\sigma}_{n_{k_l}}$ converges weakly in the L^2 norm to $\tilde{\boldsymbol{\sigma}}_0$. Also, since $\boldsymbol{\sigma}_{n_k}$ converges weakly in the H^1 norm to $\boldsymbol{\sigma}_0$, it converges weakly in the L^2 norm to $\boldsymbol{\sigma}_0$. This implies that $\boldsymbol{\sigma}_{n_{k_l}}$ converges weakly in the L^2 norm to $\boldsymbol{\sigma}_0$. Finally, since weak limits are unique, we have that $\tilde{\boldsymbol{\sigma}}_0 = \boldsymbol{\sigma}_0$. So, $\boldsymbol{\sigma}_{n_{k_l}}$ converges strongly in the L^2 norm to $\boldsymbol{\sigma}_0$.

(v) satisfy $\|\boldsymbol{\sigma}\|_{L^2} = 1$.

We now show that $\boldsymbol{\sigma}_0$ satisfies each of the above conditions (i) through (v).

(i) $\operatorname{div} \boldsymbol{\sigma}_0 = \mathbf{0}$:

Since $\boldsymbol{\sigma}_0$ is in H^1 , $\operatorname{div} \boldsymbol{\sigma}_0$ is a vector field in L^2 . Let $\boldsymbol{\gamma}$ be an arbitrary smooth vector field compactly supported over Ω . Consider the inner product of $\operatorname{div} \boldsymbol{\sigma}_0$ with $\boldsymbol{\gamma}$. Using integration by parts followed by Hölder's inequality, we have

$$\begin{aligned} \left| \int_{\Omega} \operatorname{div} \boldsymbol{\sigma}_0 \cdot \boldsymbol{\gamma} \, dA \right| &= \left| \int_{\Omega} \operatorname{div} (\boldsymbol{\sigma}_0 - \boldsymbol{\sigma}_{n_k}) \cdot \boldsymbol{\gamma} \, dA + \int_{\Omega} \operatorname{div} \boldsymbol{\sigma}_{n_k} \cdot \boldsymbol{\gamma} \, dA \right| \\ &= \left| - \int_{\Omega} (\boldsymbol{\sigma}_0 - \boldsymbol{\sigma}_{n_k}) \cdot \nabla \boldsymbol{\gamma} \, dA \right| \leq \|\boldsymbol{\sigma}_0 - \boldsymbol{\sigma}_{n_k}\|_{L^2} \|\nabla \boldsymbol{\gamma}\|_{L^2}. \end{aligned}$$

Since $\boldsymbol{\gamma}$ is smooth, $\|\nabla \boldsymbol{\gamma}\|_{L^2}$ is finite, and the right-most expression in the above equation goes to zero. So, we have

$$\int_{\Omega} \operatorname{div} \boldsymbol{\sigma}_0 \cdot \boldsymbol{\gamma} \, dA = 0.$$

Since $\boldsymbol{\gamma}$ is arbitrary, and smooth compactly supported functions are dense in L^2 [50], we conclude that

$$\operatorname{div} \boldsymbol{\sigma}_0 = \mathbf{0}.$$

(ii) $\boldsymbol{\sigma}_0 \mathbf{n} = \mathbf{0}$:

For an arbitrary smooth vector field $\boldsymbol{\chi}$, using integration by parts, we have

$$0 = \int_{\Omega} \operatorname{div} (\boldsymbol{\sigma}_0 - \boldsymbol{\sigma}_{n_k}) \cdot \boldsymbol{\chi} \, dA = \int_{\partial\Omega} \{(\boldsymbol{\sigma}_0 - \boldsymbol{\sigma}_{n_k}) \mathbf{n}\} \cdot \boldsymbol{\chi} \, ds - \int_{\Omega} (\boldsymbol{\sigma}_0 - \boldsymbol{\sigma}_{n_k}) \cdot \nabla \boldsymbol{\chi} \, dA,$$

or, since $\boldsymbol{\sigma}_{n_k} \mathbf{n} = \mathbf{0}$,

$$\int_{\partial\Omega} (\boldsymbol{\sigma}_0 \mathbf{n}) \cdot \boldsymbol{\chi} \, ds = \int_{\Omega} (\boldsymbol{\sigma}_0 - \boldsymbol{\sigma}_{n_k}) \cdot \nabla \boldsymbol{\chi} \, dA.$$

Again using Hölder's inequality, we obtain that

$$\boldsymbol{\sigma}_0 \mathbf{n} = \mathbf{0}.$$

(iii) $\int_{\Omega} \nabla \boldsymbol{\sigma} \cdot \nabla \boldsymbol{\sigma} \, dA < \infty$:

This is obvious since $\boldsymbol{\sigma}_0$ belongs to H^1 (Proposition 2.2).

(iv) $\boldsymbol{\sigma}_0$ is orthogonal to \mathcal{S}_N :

Since $\boldsymbol{\sigma}_{n_k}$ is orthogonal to \mathcal{S}_N for all n_k , and inner product is a continuous function [51], we conclude that $\boldsymbol{\sigma}_0$ is orthogonal to \mathcal{S}_N .

(v) $\|\boldsymbol{\sigma}_0\|_{L^2} = 1$:

Since $\|\boldsymbol{\sigma}_{n_k}\|_{L^2} = 1$ for all n_k , and norm is a continuous function [51], we conclude that $\|\boldsymbol{\sigma}_0\|_{L^2} = 1$.

□

Remark 2.4. $\boldsymbol{\sigma}_{n_k}$ converges to $\boldsymbol{\sigma}_0$ strongly in the L^2 norm, and the corresponding \hat{J} values converge to ψ_0 . However, it is not clear if $\hat{J}(\boldsymbol{\sigma}_0) = \psi_0$, since as a function from $\mathcal{S} \subset L^2$ to \mathbb{R} , \hat{J} is not continuous. In the following arguments, we show that \hat{J} satisfies a weaker but sufficient condition, that of lower semi-continuity.

Remark 2.5. We saw in the proof of Proposition 2.2 that if a sequence of divergence free and traction free stress fields $\boldsymbol{\sigma}_n$ converges to $\boldsymbol{\sigma}_0$ in the L^2 norm, then $\boldsymbol{\sigma}_0$ is also divergence free and traction free. Therefore, the completion $\bar{\mathcal{S}}$ of \mathcal{S} in the L^2 norm consists of divergence free and traction free stress fields. In particular, residual stress fields with finite number of simple discontinuities are elements of $\bar{\mathcal{S}}$, but not of \mathcal{S} .

Definition 2.6. A functional f is strong (respectively, weak) lower semi-continuous with respect to a norm if it satisfies

$$f(\boldsymbol{x}_0) \leq \liminf_{m \rightarrow \infty} f(\boldsymbol{x}_m)$$

whenever a sequence (\boldsymbol{x}_m) converges strongly (respectively, weakly) to \boldsymbol{x}_0 in that norm [52].

Remark 2.7. Weak and strong lower semi-continuity of a functional are related as follows. In general, weak lower semi-continuity in a norm implies strong lower semi-continuity in that norm. The converse is not true. However, if the functional is strong lower semi-continuous and convex, and is defined on a convex set, then it is weak lower semi-continuous [52].

Proposition 2.8. \hat{J} is strong lower semi-continuous in H^1 .

Proof. We first show that the quantity defined as $\|\boldsymbol{\sigma}\|_{\hat{J}} = \hat{J}(\boldsymbol{\sigma})$ is a norm over set \mathcal{S} . Since residual stresses have zero mean, $\|\boldsymbol{\sigma}\|_{\hat{J}}$ is zero only when $\boldsymbol{\sigma}$ is zero. Also, $\|\alpha\boldsymbol{\sigma}\|_{\hat{J}} = |\alpha| \|\boldsymbol{\sigma}\|_{\hat{J}}$

for a real number α . Finally, using Hölder's inequality, it can easily be shown that $\hat{J}(\boldsymbol{\sigma})$ satisfies the triangle inequality. So, $\|\boldsymbol{\sigma}\|_j$ is a norm.

Next, we note that

$$0 \leq \left(\int_{\Omega} \nabla \boldsymbol{\sigma} \cdot \nabla \boldsymbol{\sigma} \, dA \right)^{\frac{1}{2}} \leq \left(\int_{\Omega} \boldsymbol{\sigma} \cdot \boldsymbol{\sigma} \, dA + \int_{\Omega} \nabla \boldsymbol{\sigma} \cdot \nabla \boldsymbol{\sigma} \, dA \right)^{\frac{1}{2}},$$

or

$$0 \leq \|\boldsymbol{\sigma}\|_j \leq \|\boldsymbol{\sigma}\|_{H^1}. \quad (2.25)$$

Therefore, if a sequence $(\tilde{\boldsymbol{\sigma}}_m)$ converges strongly to some $\tilde{\boldsymbol{\sigma}}_0$ in the H^1 norm, i.e. $\lim_{m \rightarrow \infty} \|\tilde{\boldsymbol{\sigma}}_0 - \tilde{\boldsymbol{\sigma}}_m\|_{H^1} = 0$, it follows from the above that $\lim_{m \rightarrow \infty} \|\tilde{\boldsymbol{\sigma}}_0 - \tilde{\boldsymbol{\sigma}}_m\|_j = 0$. This implies that

$$\lim_{m \rightarrow \infty} \hat{J}(\tilde{\boldsymbol{\sigma}}_m) = \hat{J}(\tilde{\boldsymbol{\sigma}}_0).$$

Hence, \hat{J} is strong lower semi-continuous in H^1 . □

Proposition 2.9. \hat{J} is weak lower semi-continuous in H^1 .

Proof. Since all norms are convex, \hat{J} is a convex functional. The set $\bar{\mathcal{P}}$ defined earlier is convex. Including Proposition 2.8, we conclude that \hat{J} is weak lower semi-continuous in H^1 over $\bar{\mathcal{P}}$. □

Proposition 2.10. $\hat{J}(\boldsymbol{\sigma}_0) = \psi_0$.

Proof. Since \hat{J} is weak lower semi-continuous in H^1 , and $(\boldsymbol{\sigma}_{n_k}) \in \bar{\mathcal{P}}$ converges weakly to $\boldsymbol{\sigma}_0 \in \bar{\mathcal{P}}$ in the H^1 norm,

$$\hat{J}(\boldsymbol{\sigma}_0) \leq \lim_{n_k \rightarrow \infty} \hat{J}(\boldsymbol{\sigma}_{n_k}) = \psi_0.$$

But since ψ_0 is the greatest lower bound of \hat{J} over \mathcal{P} , and $\boldsymbol{\sigma}_0$ belongs to \mathcal{P} , we have

$$\psi_0 \leq \hat{J}(\boldsymbol{\sigma}_0).$$

Hence,

$$\hat{J}(\boldsymbol{\sigma}_0) = \psi_0.$$

□

Remark 2.11. We have now proved that $\boldsymbol{\sigma}_0$ is in \mathcal{P} , minimizes \hat{J} , and hence minimizes J_0 .

Remark 2.12. From Eqs. 2.24 and 2.25, we conclude that the norms \hat{J} and H^1 are equivalent. As a result, since $\|\sigma_{n_k}\|_{\hat{J}} \rightarrow \|\sigma_0\|_{\hat{J}}$, it follows that (a) $\|\sigma_{n_k}\|_{H^1} \rightarrow \|\sigma_0\|_{H^1}$. Moreover, (b) σ_{n_k} converges weakly to σ_0 in the H^1 norm. Properties (a) and (b) together imply that σ_{n_k} in fact converges strongly to σ_0 in the H^1 norm.

2.7 Summary of the chapter

In this chapter, we obtained a sequence of functions spanning the set of all residual stress fields. These functions are stationary points of a positive definite quadratic functional. The calculus of variations yielded necessary and sufficient conditions for stationarity in the form of an eigenvalue problem. We showed that the eigenfunctions are stationary points of the quadratic functional. We assumed their existence, and showed that they form an orthogonal basis for the set of residual stress fields in the L^2 and the H^1 norms. We also extended the theory to 3D and derived the corresponding eigenvalue problem. Finally, we proved the existence of the eigenfunctions.

In the next chapter, we will compute some eigenfunctions in 2D using FEM and semi-numerical methods.

Chapter 3

Computation of eigenfunctions

In general, it is not possible to solve the eigenvalue problem of Eq. 2.12 analytically, and we use numerical methods. We have used the FEM to compute the eigenfunctions ϕ_i in arbitrary two dimensional domains. For some special geometries, symmetries can be exploited to convert the eigenvalue problem into a system of ODEs or algebraic equations. We have considered four such geometries in this chapter: an annulus, a circular disk, a rectangle and an annular wedge (by which we mean an annular strip subtending an angle between 0 and 2π at the center). Our semi-numerical solutions for these geometries agree with the corresponding FEM solutions.

This chapter is arranged as follows. In Section 3.1, we first give the details of the FEM formulation, and then compute the eigenfunctions on five domains: an annulus, a circular disk, rectangle, an annular wedge, and an arbitrarily shaped domain. We discuss the stability and accuracy of the FEM solutions, and justify the choice of the shape functions used. We close the section by reporting the computation times for different mesh sizes on a desktop computer. Section 3.2 is devoted to computation of eigenfunctions in some special geometries. In Section 3.2.1, we compute the eigenfunctions on an annular domain by converting the governing PDE into an ODE system for a fixed circumferential wave number. In Section 3.2.2, we extend the treatment of the annulus to a circular disk by appropriately modifying the conditions at the center of the disk. In Section 3.2.3, we consider a square geometry. Unlike annuli and circular disks, there is no direction of periodicity, and Fourier expansion is not possible in general. We adopt a different approach: we generate a sequence of 1D functions with zero mean and zero boundary values, and assume, with due justification, that the stress eigenfunctions ϕ_i can be expanded in terms of these 1D functions. Our original problem of finding stationary points of J_0 then yields

an algebraic eigenvalue problem which can be solved using standard methods. Extension of our treatment to rectangular shapes is easy. Finally, in Section 3.2.4, we use the same approach to compute the eigenfunctions in an annular wedge.

3.1 Eigenfunctions on arbitrary domains using the FEM

3.1.1 Formulation

To solve the eigenvalue problem in Eq. 2.12 using the FEM, we first express it in Cartesian coordinates, so that

$$-\Delta\boldsymbol{\sigma} + \nabla_s\boldsymbol{\mu} = \lambda\boldsymbol{\sigma}$$

becomes

$$\begin{aligned} -\frac{\partial^2\sigma_{xx}}{\partial x^2} - \frac{\partial^2\sigma_{xx}}{\partial y^2} + \frac{\partial\mu_x}{\partial x} &= \lambda\sigma_{xx}, \\ -\frac{\partial^2\sigma_{yy}}{\partial x^2} - \frac{\partial^2\sigma_{yy}}{\partial y^2} + \frac{\partial\mu_y}{\partial y} &= \lambda\sigma_{yy}, \\ -\frac{\partial^2\sigma_{xy}}{\partial x^2} - \frac{\partial^2\sigma_{xy}}{\partial y^2} + \frac{1}{2}\left(\frac{\partial\mu_x}{\partial y} + \frac{\partial\mu_y}{\partial x}\right) &= \lambda\sigma_{xy}. \end{aligned} \tag{3.1}$$

Equilibrium,

$$\operatorname{div}\boldsymbol{\sigma} = \mathbf{0},$$

becomes

$$\begin{aligned} \frac{\partial\sigma_{xx}}{\partial x} + \frac{\partial\sigma_{xy}}{\partial y} &= 0, \\ \frac{\partial\sigma_{xy}}{\partial x} + \frac{\partial\sigma_{yy}}{\partial y} &= 0. \end{aligned} \tag{3.2}$$

The traction-free boundary condition

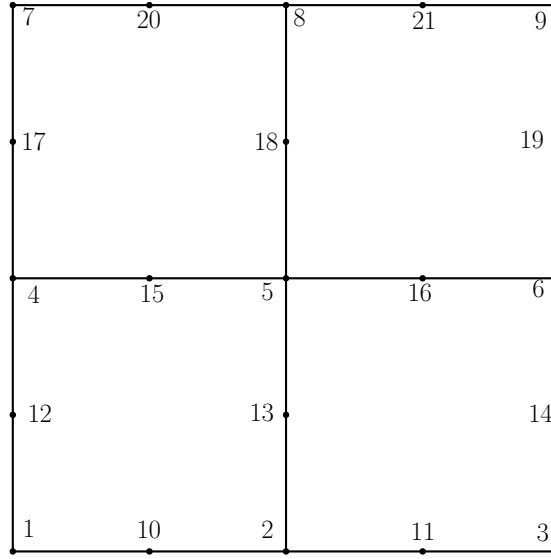
$$\boldsymbol{\sigma}\mathbf{n} = \mathbf{0}$$

gives

$$\begin{aligned} \sigma_{xx}n_x + \sigma_{xy}n_y &= 0, \\ \sigma_{xy}n_x + \sigma_{yy}n_y &= 0. \end{aligned} \tag{3.3}$$

The final, and natural, boundary condition

$$\nabla_n\boldsymbol{\sigma} \cdot (\mathbf{t} \otimes \mathbf{t}) = 0$$

FIGURE 3.1: A sample 2×2 mesh of serendipity elements

becomes

$$\frac{\partial \sigma_{xx}}{\partial x} n_x n_y^2 + \frac{\partial \sigma_{xx}}{\partial y} n_y^3 + \frac{\partial \sigma_{yy}}{\partial x} n_x^3 + \frac{\partial \sigma_{yy}}{\partial y} n_x^2 n_y - 2 \frac{\partial \sigma_{xy}}{\partial x} n_x^2 n_y - 2 \frac{\partial \sigma_{xy}}{\partial y} n_x n_y^2 = 0. \quad (3.4)$$

The above is obtained upon writing $\nabla_n \boldsymbol{\sigma} \cdot (\mathbf{t} \otimes \mathbf{t})$ in indicial notations as $\sigma_{ij,k} n_i n_j t_k$, and noting that $n_x = t_y$ and $n_y = -t_x$.

We discretise the domain with a mesh containing ‘ e ’ eight noded quadrilateral *serendipity* elements and ‘ n ’ nodes. Figure 3.1 shows a sample mesh for $e = 4$ and $n = 20$ for a square domain. We use the FEM software package Abaqus to generate the mesh.

We use piecewise cubic shape functions for the stress components. The shape function that takes the value 1 at node p , and the value zero at all other nodes, is denoted as N_p . Each such shape function is cubic within individual elements, continuous on element edges, and looks like a tent peaking at node p .

We use piecewise constant shape functions for components of the Lagrange multiplier vector field $\boldsymbol{\mu}$. The piecewise constant shape function that is 1 on element q , and zero on all the other elements, is denoted as M_q .

The discretised dependent variables are written as

$$\begin{aligned}
\sigma_{xx} &= \sigma_{xx_1}N_1 + \sigma_{xx_2}N_2 + \dots + \sigma_{xx_n}N_n, \\
\sigma_{yy} &= \sigma_{yy_1}N_1 + \sigma_{yy_2}N_2 + \dots + \sigma_{yy_n}N_n, \\
\sigma_{xy} &= \sigma_{xy_1}N_1 + \sigma_{xy_2}N_2 + \dots + \sigma_{xy_n}N_n, \\
\mu_x &= \mu_{x_1}M_1 + \mu_{x_2}M_2 + \dots + \mu_{x_e}M_e, \\
\mu_y &= \mu_{y_1}M_1 + \mu_{y_2}M_2 + \dots + \mu_{y_e}M_e,
\end{aligned} \tag{3.5}$$

where σ_{xx_p} denotes the value of the discretized σ_{xx} component at the p^{th} node (likewise for σ_{yy} and σ_{xy}); and where μ_{x_q} denotes the value of the discretized μ_x over element q (likewise for μ_y).

We arrange the $3n + 2e$ unknowns in a column vector c as follows:

$$c = \{\sigma_{xx_1} \dots \sigma_{xx_n} \sigma_{yy_1} \dots \sigma_{yy_n} \sigma_{xy_1} \dots \sigma_{xy_n} \mu_{x_1} \dots \mu_{x_e} \mu_{y_1} \dots \mu_{y_e}\}^T, \tag{3.6}$$

T denoting transpose. We need $3n + 2e$ equations. For the first n equations, we take the inner product of the first of Eqs. 3.1 with N_1 through N_n . For instance, the first such resulting equation is:

$$\int_{\Omega} (-\Delta\sigma_{xx} + \mu_{x,x} - \lambda\sigma_{xx}) N_1 dA = 0. \tag{3.7}$$

Using integration by parts, we obtain

$$\begin{aligned}
\int_{\partial\Omega} \left(-\frac{\partial\sigma_{xx}}{\partial x} n_x - \frac{\partial\sigma_{xx}}{\partial y} n_y + \mu_x n_x \right) N_1 ds - \int_{\Omega} \left(-\frac{\partial\sigma_{xx}}{\partial x} \frac{\partial N_1}{\partial x} - \frac{\partial\sigma_{xx}}{\partial y} \frac{\partial N_1}{\partial y} + \mu_x \frac{\partial N_1}{\partial x} \right) dA \\
= \lambda \int_{\Omega} \sigma_{xx} N_1 dA.
\end{aligned}$$

We substitute from Eqs. 3.5 to obtain

$$\begin{aligned}
\sum_{r=1}^n \sigma_{xx_r} \left\{ - \int_{\partial\Omega} \left(\frac{\partial N_r}{\partial x} n_x + \frac{\partial N_r}{\partial y} n_y \right) N_1 ds + \int_{\Omega} \left(\frac{\partial N_r}{\partial x} \frac{\partial N_1}{\partial x} + \frac{\partial N_r}{\partial y} \frac{\partial N_1}{\partial y} \right) dA \right\} \\
+ \sum_{s=1}^e \mu_{x_s} \left(\int_{\partial\Omega} N_1 n_x ds - \int_{\Omega} \frac{\partial N_1}{\partial x} dA \right) = \lambda \sum_{r=1}^n \sigma_{xx_r} \int_{\Omega} N_r N_1 dA.
\end{aligned} \tag{3.8}$$

The various integrals in the above equation are all meaningful because each N_r as well as its gradient ∇N_r are bounded everywhere in the domain, including on the boundary; and the shape functions used for $\boldsymbol{\mu}$ are piecewise constant. Additionally, we note that the boundary integrals above remain continuous even if n_x and n_y have a finite number of discontinuities, i.e., the domain can have a finite number of corners.

Equation 3.8 (recall Eq. 3.6) can be written compactly as

$$a_1 c = \lambda a_2 c,$$

where a_1 and a_2 are row vectors of dimensions $1 \times (3n + 2e)$. We obtain $n - 1$ more equations by taking the inner product of the first of Eqs. (3.1) with N_2 through N_n .

Similarly, we obtain $2n$ more equations by taking the inner product of the second and third of Eqs. 3.1 with N_1 through N_n .

Finally, we obtain the remaining $2e$ equations by taking the inner product of each of Eqs. 3.2 with each of M_1 through M_e . It can be verified easily, as for Eq. 3.8, that all integrals in those equations are bounded.

The complete set of $3n + 2e$ equations can be written in a compact form as follows:

$$A_1 c = \lambda A_2 c, \tag{3.9}$$

where A_1 and A_2 are square matrices of size $(3n + 2e) \times (3n + 2e)$. We have not imposed the boundary conditions (Eqs. 3.3 and 3.4) yet. We enforce these in the weak form as well (in an integral sense, on the domain boundary). If there are b nodes on the boundary, there are $3b$ conditions to be imposed. The boundary conditions can be expressed in the form $Bc = 0$, where B is a $3b \times (3n + 2e)$ matrix.

The constraint $Bc = 0$ means that the vector of unknowns is effectively $3n + 2e - 3b$ dimensional. For problems of moderate size, such as we solve here, it is conceptually simplest to compute a matrix Q whose columns span the subspace orthogonal to the rows of B . Then, Eq. (3.9) along with boundary conditions can be reduced to an equation of the form

$$\tilde{A}_1 \tilde{c} = \lambda \tilde{A}_2 \tilde{c}, \tag{3.10}$$

where $c = Q\tilde{c}$, $\tilde{A}_1 = Q^T A_1 Q$ and $\tilde{A}_2 = Q^T A_2 Q$. Equation (3.10) is a generalized eigenvalue problem. One last point is that, because of the constraints in the problem, several eigenvalues are infinite. So we solve Eq. 3.10 in the form

$$\tilde{A}_2 \tilde{c} = \frac{1}{\lambda} \tilde{A}_1 \tilde{c},$$

select the *largest* eigenvalues $1/\lambda$, and take their reciprocals. Finally, we arrange the eigenvectors (eigenfunctions) in order of increasing λ .

3.1.2 Computed eigenfunctions and their stability

We have computed the eigenfunctions, normalized to unit norm (i.e., $\int_{\Omega} \phi \cdot \phi \, dA = 1$), using the above formulation for five domains: an annular domain whose outer radius is three times its inner radius, a circular disk, a rectangular domain with an aspect ratio of 1.01, an annular wedge subtending 45° at the center, and an arbitrarily shaped domain (see Figures 3.2 - 3.6). We have performed convergence tests by refining the mesh, and displayed final results in Figures 3.2 - 3.6 using a level of refinement at which the first hundred eigenvalues varied within 0.05% upon quadrupling the number of elements. For instance, the domain corresponding to Figure 3.4 was discretized using a mesh of 2500 elements.

Our numerical results indicate that our formulation is stable. However, we have not formally verified the well known inf-sup condition (also known as the Ladyzhenskaya-Babuška-Brezzi condition) for our mixed finite element formulation. We refer the interested reader to Bathe's work [53–55] and the references therein (also see [56] for mixed finite element formulations in linear elasticity). Here, we offer the following positive and constructive points to demonstrate the correctness of our finite element results.

1. First, since our problem is similar to the Stokes problem, we observe on page 329, Table 4.8 of Bathe [53], that the 8/1 element (the eight-noded quadrilateral serendipity element with piecewise constant pressure, which is what we have used) is stable for the Stokes problem. This does not *guarantee* that it will be stable for our problem, but it is indicative, and our results have not shown instabilities.
2. Second, the qualitative consequence of instability is the appearance of spurious checkerboard type patterns in the solution. In many solutions, at different mesh refinements, for different domain shapes, we have *not seen* such checkerboard patterns with our 8/1 element.
3. Third, with other elements, which are unsuitable, we did indeed obtain checkerboard patterns. Specifically, we did so with 4/1 elements, consistent with Table 4.8 in [53]. Conversely, with 9/3 and 9/4-c, two other suitable elements mentioned in the table, we obtained similar results as with the 8/1 element, with no spurious modes. For demonstration, we plot the first ten eigenvalues obtained with 8/1, 9/3 and 9/4-c elements on a square domain meshed with 10×10 and 40×40 elements, respectively, in Figure 3.7. It is clear that the eigenvalues obtained with the three meshes agree, even at a low level of mesh refinement; and no spurious modes are obtained.

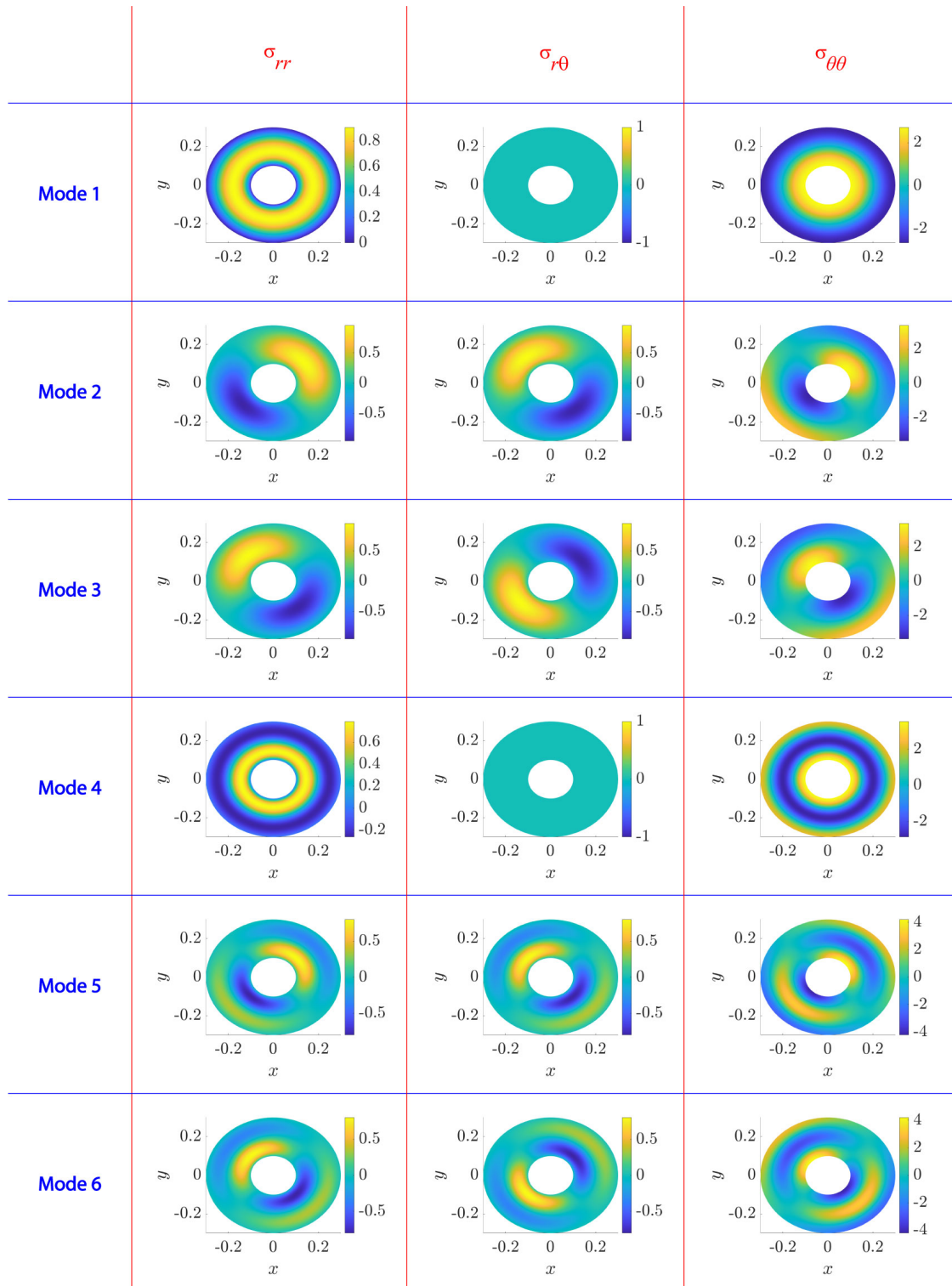


FIGURE 3.2: First six eigenfunctions for an annular domain; $\lambda_1 = 293.34$, $\lambda_2 = \lambda_3 = 348.76$, $\lambda_4 = 1065.71$, $\lambda_5 = \lambda_6 = 1104.19$.

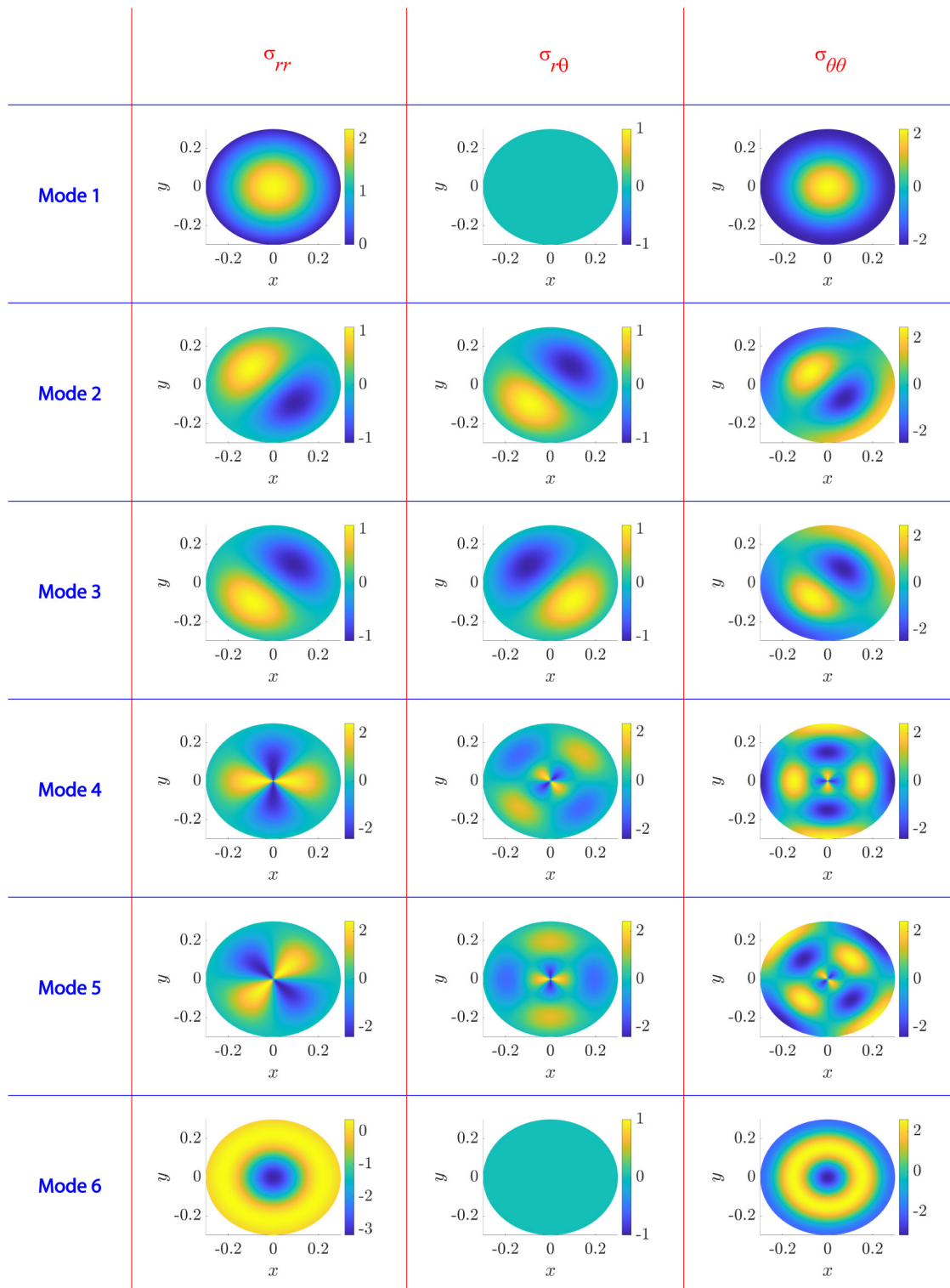


FIGURE 3.3: First six eigenfunctions for a circular disk; $\lambda_1 = 137.54$, $\lambda_2 = \lambda_3 = 293.11$, $\lambda_4 = \lambda_5 = 472.56$, $\lambda_6 = 523.84$.

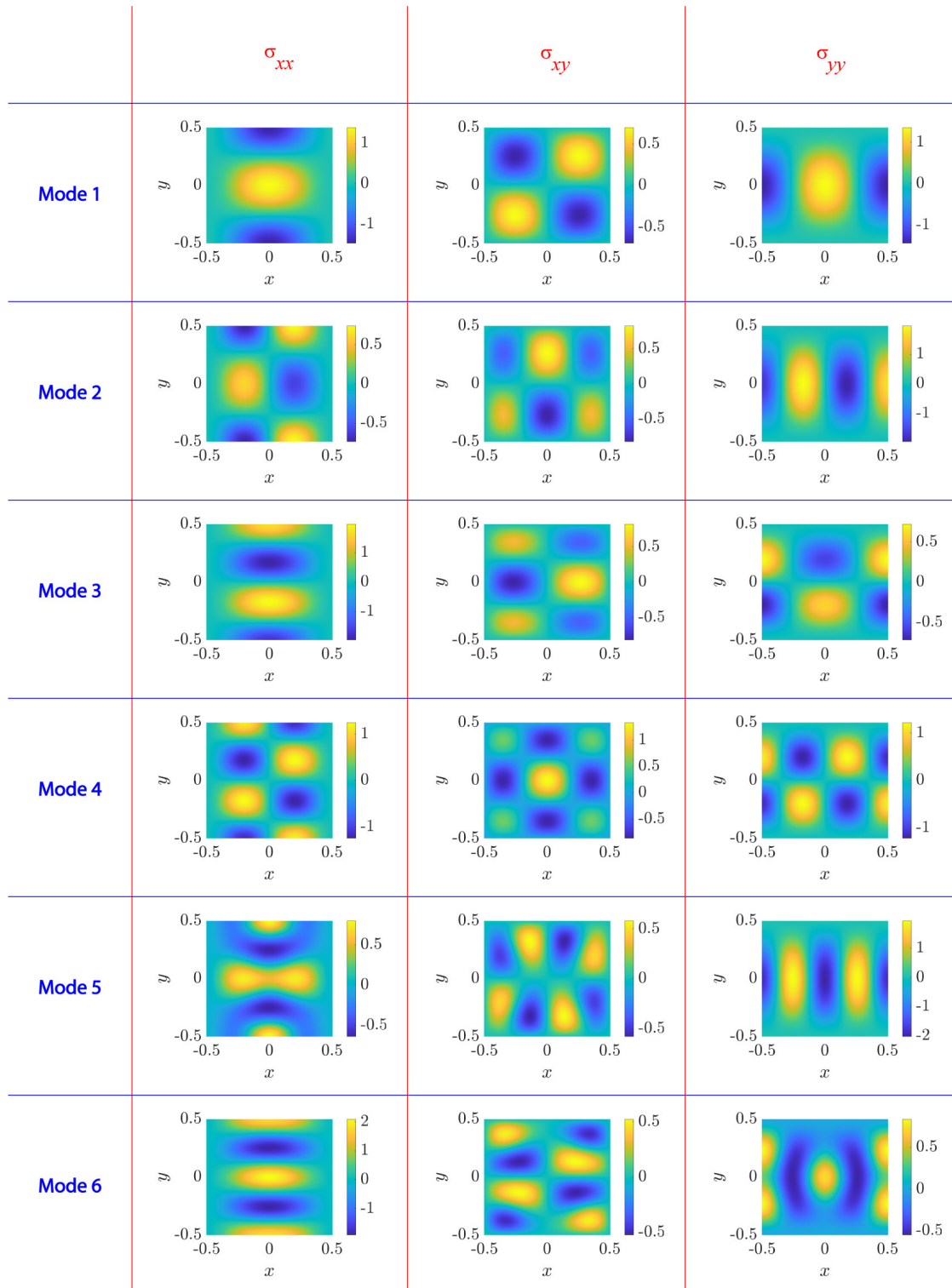


FIGURE 3.4: First six eigenfunctions for a rectangular domain; $\lambda_1 = 58.54$, $\lambda_2 = 102.37$, $\lambda_3 = 103.54$, $\lambda_4 = 144.57$, $\lambda_5 = 168.03$, $\lambda_6 = 171.31$.

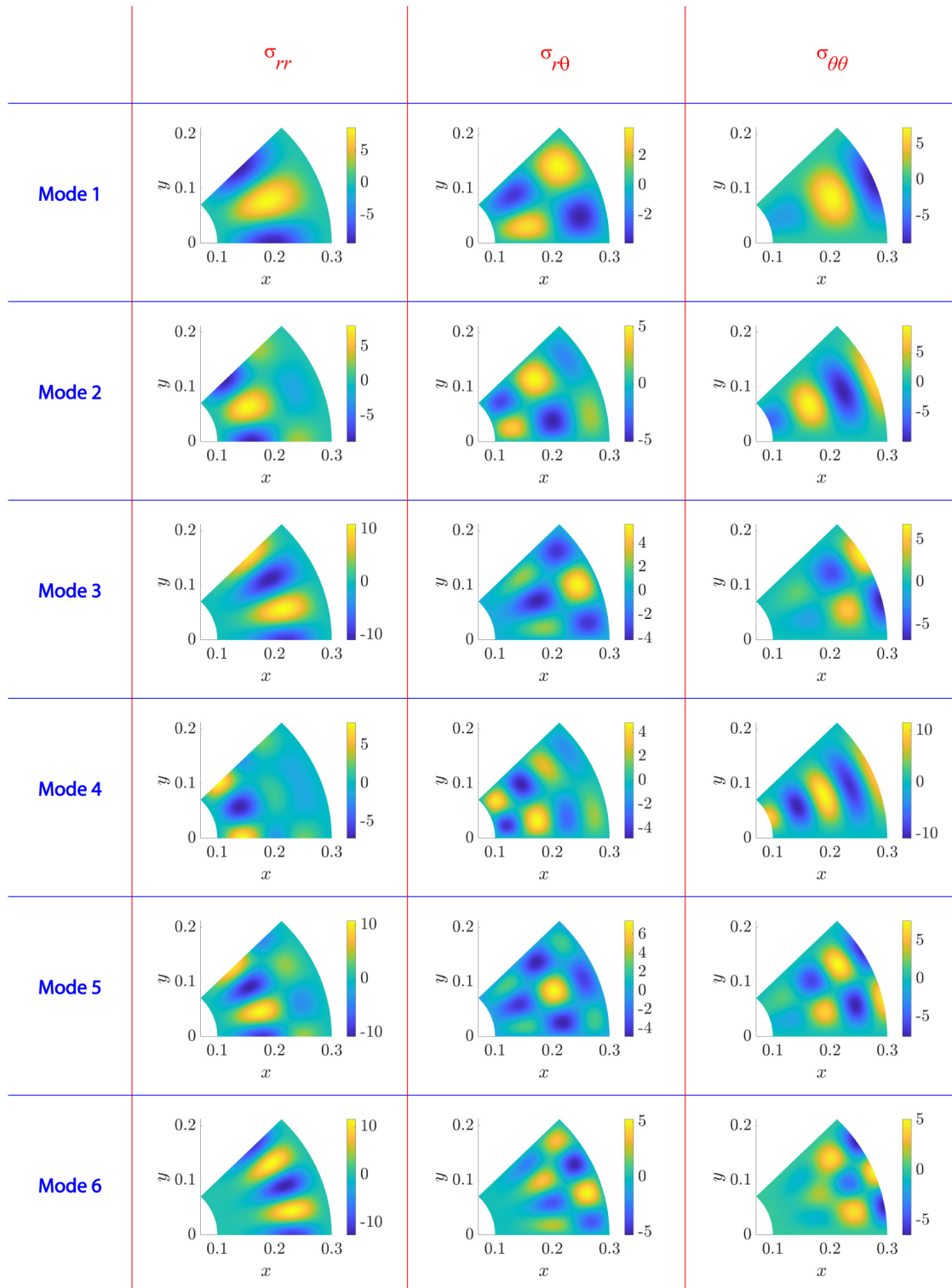


FIGURE 3.5: First six eigenfunctions for an annular wedge subtending 45° at center; $\lambda_1 = 1966.50$, $\lambda_2 = 3200.31$, $\lambda_3 = 3529.09$, $\lambda_4 = 4840.81$, $\lambda_5 = 5191.44$, $\lambda_6 = 5519.98$.

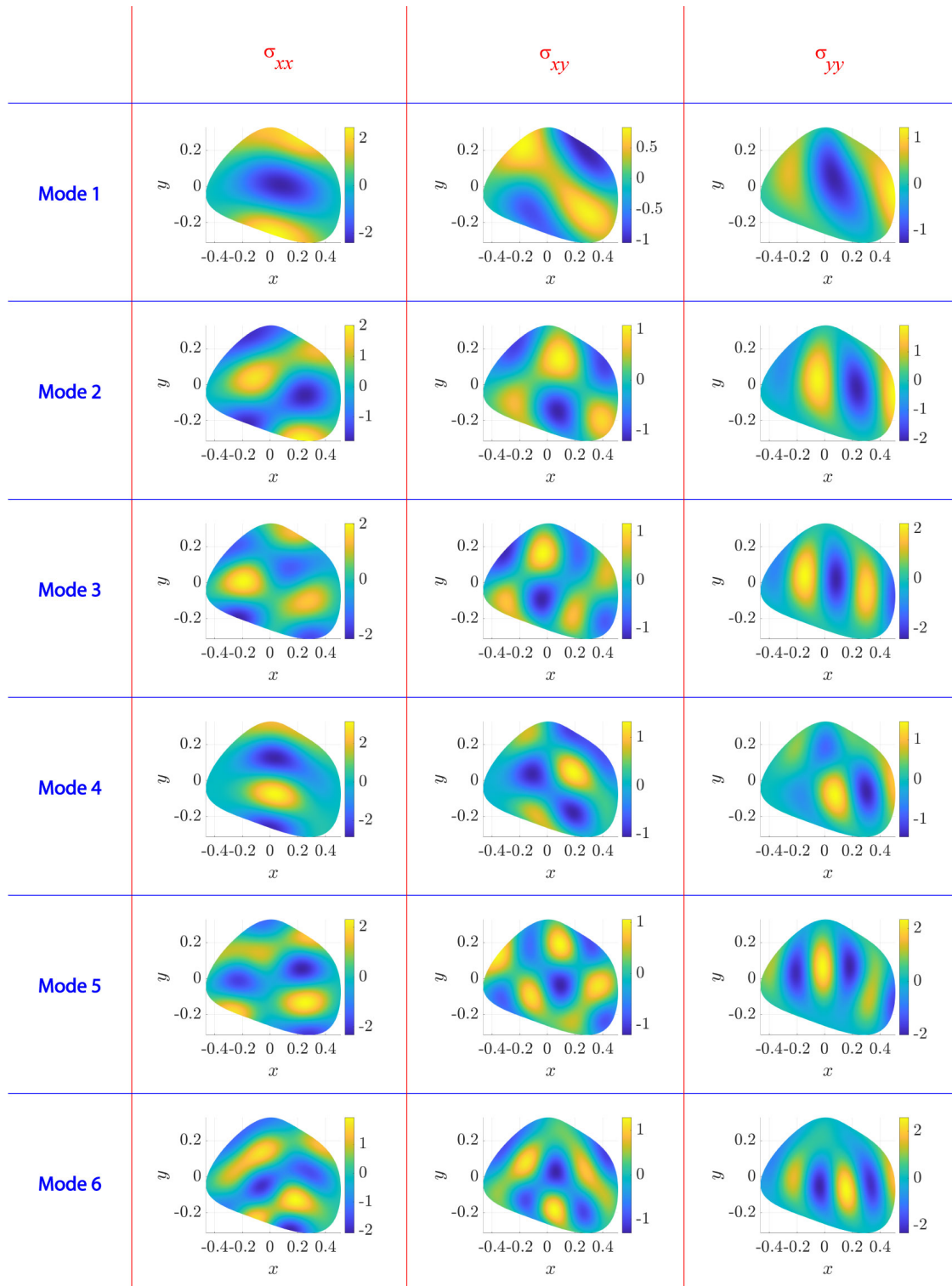


FIGURE 3.6: First six eigenfunctions for an arbitrarily shaped domain; $\lambda_1 = 131.01$, $\lambda_2 = 184.35$, $\lambda_3 = 258.56$, $\lambda_4 = 291.82$, $\lambda_5 = 339.05$, $\lambda_6 = 380.92$.

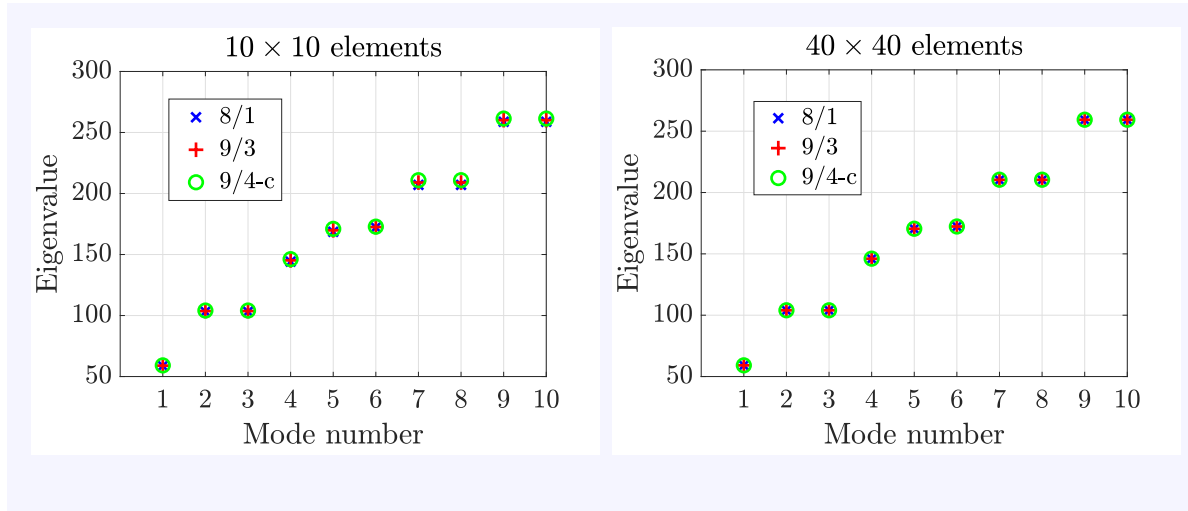


FIGURE 3.7: First ten eigenvalues on a square domain meshed with 8/1, 9/3 and 9/4-c elements; left: 10×10 elements, right: 40×40 elements.

4. Fourth, we have separately implemented independent semi-numerical methods developed later in this chapter (Section 3.2). Those results match our FE solutions near-perfectly. This tells us that our FE solutions are not only stable (no checkerboard) but also accurate.
5. Finally, for the rectangular domain shown in Figure 3.4, we demonstrate convergence numerically. We consider four meshes: 5×5 , 10×10 , 20×20 and 40×40 elements. The first ten eigenvalues from these four meshes are plotted in Figure 3.8. Convergence is clear.

To close this section, we report the time required to compute the eigenfunctions using our own code in Matlab, on a personal computer with an 8th generation i5 processor. Computation of the first 100 eigenfunctions on the rectangular domain shown in Figure 3.4 discretized with uniform meshes of 5×5 , 10×10 , 20×20 , 40×40 , 80×80 and 160×160 elements takes 0.2, 0.6, 1.6, 10.1, 71 and 852 seconds respectively. The computation times are plotted in Figure 3.9 on a log-log scale.

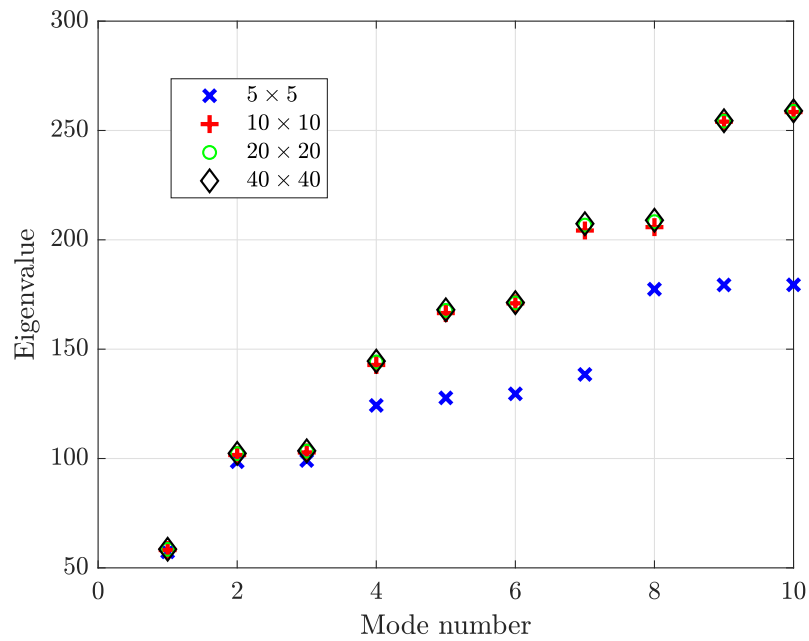


FIGURE 3.8: Convergence of eigenvalues upon mesh refinement.

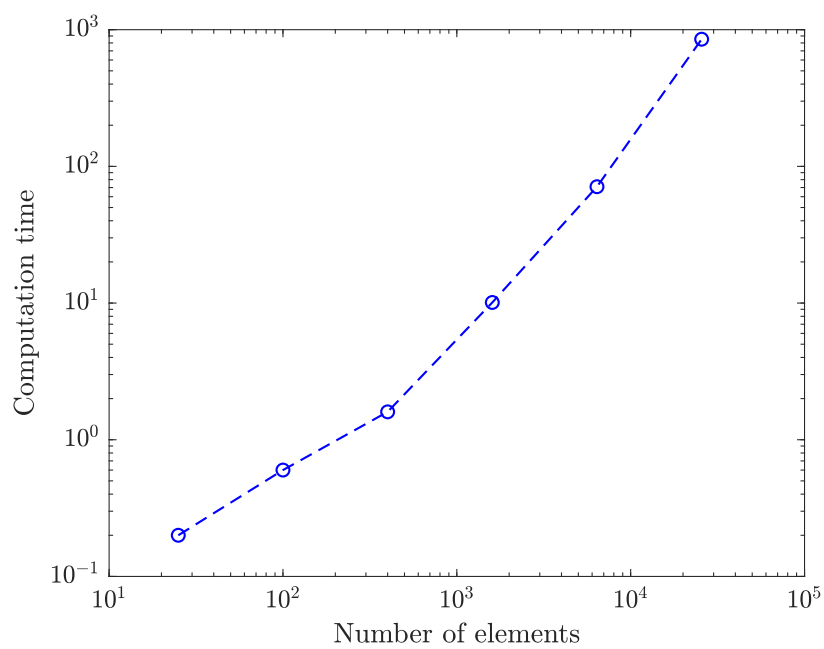


FIGURE 3.9: Time (in seconds) for computation of first one hundred eigenfunctions for different mesh refinements (log-log scale). The data points are joined by straight lines for visibility alone.

3.2 Semi-numerical methods for special domains

3.2.1 Annular domain

On an annular domain, upon choosing a circumferential wave number m , the eigenvalue problem retains one independent variable (r). Many eigenfunctions can then be computed with great accuracy using a large number of points in the radial direction.

We consider an annular domain Ω , centered at the origin, with inner radius $r_a = 0.1$ and outer radius $r_b = 0.3$. We denote the fields $\boldsymbol{\sigma}$ and $\boldsymbol{\mu}$ in polar coordinates as

$$\boldsymbol{\sigma} = \sigma_{rr}(r, \theta) \mathbf{e}_r \otimes \mathbf{e}_r + \sigma_{r\theta}(r, \theta) (\mathbf{e}_r \otimes \mathbf{e}_\theta + \mathbf{e}_\theta \otimes \mathbf{e}_r) + \sigma_{\theta\theta}(r, \theta) \mathbf{e}_\theta \otimes \mathbf{e}_\theta,$$

$$\boldsymbol{\mu} = \mu_r(r, \theta) \mathbf{e}_r + \mu_\theta(r, \theta) \mathbf{e}_\theta.$$

The equation $-\Delta \boldsymbol{\sigma} + \nabla_s \boldsymbol{\mu} = \lambda \boldsymbol{\sigma}$ yields

$$\begin{aligned} \frac{\partial^2 \sigma_{rr}}{\partial r^2} + \frac{1}{r^2} \frac{\partial^2 \sigma_{rr}}{\partial \theta^2} + \frac{1}{r} \frac{\partial \sigma_{rr}}{\partial r} - \frac{4}{r^2} \frac{\partial \sigma_{r\theta}}{\partial \theta} - \frac{2\sigma_{rr}}{r^2} + \frac{2\sigma_{\theta\theta}}{r^2} - \frac{\partial \mu_r}{\partial r} &= \lambda \sigma_{rr}, \\ \frac{\partial^2 \sigma_{\theta\theta}}{\partial r^2} + \frac{1}{r^2} \frac{\partial^2 \sigma_{\theta\theta}}{\partial \theta^2} + \frac{1}{r} \frac{\partial \sigma_{\theta\theta}}{\partial r} + \frac{4}{r^2} \frac{\partial \sigma_{r\theta}}{\partial \theta} + \frac{2\sigma_{rr}}{r^2} - \frac{2\sigma_{\theta\theta}}{r^2} - \frac{1}{r} \frac{\partial \mu_\theta}{\partial \theta} - \frac{\mu_r}{r} &= \lambda \sigma_{\theta\theta}, \\ \frac{\partial^2 \sigma_{r\theta}}{\partial r^2} + \frac{1}{r^2} \frac{\partial^2 \sigma_{r\theta}}{\partial \theta^2} + \frac{1}{r} \frac{\partial \sigma_{r\theta}}{\partial r} + \frac{2}{r^2} \frac{\partial \sigma_{rr}}{\partial \theta} - \frac{2}{r^2} \frac{\partial \sigma_{\theta\theta}}{\partial \theta} - \frac{4\sigma_{r\theta}}{r^2} + \frac{\mu_\theta}{2r} - \frac{1}{2r} \frac{\partial \mu_r}{\partial \theta} - \frac{1}{2} \frac{\partial \mu_\theta}{\partial r} &= \lambda \sigma_{r\theta}. \end{aligned} \quad (3.11)$$

The equilibrium equation $\operatorname{div} \boldsymbol{\sigma} = \mathbf{0}$ becomes

$$\frac{\partial \sigma_{rr}}{\partial r} + \frac{1}{r} \frac{\partial \sigma_{r\theta}}{\partial \theta} + \frac{\sigma_{rr} - \sigma_{\theta\theta}}{r} = 0$$

and

$$\frac{\partial \sigma_{r\theta}}{\partial r} + \frac{1}{r} \frac{\partial \sigma_{\theta\theta}}{\partial \theta} + \frac{2\sigma_{r\theta}}{r} = 0.$$

The boundary condition $\boldsymbol{\sigma} \mathbf{n} = \mathbf{0}$ gives four scalar equations,

$$\sigma_{rr} = 0 \text{ at } r = r_a \text{ and } r_b; \quad \sigma_{r\theta} = 0 \text{ at } r = r_a \text{ and } r_b.$$

The natural boundary condition $\nabla_n \boldsymbol{\sigma} \cdot (\mathbf{t} \otimes \mathbf{t}) = 0$ gives two scalar equations,

$$\frac{\partial \sigma_{\theta\theta}}{\partial r} = 0 \text{ at } r = r_a \text{ and } r_b.$$

We now choose a wave number m (any whole number). Substituting

$$\begin{aligned}\sigma_{rr} &= \tilde{\sigma}_{rr}(r) \cos m\theta, \quad \sigma_{\theta\theta} = \tilde{\sigma}_{\theta\theta}(r) \cos m\theta, \quad \sigma_{r\theta} = \tilde{\sigma}_{r\theta}(r) \sin m\theta, \\ \mu_r &= \tilde{\mu}_r(r) \cos m\theta \quad \text{and} \quad \mu_\theta = \tilde{\mu}_\theta(r) \sin m\theta\end{aligned}\tag{3.12}$$

in the above PDEs, and dropping the tildes for simplicity, we obtain the following five ODEs:

$$\begin{aligned}\sigma_{rr}'' - \frac{m^2}{r^2}\sigma_{rr} + \frac{\sigma_{rr}'}{r} - \frac{4m\sigma_{r\theta}}{r^2} - \frac{2\sigma_{rr}}{r^2} + \frac{2\sigma_{\theta\theta}}{r^2} - \mu_r' + \lambda\sigma_{rr} &= 0, \\ \sigma_{\theta\theta}'' - \frac{m^2}{r^2}\sigma_{\theta\theta} + \frac{\sigma_{\theta\theta}'}{r} + \frac{4m\sigma_{r\theta}}{r^2} + \frac{2\sigma_{rr}}{r^2} - \frac{2\sigma_{\theta\theta}}{r^2} - \frac{m\mu_\theta}{r} - \frac{\mu_r}{r} + \lambda\sigma_{\theta\theta} &= 0, \\ \sigma_{r\theta}'' - \frac{m^2}{r^2}\sigma_{r\theta} + \frac{\sigma_{r\theta}'}{r} - \frac{2m\sigma_{rr}}{r^2} + \frac{2m\sigma_{\theta\theta}}{r^2} - \frac{4\sigma_{r\theta}}{r^2} + \frac{\mu_\theta}{2r} + \frac{m\mu_r}{2r} - \frac{\mu_\theta'}{2} + \lambda\sigma_{r\theta} &= 0, \\ \sigma_{rr}' + \frac{m\sigma_{r\theta}}{r} + \frac{\sigma_{rr} - \sigma_{\theta\theta}}{r} &= 0, \\ \sigma_{r\theta}' - \frac{m\sigma_{\theta\theta}}{r} + \frac{2\sigma_{r\theta}}{r} &= 0,\end{aligned}\tag{3.13}$$

where primes denote derivatives with respect to r , and we have suppressed the r -dependence of the field variables. Equations 3.13 are differential algebraic equations, and the last two were differentiated once each for setting up as a system of first order ODEs. Introducing a new variable ϑ , we obtain the following equivalent set of six first order ODEs (with σ_{rr}'' and $\sigma_{r\theta}''$ eliminated):

$$\begin{aligned}\sigma_{rr}' &= -\frac{\sigma_{rr}}{r} - \frac{m\sigma_{r\theta}}{r} + \frac{\sigma_{\theta\theta}}{r}, \\ \sigma_{r\theta}' &= -\frac{2\sigma_{r\theta}}{r} + \frac{m\sigma_{\theta\theta}}{r}, \\ \sigma_{\theta\theta}' &= \vartheta, \\ \vartheta' &= \frac{m^2\sigma_{\theta\theta}}{r^2} - \frac{\vartheta}{r} - \frac{4m\sigma_{r\theta}}{r^2} - \frac{2\sigma_{rr}}{r^2} + \frac{2\sigma_{\theta\theta}}{r^2} + \frac{\mu_r}{r} + \frac{m\mu_\theta}{r} - \lambda\sigma_{\theta\theta}, \\ \mu_r' &= -\frac{(m^2-1)\sigma_{\theta\theta}}{r^2} - \frac{m\sigma_{r\theta}}{r^2} + \frac{\vartheta}{r} - \frac{(m^2+1)\sigma_{rr}}{r^2} + \lambda\sigma_{rr}, \\ \mu_\theta' &= \frac{2m\vartheta}{r} - \frac{2m^2\sigma_{r\theta}}{r^2} - \frac{4m\sigma_{rr}}{r^2} + \frac{m\mu_r}{r} + \frac{\mu_\theta}{r} + 2\lambda\sigma_{r\theta}.\end{aligned}\tag{3.14}$$

We already have six homogeneous boundary conditions, three at r_a and three at r_b . Non-zero solutions will be possible only for specific discrete values of λ , which must also be determined as part of the solution; but the eigenfunctions will be arbitrarily scalable. To make things definite, we introduce a normalizing boundary condition,

$$\sigma_{\theta\theta} = 1 \text{ at } r = r_a.$$

We have solved the above eigenvalue problem repeatedly using Matlab's built-in routine 'bvp4c' as well as alternative numerical routines of our own (based on the Newton-Raphson method with numerically estimated Jacobians), for chosen m . Each solution obtained gives one eigenvalue-eigenfunction pair. Initial guesses for the iterative solution method must be chosen systematically to ensure that all eigenfunctions are obtained and none missed. The foregoing finite element solutions help identify the first one or two for any m ; for the higher modes, plots of λ_p against p help to identify missed eigenvalues, as does counting the number of zero crossings of $\sigma_{\theta\theta}$.

For demonstration, we choose $m = 3$. The radial variation of stress component functions σ_{rr} , $\sigma_{r\theta}$ and $\sigma_{\theta\theta}$ for the first six eigenfunctions is shown in Figure 3.10.

Finally, for $m > 0$, all eigenvalues appear in pairs in the FEA results; and for each eigenfunction obtained using the semi-numerical method, we can obtain another one by taking the partial derivative with respect to θ in Eq. 3.12 and then dividing by m .

With this semi-numerical approach on the annular domain, for given m , we can accurately compute, say, 50 eigenfunctions. Obtaining the same number of eigenfunctions with $m = 3$ from our finite element approach would require computation of thousands of eigenfunctions with many different wave numbers.

3.2.2 Solid circular disk

A solid circular disk with radius r_b can be thought of as the limit $r_a \rightarrow 0$ of the annulus considered in the previous section. Equations 3.14 continue to remain valid in the interior of the disk, except at its center. The boundary conditions

$$\sigma_{rr} = \sigma_{r\theta} = \sigma'_{\theta\theta} = 0 \quad \text{at} \quad r = r_b$$

also continue to hold. However, we must suitably replace the boundary conditions

$$\sigma_{rr} = \sigma_{r\theta} = \sigma'_{\theta\theta} = 0 \quad \text{at} \quad r = r_a \tag{3.15}$$

by some other conditions in the event of r_a becoming zero since we no longer have a traction free boundary there. These conditions will be given by the requirement that the quantities on the left hand side in Eqs. 3.14 be finite at $r = 0$. As we will see shortly, this yields different conditions for different values of the wave number m .

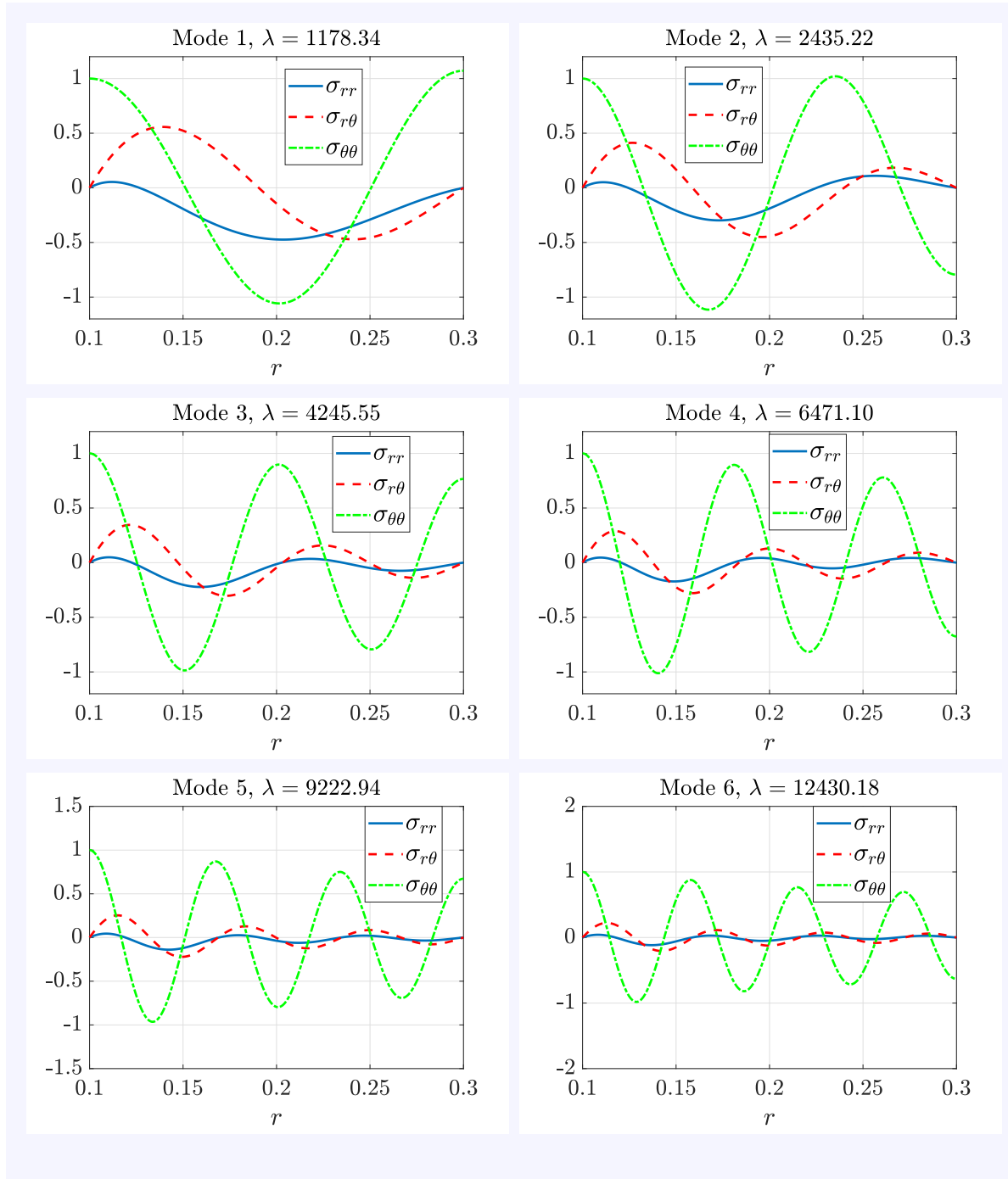


FIGURE 3.10: Radial variation of the first six eigenfunctions for the annular domain, with $m = 3$. In the finite element solution, the first three of these are mode numbers (9,10), (26,27) and (55,56). The eigenvalues from the semi-numerical approach and the FEM match near-perfectly.

The case of $m = 0$:

For $m = 0$, Eqs. 3.14 reduce to:

$$\begin{aligned}
\sigma'_{rr} &= -\frac{\sigma_{rr}}{r} + \frac{\sigma_{\theta\theta}}{r}, \\
\sigma'_{\theta\theta} &= \vartheta, \\
\vartheta' &= -\frac{\vartheta}{r} - \frac{2\sigma_{rr}}{r^2} + \frac{2\sigma_{\theta\theta}}{r^2} + \frac{\mu_r}{r} + \lambda\sigma_{\theta\theta}, \\
\mu'_r &= \frac{\sigma_{\theta\theta}}{r^2} + \frac{\vartheta}{r} - \frac{\sigma_{rr}}{r^2} - \lambda\sigma_{rr}.
\end{aligned} \tag{3.16}$$

The boundary conditions are

$$\sigma_{rr} = \vartheta = 0 \quad \text{at} \quad r = r_b.$$

For σ'_{rr} to be finite at $r = 0$, we require $\sigma_{rr0} = \sigma_{\theta\theta0}$, where the notation f_0 denotes the value of a function f at $r = 0$. For μ'_r to be finite at $r = 0$, after incorporating the previous condition, we require $\vartheta_0 = 0$. Similarly, for ϑ' to be finite at $r = 0$, $\mu_{r0} = 0$. Thus, the three conditions that should replace the conditions in Eqs. 3.15 at $r = r_a = 0$ are

$$\sigma_{rr0} = \sigma_{\theta\theta0}, \quad \vartheta_0 = 0 \quad \text{and} \quad \mu_{r0} = 0. \tag{3.17}$$

However, in the absence of a normalizing condition, the solutions are non-unique. For non-trivial (i.e., non-zero) solutions, we introduce a normalizing boundary condition,

$$\sigma_{rr0} = \sigma_{\theta\theta0} = 1.$$

But now we have more initial conditions than we require. To get around this issue, we take ϑ_0 as a variable that is to be solved as part of the boundary value problem. We know from Eq. 3.17 that if the solutions are well behaved, ϑ_0 should *come* out to be zero upon solving the boundary value problem.

In summary, we solve Eqs. 3.16 subject to the conditions

$$\sigma_{rr} = \sigma_{\theta\theta} = 1, \quad \mu_r = 0 \quad \text{at} \quad r = r_a = 0; \quad \sigma_{rr} = \vartheta = 0 \quad \text{at} \quad r = r_b.$$

To avoid numerical issues, instead of putting r_a to be zero in the ODE solver, we put it to be a small number (like 0.001 times r_b). We plot the first four eigenfunctions for $m = 0$ in Figure 3.11. The results match well with those from the FEM.

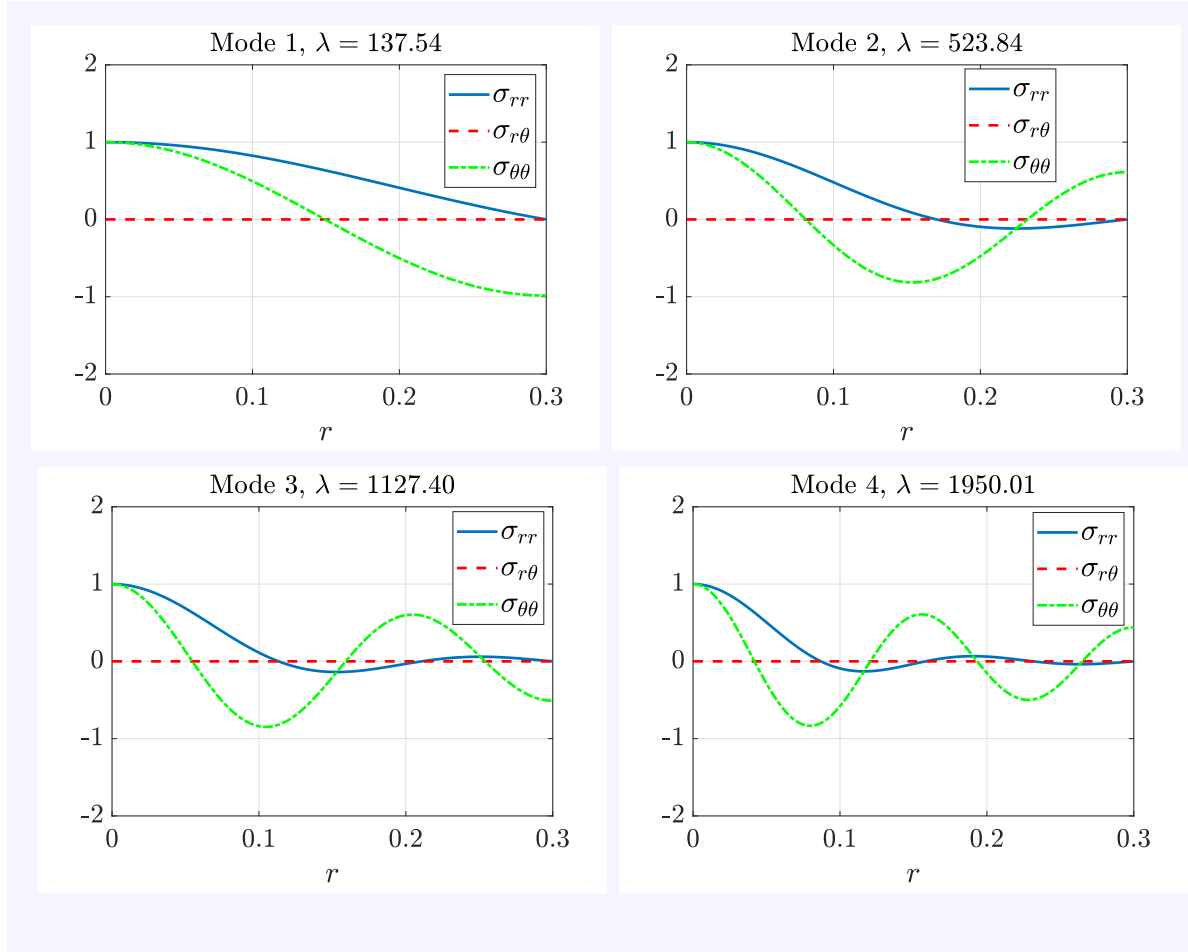


FIGURE 3.11: Radial variation of the first four eigenfunctions for a circular disk, with $m = 0$. In the finite element solution, these are mode numbers 1, 6, 15 and 30, respectively. The eigenvalues from the semi-numerical approach and the FEM match near-perfectly.

The case of $m = 1$:

For $m = 1$, Eqs. 3.14 reduce to

$$\begin{aligned}
 \sigma'_{rr} &= -\frac{\sigma_{rr}}{r} - \frac{\sigma_{r\theta}}{r} + \frac{\sigma_{\theta\theta}}{r}, \\
 \sigma'_{r\theta} &= -\frac{2\sigma_{r\theta}}{r} + \frac{\sigma_{\theta\theta}}{r}, \\
 \sigma'_{\theta\theta} &= \vartheta, \\
 \vartheta' &= \frac{3\sigma_{\theta\theta}}{r^2} - \frac{\vartheta}{r} - \frac{4\sigma_{r\theta}}{r^2} - \frac{2\sigma_{rr}}{r^2} + \frac{\mu_r}{r} + \frac{\mu_\theta}{r} + \lambda\sigma_{\theta\theta}, \\
 \mu'_r &= -\frac{\sigma_{r\theta}}{r^2} + \frac{\vartheta}{r} - \frac{2\sigma_{rr}}{r^2} - \lambda\sigma_{rr}, \\
 \mu'_\theta &= \frac{2\vartheta}{r} - \frac{2\sigma_{r\theta}}{r^2} - \frac{4\sigma_{rr}}{r^2} + \frac{\mu_r}{r} + \frac{\mu_\theta}{r} - 2\lambda\sigma_{r\theta}.
 \end{aligned} \tag{3.18}$$

For the left hand side quantities in the above equations to be finite at $r = 0$, the following five algebraic equations must be satisfied:

$$\begin{aligned} -\sigma_{rr_0} - \sigma_{r\theta_0} + \sigma_{\theta\theta_0} &= 0, \\ -2\sigma_{r\theta_0} + \sigma_{\theta\theta_0} &= 0, \\ -\vartheta_0 + \mu_{r_0} + \mu_{\theta_0} &= 0, \\ \vartheta_0 - 3\sigma_{r\theta_0} &= 0, \\ 2\vartheta_0 - 6\sigma_{r\theta_0} + \mu_{r_0} + \mu_{\theta_0} &= 0. \end{aligned}$$

Upon solving, we get

$$\sigma_{rr_0} = \sigma_{r\theta_0} = \sigma_{\theta\theta_0} = \vartheta_0 = \mu_{r_0} + \mu_{\theta_0} = 0. \quad (3.19)$$

This time we put the normalizing condition as

$$\mu_{r_0} = -\mu_{\theta_0} = 1. \quad (3.20)$$

The other conditions imposed at $r = r_a = 0$ are

$$\sigma_{rr_0} = \sigma_{r\theta_0} = 0,$$

and we consider $\sigma_{\theta\theta_0}$ and ϑ_0 as variables.

The first four eigenfunctions corresponding to $m = 1$ are plotted in Figure 3.12. As before, the results match well with the FEM.

The case of $m = 2$:

For $m = 2$, Eqs. 3.14 reduce to

$$\begin{aligned} \sigma'_{rr} &= -\frac{\sigma_{rr}}{r} - \frac{2\sigma_{r\theta}}{r} + \frac{\sigma_{\theta\theta}}{r}, \\ \sigma'_{r\theta} &= -\frac{2\sigma_{r\theta}}{r} + \frac{2\sigma_{\theta\theta}}{r}, \\ \sigma'_{\theta\theta} &= \vartheta, \\ \vartheta' &= \frac{4\sigma_{\theta\theta}}{r^2} - \frac{\vartheta}{r} - \frac{8\sigma_{r\theta}}{r^2} - \frac{2\sigma_{rr}}{r^2} + \frac{2\sigma_{\theta\theta}}{r^2} + \frac{\mu_r}{r} + \frac{2\mu_\theta}{r} + \lambda\sigma_{\theta\theta}, \\ \mu'_r &= -\frac{3\sigma_{\theta\theta}}{r^2} - \frac{2\sigma_{r\theta}}{r^2} + \frac{\vartheta}{r} - \frac{5\sigma_{rr}}{r^2} - \lambda\sigma_{rr}, \\ \mu'_\theta &= \frac{4\vartheta}{r} - \frac{8\sigma_{r\theta}}{r^2} - \frac{8\sigma_{rr}}{r^2} + \frac{2\mu_r}{r} + \frac{\mu_\theta}{r} - 2\lambda\sigma_{r\theta}. \end{aligned} \quad (3.21)$$

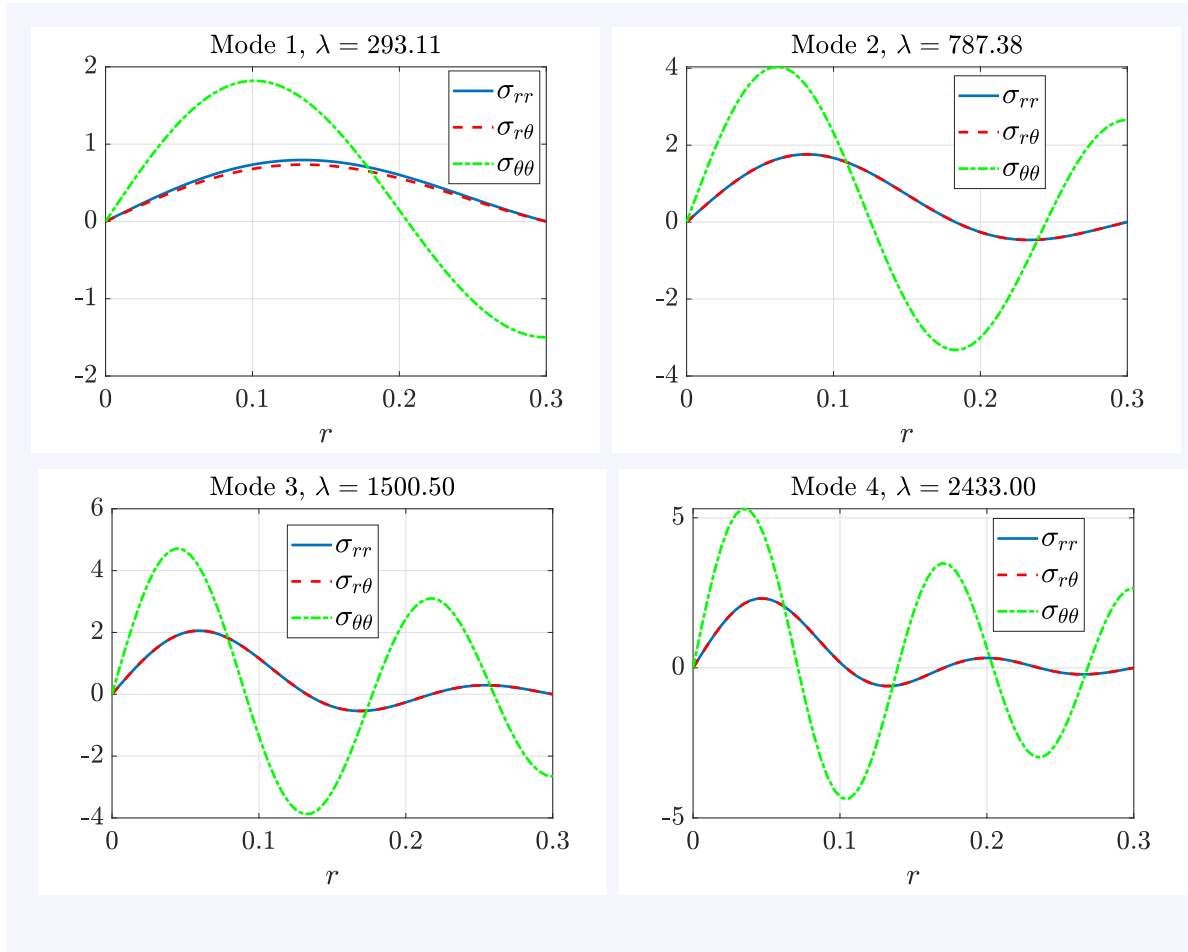


FIGURE 3.12: Radial variation of the first four eigenfunctions for a circular disk, with $m = 1$. In the finite element solution, these are mode numbers (2,3), (9,10), (22,23) and (37,38), respectively. The eigenvalues from the semi-numerical approach and the FEM match near-perfectly.

The conditions for finiteness of all quantities at $r = 0$ are

$$\begin{aligned}
 -\sigma_{rr0} - 2\sigma_{r\theta_0} + \sigma_{\theta\theta_0} &= 0, \\
 -\sigma_{r\theta_0} + \sigma_{\theta\theta_0} &= 0, \\
 3\sigma_{\theta\theta_0} - 4\sigma_{r\theta_0} - \sigma_{rr0} &= 0, \\
 -\vartheta_0 + \mu_{r_0} + 2\mu_{\theta_0} &= 0, \\
 \vartheta_0 &= 0, \\
 -3\sigma_{\theta\theta_0} - 2\sigma_{r\theta_0} - 5\sigma_{rr0} &= 0, \\
 \sigma_{rr0} + \sigma_{r\theta_0} &= 0, \\
 4\vartheta_0 + 2\mu_{r_0} + \mu_{\theta_0} &= 0.
 \end{aligned}$$

Upon solving the above equations, we find that

$$\sigma_{r\theta_0} = \sigma_{\theta\theta_0} = -\sigma_{rr_0} \quad \text{and} \quad \vartheta_0 = \mu_{r_0} = \mu_{\theta_0} = 0.$$

We choose the normalization condition to be

$$\sigma_{rr_0} = 1.$$

In the ODE solver, we put $\vartheta_0 = \mu_{r_0} = \mu_{\theta_0} = 0$, leaving $\sigma_{r\theta_0}$ and $\sigma_{\theta\theta_0}$ as variables to be computed.

The first four computed eigenfunctions are plotted in Figure 3.13, which match well with the corresponding solutions from the FEM.

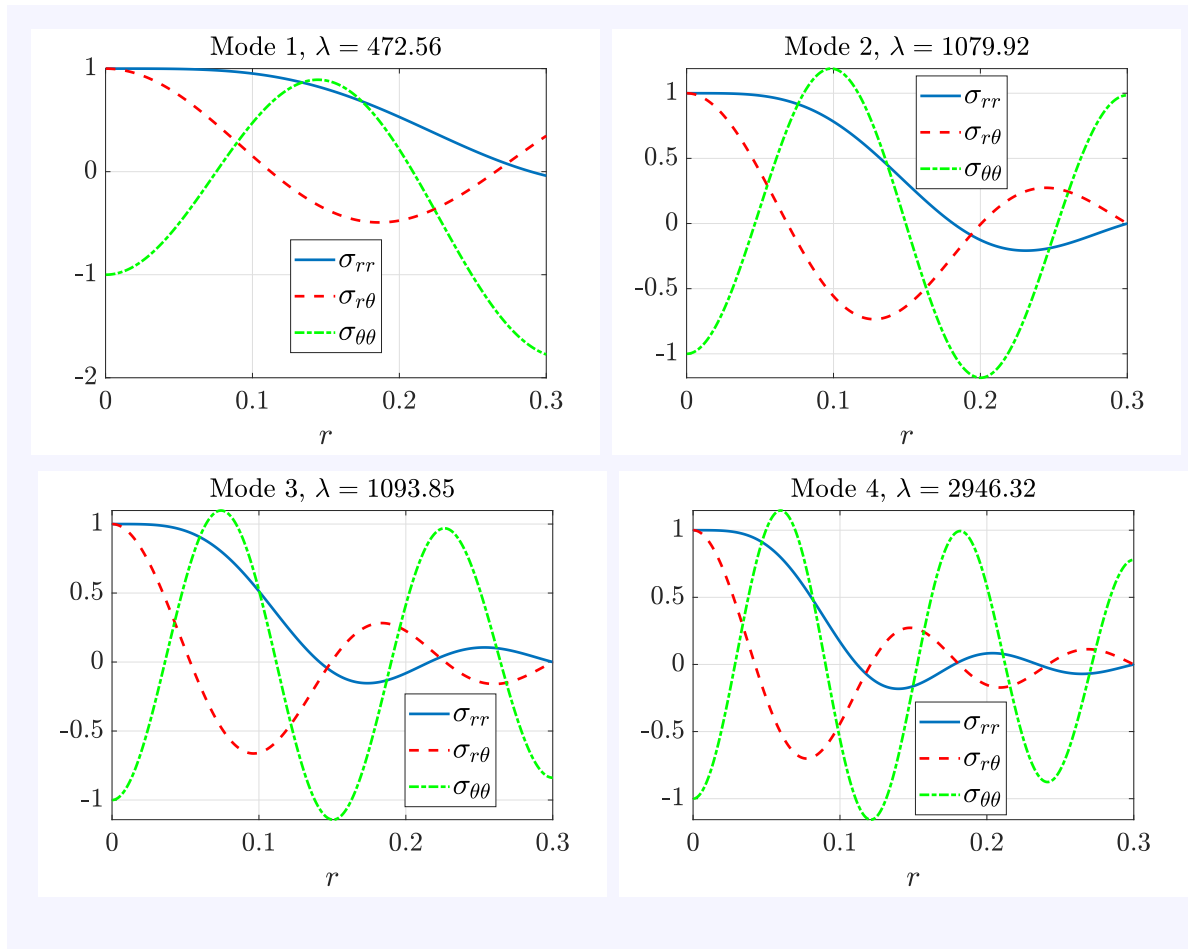


FIGURE 3.13: Radial variation of the first four eigenfunctions for a circular disk, with $m = 2$. In the finite element solution, these are mode numbers (4,5), (13,14), (28,29) and (47,48), respectively. The eigenvalues from the semi-numerical approach and the FEM match near-perfectly.

The case of $m > 2$:

It can be easily verified that for $m > 2$, the conditions for finiteness of all quantities at $r = 0$ are the same as those for $m = 1$:

$$\sigma_{rr0} = \sigma_{r\theta_0} = \sigma_{\theta\theta_0} = \vartheta_0 = \mu_{r_0} + \mu_{\theta_0} = 0.$$

Using the normalizing condition in Eq. 3.20, we compute the eigenfunctions as before. The results obtained match well with corresponding FEM solutions.

Description of stress state at the center using the Mohr's circle:

We see that all the stress components are zero at the center of the disk (let us denote this point as C) for $m = 1$ and $m > 2$. This can be explained using the Mohr's circle at C [57]. We will see below that the variation of the stress components in the circumferential direction as determined from the Mohr's circle can only correspond to either $m = 0$ or $m = 2$.

We assume for the purpose of this discussion, without loss of generality, that $\sigma_{xy} = 0$ and $\sigma_{xx} \geq \sigma_{yy}$ at C . A corresponding Mohr's circle is drawn in Figure 3.14.

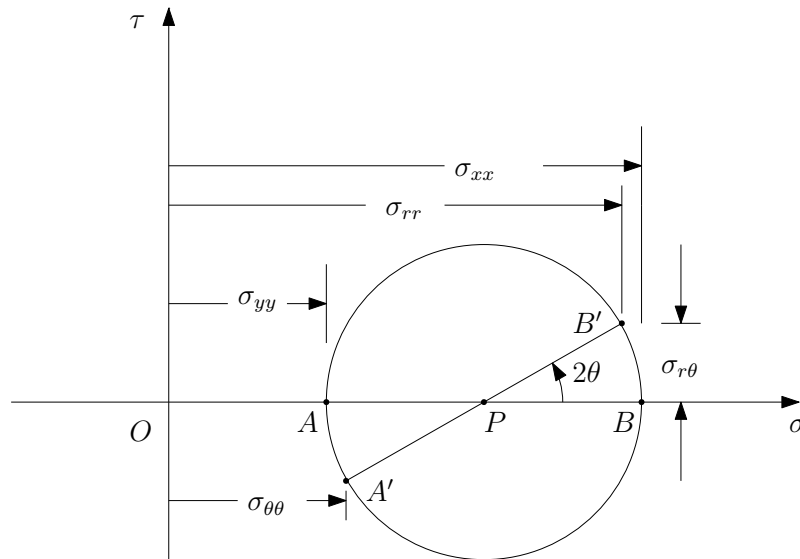


FIGURE 3.14: A representative Mohr's circle at the center C for the case $\sigma_{xy} = 0$.

We note that at C , the state of stress $(\sigma_{nn}, \sigma_{tt}, \sigma_{nt})$ on a plane with normal \mathbf{n} oriented at an angle θ is simply $(\sigma_{rr}, \sigma_{\theta\theta}, \sigma_{r\theta})$. Therefore, if the stress components σ_{xx} and σ_{yy} are known, the components σ_{rr} , $\sigma_{\theta\theta}$ and $\sigma_{r\theta}$ at an angle θ can be determined by moving along the Mohr's circle by 2θ (Figure 3.14).

We first consider $\sigma_{xx} > \sigma_{yy}$. This is depicted in Figure 3.14. To determine the functions $\sigma_{rr}(0, \theta)$, $\sigma_{\theta\theta}(0, \theta)$ and $\sigma_{r\theta}(0, \theta)$ for $0 \leq \theta \leq 2\pi$, we need to traverse 4π , i.e., two cycles, on the Mohr's circle. It is clear that these three functions will then go through two cycles of variation, corresponding to wave number $m = 2$. Thus, it is possible to have non-zero stress at C with $m = 2$.

When $\sigma_{xx} = \sigma_{yy}$, the Mohr's circle collapses to a point. This situation is depicted in Figure 3.15. The stress components σ_{rr} , $\sigma_{\theta\theta}$ and $\sigma_{r\theta}$ do not vary with θ , in agreement with $m = 0$.

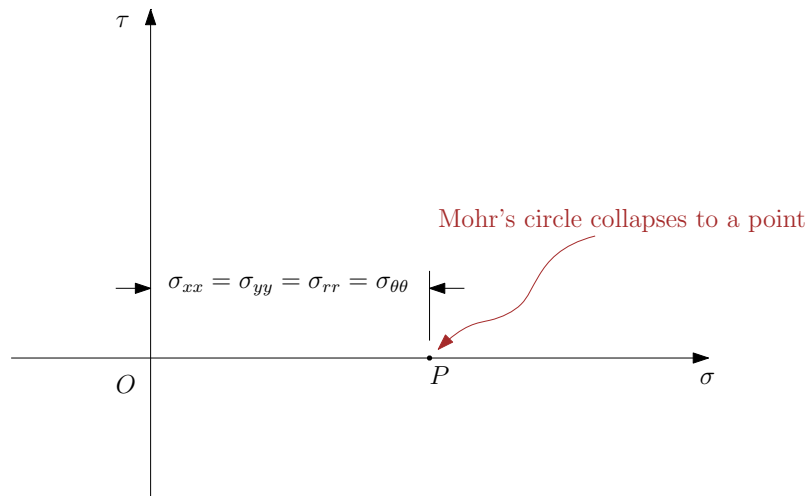


FIGURE 3.15: A representative Mohr's circle at C for $m = 0$.

For m other than 0 and $m = 2$, the variation with θ cannot agree with that deduced from the Mohr's circle, if the stress is both non-zero and well-behaved. For instance, $m = 1$ implies that $\sigma_{rr}(0, \theta)$ is maximum at $\theta = 0$ and minimum at $\theta = \pi$, with no other maximum or minimum; but from the Mohr's circle we conclude that $\sigma_{rr}(0, 0) = \sigma_{rr}(0, \pi)$. The only possibility is to have $\sigma_{rr} = 0$ at C . The other stress components must also be zero at C by similar arguments.

We point out that the Mohr's circle discussion above is just a way to pictorially support our earlier conclusions. We cannot have equilibrium at C for a non-zero well-behaved stress state with $m = 1$ or $m > 2$. These conclusions agree completely with the foregoing results, and are presented here merely to aid intuition through graphical considerations.

3.2.3 Rectangular domain

A third kind of special domain is rectangular. Here we consider the slightly simpler case of a square.

We saw in the previous sections that in annular and circular domains, periodicity in the θ -direction permits a Fourier expansion in θ , reducing the governing PDEs to ODEs in the r -coordinate. In rectangular domains, there is no such direction of guaranteed periodicity.

However, there are other symmetries that can be exploited in rectangular geometries. In this section, we use these symmetries to construct a sequence of 1D functions with zero mean and zero boundary values. This sequence provides a complete representation of all residual stress fields using a separation of variables approach. We use this representation to convert the eigenvalue problem of Eq. 2.12 into an algebraic equation.

Our approach is developed as follows. Let us consider a residually stressed square strip lying between $x = 0$, $x = 1$, $y = 0$ and $y = 1$. Extension of the approach to rectangular strips is easy. The equilibrium equations in Cartesian coordinates are

$$\begin{aligned}\sigma_{xx,x} + \sigma_{xy,y} &= 0, \\ \sigma_{xy,x} + \sigma_{yy,y} &= 0.\end{aligned}$$

The boundary conditions satisfied by the stress components are:

$$\begin{aligned}\sigma_{xx} &= 0 \text{ at } x = 0, x = 1, \\ \sigma_{yy} &= 0 \text{ at } y = 0, y = 1, \\ \sigma_{xy} &= 0 \text{ at } x = 0, x = 1, y = 0, y = 1.\end{aligned}$$

We consider a σ_{xy} of the form

$$\sigma_{xy} = \psi(x)\eta(y). \quad (3.22)$$

From the equilibrium equations, we have

$$\begin{aligned}\sigma_{xx} &= -\eta'(y) \int_0^x \psi(\xi) d\xi, \\ \sigma_{yy} &= -\psi'(x) \int_0^y \eta(\xi) d\xi,\end{aligned} \quad (3.23)$$

where the prime denotes a derivative with respect to the argument of the function. The boundary conditions on σ_{xy} imply

$$\psi(0) = \psi(1) = \eta(0) = \eta(1) = 0.$$

From Eq. 3.23, we see that σ_{xx} automatically satisfies the boundary condition at $x = 0$. Since σ_{xx} is zero on the $x = 1$ boundary as well, we have

$$\eta'(y) = 0 \quad \text{or} \quad \int_0^1 \psi(\xi) d\xi = 0.$$

The first of the above conditions, if adopted for all y , leads to the trivial solution since $\eta(0) = 0$. For non-trivial solutions, we thus require

$$\int_0^1 \psi(\xi) d\xi = 0.$$

Hence, $\psi(x)$ is a function on $0 \leq x \leq 1$ with zero mean and zero boundary values. Identical arguments in the y -direction imply that $\eta(y)$ is a function on $0 \leq y \leq 1$ with zero mean and zero boundary values.

In light of the above observations, we seek a basis for 1D scalar functions $f(\xi)$ on $0 \leq \xi \leq 1$ with zero mean and zero boundary values. To obtain such a basis, we informally use ideas similar to those used in Chapter 2.

3.2.3.1 Orthogonal bases for ψ and η

We begin by seeking the stationary points of the functional

$$F_0 = \frac{1}{2} \int_0^1 f'(\xi)^2 d\xi$$

over sufficiently regular functions that satisfy

$$\frac{1}{2} \int_0^1 f(\xi)^2 d\xi = 1, \quad \int_0^1 f(\xi) d\xi = 0 \quad \text{and} \quad f(0) = f(1) = 0.$$

We incorporate the integral constraints through constant Lagrange multipliers p and q , and seek the stationary points of the functional

$$F = \int_0^1 \left\{ \frac{f'(\xi)^2}{2} - p \left(\frac{f(\xi)^2}{2} - 1 \right) - qf(\xi) \right\} d\xi.$$

The Euler-Lagrange equation of this variational problem is

$$f''(\xi) + pf(\xi) + q = 0.$$

The general solution to the above ODE is

$$f(\xi) = A \sin \sqrt{p}\xi + B \cos \sqrt{p}\xi - \frac{q}{p}.$$

The condition $f(0) = 0$ gives

$$\frac{q}{p} = B,$$

while $f(1) = 0$, after incorporating the above equality, gives

$$A \sin \sqrt{p} + B(\cos \sqrt{p} - 1) = 0. \quad (3.24)$$

The integral constraint $\int_0^1 f(\xi) d\xi = 0$ yields

$$A(1 - \cos \sqrt{p}) + B(\sin \sqrt{p} - \sqrt{p}) = 0. \quad (3.25)$$

For non-trivial solutions of Eqs. 3.24 and 3.25, we require that

$$\sin \sqrt{p}(\sin \sqrt{p} - \sqrt{p}) + (1 - \cos \sqrt{p})^2 = 0.$$

The above equation has infinitely many roots, and the corresponding eigenfunctions have the form

$$f(\xi) = A \sin \sqrt{p}\xi$$

if $\sqrt{p} = 2n\pi$, $n = 1, 2, 3, \dots$, and

$$f(\xi) = A \left\{ \sin \sqrt{p}\xi + \frac{\sin \sqrt{p}}{1 - \cos \sqrt{p}} (\cos \sqrt{p}\xi - 1) \right\}$$

otherwise. We arrange these functions in order of increasing p to obtain the sequence (f_k) .

We now show that the eigenfunctions are mutually orthogonal. Let f_1 and f_2 be two distinct eigenfunctions with corresponding eigenvalue pairs (p_1, q_1) and (p_2, q_2) . Then,

$$\begin{aligned} f_1'' + p_1 f_1 + q_1 &= 0, \\ f_2'' + p_2 f_2 + q_2 &= 0. \end{aligned} \quad (3.26)$$

Consider the inner product of the first of Eqs. 3.26 with f_2 , i.e.,

$$\int_0^1 f_1'' f_2 d\xi + p_1 \int_0^1 f_1 f_2 d\xi + q_1 \int_0^1 f_2 d\xi = 0.$$

Upon integrating by parts, the first term on the left hand side can be simplified to

$$\int_0^1 f_1'' f_2 d\xi = f_1'(1)f_2(1) - f_1'(0)f_2(0) - \int_0^1 f_1' f_2' d\xi = - \int_0^1 f_1' f_2' d\xi$$

since f_2 is zero on the boundaries. Moreover, since it also has zero mean, the last term on the left hand side of the inner product also drops out. Thus, we obtain

$$\int_0^1 f_1' f_2' d\xi = p_1 \int_0^1 f_1 f_2 d\xi.$$

Similarly,

$$\int_0^1 f_1' f_2' d\xi = p_2 \int_0^1 f_1 f_2 d\xi.$$

If $p_1 \neq p_2$, we have

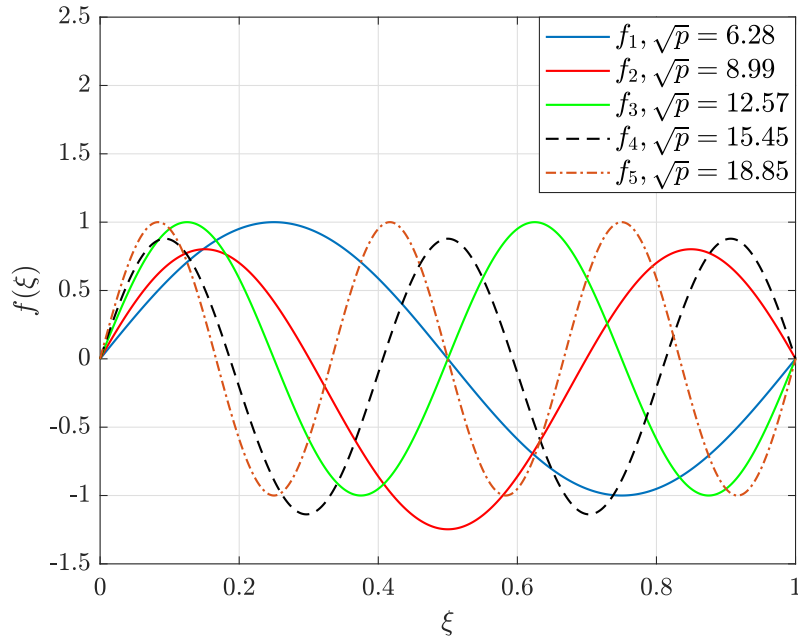
$$\int_0^1 f_1' f_2' d\xi = \int_0^1 f_1 f_2 d\xi = 0. \quad (3.27)$$

If $p_1 = p_2$, then we can choose f_1 and f_2 to be orthogonal, and the above equation still holds.

The first five functions of this sequence, normalized by setting $A = 1$, are plotted in Figure 3.16.

We assume here, and our numerics will indicate as well, that the sequence (f_k) spans the set of all sufficiently regular functions on $0 \leq \xi \leq 1$ with zero mean and zero boundary values. A proof could be attempted along similar lines to the one presented in Chapter 2, but is omitted because of the excellent numerical support obtained below. However, we indicate in Section 7.2 how the proof of Chapter 2 could be adapted for the functions f .

Recalling that the functions $\psi(x)$ and $\eta(y)$ (Eq. 3.22) have zero mean and zero boundary values on their respective unit domains, we can express each of them as linear combinations of these basis functions f_k .

FIGURE 3.16: First five functions in the sequence (f_k) .

3.2.3.2 A basis of variable separable residual stress fields

We now return to residual stresses σ with (Eq. 3.22):

$$\sigma_{xy} = \psi(x)\eta(y).$$

We showed above that $\psi(x)$ has zero mean on $0 \leq x \leq 1$, and $\psi(0) = \psi(1) = 0$. Therefore,

$$\psi(x) = \sum_{i=1}^{\infty} b_i f_i(x)$$

for some coefficients b_i . Similarly,

$$\eta(y) = \sum_{i=1}^{\infty} \tilde{b}_i f_i(y).$$

Accordingly, we write

$$\sigma_{xy} = \sum_{i=1}^{\infty} \sum_{j=1}^{\infty} a_{ij} f_i(x) f_j(y),$$

where a_{ij} are constant coefficients.

Using the first equilibrium equation, we have

$$\sigma_{xx}(x, y) = - \sum_{i=1}^{\infty} \sum_{j=1}^{\infty} a_{ij} f_j'(y) \int_{\xi=0}^x f_i(\xi) d\xi.$$

From the second equilibrium equation, we have

$$\sigma_{yy}(x, y) = - \sum_{i=1}^{\infty} \sum_{j=1}^{\infty} a_{ij} f_i'(x) \int_{\xi=0}^y f_j(\xi) d\xi.$$

The above representations ensure that all differential constraints and boundary conditions on $\boldsymbol{\sigma}$ are satisfied. We have thus obtained a representation for all residual stresses having the variable separable form of Eqs. 3.22–3.23, and linear combinations thereof. We arrange our basis functions using a single index, say k , and call them $\boldsymbol{\varsigma}_k$. For instance, the representation of the first basis function $\boldsymbol{\varsigma}_1$ in Cartesian coordinates is as follows:

$$\begin{bmatrix} \varsigma_{1xx} & \varsigma_{1xy} \\ \varsigma_{1xy} & \varsigma_{1yy} \end{bmatrix} = \begin{bmatrix} -f_1'(y) \int_{\xi=0}^x f_1(\xi) d\xi & f_1(x)f_1(y) \\ f_1(x)f_1(y) & -f_1'(x) \int_{\xi=0}^y f_1(\xi) d\xi \end{bmatrix}.$$

We anticipate that $\boldsymbol{\varsigma}_i$ form a basis for *all* sufficiently regular residual stress fields on the square geometry considered and will obtain empirical support for this below; however we do not attempt a proof here. We will see that the results obtained using this semi-numerical approach match well with those from the FEM. In particular, the first one hundred eigenvalues from the two approaches match near-perfectly. This empirical evidence does not only strongly support that we do indeed have a basis, but also that our FE results are correct.

We now compute the eigenfunctions ϕ_i .

3.2.3.3 Alternative computation of residual stress eigenfunctions ϕ_i

We now use the sequence $\boldsymbol{\varsigma}_i$ above, which we suppose to be a basis, to compute our residual stress eigenfunctions.

To this end, we again seek the stationary points of the functional

$$J_0(\tilde{\boldsymbol{\sigma}}) = \frac{1}{2} \int_{\Omega} \nabla \tilde{\boldsymbol{\sigma}} \cdot \nabla \tilde{\boldsymbol{\sigma}} dA$$

subject to the normalization constraint $\int_{\Omega} \tilde{\sigma} \cdot \tilde{\sigma} dA = 1$. The normalization constraint is incorporated through a constant Lagrange multiplier $\frac{\lambda}{2}$. Accordingly, we seek the stationary points of

$$J(\hat{\sigma}) = \int_{\Omega} \left\{ \frac{1}{2} \nabla \hat{\sigma} \cdot \nabla \hat{\sigma} - \frac{\lambda}{2} \left(\hat{\sigma} \cdot \hat{\sigma} - \frac{1}{|\Omega|} \right) \right\} dA,$$

where $\hat{\sigma} = \sum_{i=1}^N a_i \varsigma_i$ for some suitably large N . The functional J can be represented in terms of the coefficient vector a , after dropping a constant, as

$$J(a) = a^T M a - \lambda a^T W a,$$

where T denotes matrix transpose. The stationary values of J are obtained by solving the generalized eigenvalue problem

$$M a = \lambda W a. \quad (3.28)$$

The orthogonality of functions f (see Eq. 3.27) leads to sparse M and W . Because N is finite, we obtain approximate λ and a . The first 100 eigenvalues obtained using this approach are plotted in Figure 3.17. We also plot the eigenvalues obtained with the FEM using a fine mesh of 6400 elements for comparison. We observe that the match is near-perfect.

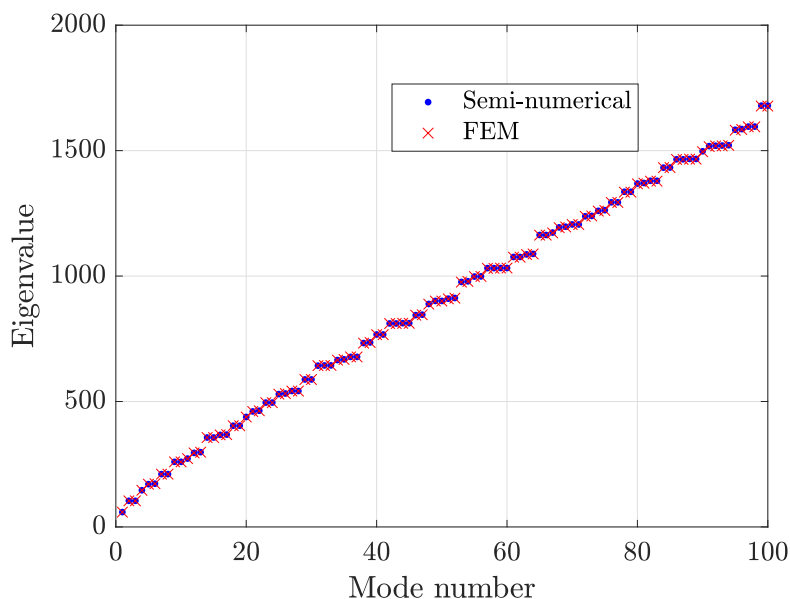


FIGURE 3.17: First 100 eigenvalues for a square domain obtained using the semi-numerical approach and the FEM.

3.2.4 Annular wedge

An annular wedge, with inner radius r_a and outer radius r_b , subtending an angle θ_0 at the center is shown schematically in Figure 3.18.

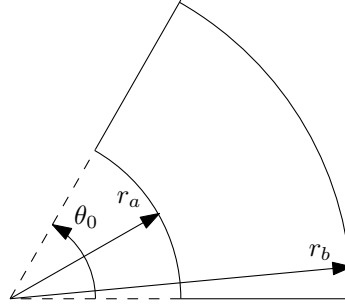


FIGURE 3.18: An annular wedge.

The strip lies between $\theta = 0$ and $\theta = \theta_0$. The equilibrium equations in polar coordinates are

$$\begin{aligned}\sigma_{rr,r} + \frac{1}{r}\sigma_{r\theta,\theta} + \frac{\sigma_{rr} - \sigma_{\theta\theta}}{r} &= 0, \\ \sigma_{r\theta,r} + \frac{1}{r}\sigma_{\theta\theta,\theta} + \frac{2}{r}\sigma_{r\theta} &= 0.\end{aligned}$$

The boundary conditions are

$$\begin{aligned}\sigma_{rr} &= 0 \text{ at } r = r_a, r = r_b, \\ \sigma_{\theta\theta} &= 0 \text{ at } \theta = 0, \theta = \theta_0, \\ \sigma_{r\theta} &= 0 \text{ at } r = r_a, r = r_b, \theta = 0, \theta = \theta_0.\end{aligned}$$

We will now use an approach similar to that used in Section 3.2.3. Let

$$\sigma_{r\theta} = \psi(r)\eta(\theta).$$

The boundary conditions on $\sigma_{r\theta}$ imply that

$$\psi(r_a) = \psi(r_b) = 0 \quad \text{and} \quad \eta(0) = \eta(\theta_0) = 0.$$

Introducing two new functions $\Lambda(r)$ and $\vartheta(\theta)$ for brevity, from the second equilibrium equation, we have

$$\sigma_{\theta\theta} = \{-2\psi(r) - r\psi'(r)\} \int_0^\theta \eta(\xi) d\xi = \Lambda(r)\vartheta(\theta),$$

say. We see that the boundary condition on $\sigma_{\theta\theta}$ at $\theta = 0$ is satisfied automatically. The boundary condition at θ_0 is satisfied if

$$\int_0^{\theta_0} \eta(\xi) d\xi = 0,$$

i.e., η must have zero mean (setting $\Lambda(r)$ to zero yields the trivial solution).

Similarly, to obtain σ_{rr} , we rewrite the first equilibrium equation as

$$(r\sigma_{rr})_{,r} = -\sigma_{r\theta,\theta} + \sigma_{\theta\theta}.$$

Integrating both sides and dividing by r , we obtain

$$\begin{aligned} \sigma_{rr} &= \frac{1}{r} \left\{ \vartheta(\theta) \int_{r_a}^r \Lambda(\xi) d\xi - \eta'(\theta) \int_{r_a}^r \psi(\xi) d\xi \right\} \\ &= \frac{1}{r} \left[\vartheta(\theta) \int_{r_a}^r \{-2\psi(\xi) - \xi\psi'(\xi)\} d\xi - \eta'(\theta) \int_{r_a}^r \psi(\xi) d\xi \right] \\ &= \frac{1}{r} \left[-\vartheta(\theta) \int_{r_a}^r \psi(\xi) d\xi - \vartheta(\theta) \int_{r_a}^r \{\xi\psi(\xi)\}' d\xi - \eta'(\theta) \int_{r_a}^r \psi(\xi) d\xi \right] \\ &= \frac{1}{r} \left[(-\vartheta(\theta) - \eta'(\theta)) \int_{r_a}^r \psi(\xi) d\xi - \vartheta(\theta) \{r\psi(r) - r_a\psi(r_a)\} \right]. \end{aligned}$$

The boundary condition $\sigma_{rr} = 0$ at $r = r_a$ is automatically satisfied. Since $\psi(r_a) = \psi(r_b) = 0$, the boundary condition $\sigma_{rr} = 0$ at $r = r_b$ is satisfied if

$$\int_{r_a}^{r_b} \psi(\xi) d\xi = 0,$$

i.e., ψ has zero mean (note that taking $\vartheta(\theta) + \eta'(\theta) = 0$ leads to the trivial solution).

Thus, the situation is similar to that in the previous section (Section 3.2.3). The shear component $\sigma_{r\theta}$ is the product of two single-variable functions, each with zero boundary values and zero mean. There is one notable difference from the previous section, however. There, the domain of the functions $f_k(\xi)$ was $0 \leq \xi \leq 1$ (recall that $f_k(\xi)$ form a basis for 1D functions with zero mean on $0 \leq \xi \leq 1$ and zero boundary values). For the annular wedge of Figure 3.18, the corresponding 1D domains are $r_a \leq r \leq r_b$ and $0 \leq \theta \leq \theta_0$, for the radial and the azimuthal directions, respectively. Accordingly, we modify the basis functions obtained in the previous section. We call these functions $\tilde{f}_k(r)$ and $\hat{f}_k(\theta)$, respectively, using the tilde and the cap to distinguish between the different independent

variables to be used. The functions $\tilde{f}_k(r)$ are given as:

$$\tilde{f}_k(r) = \sin \sqrt{p_k} r - \sin \sqrt{p_k} r_a - \frac{\sin \sqrt{p_k} r_b - \sin \sqrt{p_k} r_a}{\cos \sqrt{p_k} r_b - \cos \sqrt{p_k} r_a} (\cos \sqrt{p_k} r - \cos \sqrt{p_k} r_a),$$

where p_k are the solutions of the equation

$$\sqrt{p}(r_b - r_a) \sin(\sqrt{p}r_b - \sqrt{p}r_a) + 2 \cos(\sqrt{p}r_b - \sqrt{p}r_a) - 2 = 0.$$

The functions $\hat{f}_k(\theta)$ are given as:

$$\hat{f}_k(\theta) = \sin \sqrt{p_k} \theta$$

when

$$p_k = \frac{4n^2\pi^2}{\theta_0^2}, n = 1, 2, 3, \dots,$$

and

$$\hat{f}_k(\theta) = \sin \sqrt{p_k} \theta - \frac{\sin \sqrt{p_k} \theta_0}{\cos \sqrt{p_k} \theta_0 - 1} (\cos \sqrt{p_k} \theta - 1)$$

when

$$\sqrt{p_k} \theta_0 \sin \sqrt{p_k} \theta_0 + 2 \cos \sqrt{p_k} \theta_0 - 2 = 0 \quad \text{and} \quad p_k \neq \frac{4n^2\pi^2}{\theta_0^2}.$$

The rest of the treatment follows closely along the lines of the previous section, and we omit those details. We plot the first 100 eigenvalues computed using this approach, for $r_a = 0.1, r_b = 0.3, \theta_0 = \frac{\pi}{4}$, in Figure 3.19. We also plot the corresponding values obtained from the FEM. We see that the match is near-perfect. We recall that the first six eigenfunctions for this annular wedge obtained using the FEM were shown in Figure 3.5.

3.3 Summary of the chapter

In this chapter, we computed the eigenfunctions ϕ_i on several 2D domains. In the first part of the chapter, we used the FEM to compute ϕ_i on planar geometries of arbitrary shapes. We described our FEM formulation in detail, and justified our choice of the finite elements used for discretization from the viewpoints of well-posedness, stability and convergence. In the second part of the chapter, we considered some special geometries for which alternative semi-numerical approaches are possible. We considered four such special geometries: an annulus, a circular disk, a rectangle and an annular wedge. We noted that the solutions

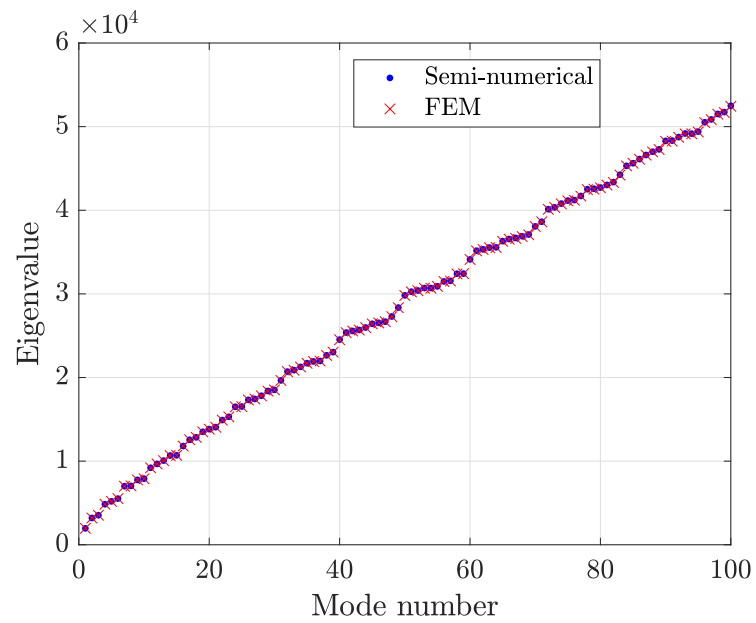


FIGURE 3.19: First 100 eigenvalues for the annular wedge with $r_a = 0.1$, $r_b = 0.3$, $\theta_0 = \frac{\pi}{4}$, obtained using the semi-numerical approach and the FEM.

from the semi-numerical approaches matched well with those from the FEM in all cases, providing empirical support for both.

In the next chapter, we will fit some candidate residual stress fields with eigenfunctions computed using both the FEM and the semi-numerical methods described in this chapter.

Chapter 4

Examples of fitting residual stress fields

In this chapter, we will consider a few candidate residual stress fields and fit them with the basis functions computed in the previous chapter. We will consider a variety of residual stress fields: of differing spatial complexity (1D and 2D), source (thermoelastic, plastic, hypothetical), and regularity (smooth, discontinuous). We will show convergence in both L^2 and H^1 (where possible) norms. Our intention in this chapter is to demonstrate that *all* residual stresses of interest, irrespective of their origin, can be expressed as linear combinations of the eigenfunctions ϕ_i , as claimed in Chapter 1.

This chapter is arranged as follows.

In Section 4.1, we consider residual stress fields on an annular domain, and fit them using the eigenfunctions computed semi-numerically in Section 3.2.1. We consider four residual stress fields with fixed azimuthal wave numbers: two hypothetical and arbitrary, one from shrink fitting of two concentric elastic cylinders, and one from non-uniform heating of an elastic annulus.

In Section 4.2, we describe in detail two 2D metal forming simulations carried out using the non-linear FE software package Abaqus: (a) rolling of an elasto-plastic workpiece, and (b) angular extrusion of an elasto-plastic workpiece through a bent die. For the rolling simulation, we consider two different strain hardening models: linear and Johnson-Cook. We then fit the resulting residual stress fields with eigenfunctions computed using our FEM formulation on the deformed geometry.

4.1 Residual stress fields in an annulus

We consider an annular domain centered at the origin with inner radius $r_a = 0.1$ and outer radius $r_b = 0.3$. As we noted in Section 3.2.1, the eigenvalue problem retains one independent variable (r) on an annular domain, along with a chosen circumferential wave number m . Many eigenfunctions can then be computed with great accuracy using a large number of r -points. Therefore, we consider residual stresses $\boldsymbol{\sigma}$ of the form

$$\boldsymbol{\sigma} = \sigma_{rr} \cos m\theta \mathbf{e}_r \otimes \mathbf{e}_r + \sigma_{r\theta} \sin m\theta (\mathbf{e}_r \otimes \mathbf{e}_\theta + \mathbf{e}_\theta \otimes \mathbf{e}_r) + \sigma_{\theta\theta} \cos m\theta \mathbf{e}_\theta \otimes \mathbf{e}_\theta, \quad (4.1)$$

where the r -dependence of the stress components has been suppressed (note the similarity with Eq. 3.12). We begin with

$$\boldsymbol{\sigma} = \sum_{i=1}^{\infty} a_i \boldsymbol{\phi}_i, \quad (4.2)$$

where the eigenfunctions $\boldsymbol{\phi}_i$ were obtained in the previous chapter using the semi-numerical approach. Using the orthogonality of $\boldsymbol{\phi}_i$, we have

$$a_i = \frac{\int_{\Omega} \boldsymbol{\sigma} \cdot \boldsymbol{\phi}_i dA}{\int_{\Omega} \boldsymbol{\phi}_i \cdot \boldsymbol{\phi}_i dA},$$

where the denominator would be unity if we had normalized our eigenfunctions. Truncating the series in Eq. 4.2, we write

$$\boldsymbol{\sigma}_N = \sum_{i=1}^N a_i \boldsymbol{\phi}_i, \quad (4.3)$$

and use the squared relative error measure

$$E_N = \frac{\int_{\Omega} (\boldsymbol{\sigma} - \boldsymbol{\sigma}_N) \cdot (\boldsymbol{\sigma} - \boldsymbol{\sigma}_N) dA}{\int_{\Omega} \boldsymbol{\sigma} \cdot \boldsymbol{\sigma} dA}$$

to study convergence in the L^2 norm (Eq. 2.2). To study convergence in the H^1 norm, wherever relevant, we will use the error measure

$$\tilde{E}_N = \frac{\int_{\Omega} (\boldsymbol{\sigma} - \boldsymbol{\sigma}_N) \cdot (\boldsymbol{\sigma} - \boldsymbol{\sigma}_N) dA + \int_{\Omega} \nabla (\boldsymbol{\sigma} - \boldsymbol{\sigma}_N) \cdot \nabla (\boldsymbol{\sigma} - \boldsymbol{\sigma}_N) dA}{\int_{\Omega} \boldsymbol{\sigma} \cdot \boldsymbol{\sigma} dA + \int_{\Omega} \nabla \boldsymbol{\sigma} \cdot \nabla \boldsymbol{\sigma} dA}. \quad (4.4)$$

We now present four examples of candidate residual stress fields, and the corresponding fits. In the first two examples we construct hypothetical residual stress fields directly, with wave number $m = 3$, from the equilibrium equations. In the third example we use the

stress field in two concentric elastic cylinders in a shrink fit, with $m = 0$. In the fourth example we consider the thermoelastic stress state in an initially unstressed elastic annular body subjected to a subsequent non-uniform rise in temperature, with $m = 3$.

4.1.1 Example 1: hypothetical stress field, $m = 3$

Let $\boldsymbol{\sigma}$ be as given in Eq. 4.1, with $m = 3$. From equilibrium,

$$\begin{aligned}\sigma'_{rr} + \frac{m\sigma_{r\theta}}{r} + \frac{\sigma_{rr} - \sigma_{\theta\theta}}{r} &= 0, \\ \sigma'_{r\theta} - \frac{m\sigma_{\theta\theta}}{r} + \frac{2\sigma_{r\theta}}{r} &= 0,\end{aligned}\tag{4.5}$$

with four boundary conditions:

$$\sigma_{rr} = \sigma_{r\theta} = 0, \text{ at } r = r_a \text{ and } r = r_b.$$

To construct hypothetical residual stress fields, we can assume an arbitrary functional form

$$\sigma_{\theta\theta} = A(r)$$

with *two* free parameters in it. We can then solve for $\sigma_{r\theta}$ from the second of Eqs. 4.5, retaining an integration constant. We finally solve for σ_{rr} from the first of Eqs. 4.5, retaining one more integration constant. The four boundary conditions can be satisfied using the two integration constants along with the two free parameters in $A(r)$. We show two specific examples of stress fields computed using this approach.

For the first example, we choose

$$A(r) = C_0 + C_1 r + 100r^2,$$

where C_0 and C_1 are free parameters, and the numerical coefficient 100 is arbitrary. Following the procedure above, we obtain $C_0 = 3.667$ and $C_1 = -40$. The resulting expressions for components of $\boldsymbol{\sigma}$ are

$$\begin{aligned}\sigma_{rr} &= -\frac{0.067}{r^2} + \frac{1.6}{r} - 12.833 + 40r - 41.667r^2, \\ \sigma_{r\theta} &= -\frac{0.022}{r^2} + 5.5 - 40r + 75r^2, \\ \sigma_{\theta\theta} &= 3.667 - 40r + 100r^2.\end{aligned}$$

Figure 4.1 shows the components of σ , along with components of the fitted σ_N ($N = 100$). The error measure E_N versus N is plotted in Figure 4.2. Convergence is rapid, like N^{-3} for large N , with $E_5 < 0.005$. The error measure \tilde{E}_N (Eq. 4.4) decays like $1/N$ for large N , as seen in Figure 4.3.

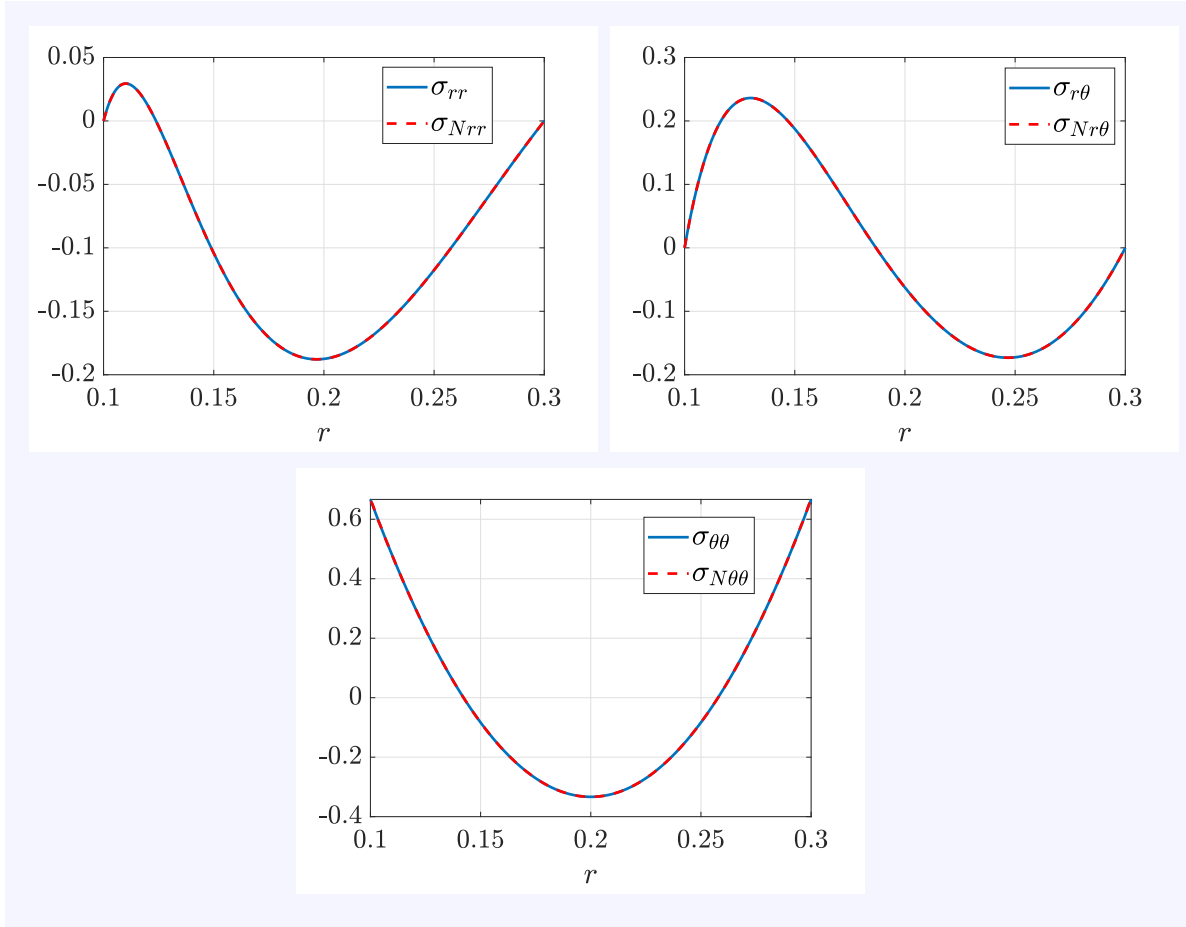


FIGURE 4.1: Radial variation of true and fitted stress fields σ and σ_N of Example 1, with $N = 100$.

We mention that the $m = 3$ normal vibration modes for the same domain (isotropic linear elasticity, plane strain) were computed separately and the stresses induced by those modes were also used in an attempted approximation of this same hypothetical stress field. The unsuccessful results of that attempt were plotted in Figure 1.1 (recall Eqs. 1.1; further details omitted). The reasons for that lack of convergence are clear by now.

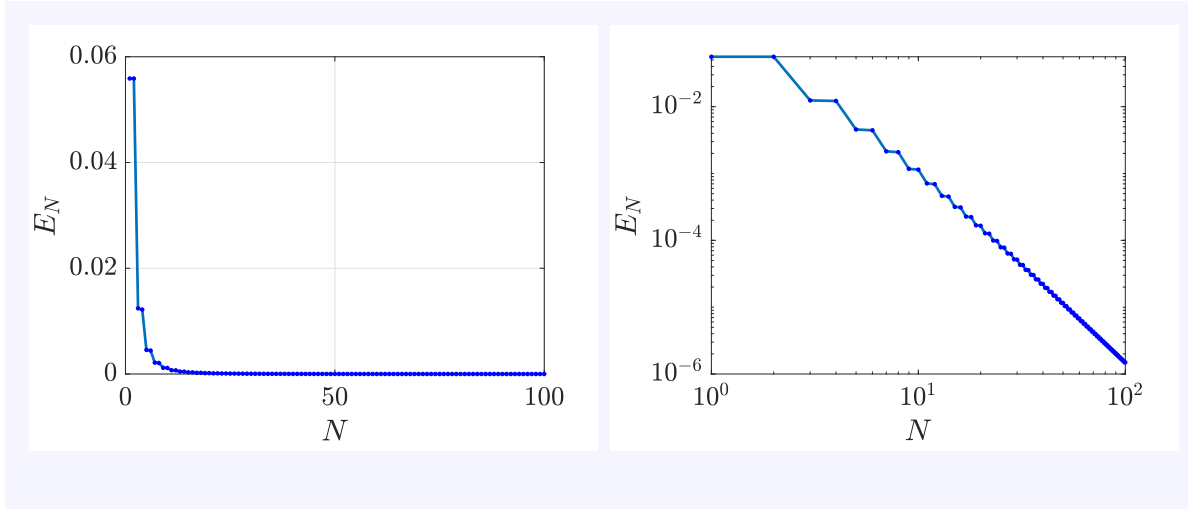


FIGURE 4.2: E_N versus N , Example 1. Left: linear scale; right: log-log scale. Compare with Figure 1.1.

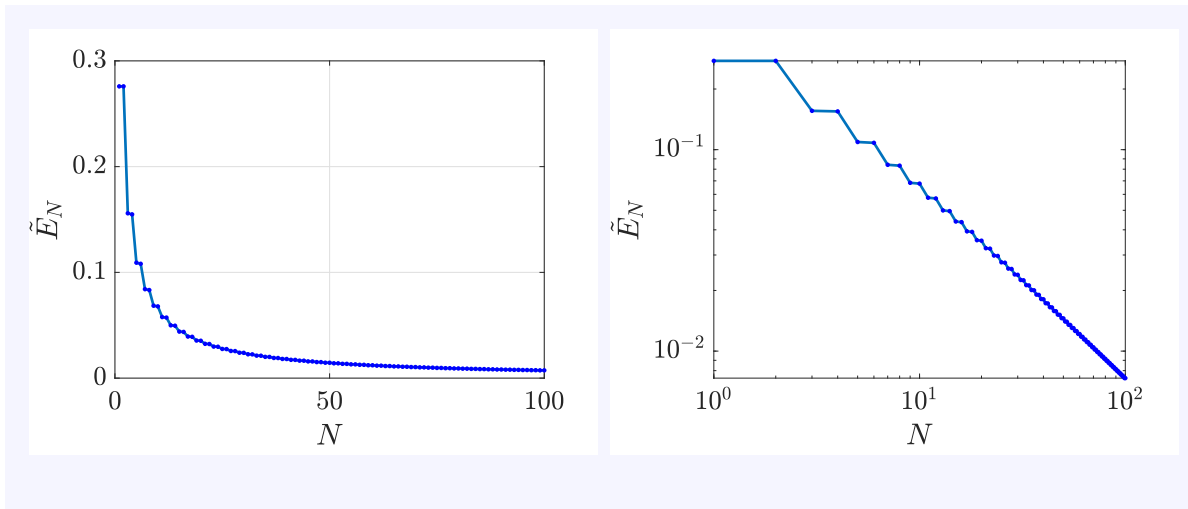


FIGURE 4.3: \tilde{E}_N versus N , Example 1. Left: linear scale; right: log-log scale.

4.1.2 Example 2: hypothetical stress field, $m = 3$

For another example following Section 4.1.1 above, we choose

$$A(r) = C_0 \sin(200r) + \frac{C_1}{r} + r.$$

The coefficient of 200 within the sine is chosen to produce several oscillations between $r_a = 0.1$ and $r_b = 0.3$. Calculations yield $C_0 = -3.805$ and $C_1 = -1.284 \times 10^{-2}$. The

resulting expressions for the components of σ are

$$\sigma_{rr} = \frac{-0.321}{r} - \frac{-4r^3 + 8.563 \times 10^{-4} \sin(200r) + 0.411 \ln(200r)r}{r^2} - \frac{9.408 \times 10^{-3} + 7.611 \times 10^{-2} r \cos(200r)}{r^2},$$

$$\sigma_{r\theta} = \frac{r^3 - 2.854 \times 10^{-4} \sin(200r) + 5.708 \times 10^{-2} r \cos(200r) - 3.853 \times 10^{-2} r + 7.840 \times 10^{-4}}{r^2},$$

$$\sigma_{\theta\theta} = -3.805 \sin(200r) - \frac{1.284 \times 10^{-2}}{r} + r.$$

The fit (for $N=100$) is shown in Figure 4.4. The error measures E_N and \tilde{E}_N are plotted in Figures 4.5 and 4.6, respectively.

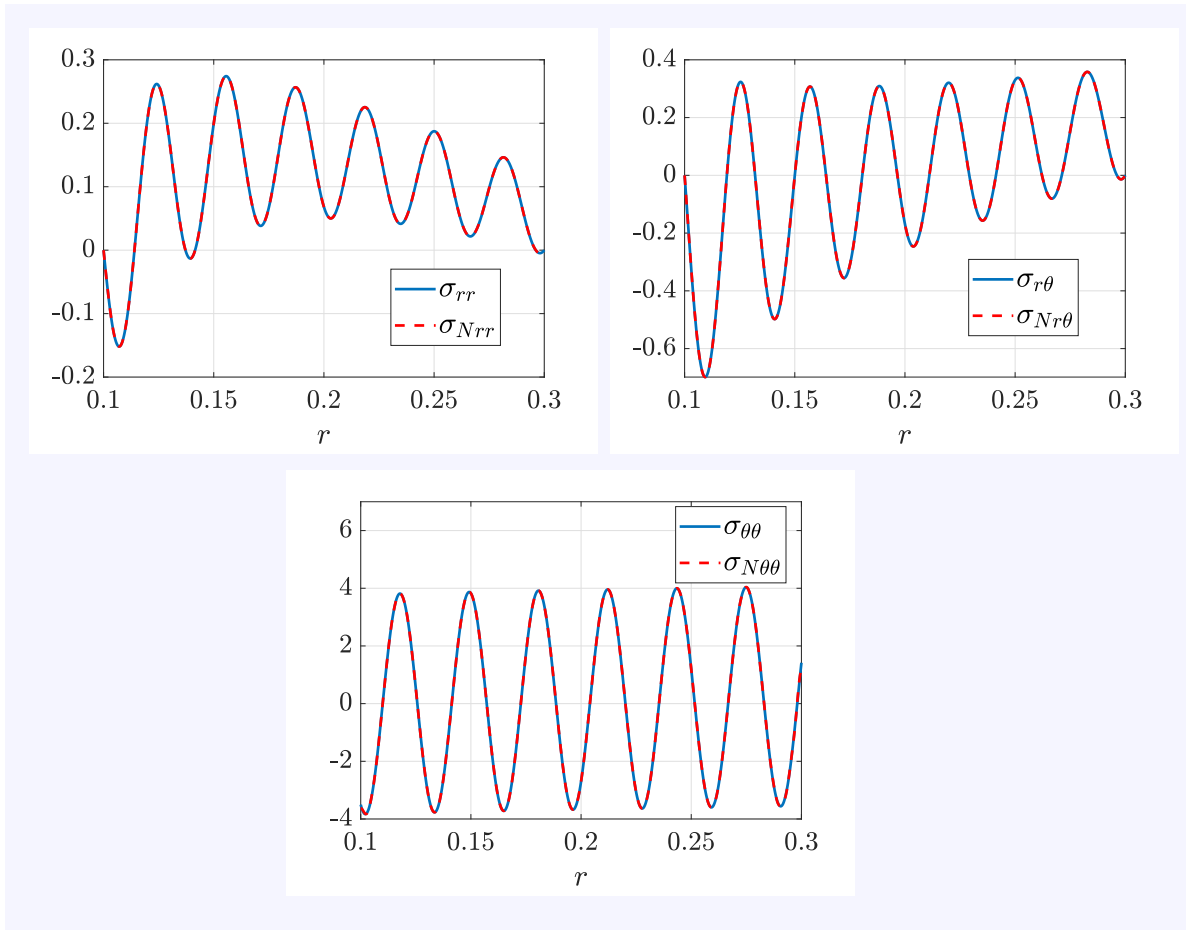
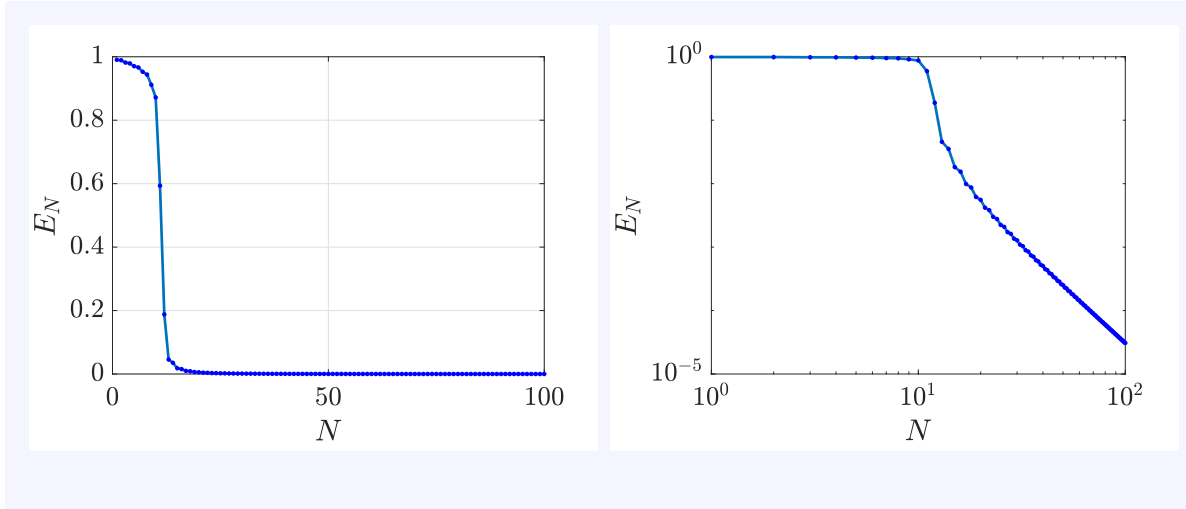
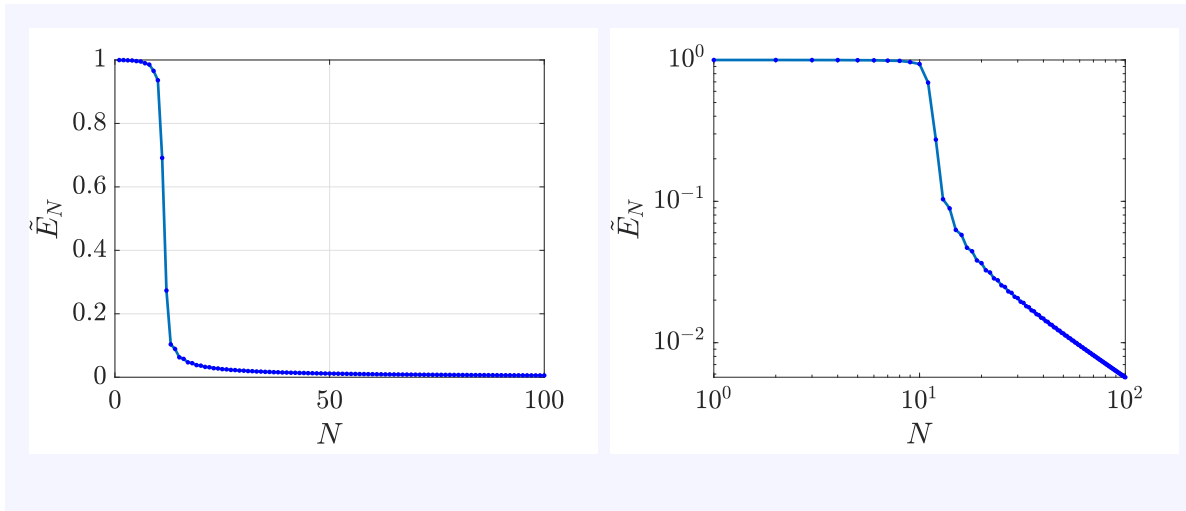


FIGURE 4.4: Radial variation of true and fitted stress fields σ and σ_N of Example 2, with $N = 100$.

In Figure 4.5 (left), we see that E_{13} drops low. This is because, by choice, $\sigma_{\theta\theta}$ has 13 zero crossings. By Figure 3.10, we expect the n^{th} eigenfunction to have $n + 1$ zero crossings in

FIGURE 4.5: E_N versus N , Example 2. Left: linear scale; right: log-log scale.FIGURE 4.6: \tilde{E}_N versus N , Example 2. Left: linear scale; right: log-log scale.

$\sigma_{\theta\theta}$. Therefore the 12th eigenfunction has 13 zero crossings, and E_{13} is small. Subsequent convergence is rapid, like N^{-3} for large N , with $E_{17} < 0.01$. Convergence of \tilde{E}_N is like $\frac{1}{N}$, as it was for the previous example.

4.1.3 Example 3: shrink fitted cylinder, $m = 0$

We consider an inner cylinder with inner radius r_a and notional outer radius r_c , an outer cylinder with notional inner radius r_c and outer radius r_b , with a small radial interference equal to δ . The Young's modulus and Poisson's ratio of both cylinders are denoted by Y

and ν respectively. The expressions for the resulting axisymmetric stress field components are [58]

$$\begin{aligned}\sigma_{rr}(r) &= -\frac{p_c}{\frac{r_c^2}{r_a^2} - 1} \left(\frac{r_c^2}{r_a^2} - \frac{r_c^2}{r^2} \right) \quad \text{for } r_a \leq r \leq r_c, \\ \sigma_{rr}(r) &= -\frac{p_c}{\frac{r_b^2}{r_c^2} - 1} \left(\frac{r_b^2}{r^2} - 1 \right) \quad \text{for } r_c \leq r \leq r_b, \\ \sigma_{\theta\theta}(r) &= -\frac{p_c}{\frac{r_c^2}{r_a^2} - 1} \left(\frac{r_c^2}{r_a^2} + \frac{r_c^2}{r^2} \right) \quad \text{for } r_a \leq r < r_c, \\ \sigma_{\theta\theta}(r) &= \frac{p_c}{\frac{r_b^2}{r_c^2} - 1} \left(\frac{r_b^2}{r^2} + 1 \right) \quad \text{for } r_c < r \leq r_b, \\ \sigma_{r\theta}(r) &= 0 \quad \text{for } r_a \leq r \leq r_b,\end{aligned}$$

where

$$p_c = \frac{Y\delta}{r_c} \left(\frac{r_c^2 + r_a^2}{r_c^2 - r_a^2} + \frac{r_b^2 + r_c^2}{r_b^2 - r_c^2} \right)^{-1}.$$

We have used $r_a = 0.1$, $r_c = 0.2$, $r_b = 0.3$, $\nu = 0.3$, and $Y\delta = 10^6$, in any consistent units.

We use eigenfunctions with $m = 0$ in Eq. 4.3. Figure 4.7 shows the nonzero components of $\boldsymbol{\sigma}$ and $\boldsymbol{\sigma}_N$ ($N=100$). Because $\sigma_{\theta\theta}$ is discontinuous at the contact surface between cylinders, convergence is slower (there are Gibbs oscillations [59]). The plot of E_N against N in Figure 4.8 shows convergence like N^{-1} for large N , with $E_{43} < 0.01$. Recalling the set \mathcal{S} (Eq. 2.1) and its closure $\bar{\mathcal{S}}$, we note that $\boldsymbol{\sigma}$ belongs to $\bar{\mathcal{S}}$ but not \mathcal{S} . Convergence is still obtained because the ϕ_i form a basis for $\bar{\mathcal{S}}$. However, \tilde{E}_N is not meaningful here because both numerator and denominator of Eq. 4.4 are infinite.

4.1.4 Example 4: thermoelastic residual stress, $m = 3$

If the initially unstressed annular region, with thermal coefficient α , is subjected to a temperature change $T(r, \theta) = r \cos 3\theta$ (chosen so as to produce a residual stress with wavenumber $m = 3$ in the azimuthal direction), the resulting thermal strain

$$\boldsymbol{\varepsilon}_T = \alpha T \mathbf{I}$$

violates local compatibility, i.e., $\text{curl curl } \boldsymbol{\varepsilon}_T \neq \mathbf{0}$ (see e.g., [60]). The ‘global compatibility’ equation derived from Césaro’s integral [7], for $m = 3$, is trivially satisfied.

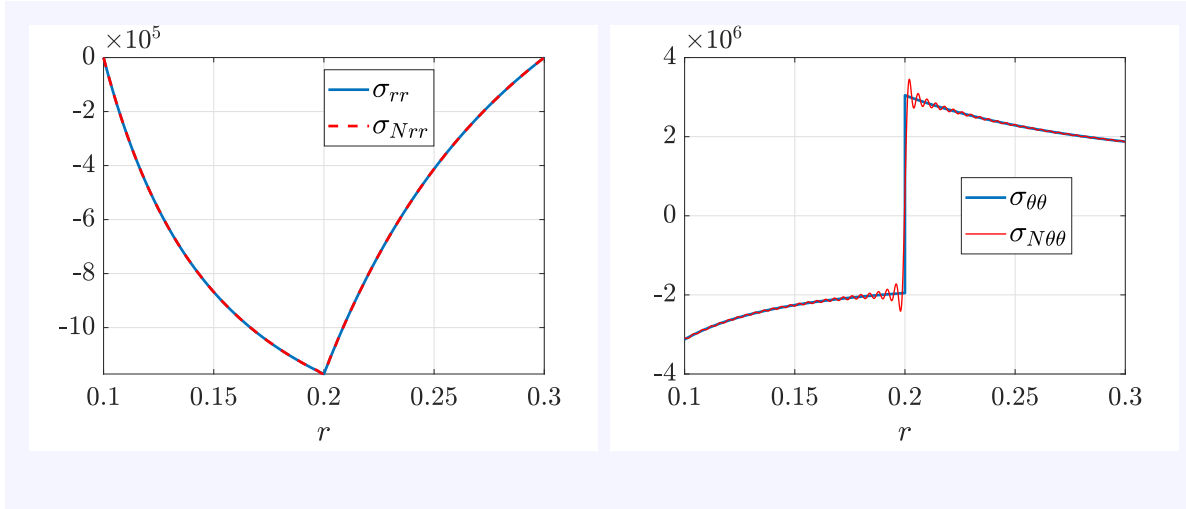


FIGURE 4.7: Radial variation of true and fitted stress fields σ and σ_N of Example 3, with $N = 100$. Note the Gibbs oscillations in $\sigma_{N\theta\theta}$.

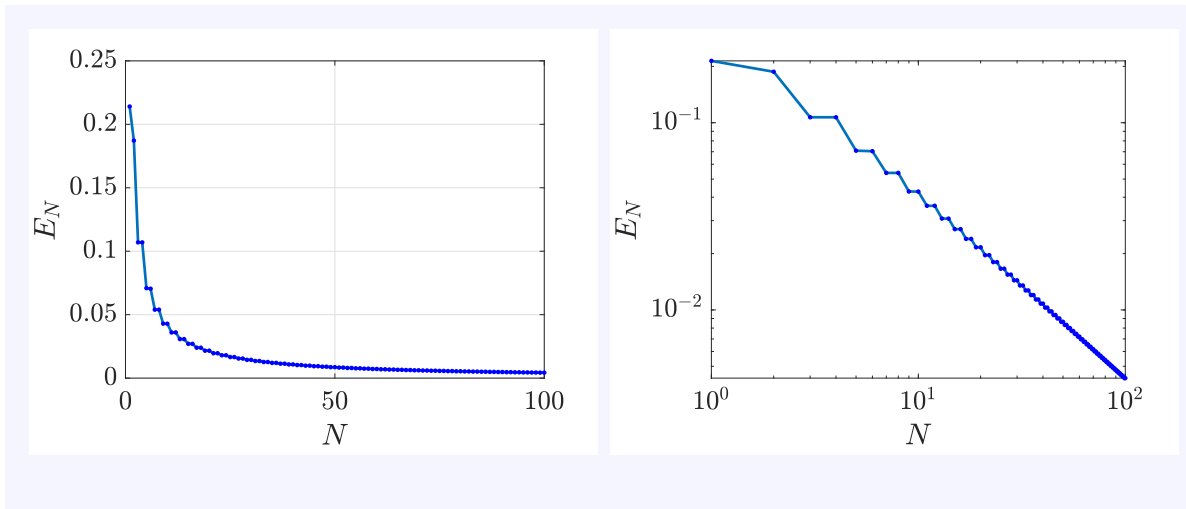


FIGURE 4.8: E_N versus N , Example 3. Left: linear scale; right: log-log scale.

The resulting stress σ satisfies (see e.g., [7])

$$\Delta(\text{tr } \sigma) = -\frac{\alpha Y}{1 - \nu} \Delta T, \quad (4.6)$$

where Y is Young's modulus, ν is Poisson's ratio, and 'tr' denotes 'trace' ($\text{tr } \sigma = \sigma_{rr} + \sigma_{\theta\theta}$). Substituting the expressions

$$\sigma = \sigma_{rr} \cos m\theta \mathbf{e}_r \otimes \mathbf{e}_r + \sigma_{r\theta} \sin m\theta (\mathbf{e}_r \otimes \mathbf{e}_\theta + \mathbf{e}_\theta \otimes \mathbf{e}_r) + \sigma_{\theta\theta} \cos m\theta \mathbf{e}_\theta \otimes \mathbf{e}_\theta,$$

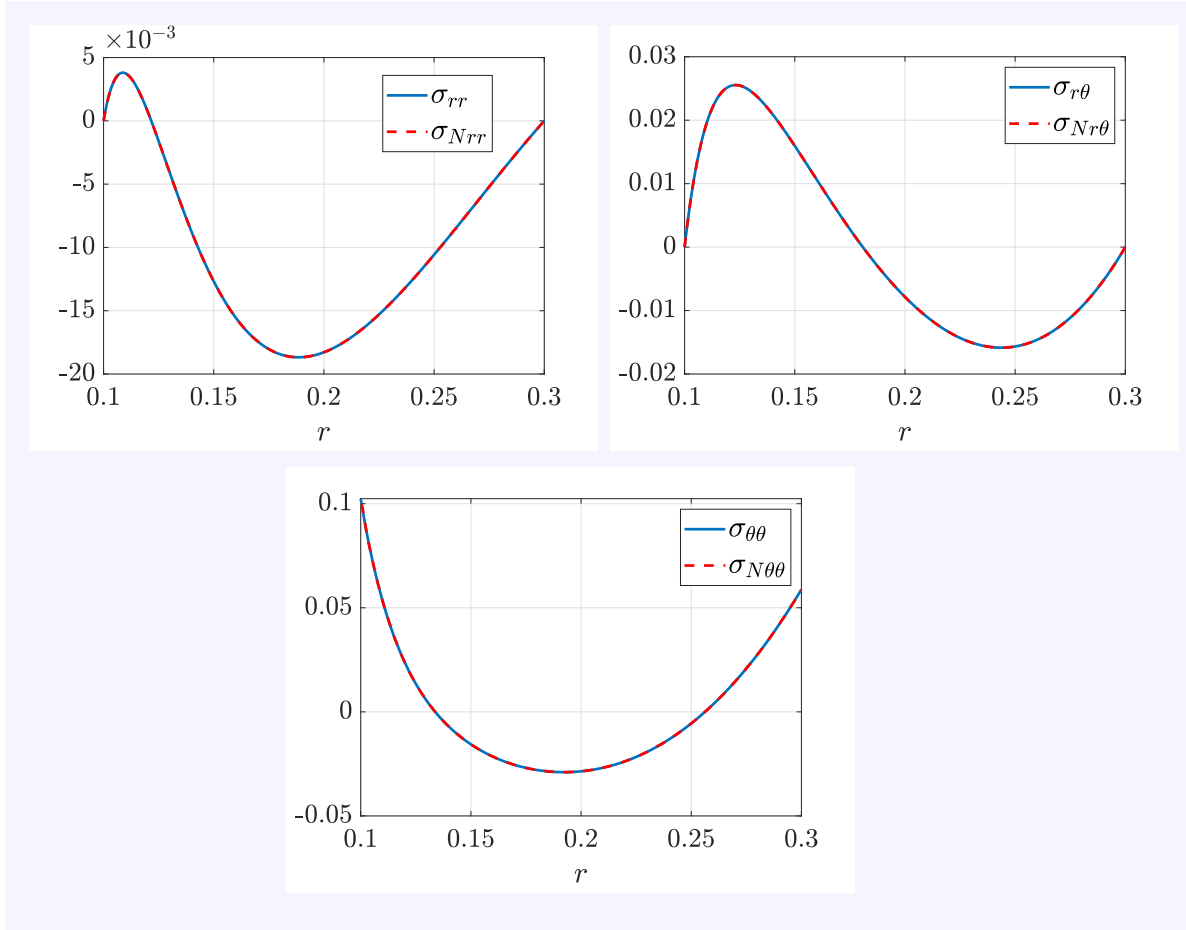


FIGURE 4.9: Radial variation of true and fitted thermoelastic stress fields $\boldsymbol{\sigma}$ (Eqs. 4.7 and 4.8) and $\boldsymbol{\sigma}_N$ of Example 4, with $N = 100$.

$$T(r, \theta) = r \cos 3\theta$$

in Eq. 4.6 gives

$$(\sigma_{rr} + \sigma_{\theta\theta})'' + \frac{(\sigma_{rr} + \sigma_{\theta\theta})'}{r} - \frac{m^2(\sigma_{rr} + \sigma_{\theta\theta})}{r^2} = -\frac{(m^2 - 1)\beta}{r}, \quad (4.7)$$

where $\beta = \frac{-\alpha Y}{(1 - \nu)}$, $m = 3$, and primes denote r -derivatives. Eliminating $\sigma_{r\theta}$ from the equilibrium equations (Eq. 4.5), we obtain another ODE:

$$\sigma_{rr}'' + \frac{4\sigma_{rr}'}{r} - \frac{\sigma_{\theta\theta}'}{r} + \frac{2\sigma_{rr}}{r^2} + \frac{(m^2 - 2)\sigma_{\theta\theta}}{r^2} = 0. \quad (4.8)$$

Traction free boundary conditions on the inner and outer radii, in terms of σ_{rr} and $\sigma_{\theta\theta}$, are

$$\begin{aligned} \sigma_{rr} &= 0 \text{ at } r = r_a \text{ and } r_b, \\ \sigma'_{rr} &= \frac{\sigma_{\theta\theta}}{r} \text{ at } r = r_a \text{ and } r_b. \end{aligned} \quad (4.9)$$

Note that the second equation in Eq. 4.9 is obtained upon substituting $\sigma_{rr} = \sigma_{r\theta} = 0$ in the first equilibrium equation (Eq. 4.5).

The two-point boundary value problem described by Eqs. 4.7, 4.8 and 4.9 can be solved numerically (iteratively; details omitted). The numerical values of the problem's parameters are chosen to be $Y = 1$, $\alpha = 0.5$ and $\nu = 0.33$, in any consistent units.

Figure 4.9 shows the components of σ and the fitted σ_N ($N=100$). Figure 4.10 shows E_N versus N . Convergence is rapid, like N^{-3} , as expected, with $E_7 < 0.01$. \tilde{E}_N is plotted in Figure 4.11, and shows convergence like N^{-1} .

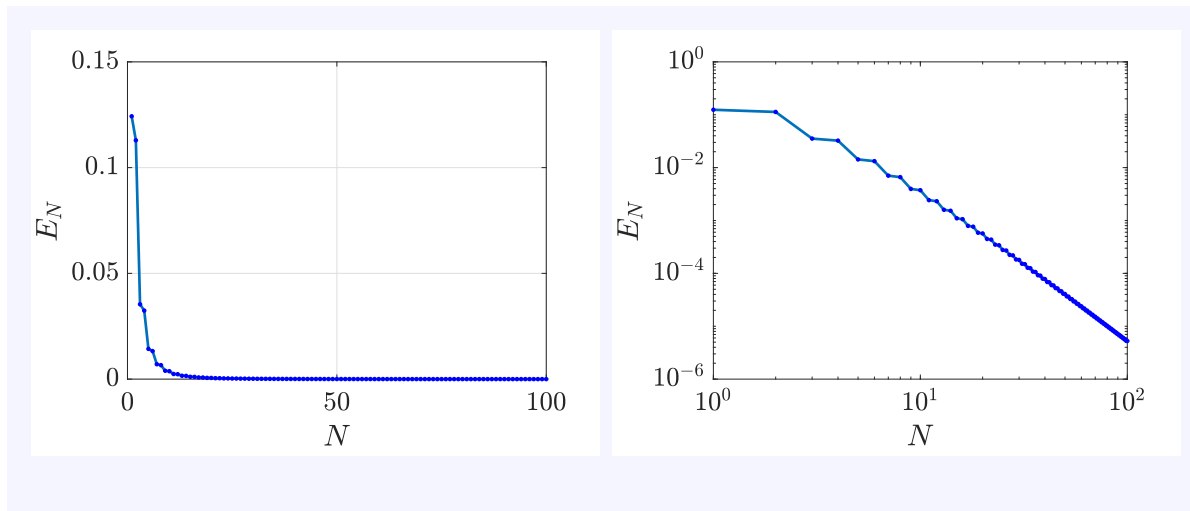


FIGURE 4.10: E_N versus N , Example 4. Left: linear scale; right: log-log scale.

This concludes our demonstration of fitting reasonable but arbitrary residual stresses on an annular domain using the basis functions developed earlier. In the next section, we fit residual stress fields obtained from metal forming simulations in Abaqus.

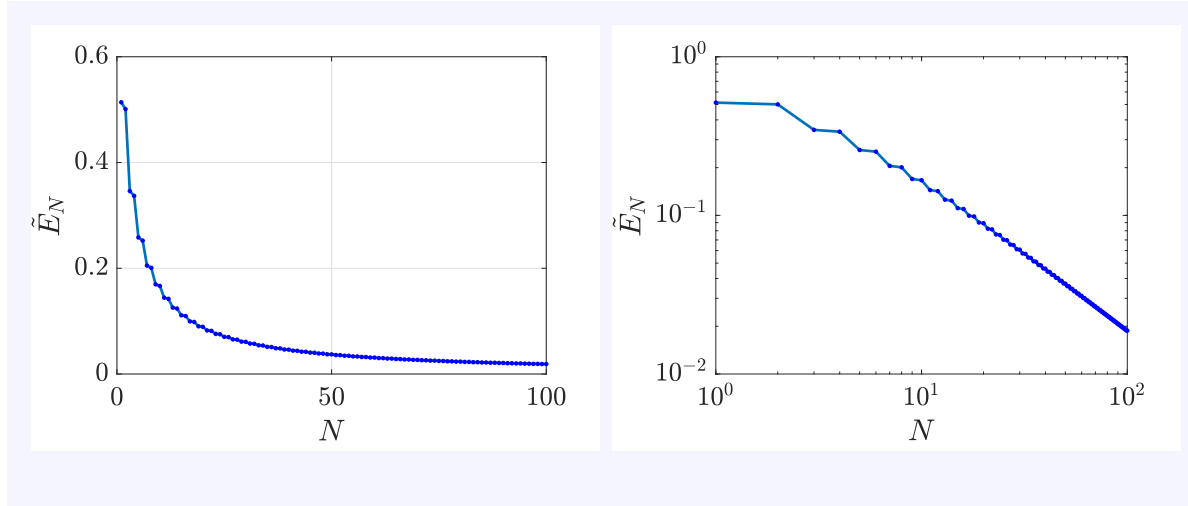


FIGURE 4.11: \tilde{E}_N versus N , Example 4. Left: linear scale; right: log-log scale.

4.2 Residual stresses from metal forming simulations

In this section, we simulate the 2D plane strain metal forming processes of rolling and angular extrusion using the FE software package Abaqus. We then fit the resulting residual stress fields using our eigenfunctions, computed on the same (final) mesh with our own finite element code described earlier in Section 3.1.

4.2.1 Rolling simulation

4.2.1.1 Details of the simulation

The schematic of the set-up is shown in Figure 4.12. The simulation is quasi-static, in the implicit analysis mode of Abaqus. A general description of the simulation is as follows: the workpiece is first nudged to the right using a rigid punch moving with a constant velocity, until the former comes in contact with the rotating rigid rollers. The friction between the workpiece and the rollers pulls the workpiece away from the rigid punch, and the formed workpiece is then released at the other side.

The geometric, material and contact details are as follows. The workpiece is 48 mm long and 32 mm wide, and is made of an isotropic elasto-plastic material with linear strain hardening. Its Young's modulus is 210 GPa, Poisson's ratio is 0.3, yield stress is 400 MPa, and slope of the hardening curve is such that the equivalent plastic strain is 10 when the von Mises stress is 6000 MPa. Since the process is quasi-static, the density of the

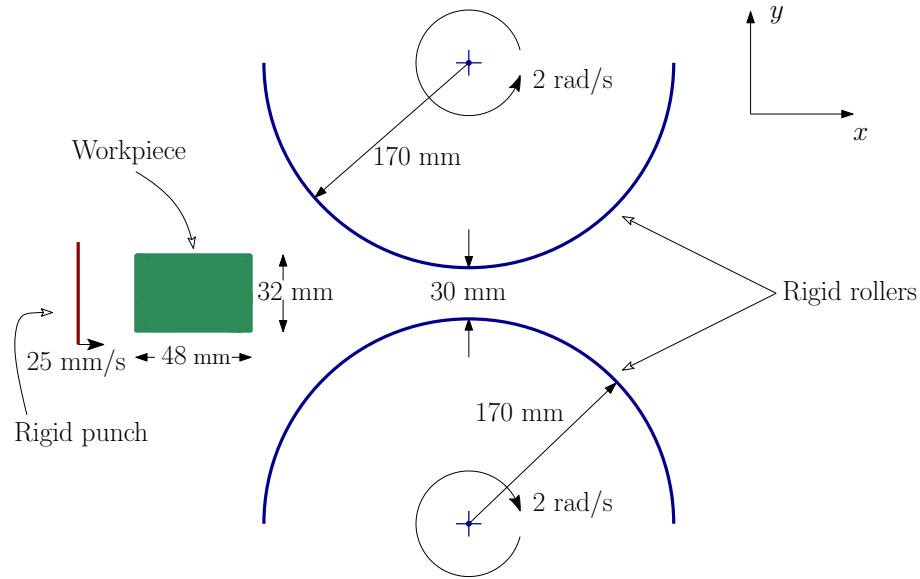


FIGURE 4.12: Schematic of the rolling simulation (figure not to scale).

workpiece is not required. The punch is rigid. It moves with a velocity of 25 mm/s to right. Both rollers are rigid and each has a radius of 170 mm. They rotate at 2 rad/s in the directions indicated in Figure 4.12. The minimum gap between the rollers is 30 mm, so that the width of the formed workpiece is reduced by 2 mm in the process. A ‘hard’ normal contact is assumed between the punch and the workpiece, as well as the workpiece and the rollers. ‘Penalty’ friction with a coefficient of 0.3 is assumed in each of these contacts.

The mesh details are as follows. The rollers and punch are meshed with ‘discrete rigid’ and ‘analytical rigid’ line elements, respectively. The workpiece is meshed with 20184 plane strain four-noded quadrilateral elements of size 0.275 mm and aspect ratio 1. Mesh convergence tests are performed by comparing the nodal values of different stress components along material lines for different element sizes, based on which we conclude that an element size of 0.275 mm provides a converged solution.

The simulation is quasi-static, and is carried out in an implicit step of duration 6 seconds, with minimum increment size of 10^{-9} seconds, and initial increment of size 10^{-3} seconds. The mid-line ($y = 0$) running across the length of the workpiece is constrained to not move in the y direction by using rollers. This ensures that the normal (respectively, shear) stress components remain symmetric (respectively, anti-symmetric) with respect to $y = 0$.

Readers can access the input file of this Abaqus simulation here:

<https://tinyurl.com/wefcwps>.

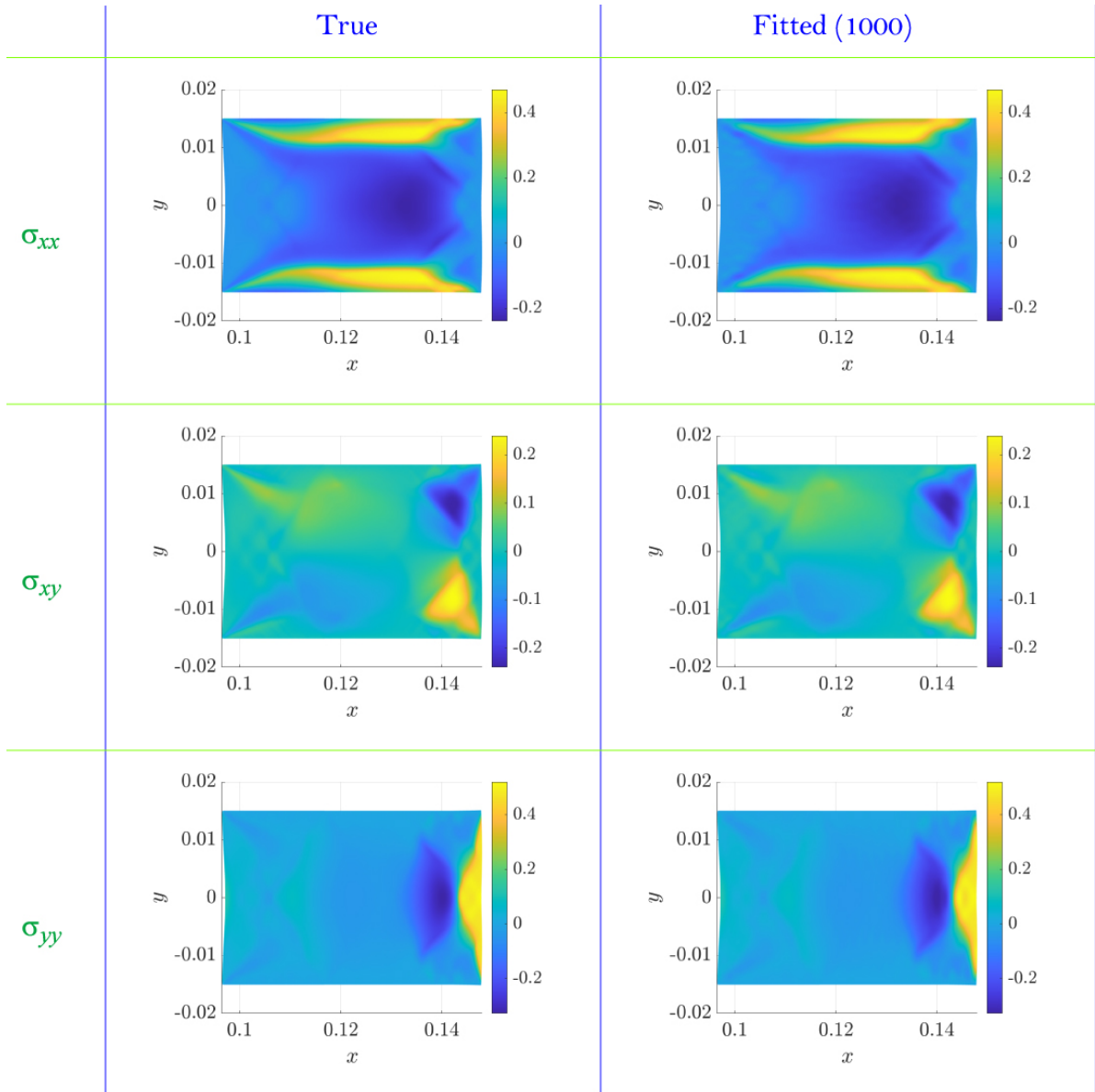


FIGURE 4.13: True and fitted stress components (GPa) for the rolling simulation with linear strain hardening (1000 eigenfunctions).

4.2.1.2 Results

We show the stress components obtained from the Abaqus simulation in the left column of Figure 4.13. This stress field is fitted using the first 1000 eigenfunctions computed over the same (deformed) mesh as obtained from the simulation, using the procedure described in Section 3.1. The fitted components are shown in the right column of Figure 4.13. We observe that the fit is very good. We also plot the fitted components using 10, 50 and 100 eigenfunctions respectively in Figure 4.14 to indicate how the fits get progressively

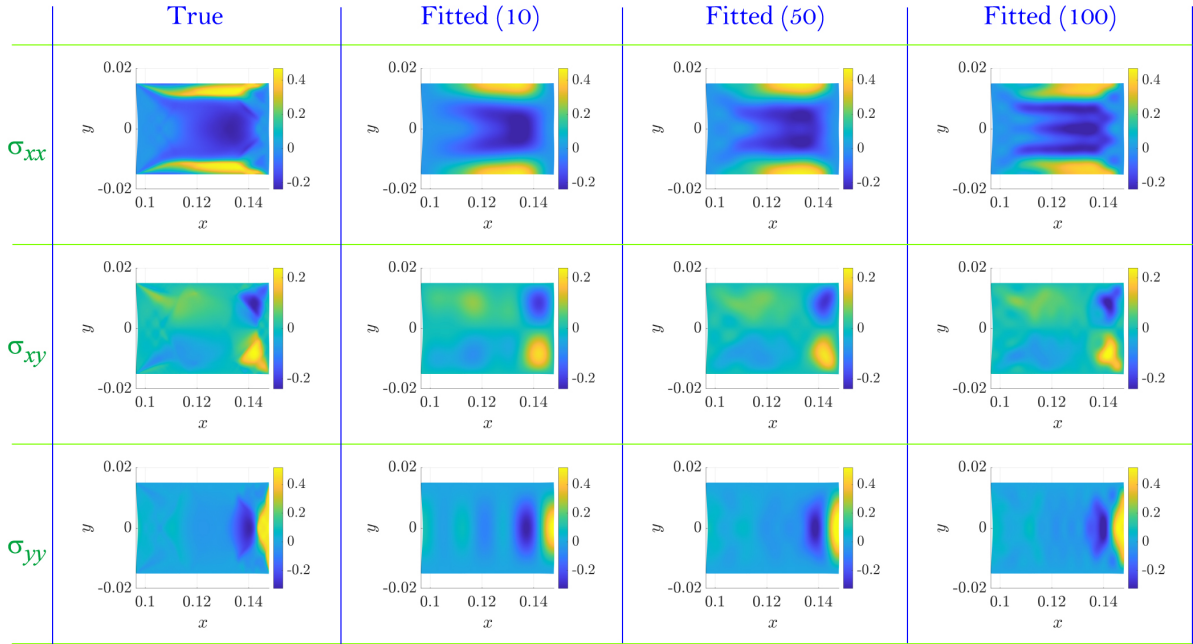


FIGURE 4.14: True and fitted stress components (GPa) for the rolling simulation with linear strain hardening (using 10, 50 and 100 eigenfunctions, respectively).

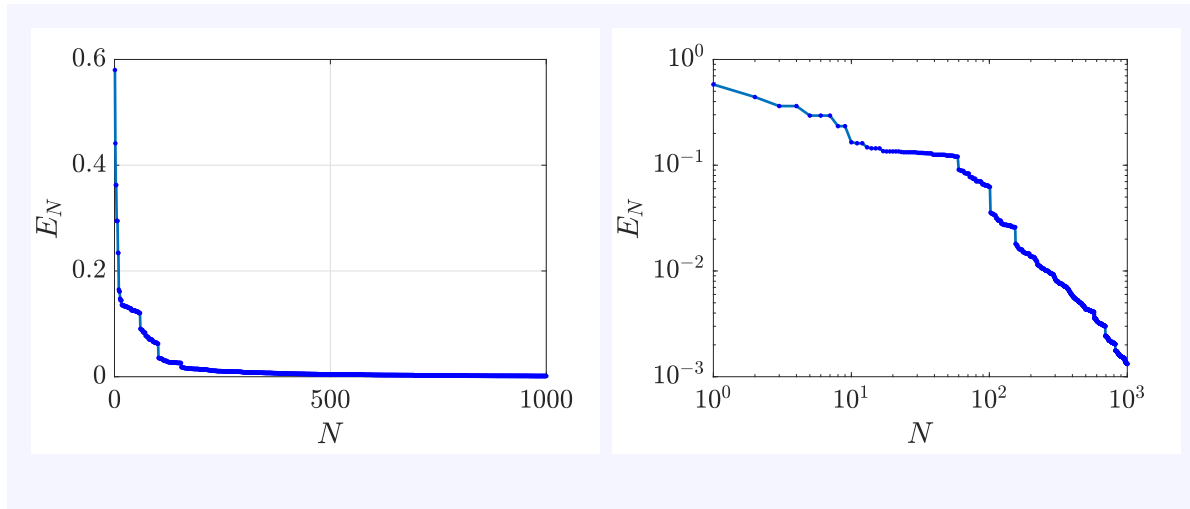


FIGURE 4.15: E_N versus N , rolling simulation with linear strain hardening. Left: linear scale; right: log-log scale.

better with incorporation of more eigenfunctions. Next, we plot the squared relative error measure E_N , described in Section 4.1, versus N in Figure 4.15. Convergence is like N^{-2} , and may improve for even larger N , with $E_{318} < 0.01$. We plot the error measure \tilde{E}_N in Figure 4.16 and note that the error decreases more slowly, like N^{-1} . Finally, we plot the time required in seconds for computation of the first 1000 eigenfunctions using our code in Matlab, on a personal computer with an 8th generation i5 processor, for different

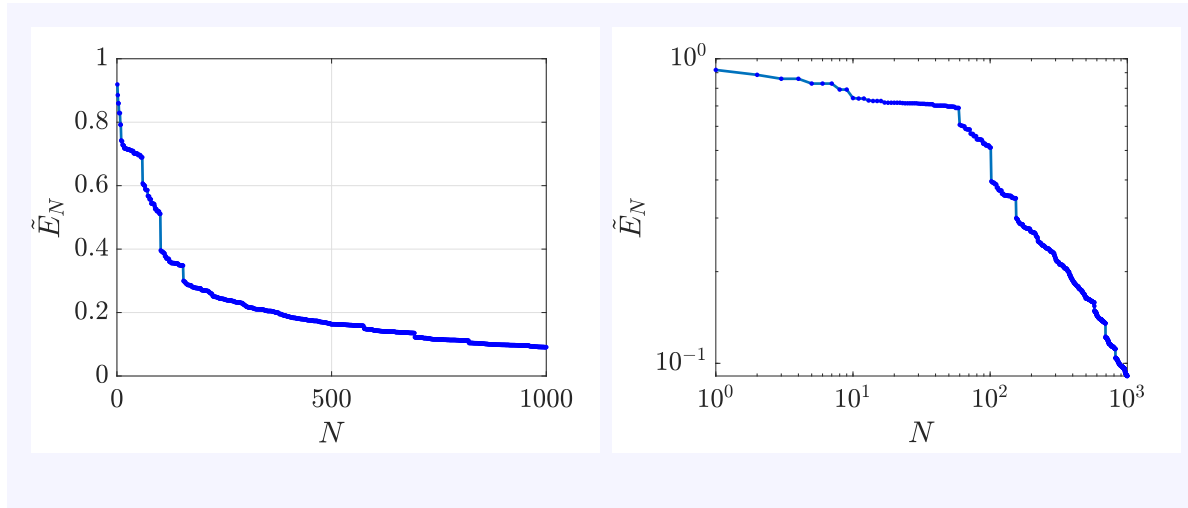


FIGURE 4.16: \tilde{E}_N versus N , rolling simulation with linear strain hardening. Left: linear scale; right: log-log scale.

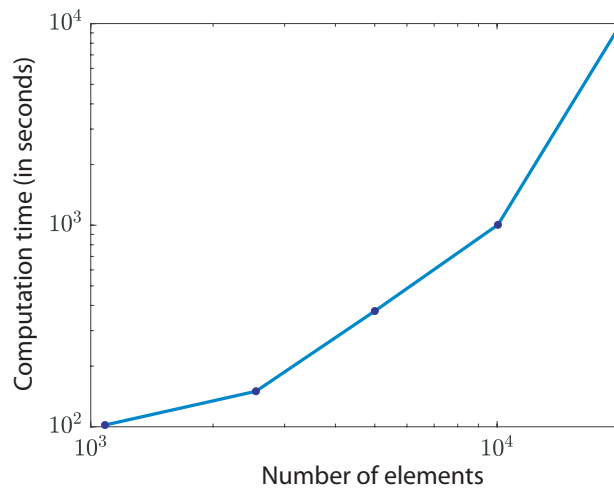


FIGURE 4.17: Time (in seconds) for computation of first one thousand eigenfunctions for different refinements of mesh used in rolling simulation (log-log scale). The data points are joined by straight lines for visibility alone.

refinements of the mesh used for the rolling simulation in Figure 4.17. The coarser meshes used for this figure were obtained from earlier simulations done to study mesh convergence: the stresses from those simulations are not reported here. We note that the computation time is not unreasonably large: it takes about 17 minutes to compute 1000 eigenfunctions on a fine mesh of 10000 elements, for example.

This example shows that an arbitrary residual stress field can indeed be fitted using our physics-independent basis functions.

4.2.1.3 Rolling simulation with Johnson-Cook hardening

To demonstrate that the constitutive behaviour of the material is irrelevant to our basis functions, we repeat the above rolling simulation with a material that exhibits Johnson-Cook hardening, keeping the elastic properties the same as before. The hardening parameters used in the Johnson-Cook model are as follows: $A = 50.103$ MPa, $B = 176.091$ MPa, $n = 0.5176$, $m = 0.5655$, $T_{melting} = 1623^\circ\text{C}$ and $T_{transition} = 1223^\circ\text{C}$. These parameters correspond to AISI-1045 steel [61]. The fit with 1000 eigenfunctions is shown in Figure 4.18. The error measures E_N and \tilde{E}_N are shown in Figures 4.19 and 4.20, respectively. The fits are good and the convergence at least for E_N is clear. Our key conclusion is that the eigenfunctions do capture residual stress fields regardless of the material used, as expected from the theory of Chapter 2.

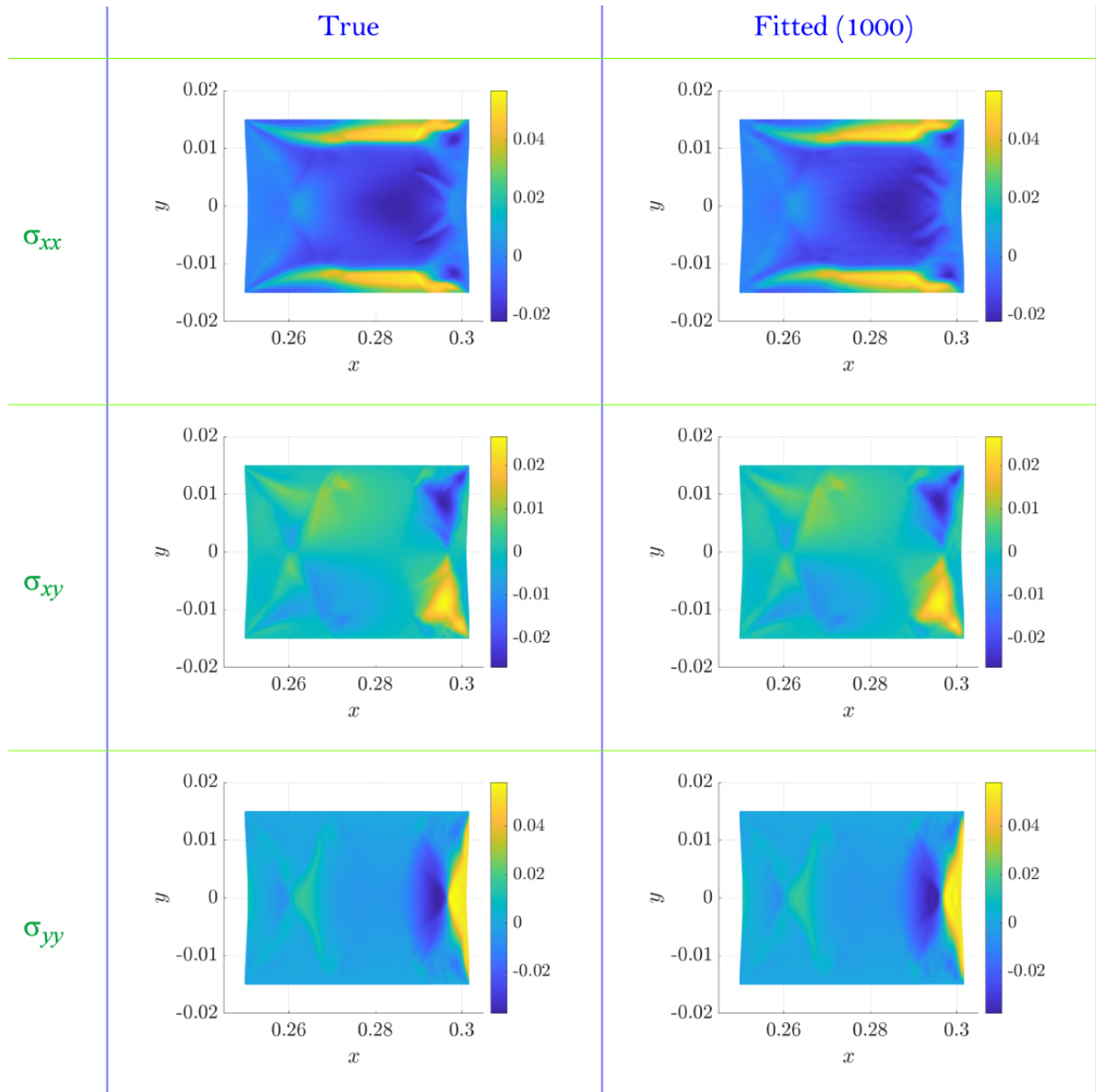


FIGURE 4.18: True and fitted stress components (GPa) for the rolling simulation with Johnson-Cook hardening (1000 eigenfunctions).

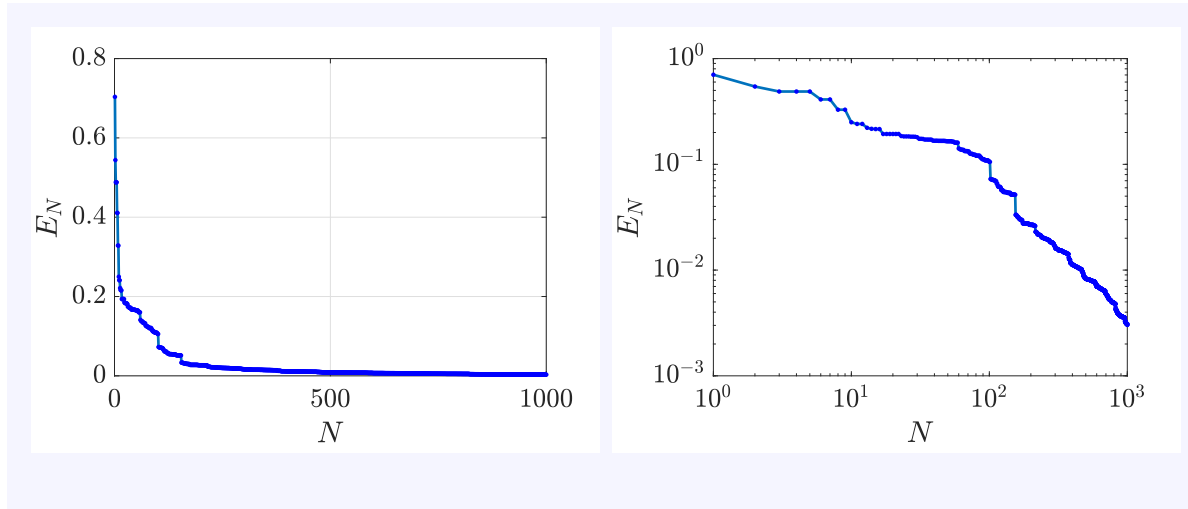


FIGURE 4.19: E_N versus N , rolling simulation with Johnson-Cook hardening. Left: linear scale; right: log-log scale.

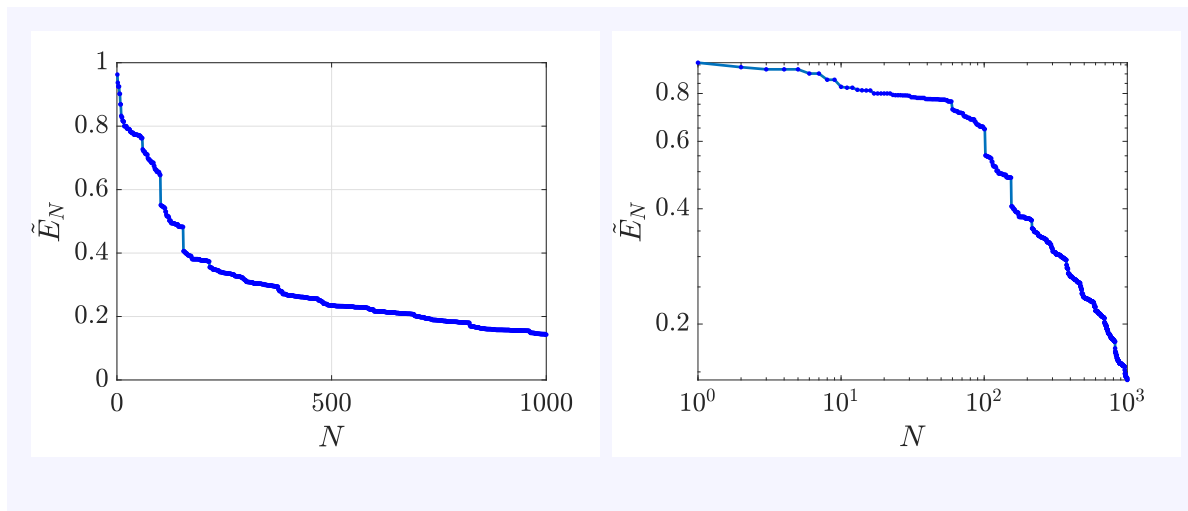


FIGURE 4.20: \tilde{E}_N versus N , rolling simulation with Johnson-Cook hardening. Left: linear scale; right: log-log scale.

4.2.2 Angular extrusion simulation

4.2.2.1 Details of the simulation

We show the schematic of an angular extrusion simulation in Figure 4.21. This simulation is also quasi-static and is carried out in the implicit analysis mode of Abaqus. The simulation is divided into three steps. In the first step, the rigid punch is pushed down by giving a downward velocity to the point R, until the latter coincides with the point P on the die (the die is kept fixed for the entire duration of the simulation). In the second step, the point R is given a pre-computed velocity profile so that it moves along the circular arc PQ. At the end of this step, R is at Q. In the third step, the punch is kept fixed, and the workpiece is pulled out of the die by giving the edge CD of the workpiece a constant rightwards velocity. At the end of the third step, the workpiece is completely out of the die, and is moving with a constant velocity, and the stress in the workpiece is a residual stress.

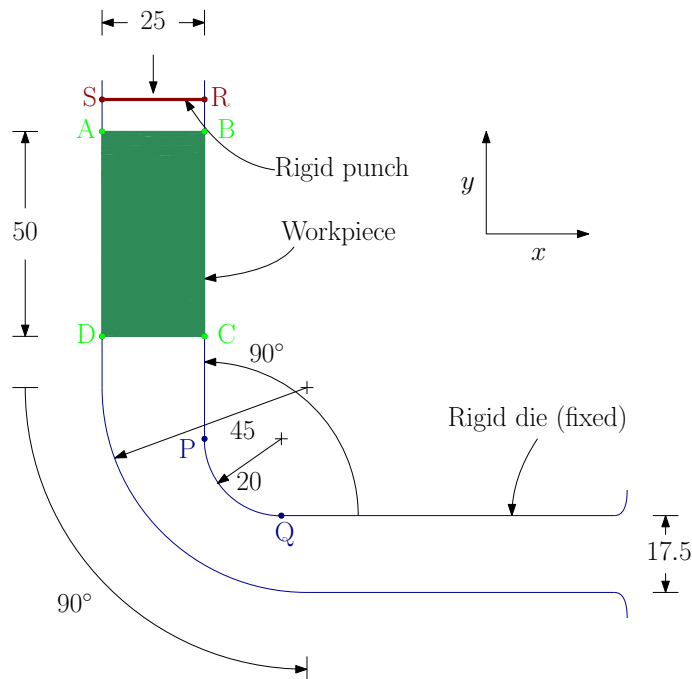


FIGURE 4.21: Schematic of the angular extrusion process at the beginning of the simulation (figure not to scale). All dimensions are in millimetres.

We point out that the motion of the punch is effected by assigning the point R located on it a pre-computed velocity profile. This profile is chosen so as to make sure that R always moves along the edge of the die. There is no such restriction on the point S on the punch. Consequently, as the die narrows, S is free to ‘move out’ of the die to maintain rigidity of

the punch. This is depicted schematically in Figure 4.22. The only interactions that we allow in the simulation are those between the punch and the workpiece, and between the workpiece and the die. Interpenetration of the punch and the die is allowed without any restriction.

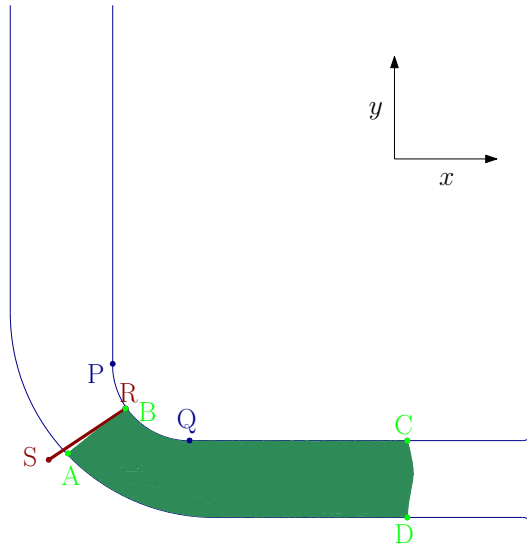


FIGURE 4.22: A schematic of the angular extrusion process *during* the simulation.

The geometric, material and contact details are as follows. The workpiece is 50 mm long and 25 mm wide, and is made of an isotropic elasto-plastic material with linear strain hardening. Its Young's modulus is 210 GPa, Poisson's ratio is 0.3, yield stress is 400 MPa, and the slope of the hardening curve is such that the equivalent plastic strain is 10 when the von Mises stress is 6000 MPa. The mass density of the workpiece is not important because the simulation is quasi-static. The punch is rigid. It moves downwards with a velocity of 5 mm/s in the first step, pushing the workpiece along. In the second step, it rotates in such a way that the material point R always coincides with the right edge of the die; in the third step, it is stationary. The workpiece is pulled out of the die by imparting a constant rightwards velocity of 5 mm/s to the edge CD in the third step. The die is kept fixed in all the three steps. The width of the exit channel of the die is 0.7 times that of its input channel, so that the nominal width of the workpiece is reduced to 70% of its initial value. A 'hard' normal frictionless contact is assumed in all the contacts.

The mesh details are as follows. The punch and the die are meshed with 'analytic rigid' elements. The workpiece is meshed with 10153 plane strain four-noded quadrilateral elements of size 0.35 mm and aspect ratio 1.

The simulation is quasi-static and is carried out in three steps of sizes 20, 35 and 30 seconds, respectively. The minimum increment size is taken to be 10^{-9} seconds, with initial increment of 10^{-3} seconds, for each step.

Readers can access the input file of this Abaqus simulation here:

<https://tinyurl.com/46t5kdpc>.

4.2.2.2 Results

We show the stress components obtained from the Abaqus simulation in the left column of Figure 4.23. This stress field is fitted using the first 1000 eigenfunctions computed over the same (deformed) mesh as obtained from the simulation. The fitted components are shown in the right column of Figure 4.23. We observe that the fit quality is not as good as that for the rolling simulation. This is because the workpiece undergoes severe deformation in the angular extrusion process, especially at the corners, where the mesh distortion is excessive (see Figure 4.25). As a result, the resulting stress is equilibrated only in a weak sense. These matters are discussed in detail in [62].

We also plot the fitted components using 10, 50 and 100 eigenfunctions respectively in Figure 4.24 to indicate how the fits get progressively better with incorporation of more eigenfunctions. Finally, we plot the error measures E_N and \tilde{E}_N in Figures 4.26 and 4.27, respectively. We see from Figure 4.26 that E_N seems to be saturating at about 0.05 even as more eigenfunctions are included, reflecting the separately known fact that the stress field obtained from the Abaqus simulation is only approximately valid, i.e., only approximately divergence free and traction free. \tilde{E}_N does not decrease to acceptably low values for any practical purposes.

This concludes our demonstration of fitting candidate residual stress fields obtained from metal forming simulations.

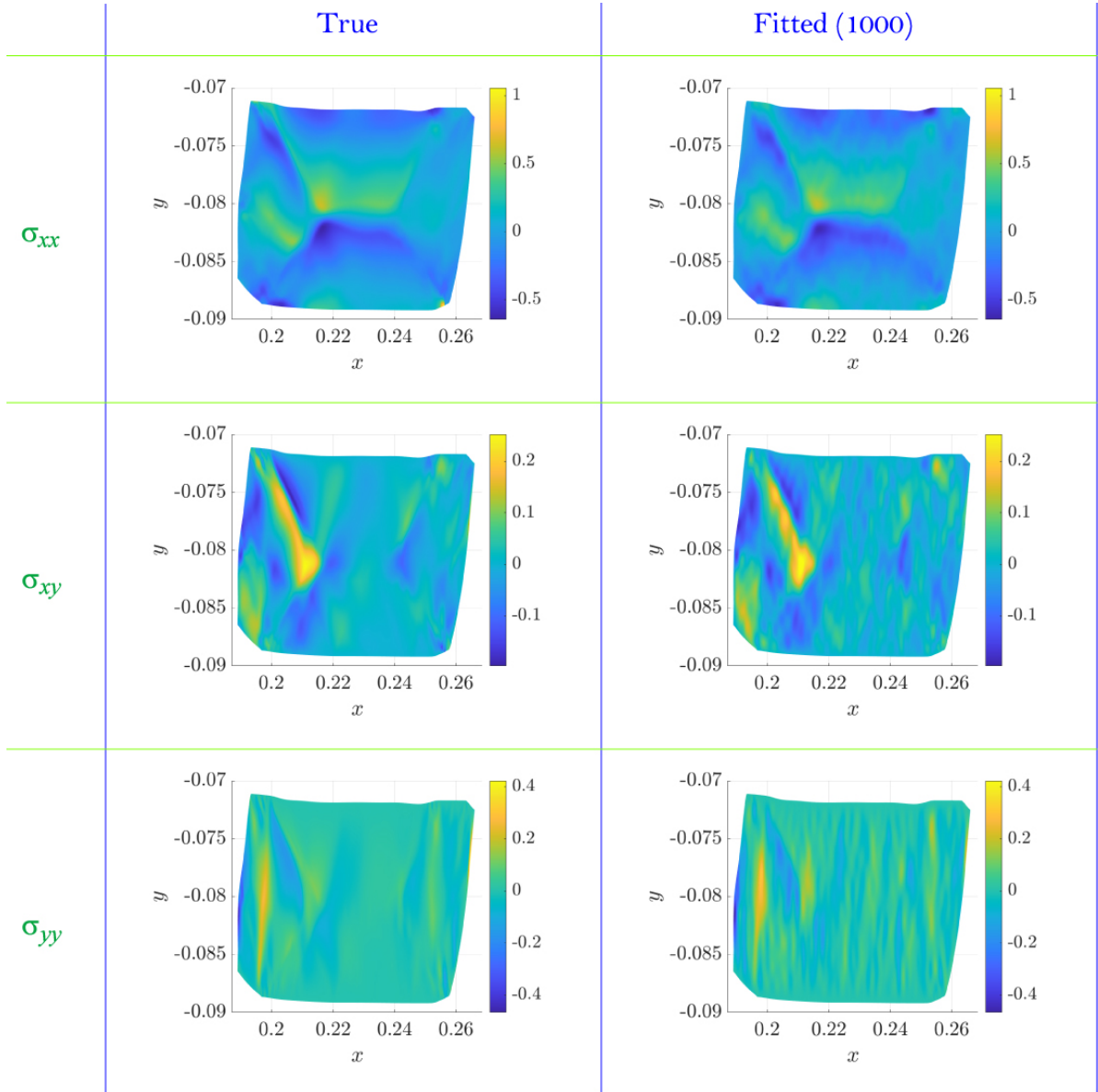


FIGURE 4.23: True and fitted (using 1000 eigenfunctions) stress components for the angular extrusion simulation (in GPa). Note that x and y axes are unequally scaled for better visibility.

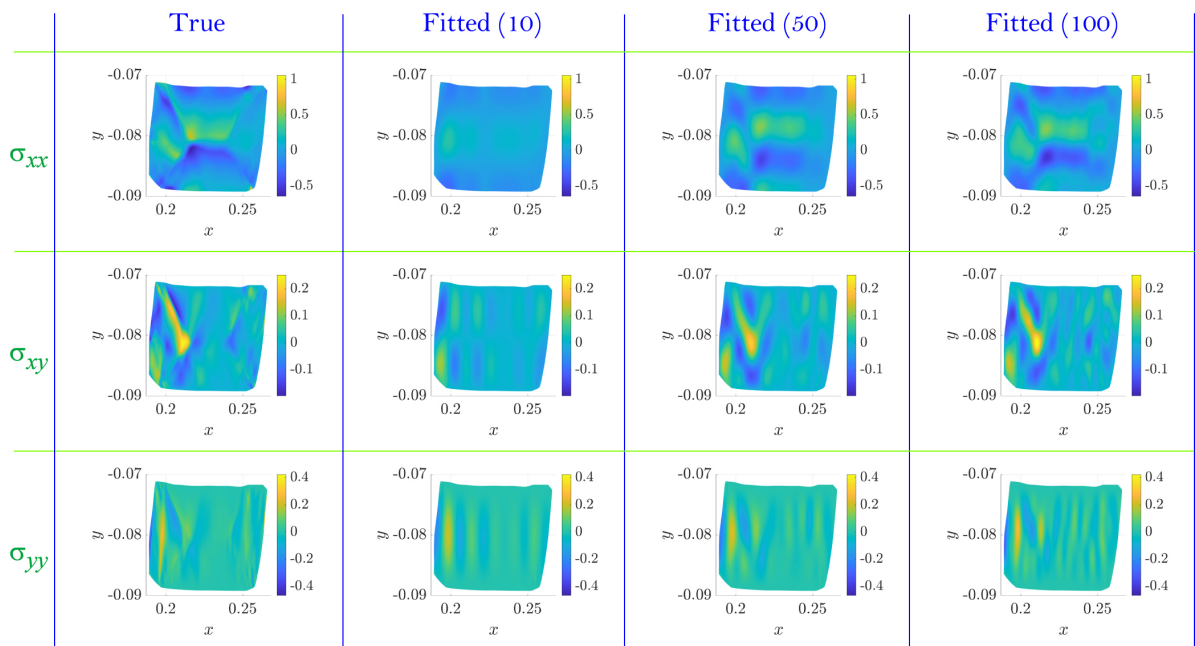


FIGURE 4.24: True and fitted (using 10, 50 and 100 eigenfunctions, respectively) stress components for the angular extrusion simulation (in GPa). Note that x and y axes are unequally scaled for better visibility.

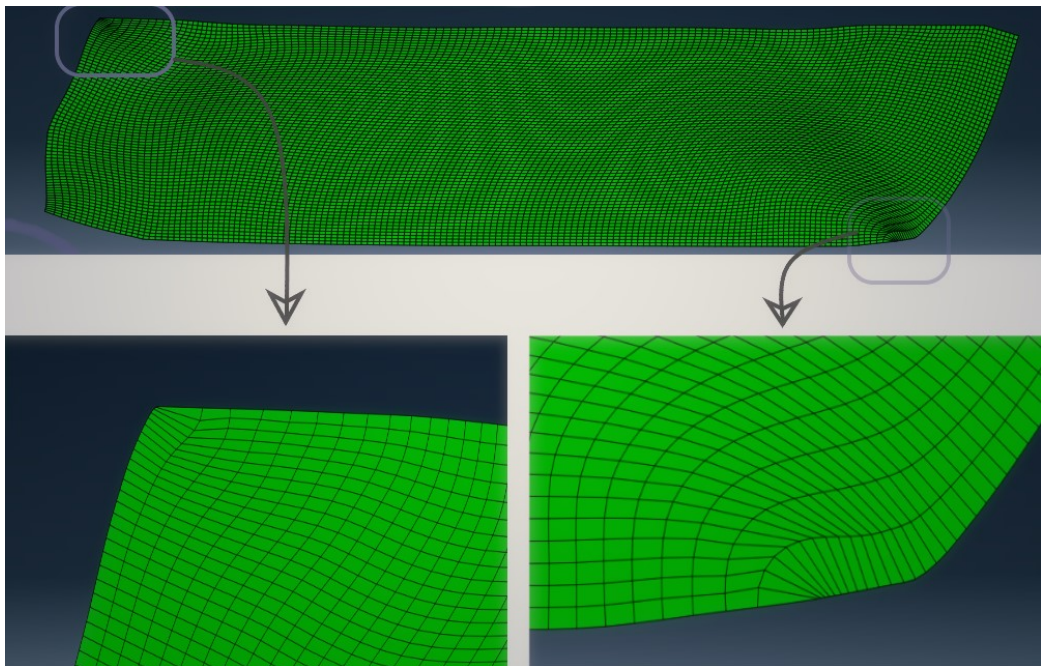


FIGURE 4.25: The workpiece mesh at the end of the angular extrusion simulation. We see that the corner elements are heavily distorted.

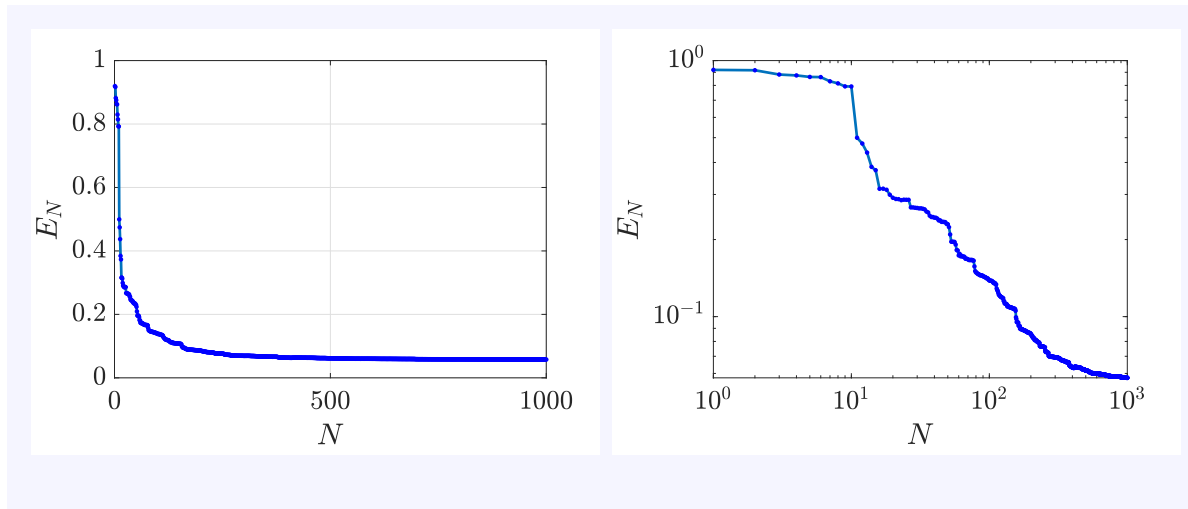


FIGURE 4.26: E_N versus N , angular extrusion simulation. Left: linear scale; right: log-log scale.

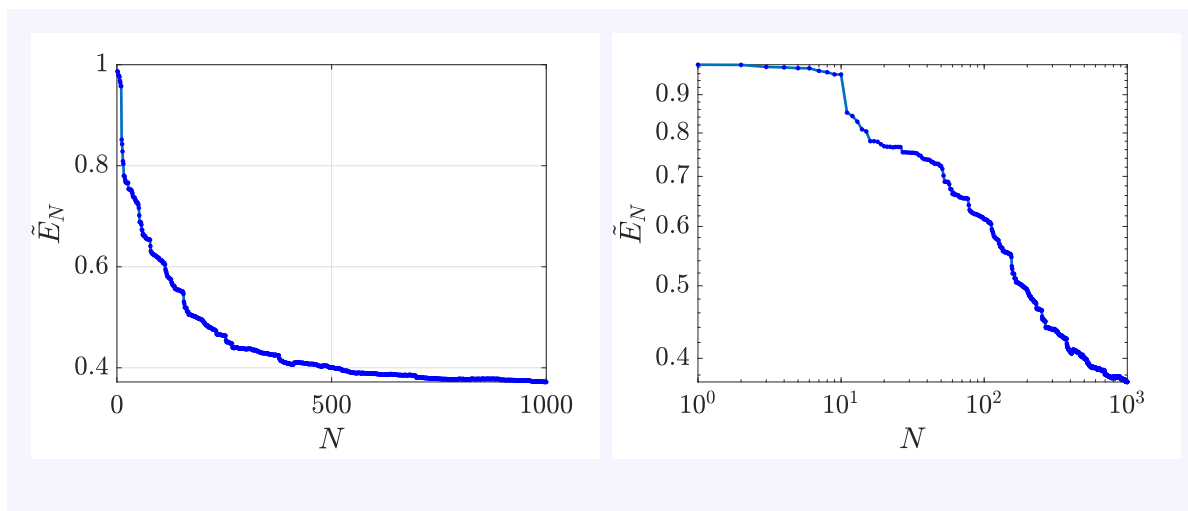


FIGURE 4.27: \tilde{E}_N versus N , angular extrusion simulation. Left: linear scale; right: log-log scale.

4.3 Summary of the chapter

In this chapter, we considered several different arbitrary but reasonable residual stress fields and fitted them using our eigenfunctions ϕ_i . In the first part of the chapter, we considered residual stress fields on an annular geometry, where the eigenfunctions essentially depend only on the radial coordinate upon choosing a wave number in the circumferential direction. This enables us to compute many eigenfunctions with great accuracy, and allows for a convenient visual representation of convergence. We considered four different residual stress fields on an annular geometry: two hypothetical, a third from shrink fitting of two concentric elastic cylinders and the fourth from non-uniform heating of an elastic annulus. Upon fitting them using the eigenfunctions having the same wave number as the given field, we observed convergence in both the L^2 and the H^1 norms in all but one example. In the shrink fit example, we obtained slower convergence in the L^2 norm and no convergence in the H^1 norm because the underlying field was discontinuous.

In the second part of the chapter, we considered residual stress fields obtained from simulation of two metal forming processes in Abaqus: rolling and angular extrusion. We presented details of both the simulations, and fitted the obtained residual stress fields using eigenfunctions computed on the same (deformed) mesh using our own FEM code.

We considered an elasto-plastic workpiece for the rolling simulation with two different hardening models: linear and Johnson-Cook. In both cases, we obtained good fits with quicker convergence in the L^2 norm and slower convergence in the H^1 norm. For the angular extrusion simulation, we considered an elasto-plastic workpiece with linear strain hardening. We observed that the fit quality in this case was not as good as those for the rolling simulations, with the fitting error E_N saturating at about 0.05. This is not entirely unexpected: the deformation is severe in the angular extrusion process, and the stress computed by Abaqus is equilibrated only in a weak sense.

In the next chapter, we show that the extremization problem considered in Chapter 2 is amenable to useful modifications. We consider two problems: (i) residual stresses in long prismatic bodies and (ii) spatially localized residual stresses in 2D. The modified extremization problems yield eigenfunctions that suit our purposes.

Chapter 5

Modifications of the eigenvalue problem for special purposes

The question that we consider in this chapter is the following: how amenable is our theoretical formulation of Chapter 2 to modifications?

We consider two special cases. In the first case, discussed in Section 5.1, we consider residual stress fields in long prismatic bodies. In such bodies, all the spatial fields are assumed to have zero partial derivatives in the axial direction, away from the ends. Accordingly, we modify the 3D eigenvalue problem of Section 2.5 by putting all the partial derivatives in the axial direction to zero in the functional J_0 (Eq. 2.3). We will see that this leads to splitting of the problem into three planar sub-problems: one for the planar stresses, one for the out of plane shear stresses and one for the axial stress. In the second case, presented in Section 5.2, we look at residual stress fields localized in a 2D region, decaying rapidly away from it. For this case we multiply the functional J_0 , and the normalizing constraint, with appropriate weighting factors to make our eigenfunctions spatially localized.

Examples of such stresses abound in nature as well as engineering, and our motivation behind discussing these two special cases is of both academic and practical interest. Prismatic geometries with residual stresses are found in rails [63] and blood vessels [23], for instance; some examples of spatially localized residual stresses include stresses around crack tips and those near the surface of a shot peened component [1].

5.1 Basis functions for residual stress fields in infinitely long prismatic bodies

5.1.1 Properties of residual stress fields in such bodies

Let us assume that our residually stressed body is infinitely long and prismatic in the z direction. We may then suppose that the spatial fields do not vary in the z direction and depend only on the spatial coordinates x and y . All the partial derivatives in the z direction are zero, and the equilibrium equations simplify to:

$$\begin{aligned}\sigma_{xx,x} + \sigma_{xy,y} &= 0, \\ \sigma_{xy,x} + \sigma_{yy,y} &= 0, \\ \sigma_{xz,x} + \sigma_{yz,y} &= 0.\end{aligned}\tag{5.1}$$

Since the body is prismatic, the unit normal \mathbf{n} to its surface lies in the x - y plane, so that $n_z = 0$. The traction-free boundary conditions are

$$\begin{aligned}\sigma_{xx}n_x + \sigma_{xy}n_y &= 0, \\ \sigma_{xy}n_x + \sigma_{yy}n_y &= 0, \\ \sigma_{xz}n_x + \sigma_{yz}n_y &= 0.\end{aligned}\tag{5.2}$$

Finally, since the body is in equilibrium on the whole, and things do not vary in the z direction, it is also reasonable to suppose that the force resultant \mathbf{N} and the moment resultant \mathbf{M} across any z cross-section is zero. Accordingly, we have new integral constraints

$$\begin{aligned}N_x &= \int_{\Omega_l} \sigma_{xz} dA = 0, \\ N_y &= \int_{\Omega_l} \sigma_{yz} dA = 0, \\ N_z &= \int_{\Omega_l} \sigma_{zz} dA = 0,\end{aligned}\tag{5.3}$$

as well as

$$\begin{aligned}M_x &= \int_{\Omega_l} x\sigma_{zz} dA = 0, \\ M_y &= \int_{\Omega_l} y\sigma_{zz} dA = 0, \\ M_z &= \int_{\Omega_l} (x\sigma_{yz} - y\sigma_{xz}) dA = 0.\end{aligned}\tag{5.4}$$

In the above equations, Ω_l represents any two-dimensional section with constant z , the subscript l denoting ‘lateral’. The origin (i.e., the point with $x = 0$ and $y = 0$ in Ω_l) can be chosen to be any convenient fixed point (for example, the centroid of Ω_l).

The first and the second equations in Eqs. 5.3 need not be assumed explicitly, as they follow from the vector field

$$[\mathbf{v}] = \begin{bmatrix} \sigma_{xz} \\ \sigma_{yz} \end{bmatrix}$$

being divergence-free in Ω_l (third of Eqs. 5.1) and having zero flux on $\partial\Omega_l$ (third of Eqs. 5.2). We show this below using indicial notation. If \mathbf{r} denotes position vector, then

$$\int_{\Omega_l} v_i dA = \int_{\Omega_l} v_j \delta_{ij} dA = \int_{\Omega_l} v_j r_{i,j} dA = \int_{\Omega_l} \{(v_j r_i)_{,j} - v_{j,j} r_i\} dA = \int_{\partial\Omega_l} v_j n_j r_i ds = 0, \quad (5.5)$$

since $v_{j,j} = 0$ in Ω_l and $v_j n_j = 0$ on $\partial\Omega_l$.

To summarize, the residual stress fields in infinitely long prismatic bodies satisfy Eqs. 5.1–5.4. We note from these equations that we can split the stress components into three groups: $(\sigma_{xx}, \sigma_{yy}, \sigma_{xy})$, (σ_{zz}) and $(\sigma_{xz}, \sigma_{yz})$, such that the components in each group are coupled with each other, but independent of components in the other groups.

We now find a basis for such residual stress fields.

5.1.2 Development of basis functions

We seek the stationary points of the functional

$$J_0(\boldsymbol{\sigma}) = \frac{1}{2} \int_{\Omega_l} (\sigma_{xx,x}^2 + \sigma_{xx,y}^2 + \sigma_{yy,x}^2 + \sigma_{yy,y}^2 + \sigma_{zz,x}^2 + \sigma_{zz,y}^2 + 2\sigma_{xy,x}^2 + 2\sigma_{xy,y}^2 + 2\sigma_{xz,x}^2 + 2\sigma_{xz,y}^2 + 2\sigma_{yz,x}^2 + 2\sigma_{yz,y}^2) dA$$

over symmetric second-order tensors $\boldsymbol{\sigma}$ which satisfy Eqs. 5.1–5.4, subject to the normalization constraint

$$\int_{\Omega_l} \boldsymbol{\sigma} \cdot \boldsymbol{\sigma} dA = \int_{\Omega_l} (\sigma_{xx}^2 + \sigma_{yy}^2 + \sigma_{zz}^2 + 2\sigma_{xy}^2 + 2\sigma_{xz}^2 + 2\sigma_{yz}^2) dA = 1.$$

This extremization problem is the same as the 3D version of the problem studied in Chapter 2, except that all partial derivatives with respect to z have been dropped, and the invariance in the z direction has rendered the spatial domain planar.

Let $\lambda/2$, $\tilde{\lambda}_1$, $\tilde{\lambda}_2$, $\tilde{\lambda}_3$ and $\tilde{\lambda}_4$ be the constant Lagrange multipliers corresponding to the integral constraints $\int_{\Omega_l} \boldsymbol{\sigma} \cdot \boldsymbol{\sigma} dA = 1$, $\int_{\Omega_l} \sigma_{zz} dA = 0$, $\int_{\Omega_l} x\sigma_{zz} dA = 0$, $\int_{\Omega_l} y\sigma_{zz} dA = 0$ and $\int_{\Omega_l} (x\sigma_{yz} - y\sigma_{xz}) dA = 0$, respectively; and μ_x , μ_y and μ_z be the spatially varying Lagrange multipliers corresponding to the differential constraints in Eqs. 5.1. Then, proceeding in the usual manner, it is not difficult to see that we obtain the following Euler-Lagrange equations:

$$\begin{aligned}
-\Delta\sigma_{xx} + \mu_{x,x} &= \lambda\sigma_{xx}, \\
-\Delta\sigma_{yy} + \mu_{y,y} &= \lambda\sigma_{yy}, \\
-\Delta\sigma_{xy} + \frac{\mu_{x,y} + \mu_{y,x}}{2} &= \lambda\sigma_{xy}, \\
-\Delta\sigma_{zz} - \tilde{\lambda}_1 - \tilde{\lambda}_2x - \tilde{\lambda}_3y &= \lambda\sigma_{zz}, \\
-\Delta\sigma_{xz} + \tilde{\lambda}_4y + \frac{\mu_{z,x}}{2} &= \lambda\sigma_{xz}, \\
-\Delta\sigma_{yz} - \tilde{\lambda}_4x + \frac{\mu_{z,y}}{2} &= \lambda\sigma_{yz},
\end{aligned} \tag{5.6}$$

where Δ denotes the 2D Laplacian: $\frac{\partial^2}{\partial x^2} + \frac{\partial^2}{\partial y^2}$. We also obtain the following ‘natural’ boundary conditions (\mathbf{t} is the tangent vector to $\partial\Omega_l$ in the plane of Ω_l):

$$\begin{aligned}
\sigma_{xx,x}n_xn_y^2 + \sigma_{xx,y}n_y^3 + \sigma_{yy,x}n_x^3 + \sigma_{yy,y}n_x^2n_y - 2\sigma_{xy,x}n_x^2n_y - 2\sigma_{xy,y}n_xn_y^2 &= 0, \\
\sigma_{zz,x}n_x + \sigma_{zz,y}n_y &= 0, \\
(\sigma_{xz,x}n_x + \sigma_{xz,y}n_y)t_x + (\sigma_{yz,x}n_x + \sigma_{yz,y}n_y)t_y &= 0.
\end{aligned} \tag{5.7}$$

Eqs. 5.1–5.7 represent the complete boundary value problem that must be solved to compute the eigenfunctions. We see from these equations that the three groups of stress components mentioned in the previous section are coupled with each other only through the Lagrange multiplier λ , and we can split the system of Eqs. 5.1–5.7 into three sub-systems mutually related only through λ . However, λ can be determined using either of the three sub-systems independently, and unless those values match, we have an ill-posed problem in our hands. The simplest remedy is to have three independent norm constraints:

$$\begin{aligned}
\int_{\Omega_l} (\sigma_{xx}^2 + \sigma_{yy}^2 + 2\sigma_{xy}^2) dA &= 1, \\
\int_{\Omega_l} \sigma_{zz}^2 dA &= 1, \\
\int_{\Omega_l} (\sigma_{xz}^2 + \sigma_{yz}^2) dA &= 1.
\end{aligned}$$

This completely decouples the three groups of stress components, and we can state three separate extremization problems as below. We will see that the solutions of each problem span the corresponding space of stress components.

In what follows, all the operators are meant to act on 2D fields. For instance, if $u(x, y)$ is a scalar field and $\mathbf{v}(x, y)$ is a vector field, then $\nabla u = \frac{\partial u}{\partial x} \mathbf{e}_x + \frac{\partial u}{\partial y} \mathbf{e}_y$ and $\operatorname{div} \mathbf{v} = \frac{\partial v_x}{\partial x} + \frac{\partial v_y}{\partial y}$.

We now state the three extremization problems.

Problem 1: Find the stationary points of the functional

$$J_1(\boldsymbol{\sigma}) = \frac{1}{2} \int_{\Omega_l} \nabla \boldsymbol{\sigma} \cdot \nabla \boldsymbol{\sigma} \, dA$$

over the set

$$\mathcal{S}_1 = \left\{ \boldsymbol{\sigma} \mid \boldsymbol{\sigma} \in \text{Sym}, \operatorname{div} \boldsymbol{\sigma} = \mathbf{0}, \boldsymbol{\sigma} \mathbf{n}|_{\partial\Omega_l} = \mathbf{0}, \int_{\Omega_l} \boldsymbol{\sigma} \cdot \boldsymbol{\sigma} \, dA < \infty, \int_{\Omega_l} \nabla \boldsymbol{\sigma} \cdot \nabla \boldsymbol{\sigma} \, dA < \infty \right\},$$

where ‘Sym’ is the set of all *planar* symmetric second order tensors over Ω , subject to the normalization constraint

$$\int_{\Omega_l} \boldsymbol{\sigma} \cdot \boldsymbol{\sigma} \, dA = 1.$$

We have already solved this problem in Chapter 2, where we saw that the solutions span the closure of \mathcal{S}_1 . The next two problems are more interesting in the context of this chapter.

Problem 2: Find the stationary points of the functional

$$J_2(\sigma_{zz}) = \frac{1}{2} \int_{\Omega_l} \nabla \sigma_{zz} \cdot \nabla \sigma_{zz} \, dA$$

over the unit norm elements $\int_{\Omega_l} \sigma_{zz}^2 \, dA = 1$ of the following set of scalar functions:

$$\mathcal{S}_2 = \left\{ \sigma_{zz} \mid \int_{\Omega_l} \sigma_{zz}^2 \, dA < \infty, \int_{\Omega_l} \nabla \sigma_{zz} \cdot \nabla \sigma_{zz} \, dA < \infty, \int_{\Omega_l} \sigma_{zz} \, dA = 0, \int_{\Omega_l} \mathbf{r} \sigma_{zz} \, dA = \mathbf{0} \right\},$$

where \mathbf{r} is the position vector ($\mathbf{r} = x\mathbf{e}_x + y\mathbf{e}_y$ in Cartesian coordinates); and the four conditions included imply square integrability of σ_{zz} , square integrability of its gradient, zero net force in z direction across Ω_l , and zero net bending moment across Ω_l .

This extremization problem leads us to the following eigenvalue problem, with eigenvalue λ and eigenvector $\{\sigma_{zz}, \tilde{\lambda}_1, \boldsymbol{\varpi}\}$:¹

$$\begin{aligned} -\Delta\sigma_{zz} - \tilde{\lambda}_1 - \boldsymbol{\varpi} \cdot \mathbf{r} &= \lambda\sigma_{zz} \quad \text{in } \Omega_l, \\ \nabla\sigma_{zz} \cdot \mathbf{n} &= 0 \quad \text{on } \partial\Omega_l, \\ \int_{\Omega_l} \sigma_{zz} dA &= 0, \\ \int_{\Omega_l} \mathbf{r}\sigma_{zz} dA &= \mathbf{0}, \end{aligned} \tag{5.8}$$

where $\frac{\lambda}{2}$ is the constant Lagrange multiplier corresponding to the normalization constraint; and $\tilde{\lambda}_1$ and $\boldsymbol{\varpi}$ are the constant Lagrange multipliers corresponding to the constraints $\int_{\Omega_l} \sigma_{zz} dA = 0$ and $\int_{\Omega_l} \mathbf{r}\sigma_{zz} dA = \mathbf{0}$, respectively.

In Cartesian coordinates, the above equations become

$$\begin{aligned} -\Delta\sigma_{zz} + \tilde{\lambda}_1 - \tilde{\lambda}_2x - \tilde{\lambda}_3y &= \lambda\sigma_{zz} \quad \text{in } \Omega_l, \\ \sigma_{zz,x}n_x + \sigma_{zz,y}n_y &= 0 \quad \text{on } \partial\Omega_l, \\ \int_{\Omega_l} \sigma_{zz} dA = \int_{\Omega_l} x\sigma_{zz} dA = \int_{\Omega_l} y\sigma_{zz} dA &= 0, \end{aligned} \tag{5.9}$$

where $\tilde{\lambda}_2 = \boldsymbol{\varpi} \cdot \mathbf{e}_x$ and $\tilde{\lambda}_3 = \boldsymbol{\varpi} \cdot \mathbf{e}_y$.

We now show that the solutions of the above eigenvalue problem form an orthogonal sequence. Let ϕ_{zzi} and ϕ_{zzj} be two distinct solutions of Eq. 5.8 with corresponding Lagrange multipliers $(\lambda_i, \tilde{\lambda}_{1i}, \boldsymbol{\varpi}_i)$ and $(\lambda_j, \tilde{\lambda}_{1j}, \boldsymbol{\varpi}_j)$, respectively. Then, they satisfy

$$\begin{aligned} -\Delta\phi_{zzi} - \tilde{\lambda}_{1i} - \boldsymbol{\varpi}_i \cdot \mathbf{r} &= \lambda_i\phi_{zzi}, \\ -\Delta\phi_{zzj} - \tilde{\lambda}_{1j} - \boldsymbol{\varpi}_j \cdot \mathbf{r} &= \lambda_j\phi_{zzj}. \end{aligned}$$

Consider the inner product of the first of the above equations with ϕ_{zzj} , i.e.,

$$\int_{\Omega_l} \left(-\Delta\phi_{zzi} - \tilde{\lambda}_{1i} - \boldsymbol{\varpi}_i \cdot \mathbf{r} \right) \phi_{zzj} dA = \lambda_i \int_{\Omega_l} \phi_{zzi} \phi_{zzj} dA.$$

¹In our FEM code for solving this eigenvalue problem, we arrange σ_{zz} , $\tilde{\lambda}_1$ and $\boldsymbol{\varpi}$ in a column vector a to obtain a generalized eigenvalue problem $Aa = \lambda Ba$, for some square matrices A and B .

Integrating by parts, and using the divergence theorem, we obtain

$$\begin{aligned} - \int_{\partial\Omega_i} \nabla_n \phi_{zzi} \phi_{zzj} ds + \int_{\Omega_i} \nabla \phi_{zzi} \cdot \nabla \phi_{zzj} dA - \tilde{\lambda}_{1i} \int_{\Omega_i} \phi_{zzj} dA - \boldsymbol{\varpi}_i \cdot \int_{\Omega_i} \mathbf{r} \phi_{zzj} dA \\ = \lambda_i \int_{\Omega_i} \phi_{zzi} \phi_{zzj} dA. \end{aligned}$$

Using the boundary condition and the integral constraints given in Eqs. 5.8, we obtain

$$\int_{\Omega_i} \nabla \phi_{zzi} \cdot \nabla \phi_{zzj} dA = \lambda_i \int_{\Omega_i} \phi_{zzi} \phi_{zzj} dA.$$

Similarly,

$$\int_{\Omega_i} \nabla \phi_{zzj} \cdot \nabla \phi_{zzi} dA = \lambda_j \int_{\Omega_i} \phi_{zzj} \phi_{zzi} dA.$$

If $\lambda_i \neq \lambda_j$, then

$$\int_{\Omega_i} \phi_{zzi} \phi_{zzj} dA = 0 \quad \text{and} \quad \int_{\Omega_i} \nabla \phi_{zzi} \cdot \nabla \phi_{zzj} dA = 0, \quad (5.10)$$

i.e., ϕ_{zzi} and ϕ_{zzj} are orthogonal. If $\lambda_i = \lambda_j$ but $\phi_{zzi} \neq \phi_{zzj}$, then we can choose ϕ_{zzi} and ϕ_{zzj} to be orthogonal, and Eq. 5.10 still holds. We thus have an orthogonal sequence of eigenfunctions.

Our numerics below will indicate that these eigenfunctions span the set \mathcal{S}_2 , and we do not attempt to prove this formally here. However, we point out that the above eigenvalue problem (Eq. 5.8) is similar to our original eigenvalue problem of Chapter 2 (Eq. 2.12), with only a few differences (e.g., the presence of additional integral constraints in the former). Hence, a formal proof could be attempted along similar lines to the one presented in Chapter 2. We also refer the reader to Section 7.3, where we indicate how these differences might be handled.

We solve Eq. 5.9 using our own FE formulation, which is similar to that presented in Section 3.1. The first four eigenfunctions computed on an annulus of inner radius 0.1 and outer radius 0.3 are shown in Figure 5.1.

We now demonstrate that the eigenfunctions ϕ_{zzi} lead to quick convergence when used to fit a given axial stress. Let us consider a candidate σ_{zz} field in a prismatic geometry with the square cross section $0 \leq x, y \leq 1$:

$$\sigma_{zz} = \left(x - \frac{3}{2}x^2 \right) \left(-\frac{2}{3}y + y^2 \right).$$

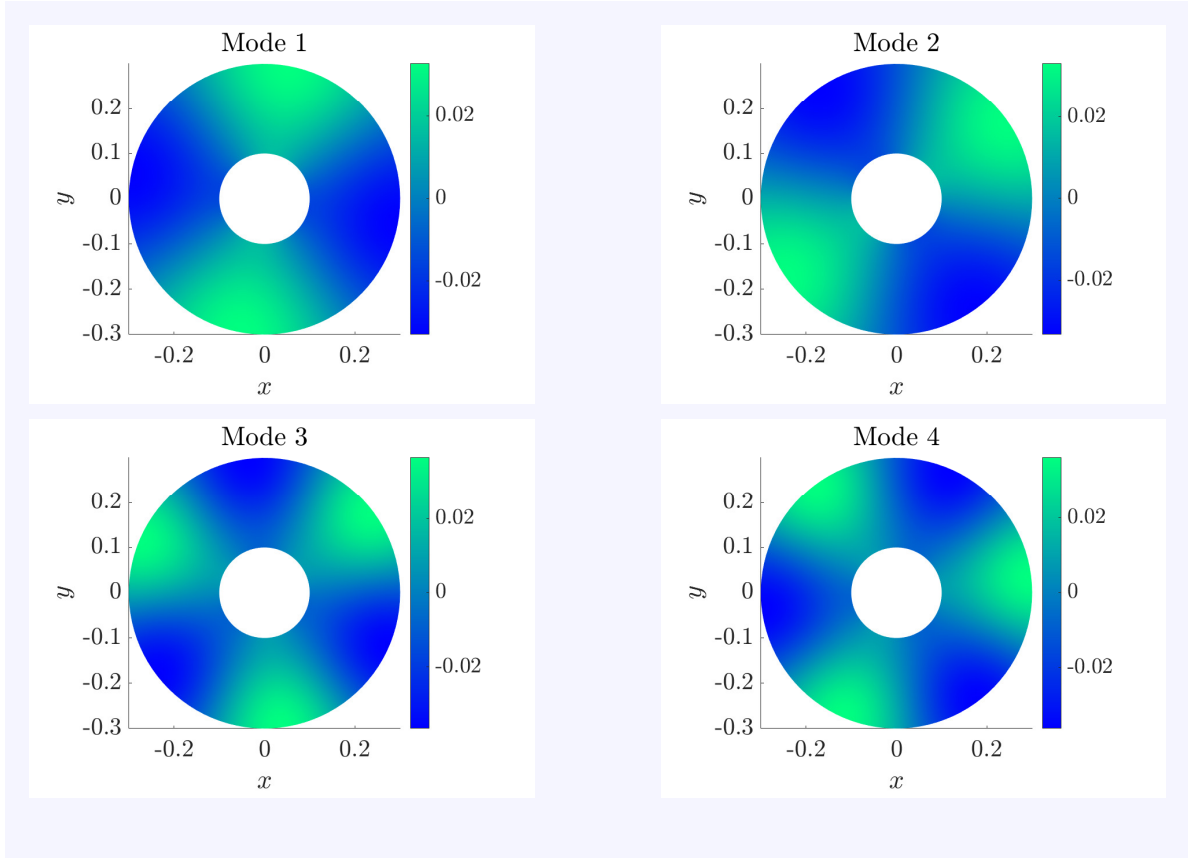


FIGURE 5.1: First four eigenfunctions for σ_{zz} computed using our own FEM code on an annular domain, with eigenvalues $\lambda = 95.58, 95.58, 192.71, 192.71$, respectively.

It can be verified that σ_{zz} satisfies the zero mean condition (third of Eqs. 5.3) and the zero net bending moment condition (first and second of Eqs. 5.4). We fit σ_{zz} with ϕ_{zzi} . For comparison, we also fit it using another standard basis: scalar eigenfunctions of the Laplace operator

$$-\Delta \tilde{u}_i = \lambda \tilde{u}_i$$

with zero boundary value [64].

The field σ_{zz} , along with fits obtained using the first 100 functions of each of these bases, is plotted in Figure 5.2. The corresponding fitting errors E_N are plotted in Figures 5.3 and 5.4. It is evident from the figures that while convergence is obtained with both the bases, it is much faster with ϕ_{zzi} . The reason is that the elements of the second basis do not satisfy the zero net force and moment constraints, while each element of the first basis does satisfy them.

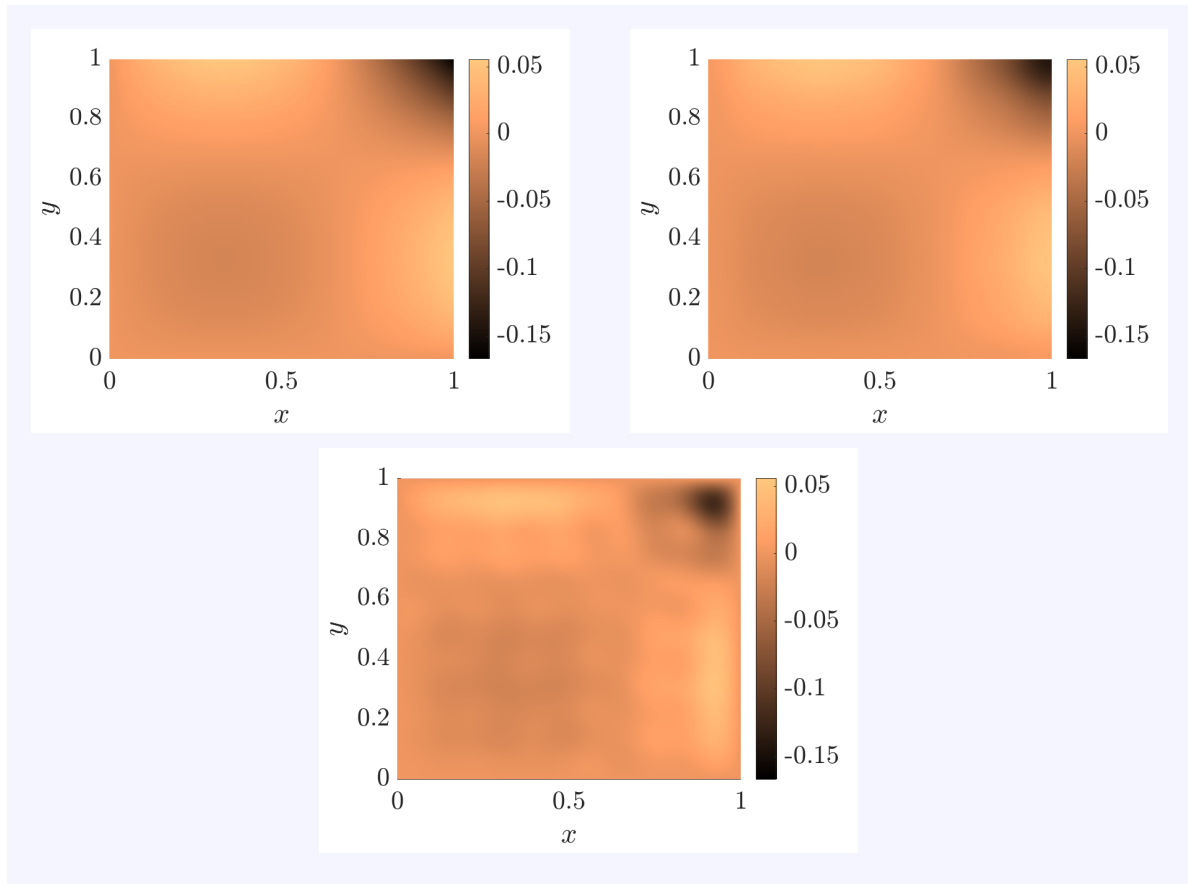


FIGURE 5.2: A candidate σ_{zz} field (top-left), and fits obtained with the first 100 basis functions ϕ_{zzi} (top-right) and the first 100 Laplace eigenfunctions \tilde{u}_i (bottom).

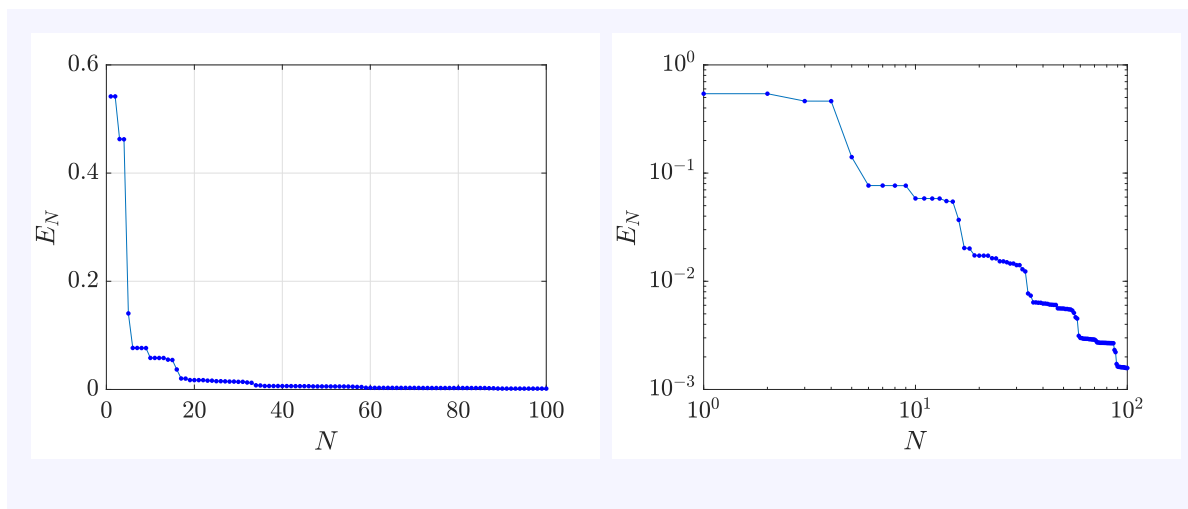


FIGURE 5.3: E_N versus N with our basis ϕ_{zzi} . Left: linear scale; right: log-log scale.

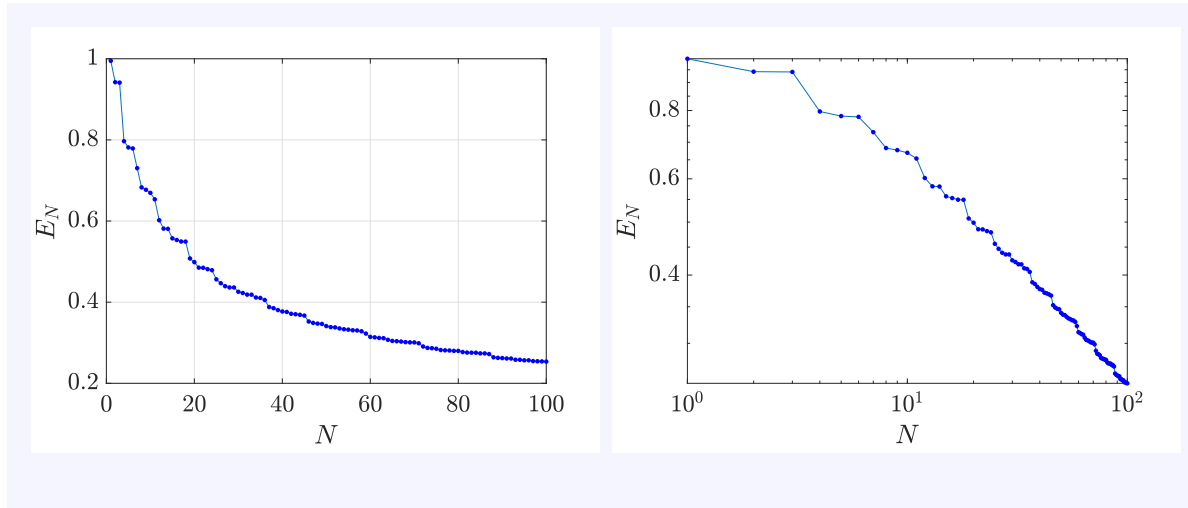


FIGURE 5.4: E_N versus N with Laplace eigenfunctions \tilde{u}_i . Left: linear scale; right: log-log scale.

We demonstrate yet another utility of the functions ϕ_{zzi} by using them to interpolate an axial stress in a rail given its value at a few points. Figure 5.5 (adapted from Figure 1.12 of [1]) shows the schematic of the cross section of a typical axially stressed rail. We roughly estimate the values of this axial stress at 10 points (marked with light yellow crosses in the figure) using the contours provided in the Figure 1.12 of [1], and use these values to interpolate with ϕ_{zzi} . These values are reported in Table 5.1.

We first show the first four eigenfunctions ϕ_{zzi} on the rail geometry in Figure 5.6. In Figure 5.7, we show the interpolated stress using the first N eigenfunctions, with $N = 2, 4, 6$ and 8 . Note that the interpolation has been done using the least squares method. We see that the interpolants are reasonably good, except for $N = 2$. For comparison, we also interpolate with the first four and six Laplace operator eigenfunctions \tilde{u}_i , respectively, and plot in Figure 5.8. Although this is a limited comparison, it appears that the ϕ_{zzi} yield a physically more realistic picture. Moreover, with the Laplace operator eigenfunctions, the $N = 6$ interpolant is significantly less correct than the $N = 4$ interpolant, and both these interpolants also violate the zero net force and moment conditions.

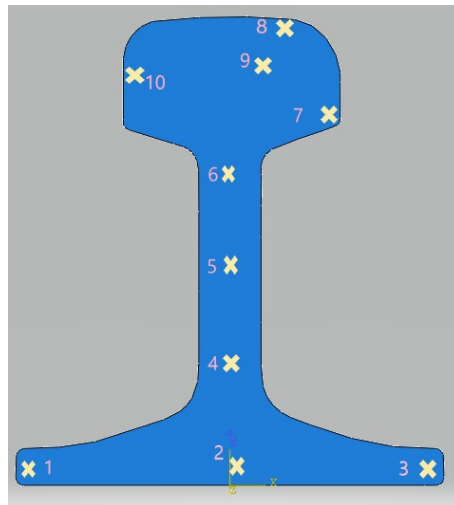
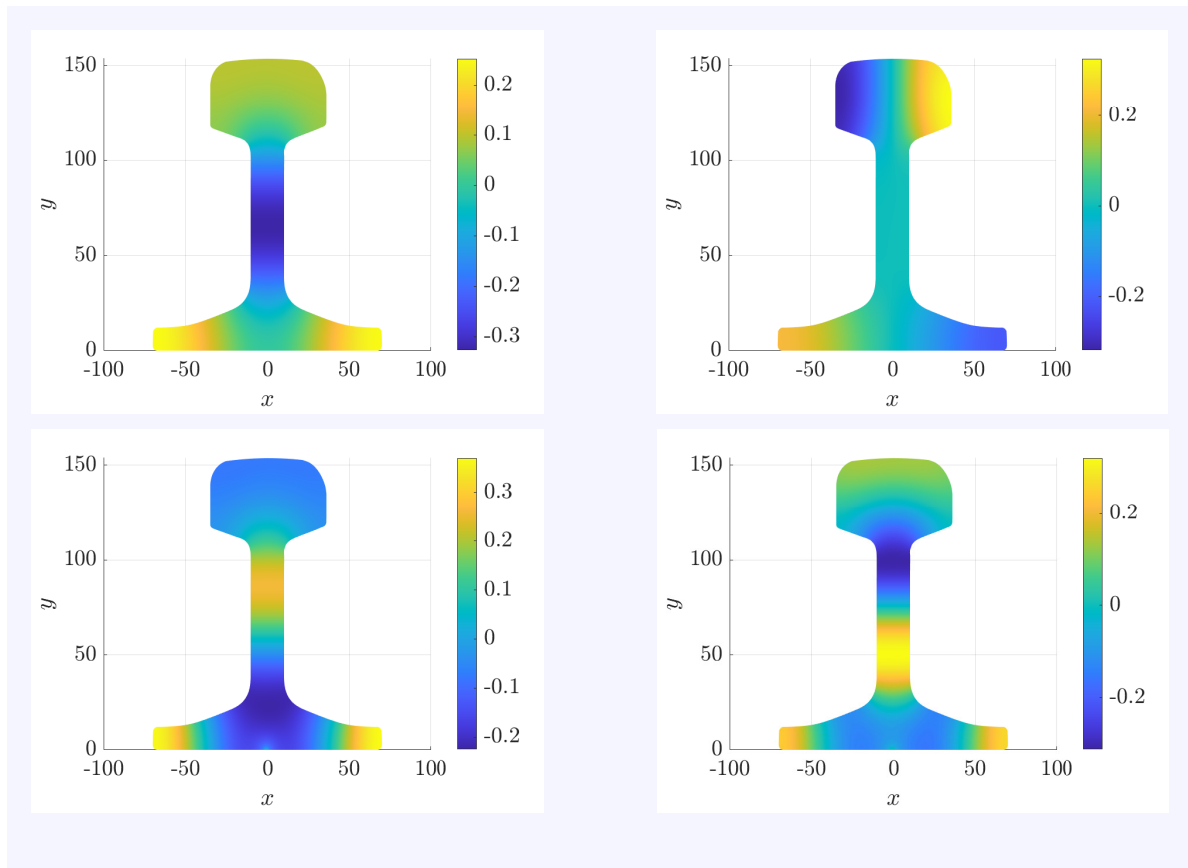


FIGURE 5.5: Schematic of an axially stressed rail (adapted from Figure 1.12 of [1]). We use the values of the axial stress at 10 points, marked with light yellow crosses, for interpolation.

Point label in Figure 5.5	Axial stress (in MPa)
1	-420
2	300
3	-420
4	-150
5	-240
6	-90
7	60
8	-420
9	270
10	-60

TABLE 5.1: Axial stress values at points marked with light yellow crosses in Figure 5.5 (as estimated from Figure 1.12 of [1]).

FIGURE 5.6: The first four eigenfunctions ϕ_{zzi} on the rail geometry.

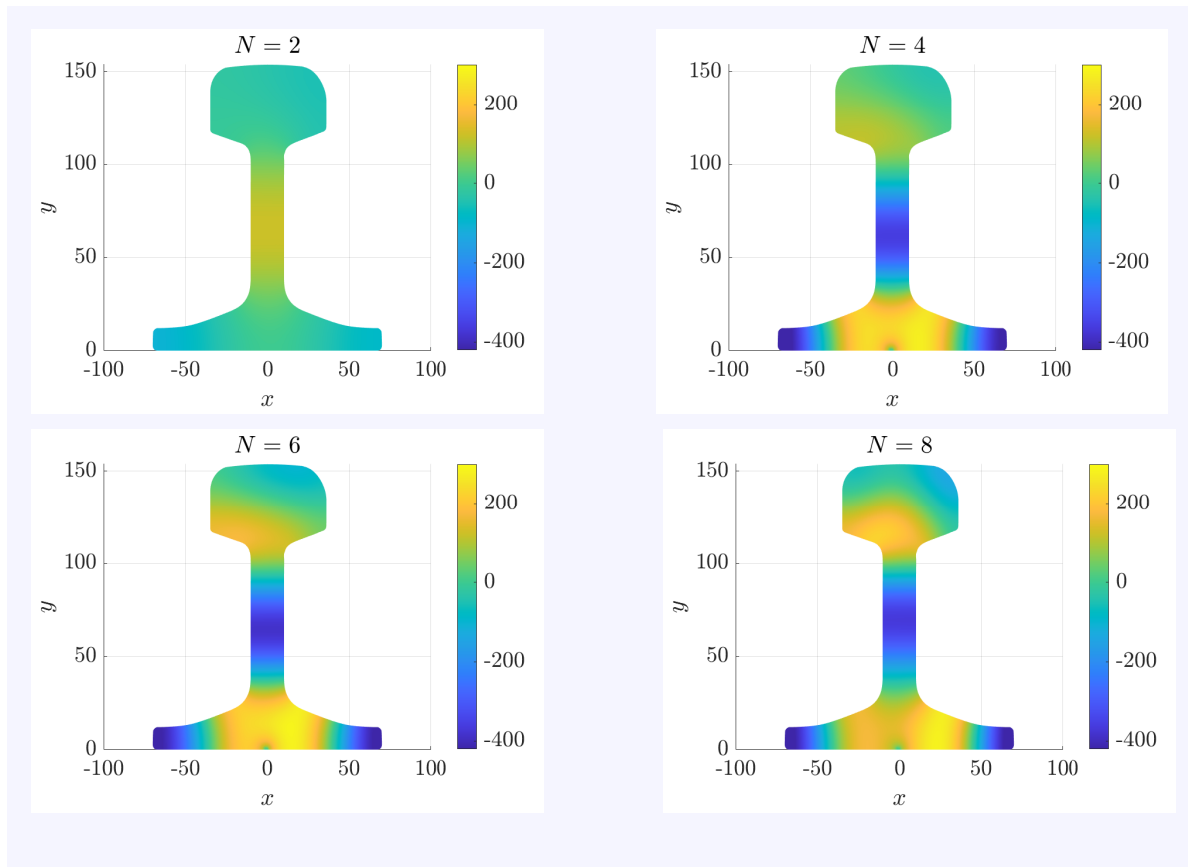


FIGURE 5.7: Interpolated axial stress (in MPa) using the first N eigenfunctions ϕ_{zzi} , with $N = 2, 4, 6$ and 8 .

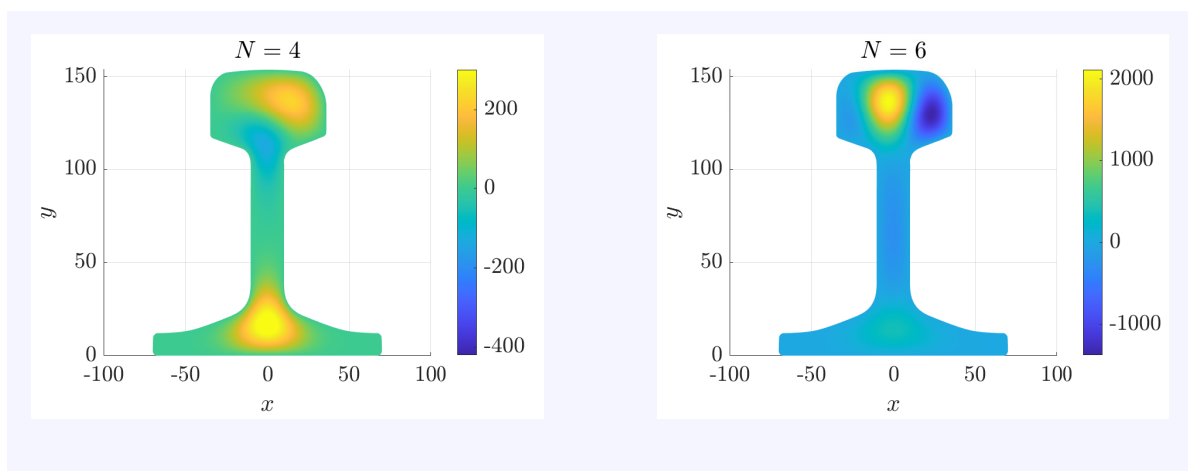


FIGURE 5.8: Interpolated axial stress (in MPa) using the first N Laplace operator eigenfunctions with zero boundary value \tilde{u}_i , with $N = 4$ and 6 .

Problem 3: Before stating the third extremization problem, we mention a useful point.

Let

$$[\mathbf{v}] = \begin{bmatrix} \sigma_{xz} \\ \sigma_{yz} \end{bmatrix},$$

where by square brackets we imply representation in Cartesian coordinates. Then, the condition of zero net twisting moment,

$$\int_{\Omega_l} (x\sigma_{yz} - y\sigma_{xz}) dA = 0, \quad (5.11)$$

can be represented in a coordinate free manner as

$$\int_{\Omega_l} \mathbf{r} \times \mathbf{v} dA = \mathbf{0}, \quad (5.12)$$

where \mathbf{r} is the position vector. Note that \mathbf{r} and \mathbf{v} are to be interpreted as 3D vectors, but with zero z component, while computing the above cross product. Although Eq. 5.12 is a vector equation, only its z component is non-trivial. We have chosen this representation because with a coordinate free description, the eigenvalue problem can be written succinctly, and the algebra involved in deriving the orthogonality relations is simpler.

We now state the extremization problem.

We seek the stationary points of the functional

$$J_3(\mathbf{v}) = \frac{1}{2} \int_{\Omega_l} \nabla \mathbf{v} \cdot \nabla \mathbf{v} dA$$

over the set

$$\mathcal{S}_3 = \left\{ \mathbf{v} \mid \operatorname{div} \mathbf{v} = 0, \mathbf{v} \cdot \mathbf{n}|_{\partial\Omega_l} = 0, \int_{\Omega_l} \mathbf{v} \cdot \mathbf{v} dA < \infty, \int_{\Omega_l} \nabla \mathbf{v} \cdot \nabla \mathbf{v} dA < \infty, \int_{\Omega_l} \mathbf{r} \times \mathbf{v} dA = \mathbf{0} \right\},$$

subject to the normalization constraint $\int_{\Omega_l} \mathbf{v} \cdot \mathbf{v} dA = 1$.

Calculus of variations leads us to the following eigenvalue problem, with eigenvalue λ and eigenvector $\{\mathbf{v}, \mu_z, \boldsymbol{\varpi}\}$:²

$$\begin{aligned} -\Delta \mathbf{v} + \nabla \mu_z - \boldsymbol{\varpi} \times \mathbf{r} &= \lambda \mathbf{v} && \text{in } \Omega_l, \\ \operatorname{div} \mathbf{v} &= 0 && \text{in } \Omega_l, \\ \mathbf{v} \cdot \mathbf{n} &= 0 && \text{on } \partial\Omega_l, \\ \nabla \mathbf{v} \mathbf{n} &= \mathbf{0} && \text{on } \partial\Omega_l, \end{aligned} \tag{5.13}$$

$$\int_{\Omega_l} \mathbf{r} \times \mathbf{v} \, dA = \mathbf{0},$$

where $\frac{\lambda}{2}$ is the constant Lagrange multiplier corresponding to the normalization constraint, μ_z is the spatially varying Lagrange multiplier corresponding to the differential constraint $\operatorname{div} \mathbf{v} = 0$, and $\boldsymbol{\varpi}$ is the constant vector-valued Lagrange multiplier corresponding to the zero net twisting moment condition in Eq. 5.12. Note that the x and y components of $\boldsymbol{\varpi}$ are zero, so that $\boldsymbol{\varpi} = \tilde{\lambda}_4 \mathbf{e}_z$ for some scalar $\tilde{\lambda}_4$ ³. Also note that \mathbf{r} is to be interpreted as a 3D vector, but with zero z component, while computing the cross product in the first of Eqs. 5.13.

In Cartesian coordinates, the above equations become

$$\begin{aligned} -\Delta \sigma_{xz} + \tilde{\lambda}_4 y + \mu_{z,x} &= \lambda \sigma_{xz} && \text{in } \Omega_l, \\ -\Delta \sigma_{yz} - \tilde{\lambda}_4 x + \mu_{z,y} &= \lambda \sigma_{yz} && \text{in } \Omega_l, \\ \sigma_{xz,x} + \sigma_{yz,y} &= 0 && \text{in } \Omega_l, \\ \sigma_{xz} n_x + \sigma_{yz} n_y &= 0 && \text{on } \partial\Omega_l, \\ (\sigma_{xz,x} n_x + \sigma_{xz,y} n_y) t_x + (\sigma_{yz,x} n_x + \sigma_{yz,y} n_y) t_y &= 0 && \text{on } \partial\Omega_l, \\ \int_{\Omega_l} (x \sigma_{yz} - y \sigma_{xz}) \, dA &= 0. \end{aligned}$$

We now show that the solutions \mathbf{v} of the eigenvalue problem in Eq. 5.13 form an orthogonal sequence. Let us assume that \mathbf{v}_i and \mathbf{v}_j are two distinct solutions with corresponding

²In our FEM code for solving this eigenvalue problem, we arrange \mathbf{v} , μ_z and $\boldsymbol{\varpi}$ in a column vector a to obtain a generalized eigenvalue problem $Aa = \lambda Ba$, for some square matrices A and B .

³Since the zero net twisting moment condition is a scalar equation (Eq. 5.11), the corresponding Lagrange multiplier is also a scalar. Since we have opted to write our equations in a coordinate free manner, it is a vector pointing in the z -direction.

Lagrange multipliers $(\mu_{zi}, \boldsymbol{\varpi}_i, \lambda_i)$ and $(\mu_{zj}, \boldsymbol{\varpi}_j, \lambda_j)$, respectively. Then,

$$\begin{aligned} -\Delta \mathbf{v}_i + \nabla \mu_{zi} - \boldsymbol{\varpi}_i \times \mathbf{r} &= \lambda_i \mathbf{v}_i, \\ -\Delta \mathbf{v}_j + \nabla \mu_{zj} - \boldsymbol{\varpi}_j \times \mathbf{r} &= \lambda_j \mathbf{v}_j. \end{aligned} \quad (5.14)$$

Consider the inner product of the first of Eqs. 5.14 with \mathbf{v}_j , i.e.,

$$\int_{\Omega_l} (-\Delta \mathbf{v}_i + \nabla \mu_{zi} - \boldsymbol{\varpi}_i \times \mathbf{r}) \cdot \mathbf{v}_j dA = \lambda_i \int_{\Omega_l} \mathbf{v}_i \cdot \mathbf{v}_j dA. \quad (5.15)$$

Upon integrating by parts and using the divergence theorem, the inner product of $-\Delta \mathbf{v}_i$ and \mathbf{v}_j can be simplified as follows:

$$-\int_{\Omega_l} \Delta \mathbf{v}_i \cdot \mathbf{v}_j dA = -\int_{\partial \Omega_l} (\nabla \mathbf{v}_i \mathbf{n}) \cdot \mathbf{v}_j ds + \int_{\Omega_l} \nabla \mathbf{v}_i \cdot \nabla \mathbf{v}_j dA = \int_{\Omega_l} \nabla \mathbf{v}_i \cdot \nabla \mathbf{v}_j dA,$$

where the boundary term drops out because $\nabla \mathbf{v}_i \mathbf{n} = \mathbf{0}$ on $\partial \Omega_l$ from Eq. 5.13.

Similarly, the inner product of $\nabla \mu_{zi}$ and \mathbf{v}_j is zero since

$$\int_{\Omega_l} \nabla \mu_{zi} \cdot \mathbf{v}_j dA = \int_{\partial \Omega_l} \mu_{zi} \mathbf{v}_j \cdot \mathbf{n} ds - \int_{\Omega_l} \mu_{zi} \operatorname{div} \mathbf{v}_j dA = 0,$$

where we have used $\mathbf{v}_j \cdot \mathbf{n} = 0$ on $\partial \Omega_l$ and $\operatorname{div} \mathbf{v}_j = 0$ in Ω_l .

Finally, rearranging the scalar triple product, we obtain that the inner product of $\boldsymbol{\varpi}_i \times \mathbf{r}$ and \mathbf{v}_j is zero since

$$\int_{\Omega_l} \mathbf{v}_j \cdot (\boldsymbol{\varpi}_i \times \mathbf{r}) dA = \int_{\Omega_l} \boldsymbol{\varpi}_i \cdot (\mathbf{r} \times \mathbf{v}_j) dA = \boldsymbol{\varpi}_i \cdot \int_{\Omega_l} \mathbf{r} \times \mathbf{v}_j dA = 0.$$

So, Eq. 5.15 simplifies to:

$$\int_{\Omega_l} \nabla \mathbf{v}_i \cdot \nabla \mathbf{v}_j dA = \lambda_i \int_{\Omega_l} \mathbf{v}_i \cdot \mathbf{v}_j dA.$$

Similarly,

$$\int_{\Omega_l} \nabla \mathbf{v}_j \cdot \nabla \mathbf{v}_i dA = \lambda_j \int_{\Omega_l} \mathbf{v}_j \cdot \mathbf{v}_i dA.$$

If $\lambda_i \neq \lambda_j$, then

$$\int_{\Omega_l} \mathbf{v}_i \cdot \mathbf{v}_j dA = \int_{\Omega_l} \nabla \mathbf{v}_i \cdot \nabla \mathbf{v}_j dA = 0. \quad (5.16)$$

If $\lambda_i = \lambda_j$ while \mathbf{v}_i and \mathbf{v}_j are linearly independent, then we can choose \mathbf{v}_i and \mathbf{v}_j to be orthogonal, and the above equation still holds.

Thus, the eigenfunctions are mutually orthogonal, or can be chosen to be so.

We show the first three eigenfunctions in Figure 5.9 on an annulus of inner radius 0.1 and outer radius 0.3. For better visual representation, we show the stress components σ_{rz} and $\sigma_{\theta z}$ instead of σ_{xz} and σ_{yz} .

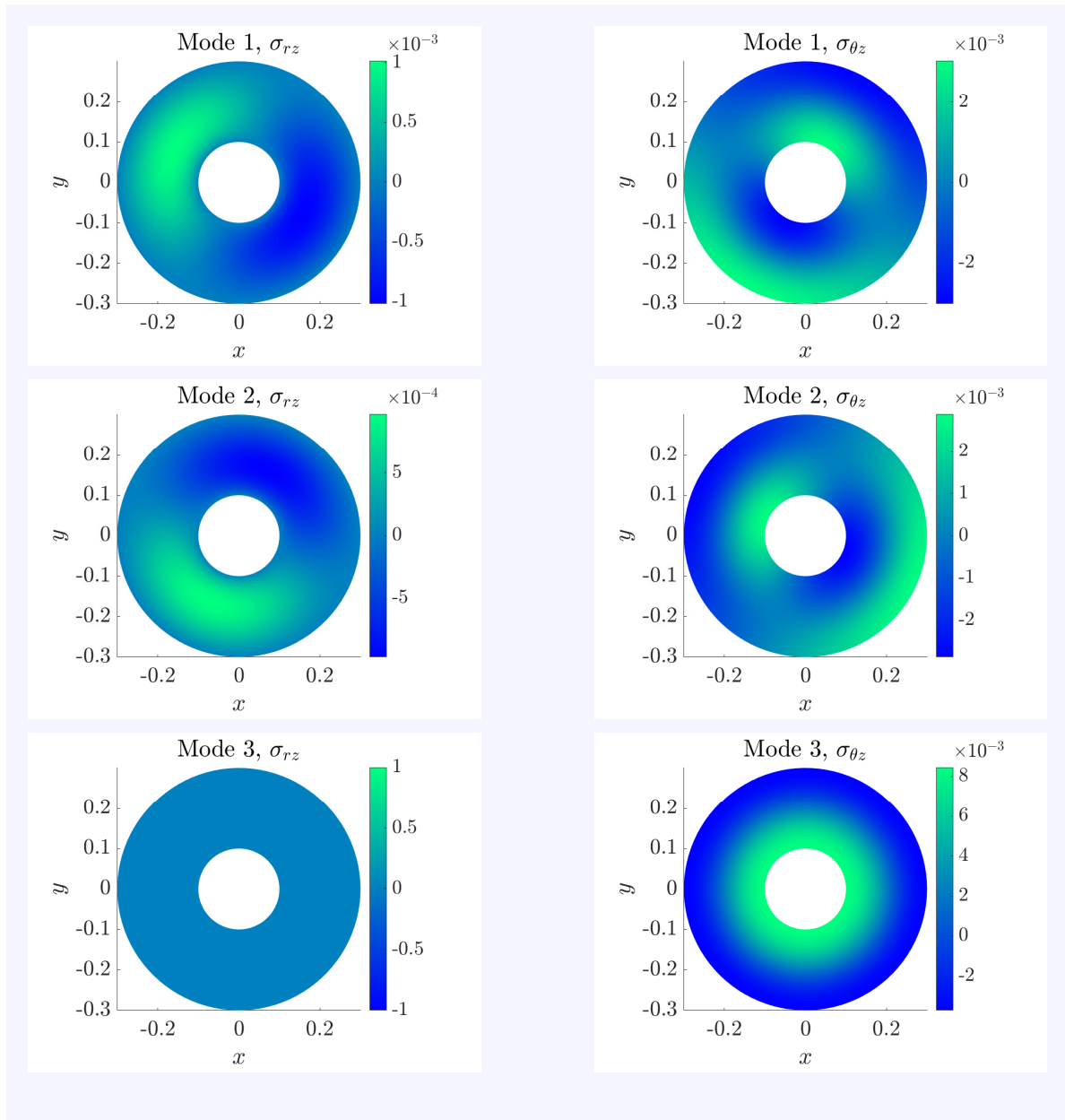


FIGURE 5.9: First three eigenfunctions for out of plane shear components computed using our own FEM code on an annular domain, with eigenvalues $\lambda = 293.41, 293.41$ and 356.19 , respectively.

We see that the eigenvalue problem in Eq. 5.13 is similar to our original eigenvalue problem of Chapter 2. Consequently, we believe that it can be formally proved that the eigenfunctions span the set \mathcal{S}_3 along similar lines to the proof presented in Chapter 2. We refer the interested reader to Section 7.4 where we discuss the points where such a formal proof, if attempted, may differ from the one presented in Chapter 2. However, a detailed proof is not attempted here.

We now demonstrate that the eigenfunctions \mathbf{v}_i lead to quick convergence when used to fit a candidate out of plane shear stress field in a prismatic geometry. Let the cross-section of the prismatic domain be the unit square $0 \leq x, y \leq 1$, and the given stress field be

$$\begin{aligned}\sigma_{xz} &= x(x-1)(2x-1)(1-2y), \\ \sigma_{yz} &= y(y-1)(6x^2-6x+1).\end{aligned}$$

It can be verified that the above stress field satisfies the divergence-free condition (third of Eqs. 5.1), traction-free boundary condition (third of Eqs. 5.2), zero mean condition (first and second of Eqs. 5.3) and zero net twisting moment condition (third of Eqs. 5.4). We fit this stress with \mathbf{v}_i . For comparison, we also fit it using another standard basis for divergence-free vector fields: the eigenfunctions with zero boundary value (i.e., with *both* the normal and the tangential components zero at the boundary) of the Stokes operator [43] (let us denote them as \mathbf{v}_i). Since \mathbf{v}_i are divergence-free and have zero flux at the boundary (i.e., $\mathbf{v}_i \cdot \mathbf{n} = 0$), it follows from Eq. 5.5 that they satisfy the zero mean condition (first and second of Eqs. 5.3), like \mathbf{v}_i . However, they do not satisfy the zero net twisting moment condition.

The actual fields σ_{xz} and σ_{yz} , along with fits obtained using the first 200 functions of each of these bases, are plotted in Figure 5.10. The corresponding fitting errors E_N are plotted in Figures 5.11 and 5.12. It is clear from the figures that while convergence is obtained with both the bases, it is much faster with \mathbf{v}_i . The reason is that both the normal and the tangential components of the eigenfunctions of the Stokes operator are zero at the boundary, while \mathbf{v}_i satisfy only the zero flux boundary condition satisfied by the candidate field. Moreover, the former do not satisfy the zero net twisting moment condition, while each \mathbf{v}_i does satisfy it.

In general, a state of stress with only the out of plane shear stress components σ_{xz} and σ_{yz} non-zero is difficult to achieve in long prismatic bodies. For instance, when the material is linear elastic and deformations are infinitesimal, 8 elastic constants (out of 21) in the fourth-order elasticity tensor \mathbf{C} have to be zero if such a stress state is to be possible [65].

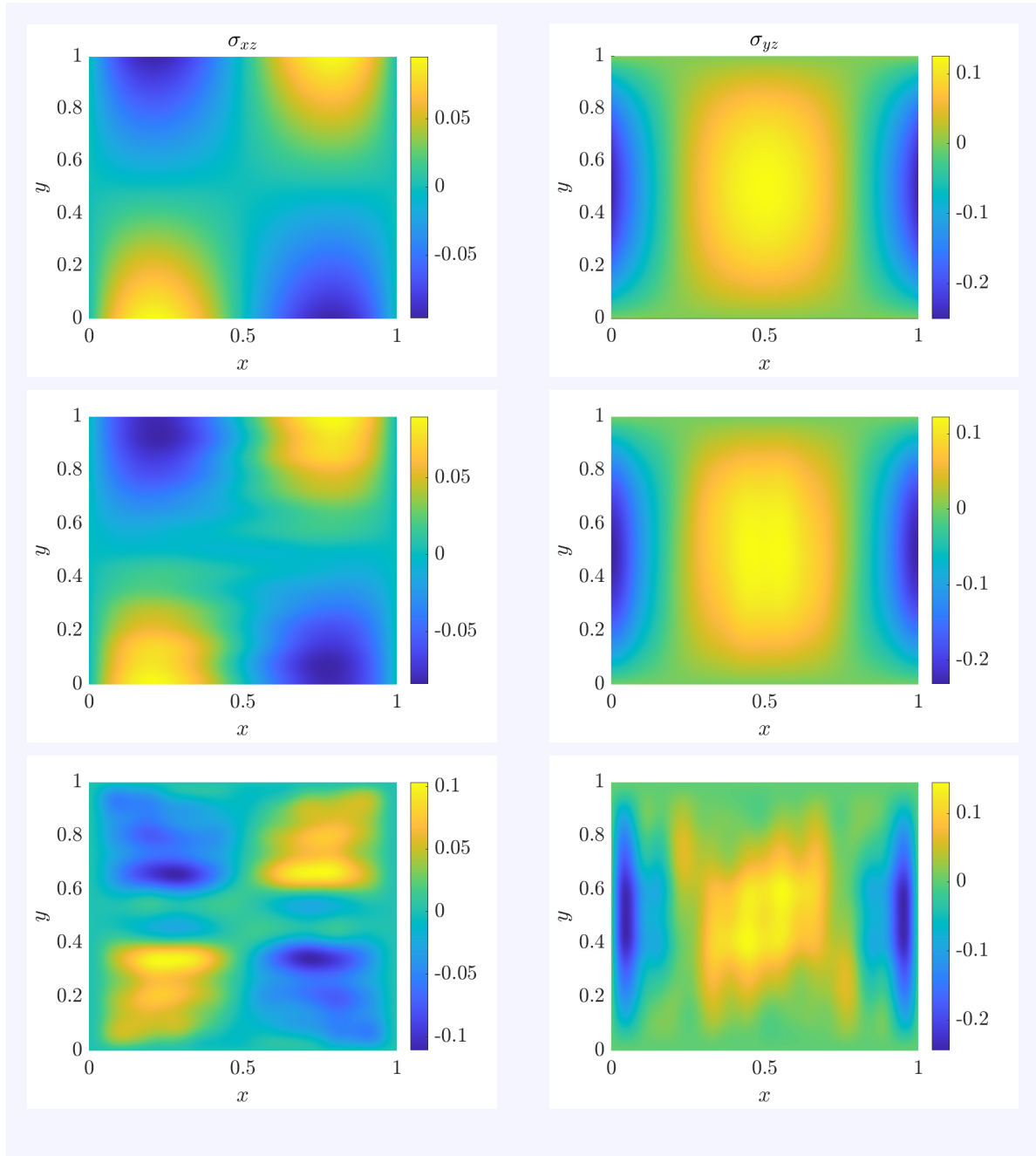
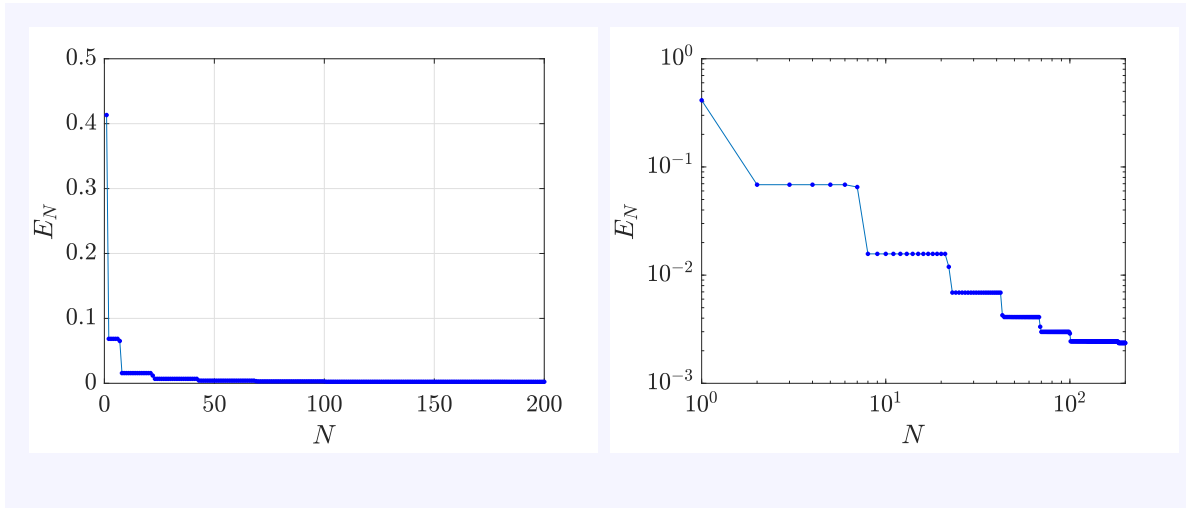
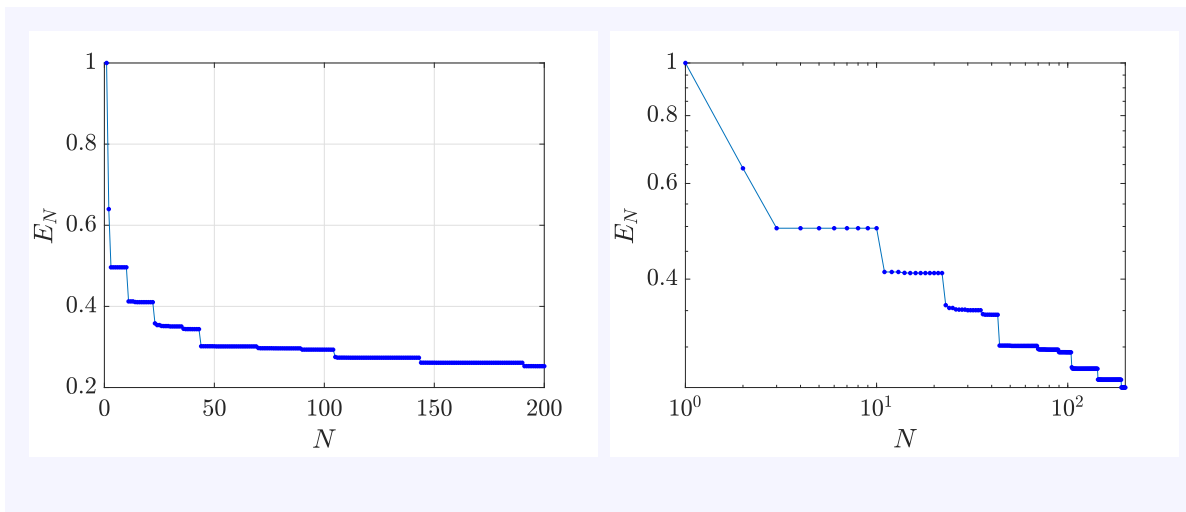


FIGURE 5.10: A candidate out of plane shear stress field (top row), and fits obtained with the first 200 basis functions \mathbf{v}_i (middle row) and the first 200 Stokes operator eigenfunctions \mathbf{v}_i (bottom row).

Similarly, it seems difficult to think of a practical loading history that will leave a prismatic body with a residual stress state dominated by the out of plane shear stress components. Thus, although our basis computation problem splits into three sub-problems for such bodies, it seems likely that actual residual stress states encountered may involve basis

FIGURE 5.11: E_N versus N with our basis \mathbf{v}_i . Left: linear scale; right: log-log scale.FIGURE 5.12: E_N versus N with the Stokes operator eigenfunctions \mathbf{v}_i . Left: linear scale; right: log-log scale.

elements from all three sub-problems.

With this, we conclude our presentation of how the extremization problem of Chapter 2 can be modified for long prismatic geometries, and move on to another practically important problem.

5.2 Basis functions for localized 2D residual stress fields

Sometimes, residual stresses are localized in a small region, e.g., around a crack tip or near the surface after shot peening. Far from these regions, the residual stresses decay rapidly and have little practical significance. The residual stress basis we developed in Chapter 2 may not be effective in such cases. Here we seek a basis that whose elements are spatially localized. To this end, we modify the extremization problem of Chapter 2 by multiplying the objective function and the normalizing constraint by suitable weighting functions. We will see that the localized basis fares better in capturing localized residual stresses in comparison with the original (unweighted) basis of Chapter 2.

5.2.1 Demonstration of the concept in 1D

To explain the basic idea, we first solve a simpler problem of developing a spatially localized basis in 1D. The insights gained from the 1D problem will be directly transferable to 2D.

Let us consider the following extremization problem. For given everywhere positive smooth functions w_1 and w_2 , we seek the stationary points of

$$J_0 = \int_{x=0}^1 w_1 y'^2 dx,$$

over scalar functions y satisfying the boundary conditions

$$y'(0) = 0 \text{ and } y(1) = 0,$$

and the normalization constraint

$$\int_{x=0}^1 w_2 y^2 dx = 1. \tag{5.17}$$

Incorporating the normalization constraint through the Lagrange multiplier λ , we seek variations of

$$J = \int_{x=0}^1 \{w_1 y'^2 - \lambda (w_2 y^2 - 1)\} dx.$$

If y_0 is a stationary point (an extremizing function), then it satisfies the boundary value problem

$$(w_1 y_0')' + \lambda w_2 y_0 = 0, \quad y_0'(0) = 0 \text{ and } y_0(1) = 0. \tag{5.18}$$

This is a Sturm-Liouville eigenvalue problem, and the corresponding eigenfunctions form a basis for functions in $0 \leq x \leq 1$ with the same boundary conditions as above [66].

We want y_0 to decay as x goes from 0 to 1, and hence w_2 should be an increasing function. Also, we want to arrest the oscillations of y_0 as x increases, and hence w_1 should also be an increasing function. We choose $w_1(x) = w_2(x) = e^{nx}$. Then, Eq. 5.18 becomes

$$y_0'' + ny_0' + \lambda y_0 = 0, \quad y_0'(0) = 0 \quad \text{and} \quad y_0(1) = 0.$$

Substituting $y_0 = Ce^{sx}$, we obtain

$$s^2 + ns + \lambda = 0,$$

whose solutions are

$$s = \frac{-n \pm \sqrt{n^2 - 4\lambda}}{2}.$$

To have oscillatory solutions, $n^2 < 4\lambda$. The general form of y_0 then is

$$y_0 = e^{\frac{-nx}{2}} \left(C_1 e^{\frac{i\sqrt{4\lambda - n^2}}{2}x} + C_2 e^{-\frac{i\sqrt{4\lambda - n^2}}{2}x} \right).$$

This can equivalently be written as

$$y_0 = e^{\frac{-nx}{2}} \left(A \sin \sqrt{\lambda - \frac{n^2}{4}} x + B \cos \sqrt{\lambda - \frac{n^2}{4}} x \right),$$

where A and B are arbitrary constants. The condition $y_0'(0) = 0$ gives

$$A = \frac{n}{2\sqrt{\lambda - \frac{n^2}{4}}} B,$$

so that

$$y_0 = B e^{\frac{-nx}{2}} \left(\frac{n}{2\sqrt{\lambda - \frac{n^2}{4}}} \sin \sqrt{\lambda - \frac{n^2}{4}} x + \cos \sqrt{\lambda - \frac{n^2}{4}} x \right). \quad (5.19)$$

The other boundary condition implies that

$$\frac{n}{2\sqrt{\lambda - \frac{n^2}{4}}} \sin \sqrt{\lambda - \frac{n^2}{4}} + \cos \sqrt{\lambda - \frac{n^2}{4}} = 0.$$

We solve for the eigenvalue λ from the above equation using a Newton-Raphson scheme (for a fixed n). The solutions are then substituted in Eq. 5.19 to obtain the corresponding

eigenfunctions. Finally, since the eigenfunctions are arbitrary up to a scalar multiplicative factor, we scale them so that they have the value 1 at $x = 0$ (in place of the normalization of Eq. 5.17). We plot the first five localized eigenfunctions for $n = 10$ and $n = 20$ in Figure 5.13. It is seen that the eigenfunctions decay as we move towards $x = 1$; the decay is larger for greater n .

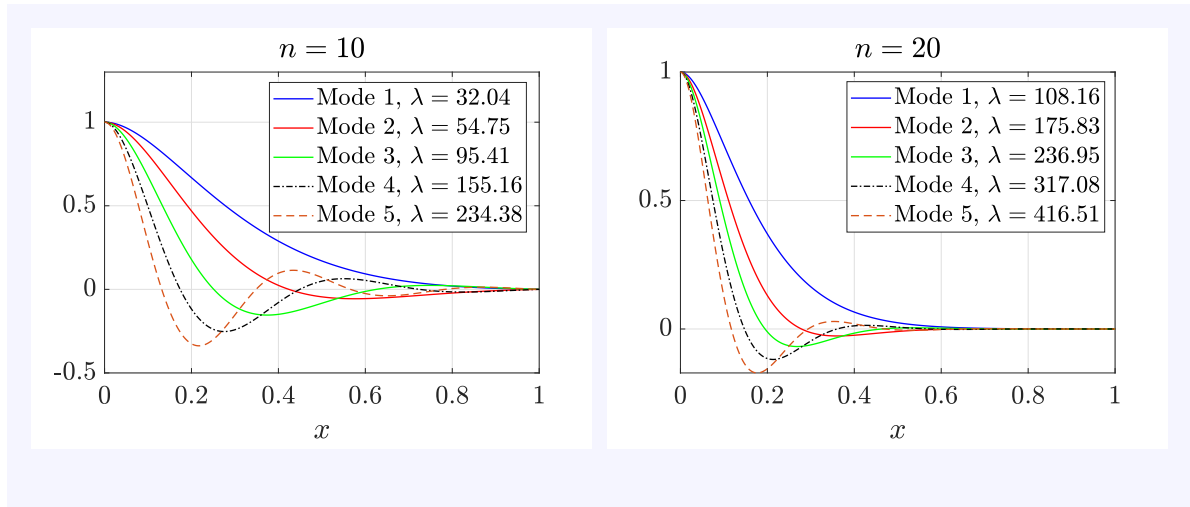


FIGURE 5.13: First five localized 1D eigenfunctions for $n = 10$ and $n = 20$.

5.2.2 Spatially localized basis functions in 2D

Taking a cue from the 1D example, we modify our extremization problem of Chapter 2 by appropriately weighting the objective function and the normalization constraint to obtain spatially localized basis functions in 2D.

5.2.2.1 Extremization problem

Recall the set \mathcal{S} of residual stress fields defined in Chapter 2:

$$\mathcal{S} = \left\{ \boldsymbol{\sigma} \mid \boldsymbol{\sigma} \in \text{Sym}, \operatorname{div} \boldsymbol{\sigma} = \mathbf{0}, \boldsymbol{\sigma} \mathbf{n}|_{\partial\Omega} = \mathbf{0}, \int_{\Omega} \boldsymbol{\sigma} \cdot \boldsymbol{\sigma} \, dA < \infty, \int_{\Omega} \nabla \boldsymbol{\sigma} \cdot \nabla \boldsymbol{\sigma} \, dA < \infty \right\}.$$

This time, we seek stationary points of the functional

$$J_0(\boldsymbol{\sigma}) = \frac{1}{2} \int_{\Omega} w_1 \nabla \boldsymbol{\sigma} \cdot \nabla \boldsymbol{\sigma} \, dA$$

in \mathcal{S} , subject to the normalization constraint

$$\int_{\Omega} w_2 \boldsymbol{\sigma} \cdot \boldsymbol{\sigma} dA = 1. \quad (5.20)$$

We assume the following about w_1, w_2 :

1. They are smooth.
2. They are positive everywhere in Ω .

We note that $J_0(\boldsymbol{\sigma})$ is finite for all $\boldsymbol{\sigma} \in \mathcal{S}$, since

$$J_0(\boldsymbol{\sigma}) = \frac{1}{2} \int_{\Omega} w_1 \nabla \boldsymbol{\sigma} \cdot \nabla \boldsymbol{\sigma} dA \leq \frac{\|w_1\|_{\infty}}{2} \int_{\Omega} \nabla \boldsymbol{\sigma} \cdot \nabla \boldsymbol{\sigma} dA,$$

where $\|w_1\|_{\infty}$ is the supremum of w_1 on Ω ⁴. Since w_1 is smooth, $\|w_1\|_{\infty}$ is finite.

Upon introducing Lagrange multipliers $\frac{\lambda}{2}$ and $\boldsymbol{\mu}$, we consider variations of

$$J(\hat{\boldsymbol{\sigma}}) = \int_{\Omega} \left\{ \frac{1}{2} w_1 \nabla \hat{\boldsymbol{\sigma}} \cdot \nabla \hat{\boldsymbol{\sigma}} - \frac{\lambda}{2} \left(w_2 \hat{\boldsymbol{\sigma}} \cdot \hat{\boldsymbol{\sigma}} - \frac{1}{|\Omega|} \right) - \boldsymbol{\mu} \cdot (\operatorname{div} \hat{\boldsymbol{\sigma}}) \right\} dA,$$

in the set

$$\mathcal{R} = \left\{ \hat{\boldsymbol{\sigma}} \mid \hat{\boldsymbol{\sigma}} \in \operatorname{Sym}, \hat{\boldsymbol{\sigma}} \mathbf{n}|_{\partial\Omega} = \mathbf{0}, \int_{\Omega} \hat{\boldsymbol{\sigma}} \cdot \hat{\boldsymbol{\sigma}} dA < \infty, \int_{\Omega} \nabla \hat{\boldsymbol{\sigma}} \cdot \nabla \hat{\boldsymbol{\sigma}} dA < \infty \right\}.$$

If $\boldsymbol{\sigma}$ is a stationary point of J , then for arbitrary infinitesimal variations $\boldsymbol{\zeta} \in \mathcal{R}$, after ignoring the second order terms in $\boldsymbol{\zeta}$ and simplifying, we obtain

$$\int_{\Omega} (w_1 \nabla \boldsymbol{\sigma} \cdot \nabla \boldsymbol{\zeta} - \lambda w_2 \boldsymbol{\sigma} \cdot \boldsymbol{\zeta} - \boldsymbol{\mu} \cdot \operatorname{div} \boldsymbol{\zeta}) dA = 0.$$

The gradient of $\boldsymbol{\zeta}$ in the above can be eliminated as follows. Using the divergence theorem, we have

$$\int_{\Omega} w_1 \nabla \boldsymbol{\sigma} \cdot \nabla \boldsymbol{\zeta} dA = \int_{\partial\Omega} w_1 \nabla_n \boldsymbol{\sigma} \cdot \boldsymbol{\zeta} ds - \int_{\Omega} (\nabla \boldsymbol{\sigma} \odot \nabla w_1 + w_1 \Delta \boldsymbol{\sigma}) \cdot \boldsymbol{\zeta} dA, \quad (5.21)$$

where the operation $\mathbf{A} \odot \mathbf{v}$ for a third order tensor \mathbf{A} and a vector \mathbf{v} is defined as

$$\mathbf{A} \odot \mathbf{v} = A_{ijk} v_k \mathbf{e}_i \otimes \mathbf{e}_j.$$

⁴That is, the least upper bound of the set $\mathcal{W} = \{w_1(\mathbf{x}) \mid \mathbf{x} \in \Omega\}$.

Proceeding in the usual manner, we find that a stationary point, assuming one exists, satisfies the following eigenvalue problem:

$$\begin{aligned} -w_1 \Delta \boldsymbol{\sigma} - \nabla \boldsymbol{\sigma} \odot \nabla w_1 + \nabla_s \boldsymbol{\mu} &= \lambda w_2 \boldsymbol{\sigma} & \text{and} & \quad \operatorname{div} \boldsymbol{\sigma} = \mathbf{0} & \text{in } \Omega, \\ \nabla_n \boldsymbol{\sigma} \cdot (\mathbf{t} \otimes \mathbf{t}) &= 0 & \text{and} & \quad \boldsymbol{\sigma} \mathbf{n} = \mathbf{0} & \text{on } \partial\Omega, \end{aligned} \quad (5.22)$$

along with Eq. 5.20. Note that upon substituting $w_1 = w_2 = 1$ in the above, we recover our original eigenvalue problem of Chapter 2 (Eq. 2.12).

We now show that the solutions of the above problem (eigenfunctions) are orthogonal to each other in a weighted inner product that we define below.

5.2.2.2 Orthogonality of the eigenfunctions

We equip \mathcal{S} with the inner product

$$(\boldsymbol{\sigma}_1, \boldsymbol{\sigma}_2)_w = \int_{\Omega} w_2 \boldsymbol{\sigma}_1 \cdot \boldsymbol{\sigma}_2 \, dA, \quad (5.23)$$

for any $\boldsymbol{\sigma}_1, \boldsymbol{\sigma}_2 \in \mathcal{S}$. Then, the norm of any element $\boldsymbol{\sigma} \in \mathcal{S}$ is

$$\|\boldsymbol{\sigma}\|_w = \sqrt{(\boldsymbol{\sigma}, \boldsymbol{\sigma})_w} = \left(\int_{\Omega} w_2 \boldsymbol{\sigma} \cdot \boldsymbol{\sigma} \, dA \right)^{\frac{1}{2}}. \quad (5.24)$$

We show in Appendix G that the operations $(\cdot, \cdot)_w$ and $\|\cdot\|_w$ meet the criteria of being an inner product and a norm, respectively.

Let $\boldsymbol{\sigma} = \boldsymbol{\varphi}$ and $\boldsymbol{\mu}$ constitute a solution to the eigenvalue problem of Eq. 5.22, with corresponding eigenvalue λ . Let $\hat{\boldsymbol{\sigma}}$ be any element of \mathcal{S} . Consider the inner product of the first of Eqs. 5.22 with $\hat{\boldsymbol{\sigma}}$, i.e.,

$$\int_{\Omega} (-w_1 \Delta \boldsymbol{\varphi} - \nabla \boldsymbol{\varphi} \odot \nabla w_1 + \nabla_s \boldsymbol{\mu}) \cdot \hat{\boldsymbol{\sigma}} \, dA = \lambda \int_{\Omega} w_2 \boldsymbol{\varphi} \cdot \hat{\boldsymbol{\sigma}} \, dA. \quad (5.25)$$

By the reasoning given in Appendix C,

$$\int_{\Omega} \nabla_s \boldsymbol{\mu} \cdot \hat{\boldsymbol{\sigma}} \, dA = 0. \quad (5.26)$$

What remains on the left hand side can be simplified using the divergence theorem (e.g., see Eq. 5.21) and the natural boundary condition (fourth of Eqs. 5.22) to

$$\int_{\Omega} (-w_1 \Delta \varphi - \nabla \varphi \odot \nabla w_1) \cdot \hat{\sigma} \, dA = \int_{\Omega} w_1 \nabla \varphi \cdot \nabla \hat{\sigma} \, dA. \quad (5.27)$$

Substituting Eqs. 5.26 and 5.27 in Eq. 5.25, we obtain

$$\int_{\Omega} w_1 \nabla \varphi \cdot \nabla \hat{\sigma} \, dA = \lambda \int_{\Omega} w_2 \varphi \cdot \hat{\sigma} \, dA. \quad (5.28)$$

Consider now two eigenvalue-eigenfunctions pairs: $(\lambda_i, \varphi_i, \mu_i)$ and $(\lambda_j, \varphi_j, \mu_j)$, such that $\lambda_i \neq \lambda_j$. Then, from Eq. 5.28,

$$\int_{\Omega} w_1 \nabla \varphi_i \cdot \nabla \varphi_j \, dA = \lambda_i \int_{\Omega} w_2 \varphi_i \cdot \varphi_j \, dA,$$

$$\int_{\Omega} w_1 \nabla \varphi_j \cdot \nabla \varphi_i \, dA = \lambda_j \int_{\Omega} w_2 \varphi_j \cdot \varphi_i \, dA,$$

and we conclude that

$$\int_{\Omega} w_1 \nabla \varphi_i \cdot \nabla \varphi_j \, dA = \int_{\Omega} w_2 \varphi_i \cdot \varphi_j \, dA = (\varphi_i, \varphi_j)_w = 0. \quad (5.29)$$

So, φ_i and φ_j are orthogonal. If $\lambda_i = \lambda_j$ for linearly independent φ_i and φ_j , we can still choose the corresponding eigenfunctions to be orthogonal, and Eq. 5.29 still holds.

Thus the eigenfunctions φ form an orthogonal sequence. We normalize them so that

$$\int_{\Omega} w_2 \varphi_p \cdot \varphi_p \, dA = 1, \quad p = 1, 2, 3, \dots$$

We do not formally prove here that φ span the set \mathcal{S} (and its closure). However, we anticipate that a proof could be constructed along similar lines to that in Chapter 2. We refer the reader to Section 7.5 where we indicate that if such a proof is attempted, the presence of the weighting functions w_1 and w_2 , on account of our assumption that they are smooth and everywhere positive, should offer no difficulties.

5.2.2.3 Computation of eigenfunctions using the FEM

Since the eigenvalue problem in Eq. 5.22 differs from that of Chapter 2 only in the presence of the weighting functions and the term $\nabla \sigma \odot \nabla w_1$ (in the first of Eqs. 5.22), the

corresponding FEM formulation is similar to that presented in Section 3.1. In this section, we demonstrate that in the weak formulation, this additional term drops out, and our FEM formulation remains largely unaffected.

To solve the eigenvalue problem in Eq. 5.22 using the FEM, we first express it in Cartesian coordinates, so that

$$-w_1 \Delta \boldsymbol{\sigma} - \nabla \boldsymbol{\sigma} \odot \nabla w_1 + \nabla_s \boldsymbol{\mu} = \lambda w_2 \boldsymbol{\sigma}$$

becomes

$$\begin{aligned} -w_1 \left(\frac{\partial^2 \sigma_{xx}}{\partial x^2} + \frac{\partial^2 \sigma_{xx}}{\partial y^2} \right) - \frac{\partial \sigma_{xx}}{\partial x} \frac{\partial w_1}{\partial x} - \frac{\partial \sigma_{xx}}{\partial y} \frac{\partial w_1}{\partial y} + \frac{\partial \mu_x}{\partial x} &= \lambda w_2 \sigma_{xx}, \\ -w_1 \left(\frac{\partial^2 \sigma_{yy}}{\partial x^2} + \frac{\partial^2 \sigma_{yy}}{\partial y^2} \right) - \frac{\partial \sigma_{yy}}{\partial x} \frac{\partial w_1}{\partial x} - \frac{\partial \sigma_{yy}}{\partial y} \frac{\partial w_1}{\partial y} + \frac{\partial \mu_y}{\partial y} &= \lambda w_2 \sigma_{yy}, \\ -w_1 \left(\frac{\partial^2 \sigma_{xy}}{\partial x^2} + \frac{\partial^2 \sigma_{xy}}{\partial y^2} \right) - \frac{\partial \sigma_{xy}}{\partial x} \frac{\partial w_1}{\partial x} - \frac{\partial \sigma_{xy}}{\partial y} \frac{\partial w_1}{\partial y} + \frac{1}{2} \left(\frac{\partial \mu_x}{\partial y} + \frac{\partial \mu_y}{\partial x} \right) &= \lambda w_2 \sigma_{xy}. \end{aligned} \quad (5.30)$$

Consider the inner product of the first of the above equations with a shape function N_p , i.e.,

$$\int_{\Omega} \left\{ -w_1 \left(\frac{\partial^2 \sigma_{xx}}{\partial x^2} + \frac{\partial^2 \sigma_{xx}}{\partial y^2} \right) - \frac{\partial \sigma_{xx}}{\partial x} \frac{\partial w_1}{\partial x} - \frac{\partial \sigma_{xx}}{\partial y} \frac{\partial w_1}{\partial y} + \frac{\partial \mu_x}{\partial x} - \lambda w_2 \sigma_{xx} \right\} N_p dA = 0. \quad (5.31)$$

We restrict attention to the inner product of the term $-w_1 \Delta \sigma_{xx}$ with N_p . Integrating by parts, we obtain

$$\begin{aligned} - \int_{\Omega} w_1 \left(\frac{\partial^2 \sigma_{xx}}{\partial x^2} + \frac{\partial^2 \sigma_{xx}}{\partial y^2} \right) N_p dA &= - \int_{\partial \Omega} \left(\frac{\partial \sigma_{xx}}{\partial x} n_x + \frac{\partial \sigma_{xx}}{\partial y} n_y \right) w_1 N_p dA \\ + \int_{\Omega} \left(w_1 \frac{\partial \sigma_{xx}}{\partial x} \frac{\partial N_p}{\partial x} + w_1 \frac{\partial \sigma_{xx}}{\partial y} \frac{\partial N_p}{\partial y} \right) dA &+ \int_{\Omega} \left(N_p \frac{\partial \sigma_{xx}}{\partial x} \frac{\partial w_1}{\partial x} + N_p \frac{\partial \sigma_{xx}}{\partial y} \frac{\partial w_1}{\partial y} \right) dA. \end{aligned}$$

Upon substituting the above in Eq. 5.31, we see that the latter simplifies to

$$\int_{\Omega} \left(-w_1 \frac{\partial^2 \sigma_{xx}}{\partial x^2} - w_1 \frac{\partial^2 \sigma_{xx}}{\partial y^2} + \frac{\partial \mu_x}{\partial x} \right) N_p dA = \lambda \int_{\Omega} w_2 \sigma_{xx} N_p dA.$$

We note that the above equation is the same as the corresponding equation (Eq. 3.7) in Section 3.1, if we set $w_1 = w_2 = 1$.

The weak formulations corresponding to the equations for the other stress components can be obtained in a similar fashion. The rest of the equations in the eigenvalue problem are the same as in Chapter 3, and we obtain their weak forms using the procedure detailed

therein. The other details such as the elements used for discretization of the domain, the shape functions used for the stress components and the Lagrange multiplier components, etc., also remain the same.

For demonstration, we choose an arbitrarily shaped domain centered approximately at the origin, with size comparable to that of a unit square. We wish the eigenfunctions to be localized around the origin, and thus, we choose

$$w_1 = w_2 = e^{20\sqrt{x^2+y^2}}.$$

We plot the first three eigenfunctions, scaled to unit-norm, in Figure 5.14. We see, with the aid of the accompanying colour bars, that all the stress components decay as we move away from the origin. The unweighted basis functions ϕ_i on this same geometry were plotted in Figure 3.6.

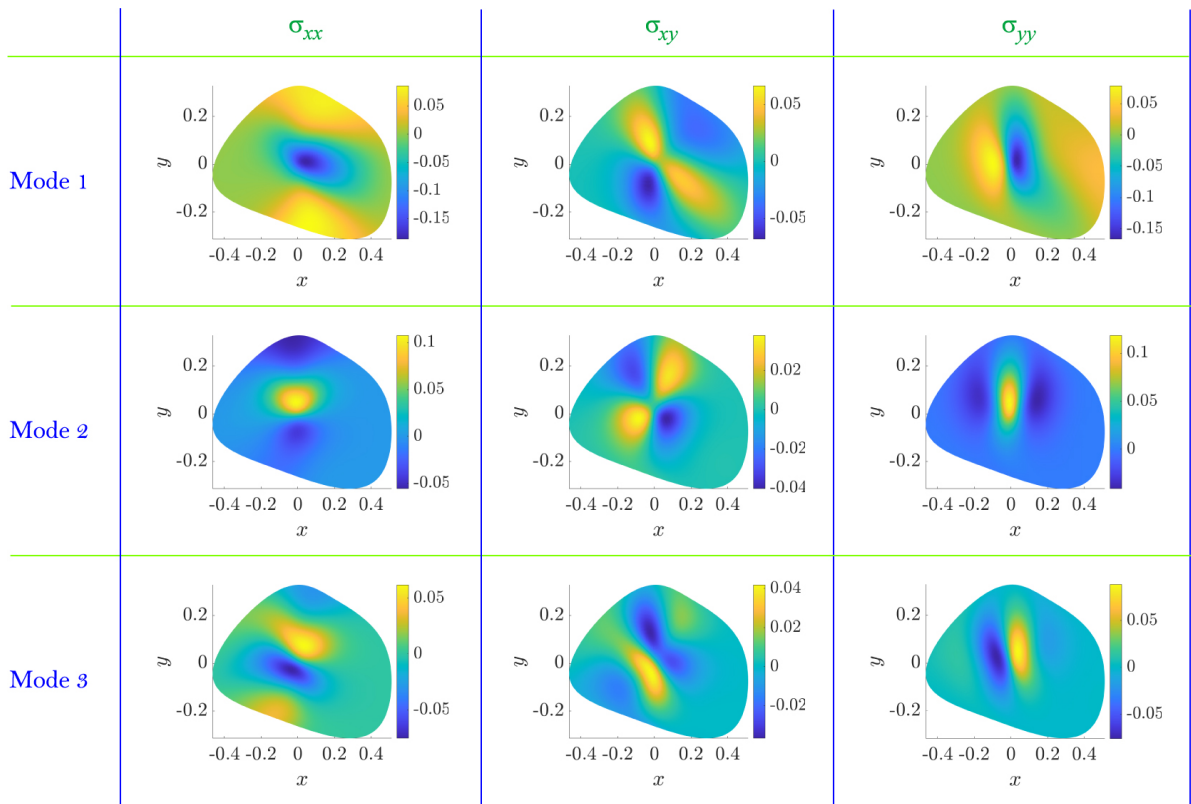


FIGURE 5.14: First three eigenfunctions on an arbitrarily shaped domain, localized around the origin.

In the next section, we compute these spatially localized residual stress basis functions on an annular domain.

5.2.2.4 Computation of eigenfunctions on an annulus

If the domain is annular, we can solve the eigenvalue problem in Eq. 5.22 as a two-point boundary value problem, upon choosing a wave number in the circumferential direction. We take the domain to be centered at the origin and having an inner radius r_a and an outer radius r_b . Taking cues from the 1D case, we choose

$$w_1(r, \theta) = w_2(r, \theta) = e^{\frac{n\theta}{L}},$$

where L is some typical dimension of the body considered.

Upon choosing $\boldsymbol{\sigma}$ and $\boldsymbol{\mu}$ of the form

$$\begin{aligned}\boldsymbol{\sigma} &= \sigma_{rr}(r) \cos m\theta \mathbf{e}_r \otimes \mathbf{e}_r + \sigma_{r\theta}(r) \sin m\theta (\mathbf{e}_r \otimes \mathbf{e}_\theta + \mathbf{e}_\theta \otimes \mathbf{e}_r) + \sigma_{\theta\theta}(r) \cos m\theta \mathbf{e}_\theta \otimes \mathbf{e}_\theta, \\ \boldsymbol{\mu} &= \mu_r(r) e^{\frac{n\theta}{L}} \cos m\theta \mathbf{e}_r + \mu_\theta(r) e^{\frac{n\theta}{L}} \sin m\theta \mathbf{e}_\theta,\end{aligned}$$

and introducing a new variable ϑ , the eigenvalue problem reduces to the following set of six first order ordinary differential equations:

$$\begin{aligned}\sigma'_{rr} &= -\frac{\sigma_{rr}}{r} - \frac{m\sigma_{r\theta}}{r} + \frac{\sigma_{\theta\theta}}{r}, \\ \sigma'_{r\theta} &= -\frac{2\sigma_{r\theta}}{r} + \frac{m\sigma_{\theta\theta}}{r}, \\ \sigma'_{\theta\theta} &= \vartheta, \\ \vartheta' &= \frac{m^2\sigma_{\theta\theta}}{r^2} - \frac{\vartheta}{r} - \frac{n\vartheta}{L} - \frac{4m\sigma_{r\theta}}{r^2} - \frac{2\sigma_{rr}}{r^2} + \frac{2\sigma_{\theta\theta}}{r^2} + \frac{\mu_r}{r} + \frac{m\mu_\theta}{r} - \lambda\sigma_{\theta\theta}, \\ \mu'_r &= -\frac{(m^2-1)\sigma_{\theta\theta}}{r^2} + \frac{n\sigma_{\theta\theta}}{rL} - \frac{m\sigma_{r\theta}}{r^2} - \frac{mn\sigma_{r\theta}}{rL} + \frac{\vartheta}{r} - \frac{(m^2+1)\sigma_{rr}}{r^2} - \frac{n\sigma_{rr}}{rL} - \frac{n\mu_r}{L} + \lambda\sigma_{rr}, \\ \mu'_\theta &= \frac{2m\vartheta}{r} - \frac{2m^2\sigma_{r\theta}}{r^2} - \frac{4n\sigma_{r\theta}}{rL} - \frac{4m\sigma_{rr}}{r^2} + \frac{2mn\sigma_{\theta\theta}}{rL} + \frac{m\mu_r}{r} + \frac{\mu_\theta}{r} - \frac{n\mu_\theta}{L} + 2\lambda\sigma_{r\theta},\end{aligned}\tag{5.32}$$

with boundary conditions

$$\sigma_{rr}(r_a) = \sigma_{r\theta}(r_a) = \sigma'_{\theta\theta}(r_a) = \sigma_{rr}(r_b) = \sigma_{r\theta}(r_b) = \sigma'_{\theta\theta}(r_b) = 0.$$

These equations resemble Eqs. 3.14, but are not identical. They are solved as described in Section 3.2.1 of Chapter 3. For demonstration, we choose $m = 3$, $r_a = 0.1$, $r_b = 0.3$ and $L = 0.2$. We show the stress components corresponding to the first four eigenfunctions in Figures 5.15 and 5.16, for $n = 10$ and $n = 20$, respectively.

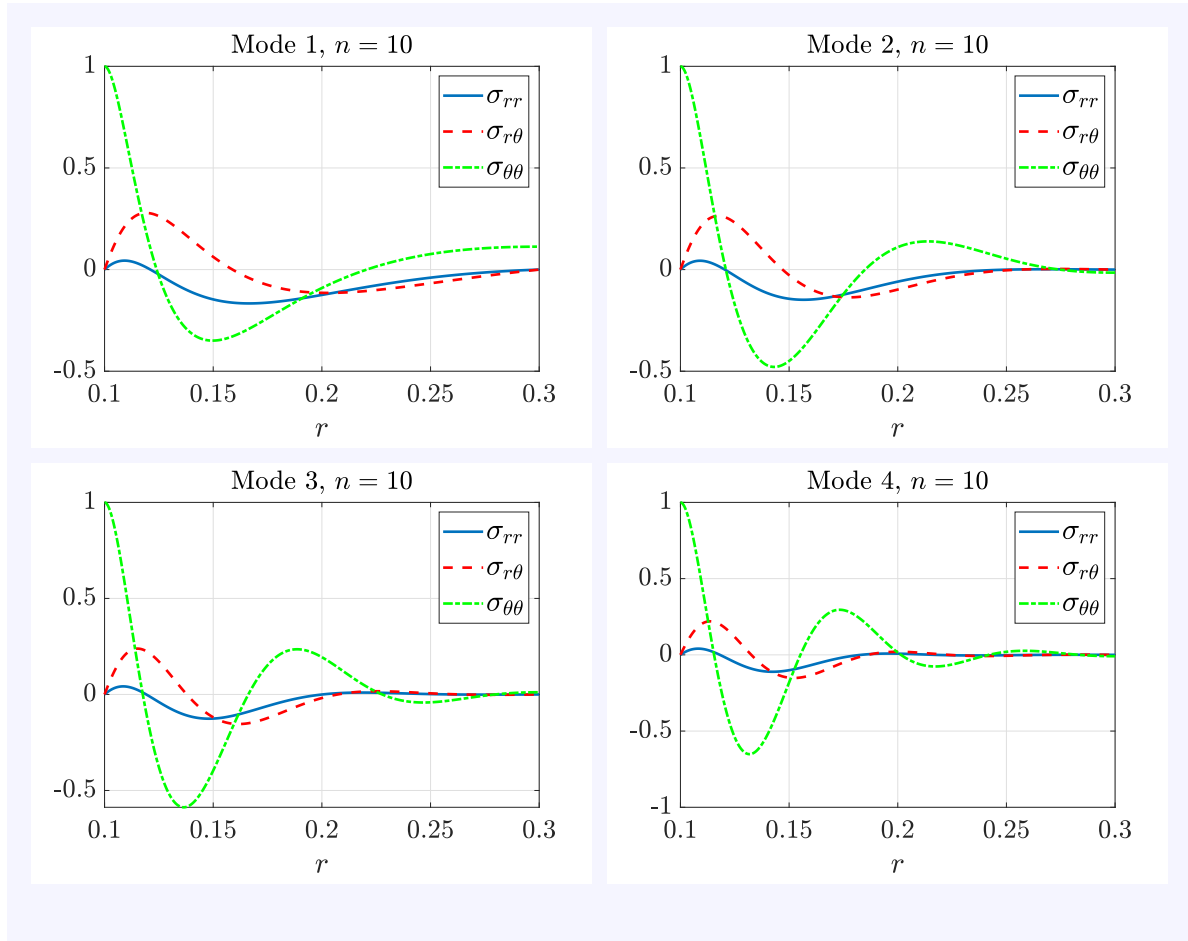


FIGURE 5.15: Radial variation of the first four spatially localized eigenfunctions on an annular geometry with $n = 10$.

5.2.2.5 Fitting a given spatially localized residual stress field

We now fit a candidate spatially localized residual stress with both the weighted eigenfunctions developed in this section, and the unweighted eigenfunctions of Chapter 2. We obtain a hypothetical localized residual stress field using the procedure employed in Section 4.1

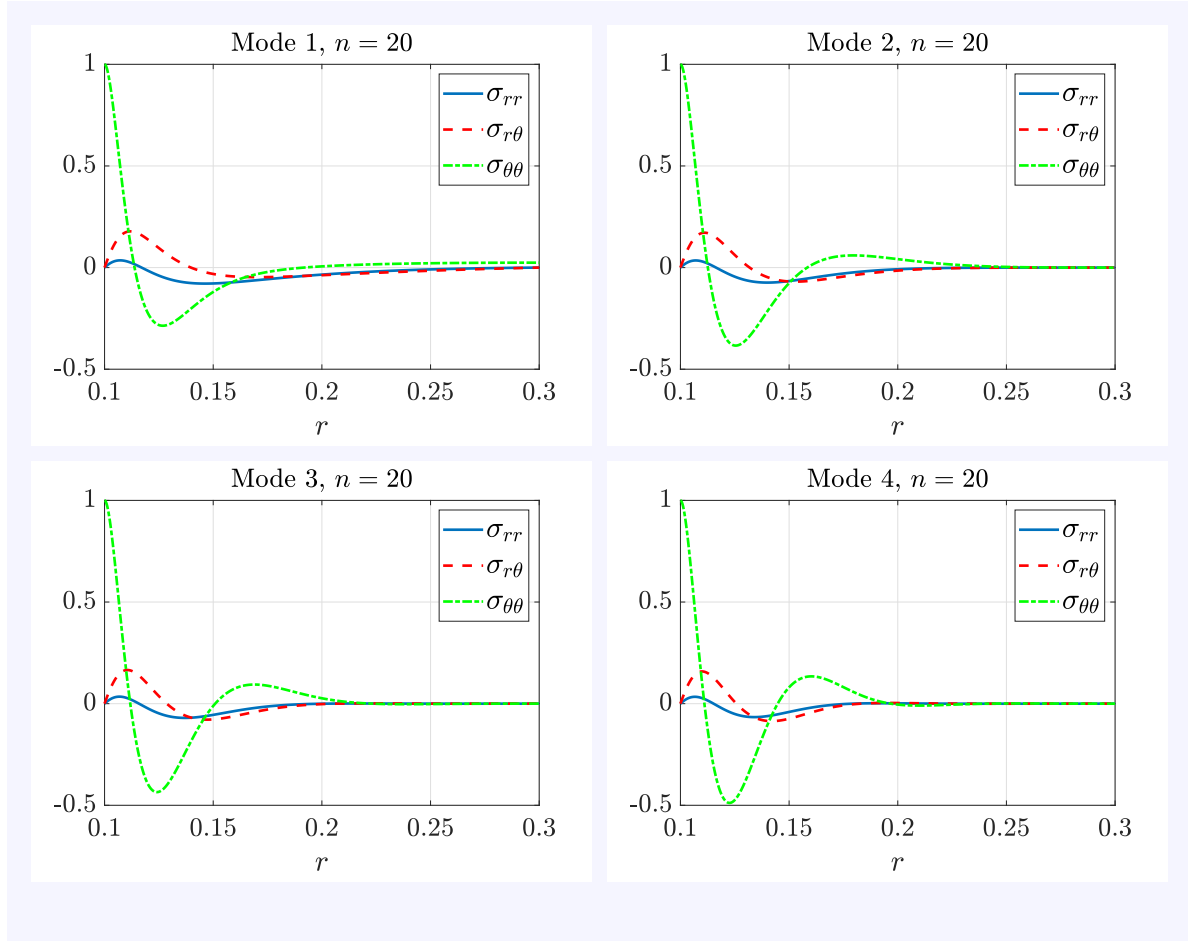


FIGURE 5.16: Radial variation of the first four spatially localized eigenfunctions on an annular geometry with $n = 20$.

(details omitted). Its components are as follows⁵:

$$\begin{aligned} \sigma_{rr} &= e^{-75r+7.5} \left(\frac{119986.4385 r^2 - 1125000 r^3 + 12749.71685 r + 1349.860391}{84375 r^2} \right) \\ &\quad - \frac{0.03386574357}{84375 r^2} - 0.000001131237818 r^{-1}, \\ \sigma_{\theta\theta} &= 1000 (r^2 - 0.2533212787 r + 0.01568753329) e^{-75r+7.5}, \\ \sigma_{r\theta} &= \frac{1}{r^2} \left(- \frac{(1125000 r^3 - 239986.4386 r^2 + 11248.83659 r + 149.9844878) e^{-75r+7.5}}{28125} \right) \\ &\quad + \frac{0.0000001337905919}{r^2}. \end{aligned}$$

⁵The background calculations were done using Maple. The expressions are reported as is, without further round-off or simplification, in the interest of avoiding new inadvertent deviations from the computed quantities.

These stress components, along with the fits obtained with both unweighted and weighted (with $n = 20$) functions are plotted in Figure 5.17. Ten eigenfunctions are used in each case for fitting. We see that the weighted basis functions give better fits. The relative square measure E_N described in Chapter 4 is plotted in Figure 5.18. We obtain a much faster convergence with the weighted functions for small N ; the behaviour for large N is the same with both sets of basis functions: E_N decays like N^{-3} . Note that while computing the fit with the weighted eigenfunctions and the corresponding fitting error, we have used the weighted inner product defined in Eq. 5.23. Therefore a direct comparison of the reported numbers, which seems to indicate superiority by a factor of about 100, would be misleading.

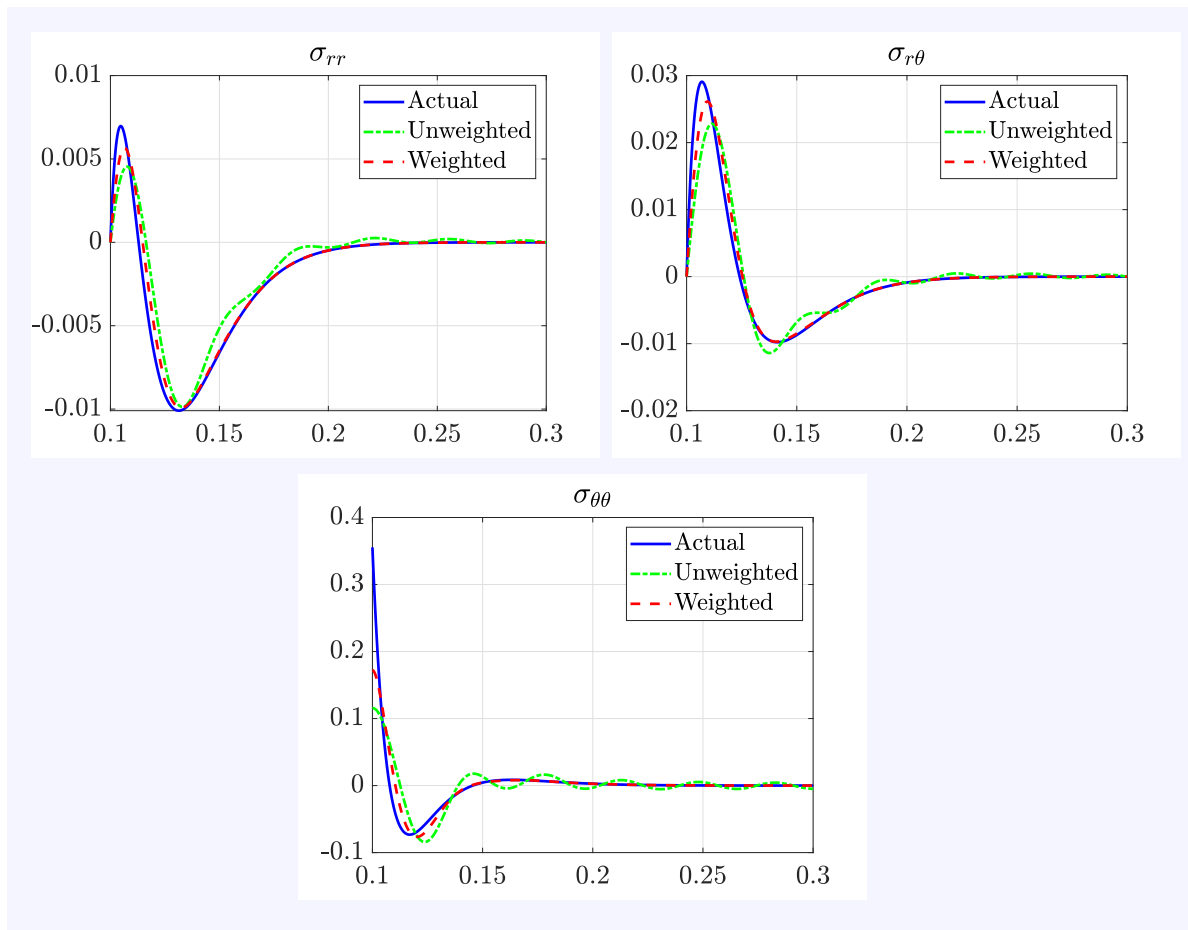


FIGURE 5.17: Radial variation of the candidate localized residual stress field fitted with 10 weighted (with $n = 20$) and 10 unweighted eigenfunctions.

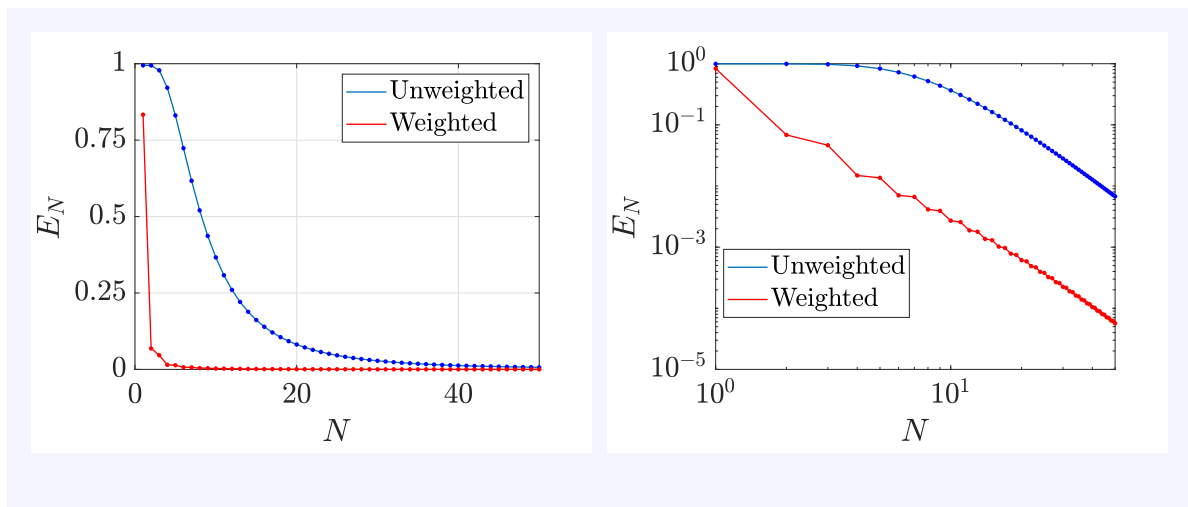


FIGURE 5.18: Fitting error E_N versus the number of eigenfunctions N ; left: linear scale, right: loglog scale.

5.3 Summary of the chapter

In Chapter 2, we developed general purpose basis functions for arbitrary domains. In this chapter we looked at two special cases.

The first special case is that of long prismatic bodies wherein the residual stresses do not vary in the axial direction. Here, we modified our original 3D eigenvalue problem of Chapter 2 by setting all axial derivatives to zero everywhere. We observed that the eigenvalue problem splits into three 2D sub-problems. The first of these sub-problems involves the planar stress components, the second concerns the axial component, and the third deals with the out of plane shear components. We showed that each sub-problem yields an orthogonal sequence of functions spanning the corresponding space of stress components. We demonstrated that, because these bases incorporate the essential properties exhibited by residual stresses in prismatic bodies, they give faster convergence in comparison with other standard bases blind to such properties, such as the Laplace operator eigenfunctions or the Stokes operator eigenfunctions. We used the axial basis to interpolate a given axial stress in a rail using its values at 10 interior points, and observed that the interpolant seems much better in comparison to that obtained using the same number of Laplace eigenfunctions.

The second special case is that of planar residual stresses that are localized in a 2D region, decaying rapidly away from it. To develop spatially localized basis functions, we first considered a 1D problem to clarify ideas. We considered an extremization problem with an objective function similar to that of Chapter 2, but with a weighting function increasing exponentially away from the region where localization is intended. Such a weighting function helps arrest oscillations in far away regions. We also weighted the normalization constraint with a similar function to make the eigenfunctions decay rapidly, away from the region of intended localization. Using the calculus of variations, we obtained a Sturm-Liouville eigenvalue problem whose solutions are known to form a basis for the space of scalar functions with the same boundary conditions. Taking cues from the 1D problem, we modified the extremization problem of Chapter 2 by incorporating appropriate weighting functions, and obtained an eigenvalue problem similar to our original eigenvalue problem of Chapter 2. We showed that the corresponding eigenfunctions are mutually orthogonal in a weighted inner product. We briefly discussed the modifications needed in our FEM formulation due to the presence of the additional term in the eigenvalue problem, and plotted the first few eigenfunctions, localized around an interior point, on an arbitrarily shaped domain. Finally, we demonstrated on an annular geometry that this

basis gives faster convergence than the global basis of Chapter 2 when used for fitting a spatially localized candidate residual stress field.

So far, we have demonstrated the utility of our residual stress basis functions ϕ_i by successfully fitting given candidate residual stresses with them. In the next chapter, we *solve* for a residual stress state, given its governing differential equation. For illustration, we will consider the problem of non-uniform heating of a thermo-elastic annulus.

Chapter 6

Solution of a thermoelasticity problem using residual stress basis

So far, we have used the residual stress basis functions ϕ_i to fit given residual stress fields. In this chapter, we *solve* for a residual stress field given its governing differential equation. For illustration, we consider the problem considered in Section 4.1.4 of non-uniform heating of a thermoelastic annulus. There, we solved this problem numerically by directly integrating the governing differential equations, and then fitted the solution σ with ϕ_i to demonstrate that σ lies in the span of ϕ_i , as expected from the theory. In this chapter, our aim is to solve for σ approximately using the weighted residual method, which is summarized below.

Let us say that we wish to solve approximately for a variable \mathfrak{r} satisfying

$$\mathcal{L}\mathfrak{r} = f,$$

where we assume for simplicity that \mathcal{L} is a linear differential operator and that \mathfrak{r} satisfies some homogeneous boundary conditions. We choose a complete basis (χ_i) satisfying the same boundary conditions as \mathfrak{r} and write

$$\mathfrak{r} = \sum_{i=1}^N a_i \chi_i$$

for some sufficiently large N . We then impose the following N conditions on the residual

$$R = f - \sum_{i=1}^N a_i \mathcal{L}\chi_i \text{ to solve for the coefficients } a_i:$$

$$(R, w_i) = 0, \quad 1 \leq i \leq N,$$

where w_i are some appropriate weighting functions and (\cdot, \cdot) denotes an inner product. The weighted residual methods with $w_i = \chi_i$ and $w_i = \mathcal{L}\chi_i$ are known as the Galerkin method and the least squares method, respectively.¹

In this chapter, we will solve the thermoelasticity problem using two weighted residual approaches. The first approach is displacement based, where we use the free vibration modes \mathbf{u}_i as the weighting functions (this approach is a special case of using virtual work, \mathbf{u}_i being the virtual displacements [68]). In the second approach, we use the traces of the residual stress basis functions ϕ_i as the weights. We see that a naive direct application of the weighted residual method with ϕ_i gives us an incorrect solution. We then carefully develop a correct approach to solving the thermoelasticity problem using the weighted residual method with ϕ_i , obtaining a much faster convergence to the true solution in comparison to the virtual work approach.

This chapter is arranged as follows. In Section 6.1, we describe the problem of non-uniform heating of a thermoelastic annulus and present the complete boundary value problem. In Section 6.2, we solve for the resulting residual stress approximately using the displacement based virtual work method. We use two different displacement bases for this purpose: the free vibration modes and the eigenfunctions of the Laplace operator, and find that the approximate stresses converge to the true stress with both the bases, albeit slowly. In Section 6.3, we solve the thermoelasticity problem using the weighted residual method with traces of ϕ_i as the weights, obtaining some interesting new results along the way. In Section 6.4, we construct a new residual stress basis whose elements are zero at the boundary. We observe that this basis spans *all* residual stress fields in the L^2 norm, and residual stress fields with zero boundary value in the H^1 norm. We use this basis to solve a thermoelasticity problem whose true solution is a stress field which is zero on the boundary, using the weighted residual method.

¹The Galerkin method and the least squares method are examples of a class of approximation methods called the ‘spectral methods’. See [67] for a comprehensive discussion of spectral methods.

6.1 Problem description

We look at the thermoelasticity problem considered in Section 4.1.4. An initially unstressed annulus with inner radius $r_a = 0.1$ and outer radius $r_b = 0.3$, obeying linear isotropic elasticity, is subjected to the temperature field

$$T(r, \theta) = r \cos 3\theta. \quad (6.1)$$

The resulting residual stress $\boldsymbol{\sigma}$ is the solution to the following boundary value problem:

$$\begin{aligned} \Delta(\text{tr } \boldsymbol{\sigma}) &= \beta \Delta T = \frac{-8\beta \cos 3\theta}{r} \quad \text{in } \Omega, \\ \text{div } \boldsymbol{\sigma} &= \mathbf{0} \quad \text{in } \Omega, \\ \boldsymbol{\sigma} \mathbf{n} &= \mathbf{0} \quad \text{on } \partial\Omega. \end{aligned} \quad (6.2)$$

In the above, $\beta = \frac{-\alpha Y}{1 - \nu}$, where Y is the Young's modulus, ν is the Poisson's ratio, α is the coefficient of thermal expansion, and $\text{tr } \boldsymbol{\sigma} = \sigma_{xx} + \sigma_{yy} = \sigma_{rr} + \sigma_{\theta\theta}$ is the sum of the planar normal stress components. Since the problem is essentially 2D, we will refer to $\text{tr } \boldsymbol{\sigma}$ as the trace of $\boldsymbol{\sigma}$ henceforth.²

In Section 4.1.4, we solved this problem by converting Eqs. 6.2 into a system of two second order ODEs in r by considering a $\boldsymbol{\sigma}$ with a fixed circumferential wave number, and integrating those ODEs numerically. Our aim in this chapter is to find approximate solutions using the weighted residual method. To this end, we use two approaches: the displacement based virtual work method, and the weighted residual method with residual stress basis ϕ_i .

In what follows, we will assume the following numerical values for the material constants: $Y = 1$, $\alpha = 0.5$ and $\nu = 0.33$, in any consistent units.

6.2 Approximate solution using the virtual work method

6.2.1 Computation of the free vibration modes

For the sake of completeness, we discuss briefly how we have computed the free vibration modes to be used in the virtual work method. We refer the interested reader to [68] for

²The trace of $\boldsymbol{\sigma}$ is $\sigma_{xx} + \sigma_{yy} + \sigma_{zz}$, while $\text{tr } \boldsymbol{\sigma}$ is $\sigma_{xx} + \sigma_{yy}$. Since this is a plane strain problem, σ_{zz} is non-zero, and the two are different.

more details on free vibration modes.

Let \mathbf{u} be a free vibration mode such that the corresponding modal stress is traction-free. In view of the azimuthal dependence of T (Eq. 6.1), we assume \mathbf{u} to be of the form

$$\mathbf{u}(r, \theta; t) = \sin \omega t \{ \mathbf{u}_r(r) \cos 3\theta \mathbf{e}_r + \mathbf{u}_\theta(r) \sin 3\theta \mathbf{e}_\theta \}. \quad (6.3)$$

In absence of any body force, the equation of motion is

$$\operatorname{div} \tilde{\boldsymbol{\sigma}} = \rho \ddot{\mathbf{u}},$$

where $\tilde{\boldsymbol{\sigma}} = \mathbf{C} \nabla_s \mathbf{u}$ is the modal stress corresponding to \mathbf{u} , \mathbf{C} is the fourth order elasticity tensor and $\nabla_s \mathbf{u}$ is the symmetric part of gradient of \mathbf{u} . Upon substituting Eq. 6.3 in the above equation and simplifying, we obtain the following second order ODEs:

$$\begin{aligned} \mathbf{u}_r'' &= - \frac{4 \mathbf{u}_r \nu^2 \omega^2 r^2 \rho + 2 \mathbf{u}_r \nu \omega^2 r^2 \rho - 2 \mathbf{u}_r \omega^2 r^2 \rho + 2 Y \mathbf{u}_r' \nu r - 2 Y \mathbf{u}_r' r - 3 Y \mathbf{u}_\theta' r}{2 Y r^2 (\nu - 1)} \\ &\quad + \frac{20 \mathbf{u}_r \nu + 12 \mathbf{u}_\theta \nu - 11 \mathbf{u}_r - 9 \mathbf{u}_\theta}{2 r^2 (\nu - 1)}, \\ \mathbf{u}_\theta'' &= - \frac{4 \nu^2 \omega^2 r^2 \rho \mathbf{u}_\theta + 2 \nu \omega^2 r^2 \rho \mathbf{u}_\theta - 2 \omega^2 r^2 \rho \mathbf{u}_\theta + 2 Y \mathbf{u}_\theta' \nu r + 3 Y \mathbf{u}_r' r - Y \mathbf{u}_\theta' r - 12 Y \nu \mathbf{u}_r}{Y r^2 (2 \nu - 1)} \\ &\quad + \frac{-20 \nu \mathbf{u}_\theta + 9 \mathbf{u}_r + 19 \mathbf{u}_\theta}{r^2 (2 \nu - 1)}. \end{aligned} \quad (6.4)$$

We also have four boundary conditions: $\tilde{\sigma}_{rr} = \tilde{\sigma}_{r\theta} = 0$ at $r = r_a$ and $r = r_b$. In terms of displacements, these become

$$\begin{aligned} \mathbf{u}_r' &= \frac{\nu (3 \mathbf{u}_\theta + \mathbf{u}_r)}{r (\nu - 1)} \quad \text{at } r = r_a \quad \text{and } r = r_b, \\ \mathbf{u}_\theta' &= \frac{\mathbf{u}_\theta + 3 \mathbf{u}_r}{r} \quad \text{at } r = r_a \quad \text{and } r = r_b. \end{aligned} \quad (6.5)$$

Finally, we scale the free vibration modes by setting

$$\mathbf{u}_r = 1 \quad \text{at } r = r_a. \quad (6.6)$$

We solve the boundary value problem of Eqs. 6.4 - 6.6 numerically using `ode45` in Matlab. The first five free vibration modes are plotted in Figure 6.1, where we have taken $\rho = 1$.

We now use a large number of these free vibration modes to solve Eq. 6.2 using the virtual work method.

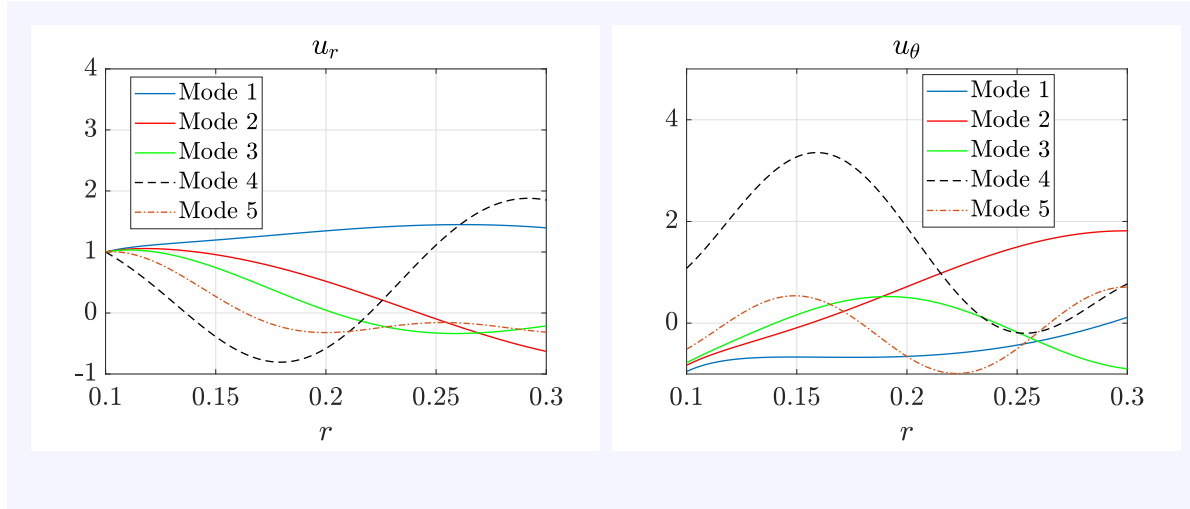


FIGURE 6.1: Radial variation of the first five free vibration modes with $m = 3$ in an annulus, corresponding to free-free boundary condition.

6.2.2 Computation of approximate residual stress

Consider the inner product of the second of Eqs. 6.2 with a free vibration mode \mathbf{u}_i , i.e.,

$$\int_{\Omega} \operatorname{div} \boldsymbol{\sigma} \cdot \mathbf{u}_i \, dA = 0. \quad (6.7)$$

Using the divergence theorem and the traction-free boundary condition (third of Eqs. 6.2), Eq. 6.7 becomes

$$\int_{\Omega} \boldsymbol{\sigma} \cdot \nabla \mathbf{u}_i \, dA = 0. \quad (6.8)$$

The residual stress field $\boldsymbol{\sigma}$ can be expressed in terms of the displacement \mathbf{u} as follows:

$$\boldsymbol{\sigma} = \mathbf{C} \boldsymbol{\varepsilon}^e = \mathbf{C} (\boldsymbol{\varepsilon} - \boldsymbol{\varepsilon}^T) = \mathbf{C} (\nabla_s \mathbf{u} - \alpha T \mathbf{I}). \quad (6.9)$$

In the above, $\boldsymbol{\varepsilon}$, $\boldsymbol{\varepsilon}^e$ and $\boldsymbol{\varepsilon}^T$ denote ‘total strain’, ‘elastic strain’ and ‘thermal strain’, respectively; and \mathbf{I} is the (3×3) second order identity tensor. Substituting the above into Eq. 6.8, we obtain

$$\int_{\Omega} (\mathbf{C} \nabla_s \mathbf{u}) \cdot \nabla \mathbf{u}_i \, dA = \alpha \int_{\Omega} T (\mathbf{C} \mathbf{I}) \cdot \nabla \mathbf{u}_i \, dA.$$

Since \mathbf{u}_i form a basis [3], we can write

$$\mathbf{u} = \sum_{j=1}^{\infty} a_j \mathbf{u}_j.$$

Substituting this into the preceding equation, we obtain

$$\sum_{j=1}^{\infty} a_j \int_{\Omega} (\mathbf{C} \nabla_s \mathbf{u}_j) \cdot \nabla \mathbf{u}_i dA = \alpha \int_{\Omega} T(\mathbf{C} \mathbf{I}) \cdot \nabla \mathbf{u}_i dA.$$

Truncating the expansion in the above to N terms, and considering $1 \leq i \leq N$, we obtain a system of N linear equations in N coefficients a_j . These equations can be written compactly as

$$Ma = f,$$

where M is an $N \times N$ matrix with

$$M(i, j) = \int_{\Omega} \nabla \mathbf{u}_i \cdot (\mathbf{C} \nabla_s \mathbf{u}_j) dA$$

and f is an $N \times 1$ column vector with

$$f(i) = \alpha \int_{\Omega} T(\mathbf{C} \mathbf{I}) \cdot \nabla \mathbf{u}_i dA.$$

If $\boldsymbol{\varepsilon}_i = \nabla_s \mathbf{u}_i$ is the strain corresponding to the free vibration mode \mathbf{u}_i , and $\boldsymbol{\sigma}_i = \mathbf{C} \boldsymbol{\varepsilon}_i = \mathbf{C} \nabla_s \mathbf{u}_i$ is the corresponding linear elastic stress, then M and f have the following simple interpretations:

$$M(i, j) = \int_{\Omega} \boldsymbol{\varepsilon}_i \cdot \boldsymbol{\sigma}_j dA \quad \text{and} \quad f(i) = \alpha \int_{\Omega} T \boldsymbol{\sigma}_i \cdot \mathbf{I} dA.$$

The actual displacement \mathbf{u} , along with the approximate displacements \mathbf{u}_N obtained with $N = 10, 20$ and 100 , are plotted in Figure 6.2. We see that this method works well if displacements are considered.

However, the convergence of the corresponding approximate stress³

$$\boldsymbol{\sigma}_N^A = \mathbf{C} (\nabla_s \mathbf{u}_N - \alpha T \mathbf{I})$$

to the actual stress $\boldsymbol{\sigma}$ is slow, as seen in Figure 6.3. The same is seen upon plotting the squared relative error

$$E_N = \frac{\int_{\Omega} (\boldsymbol{\sigma} - \boldsymbol{\sigma}_N^A) \cdot (\boldsymbol{\sigma} - \boldsymbol{\sigma}_N^A) dA}{\int_{\Omega} \boldsymbol{\sigma} \cdot \boldsymbol{\sigma} dA}$$

in Figure 6.4; E_N decays like N^{-1} for large N .

³We use the superscript 'A' to distinguish between the approximate stresses obtained using the weighted residual methods and the fits obtained by directly projecting the true stress solutions onto the basis, as in Chapter 4. The latter will be denoted with a superscript 'F' in this chapter.

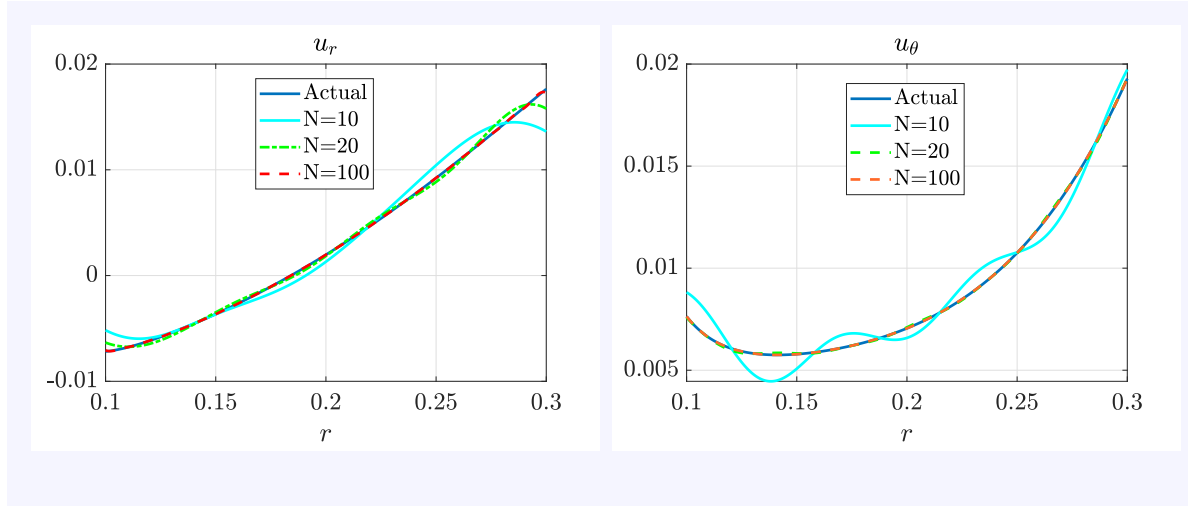


FIGURE 6.2: Radial variation of the actual and the approximate displacements obtained using the virtual work method, with 10, 20 and 100 free vibration modes.

We can also use the eigenfunctions of the Laplace operator

$$\Delta \tilde{\mathbf{u}} + \lambda \tilde{\mathbf{u}} = \mathbf{0}$$

with boundary values that correspond to zero traction (i.e., the eigenfunctions satisfy the boundary conditions in Eqs. 6.5) as the basis in the virtual work method. The results with these functions are at par with those with the free vibration modes: the convergence is fast for the displacements, but slow for the stresses. We show the fits with the Laplace operator eigenfunctions for displacements and stresses in Figures 6.5 and 6.6, respectively; the approximation error E_N is plotted in Figure 6.7. We see that the convergence to the true stress is slow: E_N decays like $1/N$ for large N . Computational details are omitted for brevity.

In the next section, we use ϕ_i to obtain the approximate stress, and study the convergence obtained.

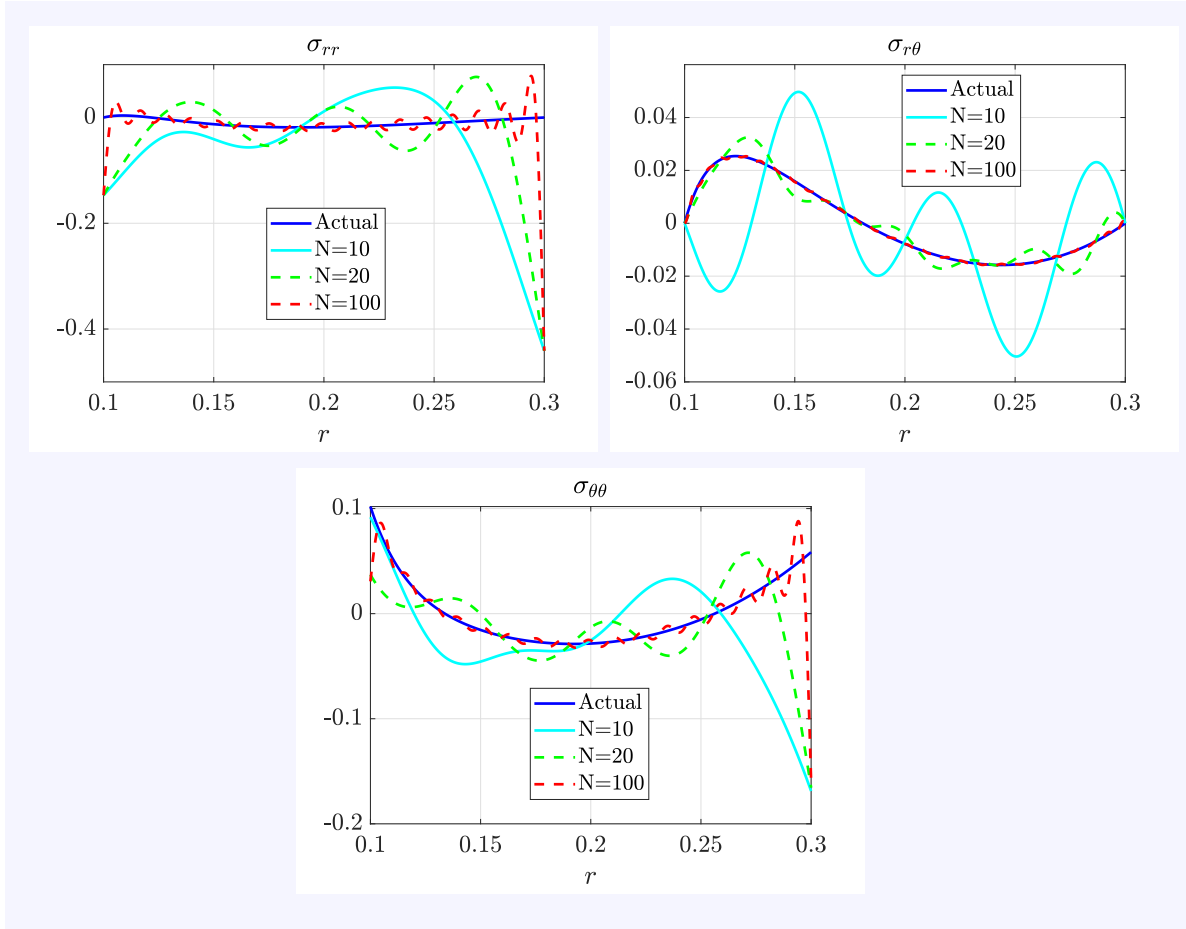


FIGURE 6.3: Radial variation of the actual and the approximate stresses obtained using the virtual work method, with 10, 20 and 100 free vibration modes.

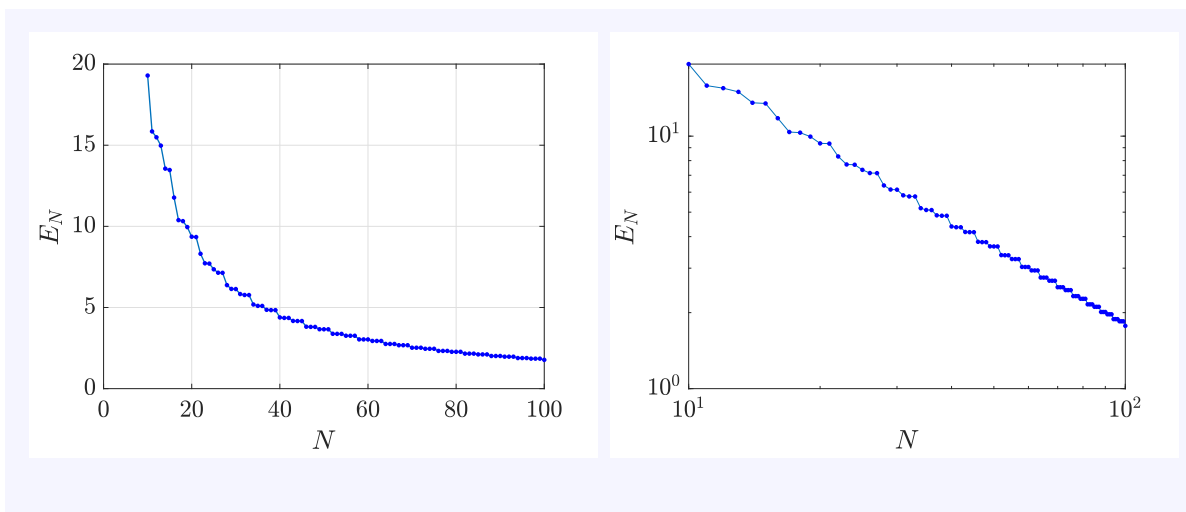


FIGURE 6.4: Approximation error E_N versus N with the free vibration modes. Left: linear scale; right: log-log scale.

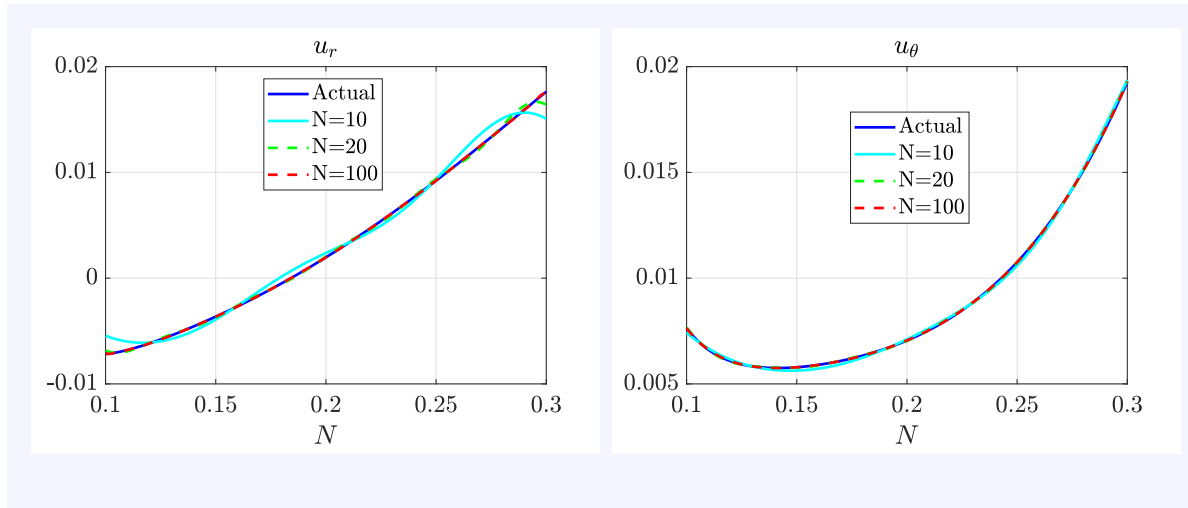


FIGURE 6.5: Radial variation of the actual and the approximate displacements obtained using virtual work, with 10, 20 and 100 Laplace operator eigenfunctions.

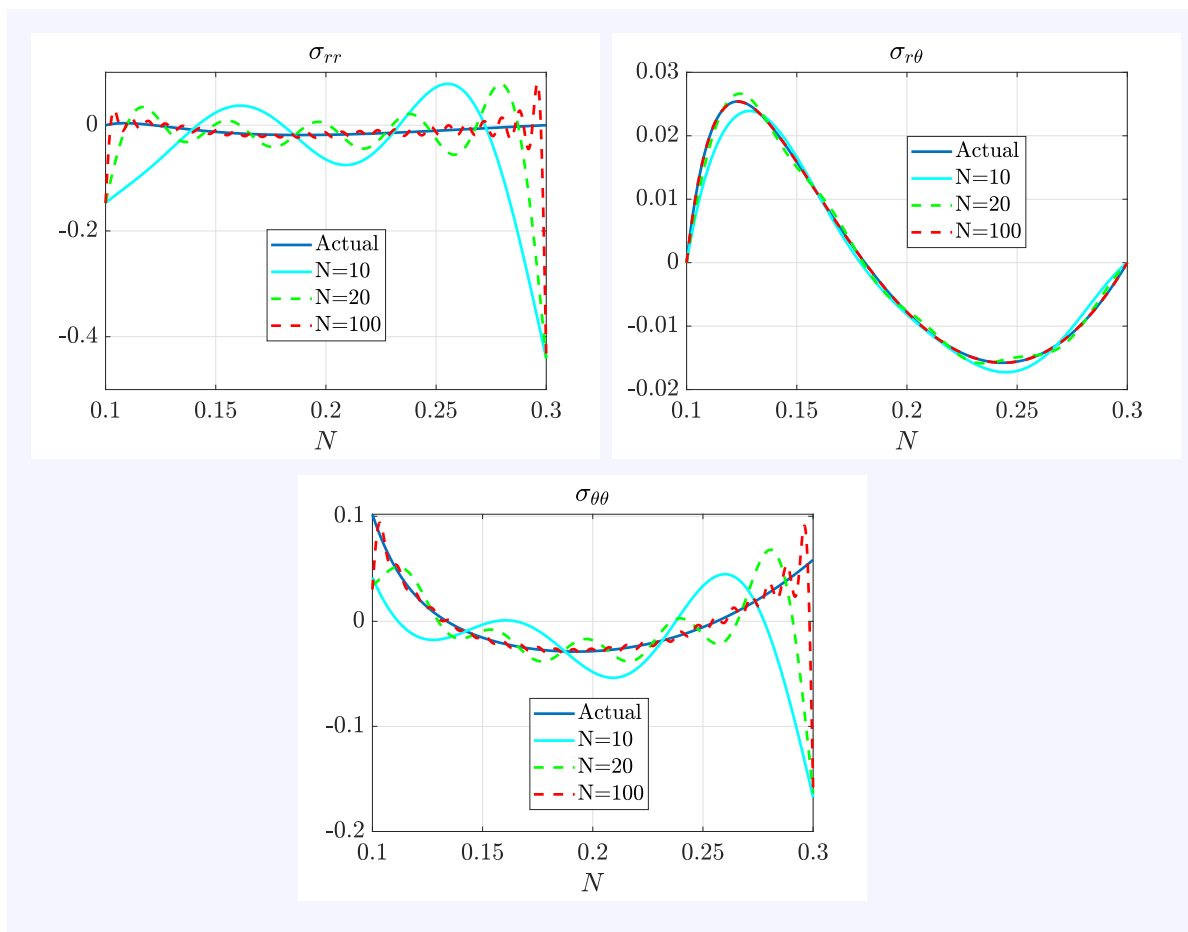


FIGURE 6.6: Radial variation of the the actual and the approximate stresses obtained using virtual work, with 10, 20 and 100 Laplace operator eigenfunctions.

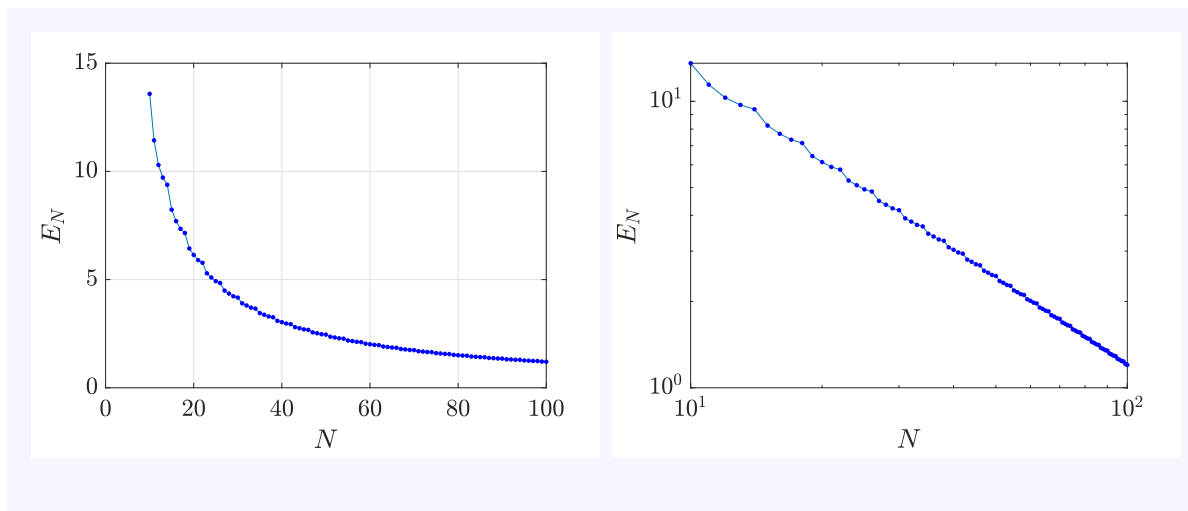


FIGURE 6.7: Approximation error E_N versus N using the Laplace operator eigenfunctions. Left: linear scale; right: log-log scale.

6.3 Approximate solution using the residual stress basis functions ϕ_i

Since the basis functions ϕ_i already satisfy the divergence-free and the traction-free conditions, we only need to worry about the first of Eqs. 6.2:

$$\Delta(\text{tr } \boldsymbol{\sigma}) = \beta \Delta T. \quad (6.10)$$

Our aim in this section is to solve the above equation using the weighted residual method with ϕ_i .

For brevity, for any second order tensor \boldsymbol{S} , we will denote $\text{tr } \boldsymbol{S}$ as \bar{S} from now on. In particular, $\text{tr } \phi_i = \bar{\phi}_i$.

6.3.1 A direct (incorrect) application of the weighted residual method

We first try the simplest approach: write $\boldsymbol{\sigma} = \sum_{i=1}^N a_i \phi_i$ in Eq. 6.10, take inner products with $\bar{\phi}_i$ for $1 \leq i \leq N$, and put the weighted residuals to zero. We then have the following system of equations:

$$Ma = f,$$

where

$$M(i, j) = \int_{\Omega} \bar{\phi}_i \Delta \bar{\phi}_j dA \quad \text{and} \quad f(i) = \beta \int_{\Omega} \Delta T \bar{\phi}_i dA.$$

Using the above expressions, we compute the coefficient vector a and compute a candidate approximate stress $\boldsymbol{\sigma}_N^A$. We plot $\bar{\sigma}$ and $\bar{\sigma}_N^A$ in Figure 6.8 for $N = 10, 20$ and 100 , $\boldsymbol{\sigma}$ being the true solution. The approximate stress does not seem to be converging to the true stress. The same is borne out by the plot of the approximation error

$$E_N = \frac{\int_{\Omega} (\bar{\sigma} - \bar{\sigma}_N^A)^2 dA}{\int_{\Omega} \bar{\sigma}^2 dA}$$

in Figure 6.9; we see E_N saturating at about 0.686.

We also try the ‘least squares’ method: we seek a_i that minimize

$$\int_{\Omega} (\Delta \bar{\sigma}_N^A - \beta \Delta T)^2 dA = \int_{\Omega} \left(\sum_{i=1}^N a_i \Delta \bar{\phi}_i - \beta \Delta T \right)^2 dA.$$

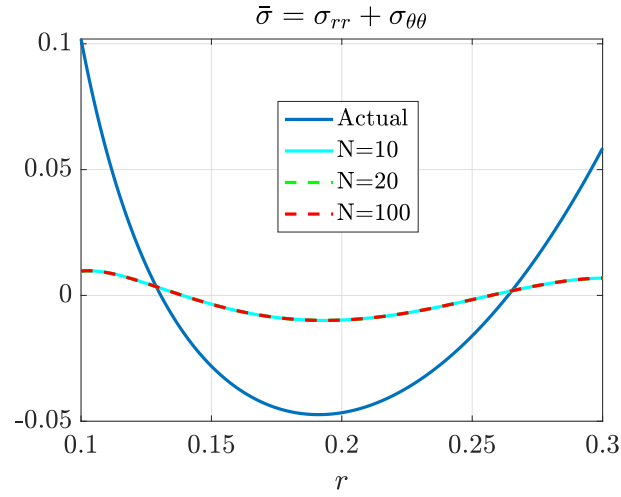


FIGURE 6.8: Radial variation of the actual and the approximate traces $\bar{\sigma}$ and $\bar{\sigma}_N^A$ using the weighted residual method, with 10, 20 and 100 residual stress basis functions.

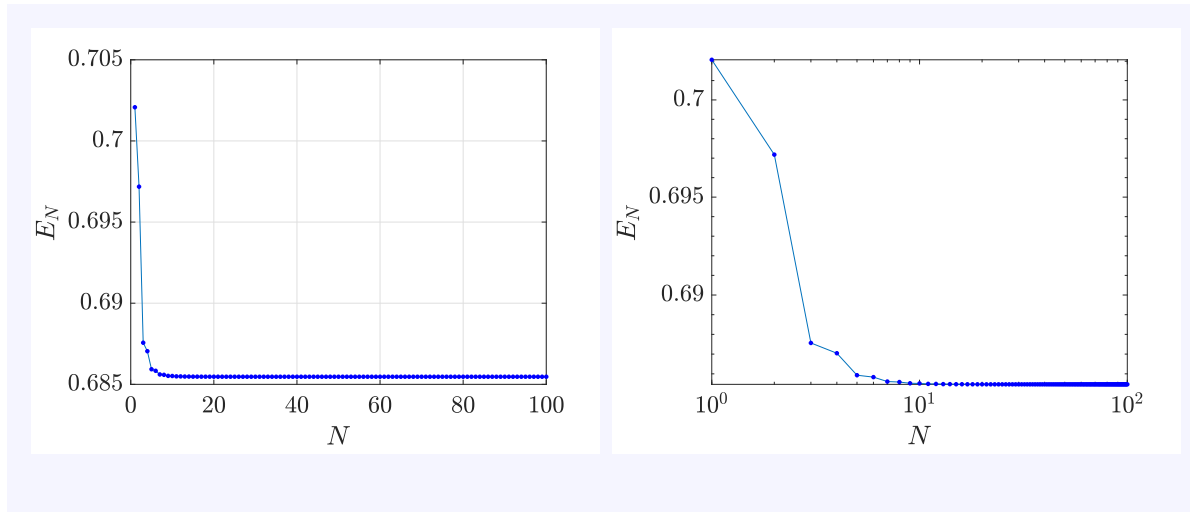


FIGURE 6.9: Approximation error E_N versus N using the weighted residual method with ϕ_i . Left: linear scale; right: log-log scale.

By setting the gradient of the above with respect to a_i equal to zero, we obtain the following set of N linear equations:

$$Ma = f,$$

with

$$M(i, j) = \int_{\Omega} \Delta \bar{\phi}_i \Delta \bar{\phi}_j dA \quad \text{and} \quad f(i) = \beta \int_{\Omega} \Delta T \Delta \bar{\phi}_i dA.$$

The least squares method does not do too well either; $\bar{\sigma}_N^A$ computed using the least squares method is plotted in Figure 6.10 and the corresponding approximation error is plotted in

Figure 6.11. In fact, E_N converges to a value greater than unity. This solution is slightly worse than nothing at all.

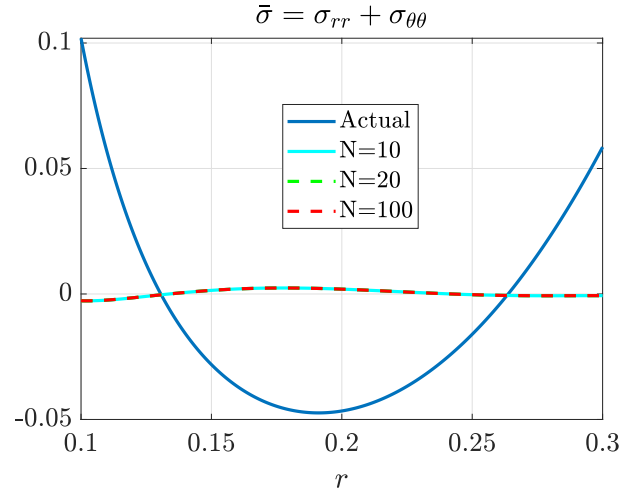


FIGURE 6.10: Radial variation of the actual and the approximate traces $\bar{\sigma}$ and $\bar{\sigma}_N^A$ using least squares approximation, with 10, 20 and 100 residual stress basis functions.

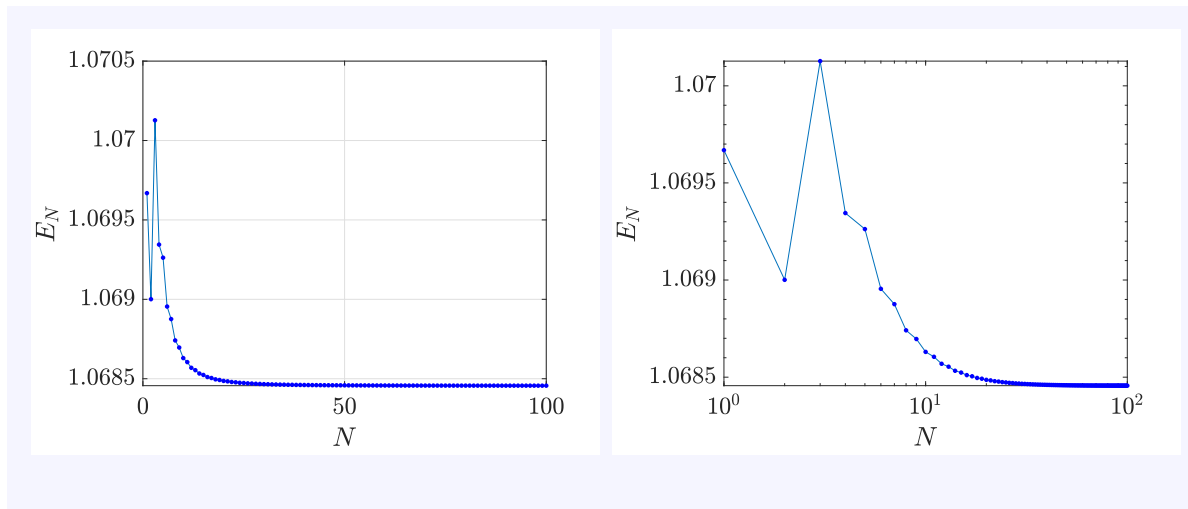


FIGURE 6.11: Approximation error E_N versus N using least squares approximation with ϕ_i . Left: linear scale; right: log-log scale.

6.3.2 Reasons for the failure of the direct approach

To understand why the direct approach does not work, we first plot the fit σ^F obtained by directly projecting the correct stress solution onto the basis functions ϕ_i (as in Chapter 4), and its derivatives. From these plots, it becomes clear that the two factors that determine

the success of a direct approach are: (a) the order of the differential operator in the governing differential equation, and (b) the order of the convergence of the basis used.

6.3.2.1 The fit σ^F , and its derivatives

Suppose we directly project the correct stress solution onto the basis functions ϕ_i (as in Chapter 4), and call that fit σ^F . We saw in Section 4.1.4 that the H^1 norm of $\sigma - \sigma^F$ goes to zero, which means that the L^2 norms of both the r -variation of $\bar{\sigma} - \bar{\sigma}^F$ and its first derivative go to zero. We see this in the top row of Figure 6.12, where we have plotted the r -variations of $\bar{\sigma}$ and $\bar{\sigma}^F$ (computed using 100 basis functions), and their first derivatives.

However, as seen in the bottom row of Figure 6.12, the second derivative of the r -variation of $\bar{\sigma}^F$ (and hence the r -variation of the Laplacian of $\bar{\sigma}^F$) is highly oscillatory, and the L^2 norm of $\Delta\bar{\sigma} - \Delta\bar{\sigma}^F$ is large. The squared relative L^2 norm of $\Delta\bar{\sigma} - \Delta\bar{\sigma}^F$,

$$E_N = \frac{\int_{\Omega} (\Delta\bar{\sigma} - \Delta\bar{\sigma}^F)^2 dA}{\int_{\Omega} \Delta\bar{\sigma}^2 dA},$$

increases with N , as seen in Figure 6.13.

We can now see why does the least squares method discussed above, for instance, not give us the correct solution. It seeks a solution that *minimizes* the L^2 norm of $\Delta\bar{\sigma} - \Delta\bar{\sigma}_N^A$ (for a fixed N), and $\bar{\sigma}^F$ is clearly not that solution. The L^2 norm of $\Delta\bar{\sigma} - \Delta\bar{\sigma}^F$ is much greater than that of $\Delta\bar{\sigma} - \Delta\bar{\sigma}_N^A$, where $\bar{\sigma}_N^A$ is obtained from the least squares method.

6.3.2.2 What role do the operator and the basis play?

We saw in Chapter 2 that ϕ_i form a basis to residual stress fields in the H^1 norm. Similarly, the free vibration modes corresponding to the traction free boundary condition span the displacements with the same boundary condition in the H^1 norm. The governing differential equations

$$\Delta \operatorname{tr} \sigma = \beta \Delta T$$

and

$$\operatorname{div} \sigma = \mathbf{0}$$

that are used in the stress and the displacement formulations of the weighted residual approach, respectively, are both second order in the corresponding variables. Despite these similarities, we see that the weighted residual method works with the free vibration

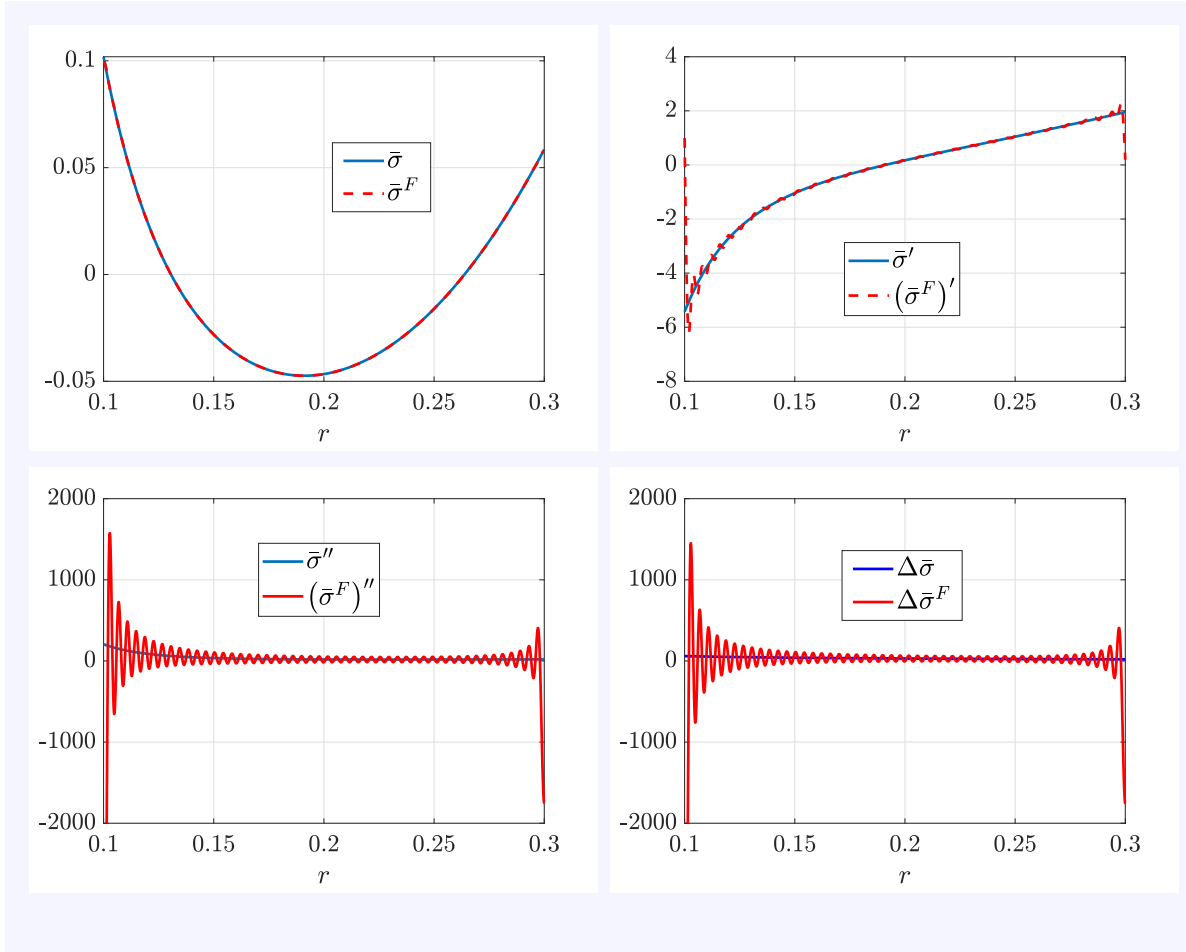


FIGURE 6.12: Radial variation of $\bar{\sigma}$ and $\bar{\sigma}^F$, and their r -derivatives. We see that the second derivatives, and hence the Laplacians, do not match well.

modes in the displacement formulation, and does not work with the residual stress basis functions in the stress formulation. The reason is that an application of the divergence theorem in the displacement formulation yields *a boundary term that drops out, lowering the order of integrand in the domain integral* (Eq. 6.7). An order reduction of this nature is not possible in the stress formulation since the boundary term is non-zero.

In separate calculations not shown here, we have noted that if in the virtual work method used in Section 6.2 we do not reduce the order of the integrand by using the divergence theorem (while using the free vibration modes), we obtain an incorrect solution. This is because the left hand side of the governing equation

$$\operatorname{div} \{C(\nabla_s \mathbf{u} - \alpha T \mathbf{I})\} = \mathbf{0}$$

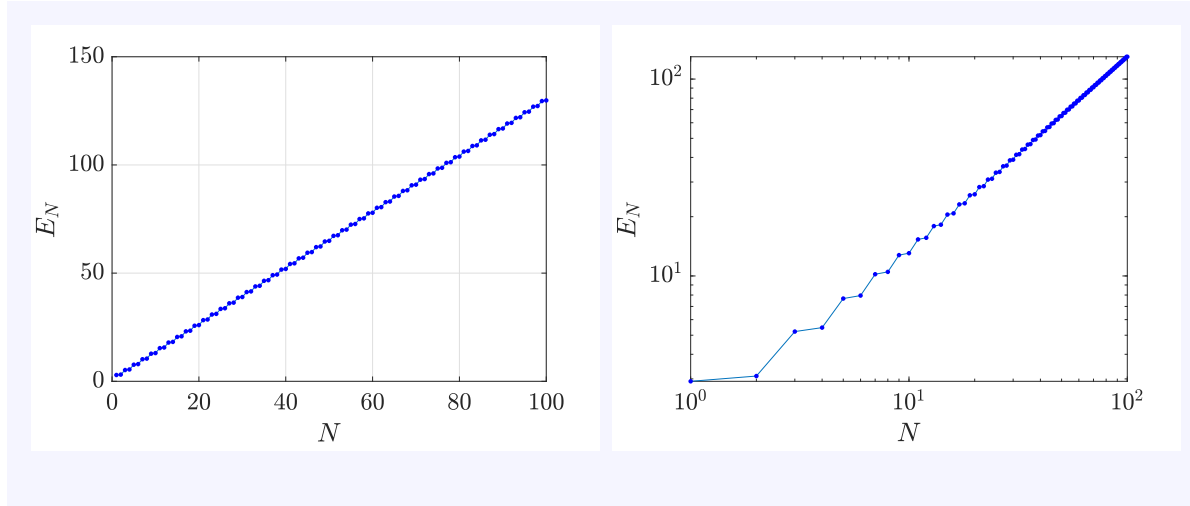


FIGURE 6.13: Squared relative L^2 norm of $\Delta\bar{\sigma} - \Delta\bar{\sigma}^F$. Left: linear scale; right: log-log scale.

has terms with second order derivatives of \mathbf{u} ; while the basis \mathbf{u}_i converges to \mathbf{u} in the H^1 norm, which only guarantees convergence up to first order derivatives.

These observations indicate that the convergence properties of the basis and the order of the operator in the governing differential equation together determine if techniques like the weighted residual method or the least squares method will work. If, after possible removal of the boundary term upon using the divergence theorem, the highest order of differentiation of the concerned variable is greater than the order of the norm in which the basis converges, the method is unlikely to work.

With this insight, in the next section, we will exploit some properties of residual stress traces to successfully solve the thermoelasticity problem using ϕ_i .

6.3.3 A characterization of harmonic functions in terms of planar residual stresses

In 2D, the ‘Airy stress function’ representation of an equilibrated stress,

$$\sigma_{xx} = \frac{\partial^2 \psi}{\partial y^2}, \quad \sigma_{yy} = \frac{\partial^2 \psi}{\partial x^2}, \quad \sigma_{xy} = -\frac{\partial^2 \psi}{\partial x \partial y}, \quad (6.11)$$

is complete, by which we mean that all stresses of the above form are divergence-free, *and* for every divergence-free stress, there exists an Airy stress function ψ [60]. It follows from

Eq. 6.11 that ψ is arbitrary up to an added factor of $c_1x + c_2y + c_3$ for arbitrary constants c_1, c_2 and c_3 , i.e., adding this to ψ does not change the corresponding stresses.

If the equilibrated stress is traction-free as well, i.e., it is a residual stress, then the necessary and sufficient boundary conditions on ψ are (see Eq. 4.5.13 and 4.5.14 in [7]):

$$\psi = c_4x + c_5y + c_6 \quad \text{and} \quad \psi_{,n} = \frac{\partial\psi}{\partial n} = c_4n_x + c_5n_y \quad \text{on} \quad \partial\Omega,$$

where c_4, c_5 and c_6 are arbitrary constants which can be chosen according to convenience. For simplicity, we choose $c_4 = c_5 = c_6 = 0$, so that

$$\psi = 0 \quad \text{and} \quad \psi_{,n} = 0 \quad \text{on} \quad \partial\Omega. \quad (6.12)$$

This choice of the constants c_4, c_5 and c_6 also exhausts the arbitrariness in ψ by fixing the constants c_1, c_2 and c_3 . Thus, for a given planar residual stress $\boldsymbol{\sigma}$, there corresponds a unique Airy stress function ψ that satisfies the boundary conditions in Eq. 6.12.

Moreover, by the definition of the Airy stress function, any given ψ satisfying the boundary conditions in Eq. 6.12 corresponds to a unique residual stress. Thus, we have established that there is a one to one correspondence between the space of planar residual stresses and the space of Airy stress functions satisfying the boundary condition in Eq. 6.12.

Note that the first condition in Eq. 6.12 implies that the derivative of ψ in the locally tangential direction \boldsymbol{t} is also zero, i.e.,

$$\psi_{,t} = 0 \quad \text{on} \quad \partial\Omega.$$

Since both normal and tangential derivatives of ψ are zero at the boundary, we have

$$\nabla\psi = \mathbf{0} \quad \text{on} \quad \partial\Omega.$$

In particular,

$$\psi_{,x} = 0 \quad \text{and} \quad \psi_{,y} = 0 \quad \text{on} \quad \partial\Omega. \quad (6.13)$$

We will use the above condition in a later section.

We also note that any residual stress trace $\bar{\sigma}$ is the Laplacian of a unique scalar function ψ satisfying the boundary conditions in Eq. 6.12 since

$$\bar{\sigma} = \sigma_{xx} + \sigma_{yy} = \frac{\partial^2\psi}{\partial y^2} + \frac{\partial^2\psi}{\partial x^2} = \Delta\psi. \quad (6.14)$$

We use Eq. 6.14 to obtain a useful characterization of harmonic functions in 2D.

Proposition 6.1. *A scalar function h in 2D is harmonic (i.e., $\Delta h = 0$) if and only if it is orthogonal to all residual stress traces.*

Proof. Let h be a harmonic function. Consider its inner product with a residual stress trace:

$$\int_{\Omega} h \bar{\sigma} \, dA = \int_{\Omega} h \Delta \psi \, dA = \int_{\partial\Omega} h \psi_{,n} \, ds - \int_{\Omega} \nabla h \nabla \psi \, dA = - \int_{\partial\Omega} h_{,n} \psi \, ds + \int_{\Omega} \Delta h \psi \, dA = 0.$$

The first equality in the above follows from Eq. 6.14; the second equality follows from the divergence theorem; the third equality follows from the second of Eqs. 6.12 followed by the divergence theorem; the final equality is because of the first of Eqs. 6.12 and the fact that $\Delta h = 0$.

We now prove the other side of the proposition. Let g be a scalar function whose inner product with all residual traces is zero. Equivalently,

$$\int_{\Omega} g \Delta \psi \, dA = 0$$

for all twice differentiable ψ satisfying the boundary conditions in Eq. 6.12. Using the divergence theorem twice, along with the boundary conditions on ψ , we have

$$\int_{\Omega} g \Delta \psi \, dA = \int_{\Omega} \Delta g \psi \, dA = 0.$$

The considered ψ include the set of all smooth functions with derivatives of all orders zero on the boundary (this set is usually denoted as \mathcal{C}_c^∞), which in turn is dense⁴ in L^2 [45]. Therefore,

$$\Delta g = 0.$$

□

We now use Proposition 6.1 to solve the thermoelasticity problem using the weighted residual method with ϕ_i .

⁴If a set A is dense in a set B , then every element of B either belongs to A or is arbitrarily close to an element of A .

6.3.4 A correct application of the weighted residual method with ϕ_i

As we mentioned in the beginning of Section 6.3, since ϕ_i are already divergence-free and traction-free, we only need to worry about the equation

$$\Delta(\bar{\sigma} - \beta T) = 0,$$

i.e., $\bar{\sigma} - \beta T$ is harmonic. According to Proposition 6.1, this is equivalent to writing

$$\int_{\Omega} (\bar{\sigma} - \beta T) \chi \, dA = 0$$

for all residual stress traces χ . But $\bar{\phi}_i$ span the set of residual stress traces⁵, and hence, the above is equivalent to

$$\int_{\Omega} (\bar{\sigma} - \beta T) \bar{\phi}_i \, dA = 0 \quad \forall \bar{\phi}_i.$$

Writing $\bar{\sigma} = \sum_{j=1}^{\infty} a_j \bar{\phi}_j$, we have

$$\int_{\Omega} \left(\sum_{j=1}^{\infty} a_j \bar{\phi}_j \right) \bar{\phi}_i \, dA = \beta \int_{\Omega} T \bar{\phi}_i \, dA.$$

Truncating the expansion to N terms, and considering $1 \leq i \leq N$, we set up a system of N linear equations

$$Ma = f,$$

where

$$M(i, j) = \int_{\Omega} \bar{\phi}_i \bar{\phi}_j \, dA \quad \text{and} \quad f(i) = \beta \int_{\Omega} T \bar{\phi}_i \, dA. \quad (6.15)$$

We know that this time the approximations σ_N^A will converge quickly to σ because ϕ_i form a basis in the H^1 norm, whereas all we require for the above approach to work is that ϕ_i form a basis in the L^2 norm.

⁵Any residual stress trace $\tilde{\chi} = \text{tr } \tilde{\sigma}$ for some residual stress $\tilde{\sigma}$, and $\tilde{\sigma} = \sum_{i=1}^{\infty} \tilde{a}_i \phi_i$ for some unique coefficients \tilde{a}_i . Thus, $\tilde{\chi} = \sum_{i=1}^{\infty} \tilde{a}_i \bar{\phi}_i$, and we have shown that an arbitrary residual stress trace $\tilde{\chi}$ can be represented as a unique linear combination of the functions $\bar{\phi}_i$. Thus, $\bar{\phi}_i$ span the set of residual stress traces.

We plot the approximations σ_N^A , along with the actual stress σ , in Figure 6.14 for $N = 10, 20$ and 100 . We plot the approximation error

$$E_N = \frac{\int_{\Omega} (\sigma - \sigma_N^A) \cdot (\sigma - \sigma_N^A) dA}{\int_{\Omega} \sigma \cdot \sigma dA}$$

in Figure 6.15. We see that the convergence is rapid, E_N decays like $1/N^3$ for large N . We note that this convergence is much faster than that obtained using the displacement based virtual work method (Figures 6.4 and 6.7).

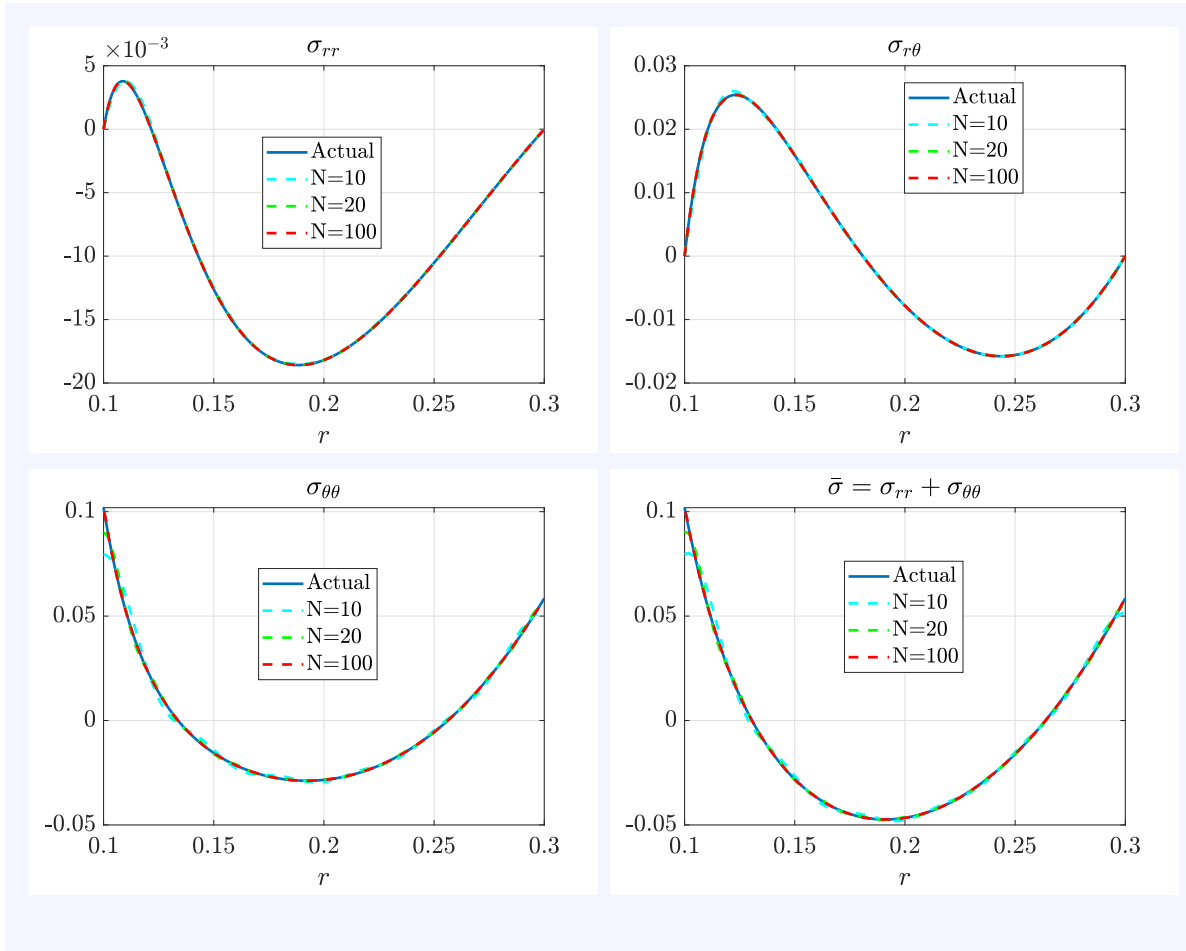


FIGURE 6.14: Radial variation of the actual and the approximate stresses with a correct application of the weighted residual method, using 10, 20 and 100 residual stress basis functions ϕ_i .

We can simplify the expressions in Eq. 6.15 using the following interesting result for residual stresses in 2D.

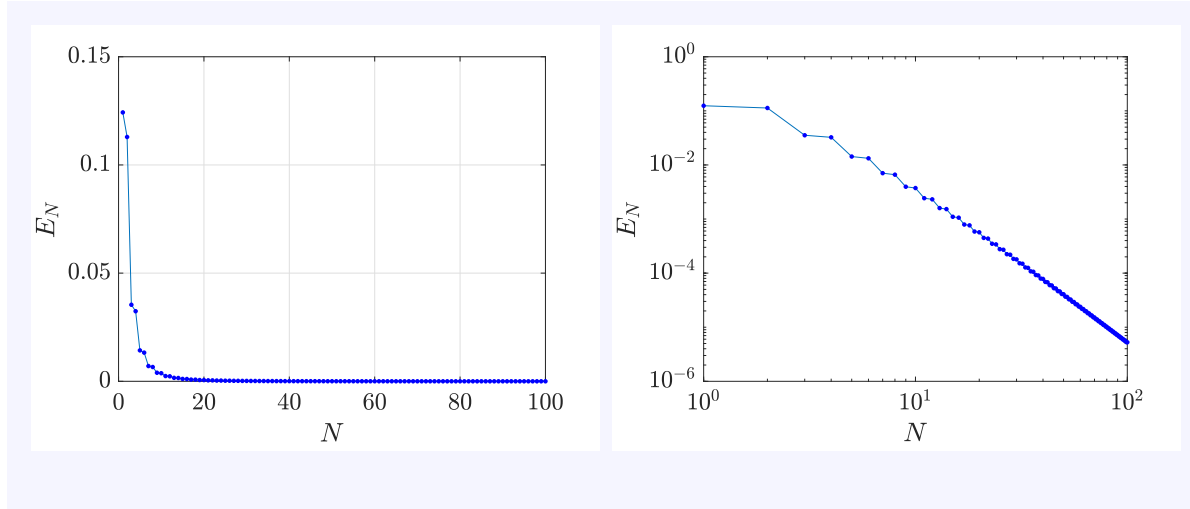


FIGURE 6.15: Approximation error E_N versus N with a correct application of the weighted residual method using ϕ_i . Left: linear scale; right: log-log scale.

Proposition 6.2. *The inner product of any two planar residual stresses $\boldsymbol{\sigma}_1$ and $\boldsymbol{\sigma}_2$ is equal to the inner product of their traces, i.e.,*

$$\int_{\Omega} \boldsymbol{\sigma}_1 \cdot \boldsymbol{\sigma}_2 dA = \int_{\Omega} \bar{\sigma}_1 \bar{\sigma}_2 dA.$$

Proof. Let the Airy stress functions corresponding to $\boldsymbol{\sigma}_1$ and $\boldsymbol{\sigma}_2$ be ψ_1 and ψ_2 . We will assume that ψ_1 and ψ_2 possess the regularity required for all the operations in this proof.

Consider the quantity $\int_{\Omega} \psi_{1,xy} \psi_{2,xy} dA$. Using Green's theorem, and boundary conditions on ψ_1 and ψ_2 (Eqs. 6.12 and 6.13), we have

$$\begin{aligned} \int_{\Omega} \psi_{1,xy} \psi_{2,xy} dA &= - \int_{\partial\Omega} \psi_{1,xy} \psi_{2,x} dx - \int_{\Omega} \psi_{1,xyy} \psi_{2,x} dA \\ &= - \int_{\partial\Omega} \psi_{1,xyy} \psi_2 dy + \int_{\Omega} \psi_{1,xyy} \psi_2 dA = \int_{\Omega} \psi_{1,xyy} \psi_2 dA. \end{aligned}$$

Similarly,

$$\begin{aligned} \int_{\Omega} \psi_{1,yy} \psi_{2,xx} dA &= \int_{\partial\Omega} \psi_{1,yy} \psi_{2,x} dy - \int_{\Omega} \psi_{1,yyx} \psi_{2,x} dA \\ &= - \int_{\partial\Omega} \psi_{1,yyx} \psi_2 dy + \int_{\Omega} \psi_{1,yyxx} \psi_2 dA = \int_{\Omega} \psi_{1,yyxx} \psi_2 dA = \int_{\Omega} \psi_{1,xyy} \psi_2 dA. \end{aligned}$$

From the above two equations, we have that

$$\int_{\Omega} \psi_{1,xy} \psi_{2,xy} dA = \int_{\Omega} \psi_{1,yy} \psi_{2,xx} dA. \quad (6.16)$$

We can similarly show that

$$\int_{\Omega} \psi_{1,xy} \psi_{2,xy} dA = \int_{\Omega} \psi_{1,xx} \psi_{2,yy} dA. \quad (6.17)$$

Let us now consider the inner product of $\boldsymbol{\sigma}_1$ and $\boldsymbol{\sigma}_2$. Using the above two identities, we have

$$\begin{aligned} \int_{\Omega} \boldsymbol{\sigma}_1 \cdot \boldsymbol{\sigma}_2 dA &= \int_{\Omega} (\sigma_{1xx}\sigma_{2xx} + \sigma_{1yy}\sigma_{2yy} + 2\sigma_{1xy}\sigma_{2xy}) dA \\ &= \int_{\Omega} (\psi_{1,yy}\psi_{2,yy} + \psi_{1,xx}\psi_{2,xx} + 2\psi_{1,xy}\psi_{2,xy}) dA \\ &= \int_{\Omega} (\psi_{1,yy}\psi_{2,yy} + \psi_{1,xx}\psi_{2,xx} + \psi_{1,xx}\psi_{2,yy} + \psi_{1,yy}\psi_{2,xx}) dA \\ &= \int_{\Omega} (\psi_{1,xx} + \psi_{1,yy})(\psi_{2,xx} + \psi_{2,yy}) dA = \int_{\Omega} \bar{\sigma}_1 \bar{\sigma}_2 dA. \end{aligned}$$

This completes the proof. \square

Using the above proposition, we conclude that the traces $\bar{\phi}_i$ of the orthonormal basis functions ϕ_i are also orthonormal. As a result, the matrix M in Eq. 6.15 is simply the identity matrix. Consequently, $a = f$, and

$$a(i) = \beta \int_{\Omega} T \bar{\phi}_i dA.$$

If ψ_i is the Airy stress function corresponding to ϕ_i , then using Green's theorem and the boundary conditions in Eqs. 6.12 and 6.13, we have

$$a(i) = \beta \int_{\Omega} T \bar{\phi}_i dA = \beta \int_{\Omega} T \Delta \psi_i dA = \beta \int_{\Omega} \Delta T \psi_i dA,$$

which implies that $a(i) = 0 \forall i$ if T is harmonic. Thus, we obtain the well known result for linear isotropic elastic materials: only a non-harmonic rise in temperature can induce strain incompatibility, and hence, non-zero residual stress (e.g., see Problem 17.4 of [8]).

Proposition 6.2 can be used to prove the following interesting corollary regarding determinants of planar residual stresses.

Corollary 6.3. *The mean (or average) of the determinant of a planar residual stress is zero.*

Proof. The determinant of a planar residual stress $\boldsymbol{\sigma}$ is

$$\det \boldsymbol{\sigma} = \sigma_{xx}\sigma_{yy} - \sigma_{xy}^2 = \psi_{,yy}\psi_{,xx} - \psi_{,xy}^2.$$

Setting $\psi_1 = \psi_2 = \psi$ in Eq. 6.16, we immediately obtain that

$$\int_{\Omega} \det \boldsymbol{\sigma} dA = \int_{\Omega} (\psi_{,yy}\psi_{,xx} - \psi_{,xy}^2) dA = 0.$$

□

In the next section, we construct a new basis for residual stresses, one whose elements are zero at the boundary. With this basis, a direct application of the weighted residual method gives us the correct solution if the true stress is also zero at the boundary.

6.4 A new basis for residual stresses

The eigenfunctions of the Laplace operator with zero boundary value form a basis for the space of all scalar square integrable functions (including those which are non-zero on the boundary) on a given domain [64]. Motivated by this, we construct a new basis for residual stresses, one whose elements are zero at the boundary. The construction will be identical to that presented in Chapter 2, the only significant difference being that the set \mathcal{S} over which the functional J_0 is minimized (see Sections 2.1 and 2.2) will now consist of tensors which are zero on the boundary.⁶

These basis functions, denoted as $\boldsymbol{\Phi}_i$, span the set of those residual stresses which are zero on the boundary in the H^1 norm, and the set of *all* residual stresses (i.e., including the ones not zero on the boundary) in the L^2 norm. Moreover, for a residual stress $\boldsymbol{\sigma}$ which is zero on the boundary, $\boldsymbol{\sigma} - \sum_{i=1}^N a_i \boldsymbol{\Phi}_i \rightarrow \mathbf{0}$ implies that $\Delta \boldsymbol{\sigma} - \Delta \left(\sum_{i=1}^N a_i \boldsymbol{\Phi}_i \right) \rightarrow \mathbf{0}$ in a sense we will make precise below. We will use this last property to demonstrate that in a thermoelasticity problem whose true solution is a residual stress with zero boundary value, a direct application of the weighted residual method with $\boldsymbol{\Phi}_i$ as the weights gives us the correct solution.

⁶It is difficult to think of practical situations in which all the components of a residual stress are zero on the boundary. However, consideration of this basis provides us with useful insights into the workings of the approximation methods we have been discussing.

6.4.1 Construction of the new basis

We seek the stationary points of the functional

$$J_0(\boldsymbol{\sigma}) = \frac{1}{2} \int_{\Omega} \nabla \boldsymbol{\sigma} \cdot \nabla \boldsymbol{\sigma} \, dA \quad (6.18)$$

over those elements of the set

$$\mathcal{S} = \left\{ \boldsymbol{\sigma} \mid \boldsymbol{\sigma} \in \text{Sym}, \operatorname{div} \boldsymbol{\sigma} = \mathbf{0}, \boldsymbol{\sigma}|_{\partial\Omega} = \mathbf{0}, \int_{\Omega} \boldsymbol{\sigma} \cdot \boldsymbol{\sigma} \, dA < \infty, \int_{\Omega} \nabla \boldsymbol{\sigma} \cdot \nabla \boldsymbol{\sigma} \, dA < \infty \right\}, \quad (6.19)$$

which satisfy

$$\int_{\Omega} \boldsymbol{\sigma} \cdot \boldsymbol{\sigma} \, dA = 1.$$

Note that the set \mathcal{S} differs from that in Chapter 2 only in the boundary condition satisfied by its elements: $\boldsymbol{\sigma} = \mathbf{0}$ here and $\boldsymbol{\sigma}\mathbf{n} = \mathbf{0}$ in Chapter 2. Proceeding along lines identical to the construction in Chapter 2, we find that a stationary point $\boldsymbol{\sigma}$ satisfies the following eigenvalue problem

$$\begin{aligned} -\Delta \boldsymbol{\sigma} + \nabla_s \boldsymbol{\mu} &= \lambda \boldsymbol{\sigma} & \text{in } \Omega, \\ \operatorname{div} \boldsymbol{\sigma} &= \mathbf{0} & \text{in } \Omega, \\ \boldsymbol{\sigma} &= \mathbf{0} & \text{on } \partial\Omega. \end{aligned}$$

It is easily seen that the eigenfunctions Φ_i are mutually orthogonal with respect to both the L^2 and the H^1 inner products. The proof of existence of the eigenfunctions and the fact that they form a basis for the set of residual stresses with zero boundary value in the H^1 norm, and the set of *all* residual stresses in the L^2 norm, is almost identical to the one presented in Chapter 2, and is omitted (for more details, see Section 7.6). This last property is closely related to a similar property of the zero boundary value eigenfunctions of the Laplace operator and the zero boundary value eigenfunctions of the Stokes operator: the former provide an L^2 basis for all scalar functions [64], and the latter form an L^2 basis for all divergence-free vector fields [43].

We plot the first four eigenfunctions on an annular domain corresponding to wave number $m = 3$ in Figure 6.16. We scale the eigenfunctions by setting $\sigma'_{\theta\theta} = 1$ at the inner boundary $r = r_a$.

Before moving on to using the weighted residual method with Φ_i , we demonstrate that Φ_i span even those residual stress fields that are non-zero on the boundary. We fit the

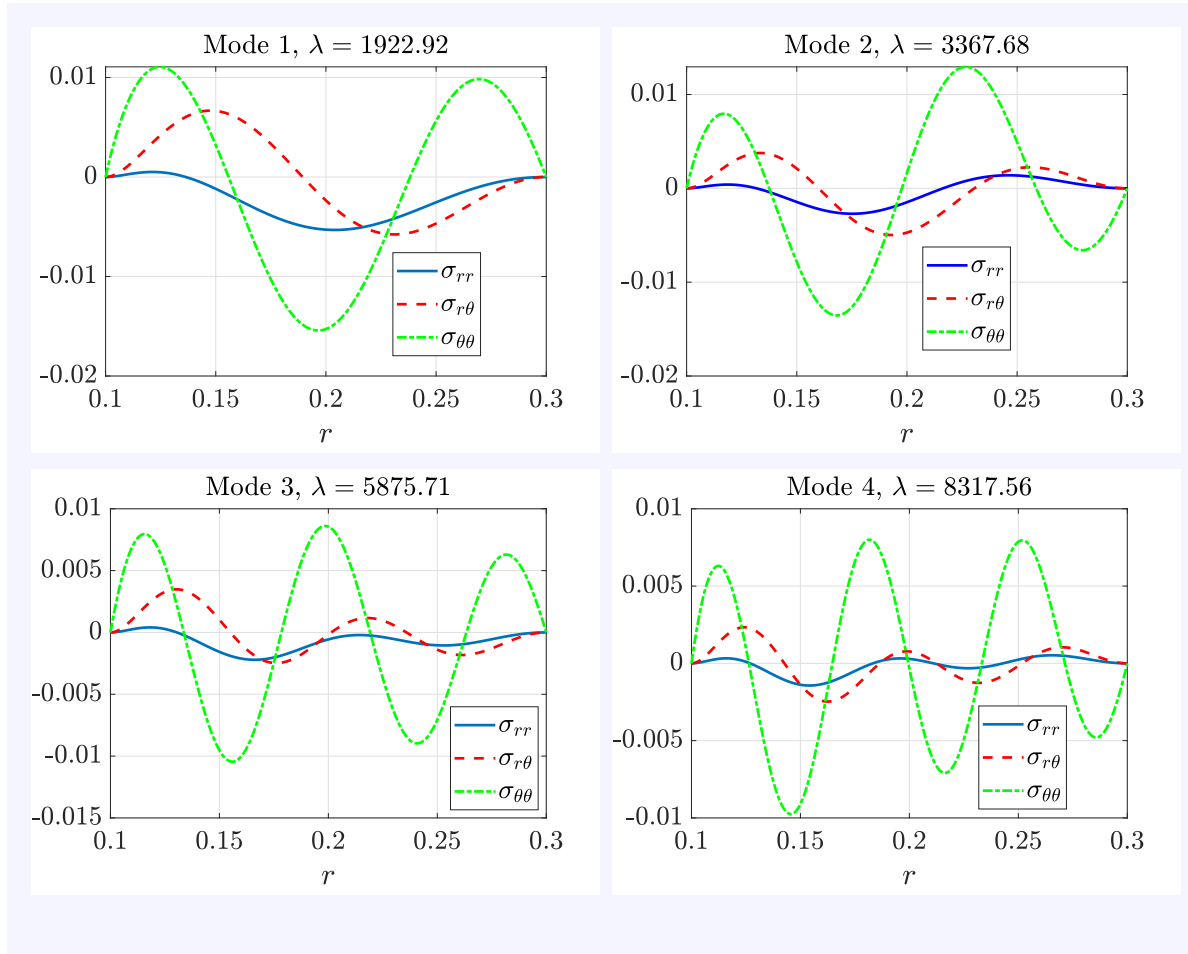


FIGURE 6.16: Radial variation of the first four residual stress eigenfunctions Φ_i for the annular domain, with $m = 3$.

thermoelastic residual stress field considered in the previous sections of this chapter (Eq. 6.2) using Φ_i , and plot the corresponding stress components in Figure 6.17. We plot the fitting error E_N in Figure 6.18. It is clear from these figures that the fits σ^F converge to σ in the L^2 norm as N increases. However, the convergence is slow: E_N decays like $1/N$ for large N . Recall that with our usual residual stress basis functions ϕ_i , E_N decays like $1/N^3$ for large N for the same residual stress σ (see Figure 4.10).

The eigenfunctions Φ_i satisfy another important property that will be useful while using the weighted residual method: if for a residual stress σ which is zero at the boundary,

$$\sum_{i=1}^N a_i \Phi_i \rightarrow \sigma, \quad (6.20)$$

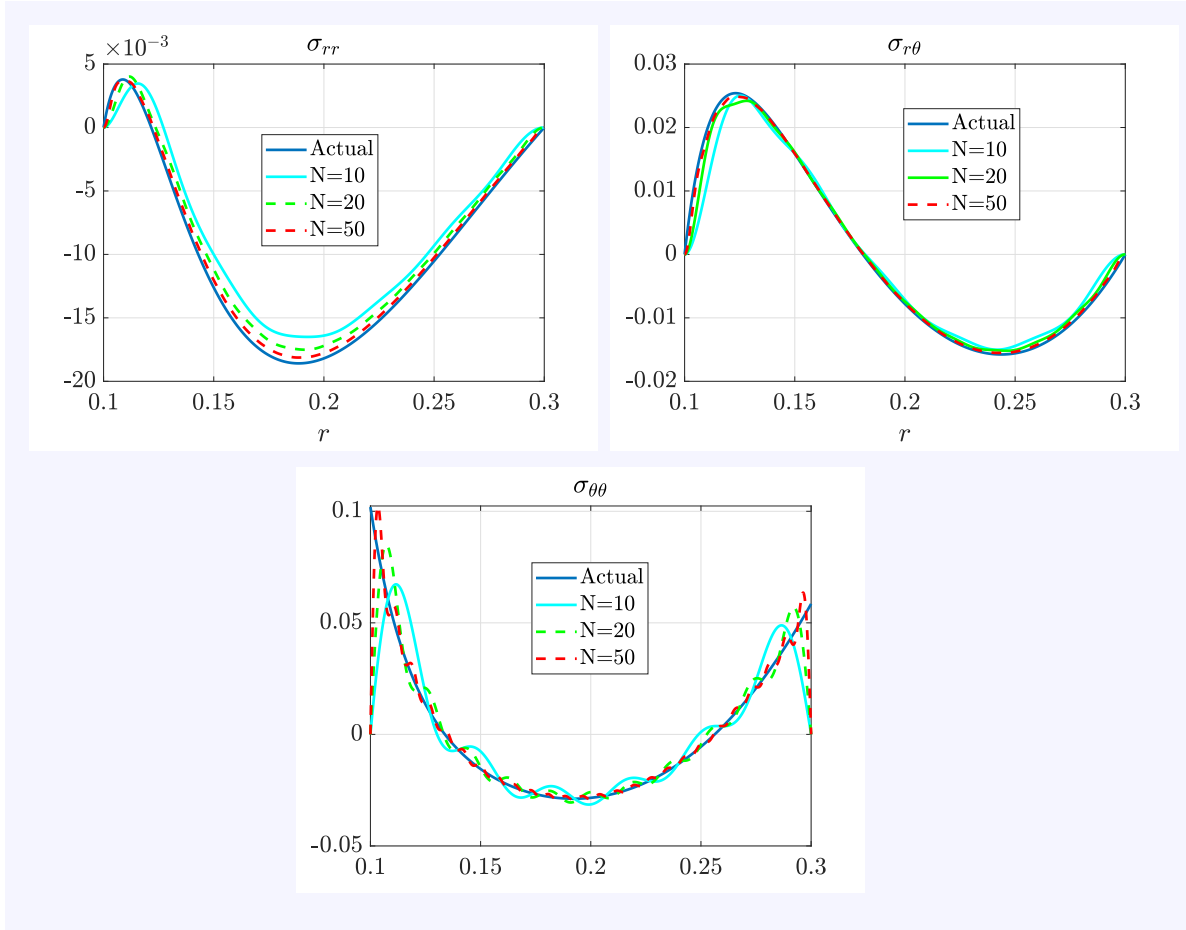


FIGURE 6.17: Radial variation of the thermal stress σ of Section 6.1 and its fits σ^F using 10, 20 and 50 residual stress basis functions Φ_i .

then,

$$\Delta \left(\sum_{i=1}^N a_i \Phi_i \right) \rightarrow \Delta \sigma. \quad (6.21)$$

Moreover, the rate of convergence in Eq. 6.21 is the same as the rate of convergence in Eq. 6.20 (the convergence in Eq. 6.20 is in the H^1 norm). The proof is technical, and we omit it. However, we point out that the proof is along similar lines to the proof of an identical property exhibited by the zero boundary value scalar eigenfunctions \tilde{u}_i of the Laplace operator. This property is as follows. If u_0 is a scalar function with zero boundary value and

$$\sum_{i=1}^N a_i \tilde{u}_i \rightarrow u_0, \quad (6.22)$$

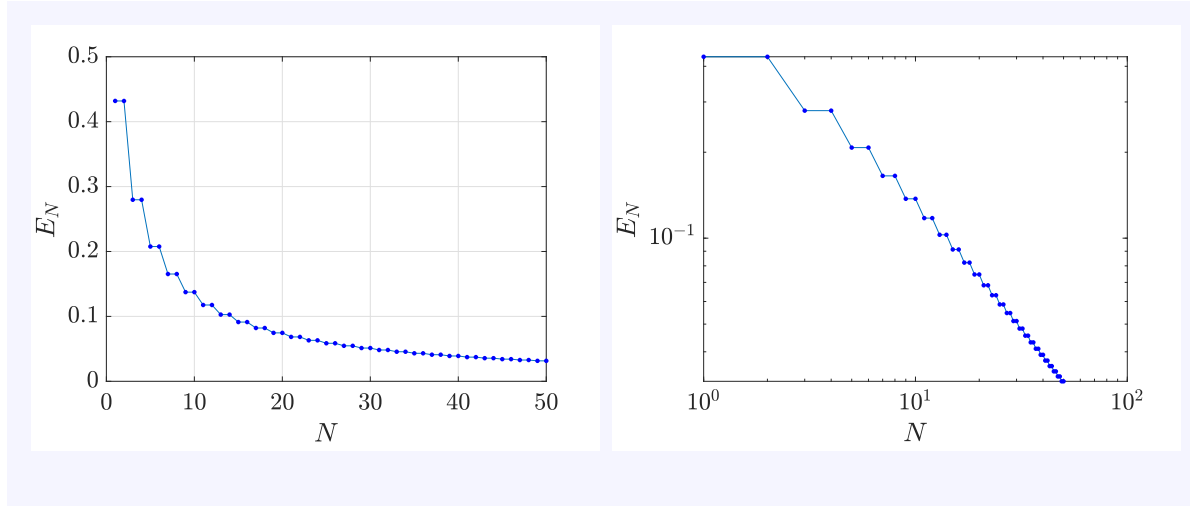


FIGURE 6.18: Fitting error E_N versus N for fitting of the thermal stress σ of Section 6.1 using Φ_i . Left: linear scale; right: log-log scale.

then

$$\Delta \left(\sum_{i=1}^N a_i \tilde{u}_i \right) \rightarrow \Delta u_0. \quad (6.23)$$

The above is true because the Laplace operator is an isomorphism from H_0^1 (the set of scalar functions with finite H^1 norm and zero boundary value) to H^{-1} (the dual space of H_0^1) [64]. Moreover, according to the definition of an isomorphism between Banach spaces⁷, there exist constants C_1 and C_2 such that⁸

$$C_1 \|u_0 - \sum_{i=1}^N a_i \tilde{u}_i\|_{H^1} \leq \|\Delta u_0 - \sum_{i=1}^N a_i \Delta \tilde{u}_i\|_{H^{-1}} \leq C_2 \|u_0 - \sum_{i=1}^N a_i \tilde{u}_i\|_{H^1},$$

i.e., the rate of convergence in Eq. 6.23 is the same as the rate of convergence in Eq. 6.22 (the convergence in Eq. 6.22 is in the H^1 norm). We omit further technical details.

In the next section, we consider a thermoelastic annulus heated in such a way that the resulting residual stress is zero at the boundary. We will see that with a direct application of the weighted residual method with $\bar{\Phi}_i$ as the weights gives us the correct solution.

⁷Let P and Q be two Banach spaces equipped with norms $\|\cdot\|_P$ and $\|\cdot\|_Q$. Let p be an arbitrary element in P and $q = Sp$. An isomorphism $S : P \rightarrow Q$ is a continuous bijective map, with a continuous inverse, so that there exist constants C_1 and C_2 independent of p and q , that satisfy $C_1 \|p\|_P \leq \|q\|_Q \leq C_2 \|p\|_P$.

⁸The norm of a function $f \in H^{-1}$ defined on Ω is $\|f\|_{H^{-1}} = \sup \{|f(g)| : \|g\|_{H^1} = 1 \text{ and } g \in H^1\}$.

6.4.2 Weighted residual method with Φ_i

We first *construct* a thermoelasticity problem in which the resulting residual stress is zero at the boundary. Let the applied temperature T be of the form

$$T = (r + c_1 r^2 + c_2 r^4) \cos 3\theta,$$

so that

$$\beta \Delta T = \beta \left(-\frac{8}{r} - 5c_1 + 7c_2 r^2 \right) \cos 3\theta. \quad (6.24)$$

The free parameters c_1 and c_2 are to be determined so that the resulting residual stress σ is zero at the boundaries. σ satisfies the following ODE system (see Eqs. 4.7 and 4.8)

$$\begin{aligned} (\sigma_{rr} + \sigma_{\theta\theta})'' + \frac{(\sigma_{rr} + \sigma_{\theta\theta})'}{r} - \frac{9(\sigma_{rr} + \sigma_{\theta\theta})}{r^2} &= \beta \left(-\frac{8}{r} - 5c_1 + 7c_2 r^2 \right), \\ \sigma_{rr}'' + \frac{4\sigma_{rr}'}{r} - \frac{\sigma_{\theta\theta}'}{r} + \frac{2\sigma_{rr}}{r^2} + \frac{7\sigma_{\theta\theta}}{r^2} &= 0. \end{aligned}$$

We see from Eq. 4.9 that with $\sigma_{rr} = \sigma_{\theta\theta} = 0$ at the boundary, the condition $\sigma_{r\theta} = 0$ implies that $\sigma_{rr}' = 0$ at the boundary. We therefore have the following boundary conditions on σ_{rr} and $\sigma_{\theta\theta}$:

$$\sigma_{rr} = \sigma_{rr}' = \sigma_{\theta\theta} = 0 \quad \text{at} \quad r = r_a \quad \text{and} \quad r = r_b.$$

We solve this boundary value problem numerically (taking $\beta = 1$ and iteratively adjusting c_1 and c_2) and obtain the required stress σ . The parameters c_1 and c_2 are found as part of the solution to be

$$c_1 = -13.04 \quad \text{and} \quad c_2 = -77.14. \quad (6.25)$$

We now show that we can also solve the above problem (with c_1 and c_2 as given in Eq. 6.25) using the weighted residual method, with $\bar{\Phi}_i$ as the weighting functions. Since Φ_i are already divergence-free and zero at the boundary, the only equation we need to worry about is (recall that $\beta = 1$)

$$\Delta \bar{\sigma} = \Delta T.$$

Substituting $\bar{\sigma} = \sum_{i=1}^N a_i \bar{\Phi}_i$, and taking the inner product of the above with $\bar{\Phi}_1$ through $\bar{\Phi}_N$, we obtain N linear equations arranged as⁹.

$$Ma = f,$$

where

$$M(i, j) = \int_{\Omega} \Delta \bar{\Phi}_j \bar{\Phi}_i dA \quad \text{and} \quad f(i) = \int_{\Omega} \Delta T \bar{\Phi}_i dA.$$

We plot the approximate solutions σ_N^A , along with the actual stress σ , in Figure 6.19 for $N = 10, 20$ and 50 . We also plot the approximation error

$$E_N = \frac{\int_{\Omega} (\sigma - \sigma_N^A) \cdot (\sigma - \sigma_N^A) dA}{\int_{\Omega} \sigma \cdot \sigma dA}$$

in Figure 6.20. We see that the convergence is rapid; E_N decays like $1/N^6$ for large N .¹⁰

⁹Although a reduction in order of derivatives is possible through the divergence theorem (since Φ_i are zero on the boundary), it is not needed since the rate of convergence of the Laplacians of the approximants to the Laplacian of the true solution is the same as the rate of convergence of the approximants to the true solution, as noted earlier (see the comment following Eq. 6.21)

¹⁰We have verified in calculations not shown here that the least squares method with Φ_i also works just as well for this problem.

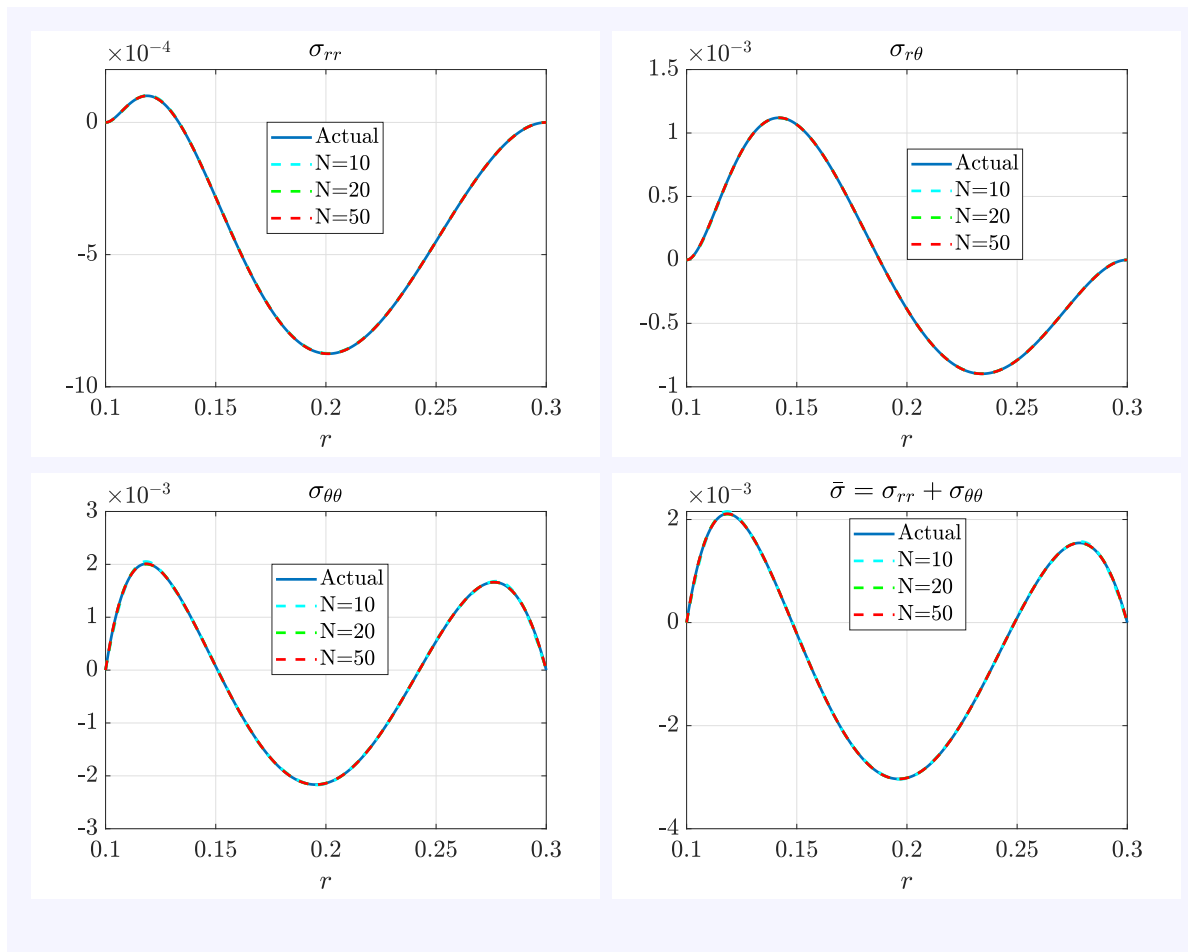


FIGURE 6.19: Radial variation of the actual and the approximate stresses using the weighted residual method with 10, 20 and 50 residual stress basis functions Φ_i .

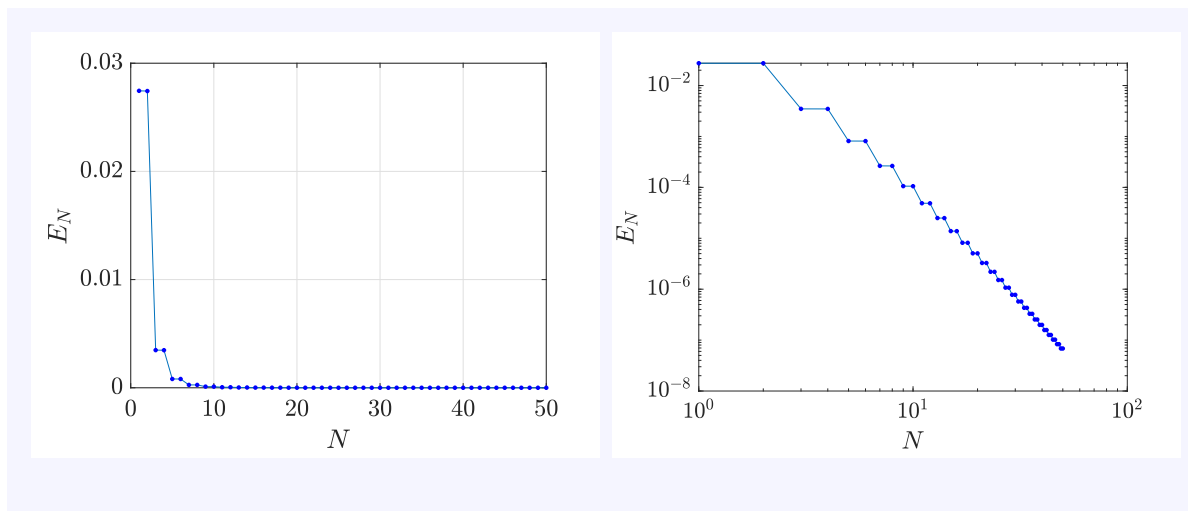


FIGURE 6.20: Approximation error E_N versus N using residual stress basis functions Φ_i .
Left: linear scale; right: log-log scale.

6.5 Summary of the chapter

This chapter was devoted to solving a thermoelasticity problem with the weighted residual method using the residual stress basis functions ϕ_i . We considered the problem of non-uniform heating of a thermoelastic annulus that induces strain incompatibility and renders the annulus residually stressed. We first solved for the approximate stress using the virtual work method employing two standard displacement bases: the free vibration modes and the eigenfunctions of the Laplace operator, both corresponding to the free-free boundary condition (Eq. 6.5). We saw that the approximated stress converges to the true stress, but the convergence is slow. Subsequently, we first used ϕ_i to approximate the stress using the weighted residual method directly, but without success. We then derived a useful characterization of harmonic functions in terms of residual stresses, using which we did a different weighted residual calculation and obtained the correct approximate stress using ϕ_i . The corresponding convergence was much faster than that obtained using the displacement based virtual work method. In the final section, we developed a new residual stress basis, one whose elements are zero at the boundary. We showed that if this new basis is used in a direct application of the weighted residual method to solve a thermoelasticity problem whose true solution is a residual stress field which is also zero at the boundary, then approximate solutions converge even more rapidly to the true solution.

We also discovered some new results along the way. We showed that a scalar function in 2D is harmonic if and only if it is orthogonal to all residual stress traces. This result is new because the study of residual stresses has so far been tied to the physical origins thereof, and such general properties have not been studied much. We proved that the inner product of any two planar residual stresses is equal to the inner product of their traces. We also showed that the mean of determinant of a planar residual stress is zero.

Perhaps the main practical takeaway from this chapter for an engineering audience is the insight into approximation methods like the weighted residual method or the least squares approximation method. We saw that for the thermoelasticity problem considered in this chapter, success depended on whether the basis used converges in the norm dictated by the order of the differential operator in the governing equation, after reduction to the lowest possible order using the divergence theorem (or similar manipulations).

We also obtained the following useful insight into the Galerkin method. When considering the weighted residual of the governing differential equation with a basis function, it is useful to integrate by parts or use the divergence theorem to see if the resulting boundary term drops out on account of a boundary condition satisfied by the true solution. The

resulting domain integral then has differentials of a reduced order, which allows us to choose the basis functions from a bigger space.

Finally, this chapter demonstrated direct use of the residual stress basis functions ϕ_i in solving forward problems using the weighted residual method. There is no comparable published result in the mechanics literature to the best of our knowledge.

Chapter 7

Comments on the modified extremization problems studied in this thesis

To obtain a basis for residual stress fields in Chapter 2, we used an indirect approach: we extremized a quadratic functional involving the gradient of an input stress and obtained a linear eigenvalue problem involving its Laplacian. The proof that the eigenfunctions exist and form a basis was lengthy and technical.

In subsequent chapters, we repeatedly employed this indirect approach of extremizing quadratic functionals involving gradient of an input field and obtained eigenvalue problems similar to the one obtained in Chapter 2. We showed that these eigenvalue problems yielded orthogonal sequences of eigenfunctions which were used for fitting or interpolation applications. In each of these applications, we assumed without proof that the sequence forms a basis for the corresponding space, and the excellent numerical support obtained justified our assumption.

Since these extremization problems (and the corresponding eigenvalue problems) are similar to that of Chapter 2, proofs that the corresponding sequences form bases could be attempted along similar lines, requiring only minor modifications. In this chapter, we discuss how the proof of Chapter 2 could be adapted for the modified extremization problems.

This chapter is arranged as follows. In Section 7.1, we present an outline of the proof presented in Chapter 2 for reference. In Section 7.2, we discuss the 1D eigenfunctions f , which have zero mean and zero boundary value, considered in Section 3.2.3.1. In Section

7.3, we discuss the axial stress eigenfunctions ϕ_{zz} considered in Problem 2 of Section 5.1.2. In Section 7.4, we discuss the eigenfunctions \mathbf{v} corresponding to the out of plane shear stresses considered in Problem 3 of Section 5.1.2. In Section 7.5, we discuss the spatially localized eigenfunctions φ considered in Section 5.2.2. Finally, in Section 7.6, we discuss the residual stress eigenfunctions with zero boundary value Φ , which were obtained in Section 6.4.

7.1 An outline of the proof presented in Chapter 2

To recall, we considered the following extremization problem in Chapter 2:

Find the stationary points of the functional

$$J_0(\boldsymbol{\sigma}) = \frac{1}{2} \int_{\Omega} \nabla \boldsymbol{\sigma} \cdot \nabla \boldsymbol{\sigma} \, dA \quad (7.1)$$

in the set

$$\mathcal{S} = \left\{ \boldsymbol{\sigma} \mid \boldsymbol{\sigma} \in \text{Sym}, \operatorname{div} \boldsymbol{\sigma} = \mathbf{0}, \boldsymbol{\sigma} \mathbf{n}|_{\partial\Omega} = \mathbf{0}, \int_{\Omega} \boldsymbol{\sigma} \cdot \boldsymbol{\sigma} \, dA < \infty, \int_{\Omega} \nabla \boldsymbol{\sigma} \cdot \nabla \boldsymbol{\sigma} \, dA < \infty \right\}, \quad (7.2)$$

subject to the normalization constraint $\int_{\Omega} \boldsymbol{\sigma} \cdot \boldsymbol{\sigma} \, dA = 1$.

We showed that the stationary points $\boldsymbol{\phi}$ are the solutions of a linear eigenvalue problem, and are mutually orthogonal in the L^2 inner product. The proof that they span \mathcal{S} , presented in Chapter 2 can be divided into two major parts: (1) *assuming* the existence of the eigenfunctions and proving by contradiction that they span \mathcal{S} , and (2) proving that the eigenfunctions exist.

We enumerate below the major steps involved in part (1):

Step 1a: We first showed that there are infinitely many eigenfunctions. To do so, we argued by contradiction, and assumed that there are only N eigenfunctions $\boldsymbol{\phi}_1$ to $\boldsymbol{\phi}_N$. We extremized J_0 within \mathcal{S}_{N^\perp} , the orthogonal complement of the span \mathcal{S}_N of $\boldsymbol{\phi}_k$ within \mathcal{S} . Using the orthogonality relations satisfied by $\boldsymbol{\phi}_k$, we showed that the solution of this new extremization problem satisfies the same conditions as $\boldsymbol{\phi}_k$, obtaining a contradiction. Hence, the eigenfunctions are infinitely many.

Step 1b: We then showed that the eigenfunctions span \mathcal{S} , again arguing by contradiction. We assumed that the eigenfunctions span a subspace \mathcal{S}_∞ of \mathcal{S} and extremized J_0 within $\mathcal{S}_{\infty^\perp}$, the orthogonal complement of \mathcal{S}_∞ within \mathcal{S} . We showed that the extremizer satisfies

the same conditions as ϕ_k , again obtaining a contradiction. Hence, the eigenfunctions span \mathcal{S} .

Part (2) of the proof, in which we showed that the minimizers of J_0 exist in the unit ball \mathcal{P} of \mathcal{S} , contained the following major steps:

Step 2a: To begin with, we noted that the problems of minimizing $J_0(\boldsymbol{\sigma})$ and minimizing $\hat{J}(\boldsymbol{\sigma}) = (2J_0(\boldsymbol{\sigma}))^{\frac{1}{2}} = \left(\int_{\Omega} \nabla \boldsymbol{\sigma} \cdot \nabla \boldsymbol{\sigma} dA \right)^{\frac{1}{2}}$ are equivalent. Since, the values of \hat{J} evaluated in \mathcal{P} have a greatest lower bound ψ_0 , there exists a minimizing sequence $(\boldsymbol{\sigma}_n)$ in \mathcal{P} such that

$$\lim_{n \rightarrow \infty} \hat{J}(\boldsymbol{\sigma}_n) = \psi_0.$$

Step 2b: Since residual stresses have zero mean, we were able to use Poincaré's inequality to show that $(\boldsymbol{\sigma}_n)$ is bounded in the H^1 norm. Consequently, there is a subsequence $(\boldsymbol{\sigma}_{n_k})$ that converges weakly in the H^1 norm and strongly in the L^2 norm to some $\boldsymbol{\sigma}_0$.

Step 2c: We then showed that $\boldsymbol{\sigma}_0$ belongs to the set \mathcal{P} .

Step 2d: We showed that \hat{J} is weak lower semi-continuous in the H^1 norm. Using this and Step 2a, we concluded $\hat{J}(\boldsymbol{\sigma}_0) = \psi_0$. Hence, at least one minimizer $\boldsymbol{\sigma}_0$ exists in the unit ball of \mathcal{S} .

Step 2e: The same line of argument was invoked repeatedly to show the existence of a minimizer in each \mathcal{S}_{N^\perp} , $N \in \mathbb{N}$.

We will see that for each of the extremization problems discussed in the subsequent chapters, a proof could be constructed along the same template as above, with small modifications to accommodate the requirements of each problem.

7.2 1D eigenfunctions f of Section 3.2.3.1

In Section 3.2.3.1, we obtained a sequence of 1D functions $f_k(\xi)$ defined on the unit interval $0 \leq \xi \leq 1$ such that each of these functions has zero mean and is zero on the boundary. We assumed there, without proof, that $f_k(\xi)$ span the set of functions on the same domain having zero mean and zero boundary values. We discuss below the modifications required if we were to construct a proof along the lines of Section 7.1.

Recall that we considered the following extremization problem in Section 3.2.3.1:

Find the stationary points of the functional

$$F_0(g) = \frac{1}{2} \int_0^1 g'^2 d\xi$$

in the set

$$\mathcal{S} = \left\{ g \mid g(0) = g(1) = 0, \int_0^1 g d\xi = 0, \int_0^1 g^2 d\xi < \infty, \int_0^1 g'^2 d\xi < \infty \right\}, \quad (7.3)$$

subject to the normalization constraint $\frac{1}{2} \int_0^1 g'^2 d\xi = 1$. Let us denote the set of g belonging to \mathcal{S} and satisfying this constraint as \mathcal{P} .

While the extremized functional is the same as that in Section 7.1, the set in which the extremizers are sought differs in the following aspects:

- g are 1D scalar functions while σ are symmetric second order tensor fields.
- There is no pointwise divergence constraint on g .
- g are zero at the boundary, while the $\mathbf{t} \otimes \mathbf{t}$ component of σ may be non-zero at the boundary.
- g satisfy an explicit integral constraint: they have zero mean. Note that while σ also satisfy this constraint, it does not need to be enforced explicitly because it follows from σ being divergence-free and traction-free.

We now run through Steps 1a through 2e of Section 7.1 and point out what changes due to the above differences.

Steps 1a and 1b: Since the eigenfunctions f_k satisfy the orthogonality conditions (Eq. 3.27)

$$\int_0^1 f'_i f'_j d\xi = \int_0^1 f_i f_j d\xi = 0, \quad i \neq j,$$

we obtain the same contradictions as Section 7.1, and we conclude that f_k span the set \mathcal{S} and its closure $\bar{\mathcal{S}}$.

Step 2a Since the extremized functional is the same, we obtain a minimizing sequence (g_n) here too.

Step 2b: Since the functions g have zero mean, we can use the Poincaré's inequality to show that (g_n) is bounded in the H^1 norm. Moreover, since g are zero on the boundary,

(g_n) belongs to the Sobolev space H_0^1 (the set of functions which have a finite H^1 norm and zero boundary value). Thus, there is a subsequence (g_{n_k}) that converges weakly in the H^1 norm and strongly in the L^2 norm to some $g_0 \in H_0^1$.

Step 2c: In showing that g_0 belongs to \mathcal{P} , we need to pay attention to the two conditions that we did not encounter in the proof of Section 7.1. The first condition is that g_0 is zero on the boundary; this is obvious since it belongs to the space H_0^1 . The second condition is that g_0 has zero mean, i.e.,

$$\int_0^1 g_0 d\xi = 0.$$

However, the above can be easily shown using the fact that g_{n_k} converges strongly in the L^2 norm to g_0 , as follows:

$$\left| \int_0^1 g_0 d\xi \right| = \left| \int_0^1 (g_0 - g_{n_k}) d\xi + \int_0^1 g_{n_k} d\xi \right| \leq \|g_0 - g_{n_k}\|_{L^2} \|1\|_{L^2} \rightarrow 0,$$

where the inequality follows from the Cauchy-Schwartz inequality.

Step 2d and 2e: These steps are identical to the corresponding steps in Section 7.1.

7.3 Axial stress eigenfunctions ϕ_{zz} of Section 5.1.2

In Problem 2 of Section 5.1.2, we obtained a sequence of orthogonal functions ϕ_{zz} corresponding to axial stresses that transmit zero net force and zero net bending moment across any lateral cross-section in a long prismatic body. To recall, these functions are solutions of the following extremization problem:

Find the stationary points of the functional

$$J_0(\sigma_{zz}) = \frac{1}{2} \int_{\Omega_l} \nabla \sigma_{zz} \cdot \nabla \sigma_{zz} dA$$

in the set

$$\mathcal{S} = \left\{ \sigma_{zz} \left| \int_{\Omega_l} \sigma_{zz}^2 dA < \infty, \int_{\Omega_l} \nabla \sigma_{zz} \cdot \nabla \sigma_{zz} dA < \infty, \int_{\Omega_l} \sigma_{zz} dA = 0, \int_{\Omega_l} \mathbf{r} \sigma_{zz} dA = \mathbf{0} \right. \right\},$$

subject to the constraint $\int_{\Omega_l} \sigma_{zz}^2 dA = 1$. We denote the set of unit-norm elements belonging to \mathcal{S} as \mathcal{P} .

Again, the functional whose stationary points are sought is the same as that in Section 7.1. However, the set in which the stationary points are sought differs from the corresponding set in Section 7.1 in the following aspects:

- σ_{zz} are 1D scalar functions while $\boldsymbol{\sigma}$ are symmetric second order tensor fields.
- There is no pointwise divergence constraint on σ_{zz} .
- $\boldsymbol{\sigma}$ satisfies the traction-free boundary condition, while there is no condition on the boundary on σ_{zz} .
- σ_{zz} satisfy the explicit integral constraint of having zero mean. We repeat that while $\boldsymbol{\sigma}$ also satisfy this constraint, it does not need to be enforced explicitly because it follows from $\boldsymbol{\sigma}$ being divergence-free and traction-free.
- σ_{zz} also satisfy an additional integral constraint of having zero first moment:

$$\int_{\Omega_l} \mathbf{r} \sigma_{zz} dA = \mathbf{0}.$$

As before, we look at Steps 1a through 2e and point out the modifications required.

Steps 1a and 1b: Since the eigenfunctions ϕ_{zzk} satisfy the orthogonality conditions (Eq. 5.10)

$$\int_{\Omega_l} \phi_{zzi} \phi_{zzj} dA = \int_{\Omega_l} \nabla \phi_{zzi} \cdot \nabla \phi_{zzj} dA = 0,$$

we obtain the same contradictions as Section 7.1, and we conclude that ϕ_{zzk} span the set \mathcal{S} and its closure $\bar{\mathcal{S}}$.

Step 2a Since the extremized functional is the same, we obtain a minimizing sequence (σ_{zzn}) here too.

Step 2b: Since the functions σ_{zz} have zero mean, we can use Poincaré's inequality to show that (σ_{zzn}) is bounded in the H^1 norm. Thus, there is a subsequence (σ_{zzn_k}) that converges weakly in the H^1 norm and strongly in the L^2 norm to some σ_{zz0} .

Step 2c: In showing that σ_{zz0} belongs to \mathcal{P} , we need to pay attention to the two conditions involving the integral constraints that we did not encounter in the proof of Section 7.1. Let us look at them one by one.

We first show that

$$\int_{\Omega_l} \sigma_{zz0} dA = 0.$$

Using the fact that each member of the sequence (σ_{zzn_k}) has zero mean, and that this sequence converges strongly in the L^2 norm to σ_{zz0} , we have

$$\left| \int_{\Omega_l} \sigma_{zz0} dA \right| = \left| \int_{\Omega_l} (\sigma_{zz0} - \sigma_{zzn_k}) dA + \int_{\Omega_l} \sigma_{zzn_k} dA \right| \leq \|\sigma_{zz0} - \sigma_{zzn_k}\|_{L^2} \|1\|_{L^2} \rightarrow 0,$$

where the inequality follows from the Cauchy-Schwartz inequality.

We also need to show that

$$\int_{\Omega} \mathbf{r} \sigma_{zz0} dA = \mathbf{0}.$$

Again, using the fact that each member of the sequence (σ_{zzn_k}) satisfies the above condition, we have

$$\begin{aligned} \left| \int_{\Omega_l} \mathbf{r} \sigma_{zz0} dA \right| &= \left| \int_{\Omega_l} \mathbf{r} (\sigma_{zz0} - \sigma_{zzn_k}) dA + \int_{\Omega_l} \mathbf{r} \sigma_{zzn_k} dA \right| \leq \|\mathbf{r} (\sigma_{zz0} - \sigma_{zzn_k})\|_{L^2} \|1\|_{L^2} \\ &\leq \|\mathbf{r}\|_{\infty} \sqrt{|\Omega_l|} \|\sigma_{zz0} - \sigma_{zzn_k}\|_{L^2} \rightarrow 0, \end{aligned}$$

where $\|\mathbf{r}\|_{\infty}$ is the supremum of magnitude of \mathbf{r} on Ω_l and $|\Omega_l|$ is the area of Ω_l .

Step 2d and 2e: These steps are identical to the corresponding steps in Section 7.1.

7.4 Out of plane shear stress eigenfunctions \mathbf{v} of Section 5.1.2

In Problem 3 of Section 5.1.2, we obtained functions \mathbf{v} with the following orthogonality property (Eq. 5.16):

$$\int_{\Omega_l} \mathbf{v}_i \cdot \mathbf{v}_j dA = \int_{\Omega_l} \nabla \mathbf{v}_i \cdot \nabla \mathbf{v}_j dA = 0, \quad i \neq j.$$

These functions correspond to the out of plane shear stress components in an infinitely long prismatic body with no stress variation in the axial direction. They are solutions of the following extremization problem:

Find the stationary points of the functional

$$J_0(\mathbf{v}) = \frac{1}{2} \int_{\Omega_l} \nabla \mathbf{v} \cdot \nabla \mathbf{v} dA$$

over the set

$$\mathcal{S} = \left\{ \mathbf{v} \left| \operatorname{div} \mathbf{v} = 0, \mathbf{v} \cdot \mathbf{n}|_{\partial\Omega_l} = 0, \int_{\Omega_l} \mathbf{v} \cdot \mathbf{v} dA < \infty, \int_{\Omega_l} \nabla \mathbf{v} \cdot \nabla \mathbf{v} dA < \infty, \int_{\Omega_l} \mathbf{r} \times \mathbf{v} dA = \mathbf{0} \right. \right\},$$

subject to the normalization constraint $\int_{\Omega_l} \mathbf{v} \cdot \mathbf{v} dA = 1$. We denote the set of \mathbf{v} belonging to \mathcal{S} and satisfying this normalization constraint as \mathcal{P} .

The set in which the stationary points are sought differs from that of Section 7.1 in the following:

- \mathbf{v} are vector fields while $\boldsymbol{\sigma}$ are symmetric second-order tensor fields.
- \mathbf{v} satisfy an additional integral constraint corresponding to zero net torque:

$$\int_{\Omega_l} \mathbf{r} \times \mathbf{v} dA = \mathbf{0}.$$

Thus we see that the above problem differs from that of Section 7.1, apart from the order of the input field, only in the presence of an additional integral constraint in the former. We have seen in the previous sections that this has a bearing only on Step 2c of the proof template that we have been following, wherein we need to show that the limit \mathbf{v}_0 of the minimizing sequence (\mathbf{v}_n) satisfies

$$\int_{\Omega_l} \mathbf{r} \times \mathbf{v}_0 dA = \mathbf{0}.$$

We show this now. Let us first note that since \mathbf{r} and $\mathbf{u}_n = \mathbf{v}_0 - \mathbf{v}_n$ are planar vectors,

$$\mathbf{r} \times \mathbf{u}_n = (xu_{yn} - yu_{xn}) \mathbf{e}_z,$$

where $u_{xn} = \mathbf{u}_n \cdot \mathbf{e}_x$ and $u_{yn} = \mathbf{u}_n \cdot \mathbf{e}_y$. Then,

$$\begin{aligned} \left| \int_{\Omega_l} \mathbf{r} \times \mathbf{v}_0 dA \right| &= \left| \int_{\Omega_l} \mathbf{r} \times (\mathbf{v}_0 - \mathbf{v}_n) dA + \int_{\Omega_l} \mathbf{r} \times \mathbf{v}_n dA \right| = \left| \int_{\Omega_l} \mathbf{r} \times \mathbf{u}_n dA \right| \\ &= \left| \int_{\Omega_l} (xu_{yn} - yu_{xn}) dA \right| \leq \|xu_{yn} - yu_{xn}\|_{L^2} \|1\|_{L^2}. \end{aligned} \quad (7.4)$$

(\mathbf{v}_n) converging strongly to \mathbf{v}_0 in the L^2 norm means that

$$\|\mathbf{v}_0 - \mathbf{v}_n\|_{L^2}^2 = \|\mathbf{u}_n\|_{L^2}^2 \rightarrow 0,$$

which in turn implies that

$$\int_{\Omega_l} (u_{xn}^2 + u_{yn}^2) dA \rightarrow 0,$$

or,

$$\int_{\Omega_l} u_{xn}^2 dA \rightarrow 0 \quad \text{and} \quad \int_{\Omega_l} u_{yn}^2 dA \rightarrow 0. \quad (7.5)$$

So,

$$\begin{aligned} \|xu_{yn} - yu_{xn}\|_{L^2}^2 &= \int_{\Omega_l} (xu_{yn} - yu_{xn})^2 dA = \int_{\Omega_l} (x^2u_{yn}^2 + y^2u_{xn}^2 - 2xyu_{xn}u_{yn}) dA \\ &\leq \int_{\Omega_l} (x^2u_{yn}^2 + y^2u_{xn}^2 + 2|x||y||u_{xn}||u_{yn}|) dA \\ &\leq \int_{\Omega_l} \{x^2u_{yn}^2 + y^2u_{xn}^2 + |x||y|(u_{xn}^2 + u_{yn}^2)\} dA \\ &\leq \|x\|_\infty^2 \int_{\Omega_l} u_{yn}^2 dA + \|y\|_\infty^2 \int_{\Omega_l} u_{xn}^2 dA + \|xy\|_\infty \int_{\Omega_l} (u_{xn}^2 + u_{yn}^2) dA \rightarrow 0, \end{aligned}$$

where in the last step we have used Eq. 7.5. Substituting the above result in Eq. 7.4, we obtain

$$\int_{\Omega_l} \mathbf{r} \times \mathbf{v}_0 dA = \mathbf{0}.$$

The rest of the proof follows along identical lines to that in Section 7.1.

7.5 Spatially localized residual stress eigenfunctions φ of Section 5.2.2

In Section 5.2.2, we obtained a sequence of functions (φ_n) which are localized in a 2D region, decaying rapidly away from it. These functions are the solutions of the following extremization problem:

Find the stationary points of the functional

$$J_0(\boldsymbol{\sigma}) = \frac{1}{2} \int_{\Omega} w_1 \nabla \boldsymbol{\sigma} \cdot \nabla \boldsymbol{\sigma} dA$$

in the set

$$\mathcal{S} = \left\{ \boldsymbol{\sigma} \mid \boldsymbol{\sigma} \in \text{Sym}, \operatorname{div} \boldsymbol{\sigma} = \mathbf{0}, \boldsymbol{\sigma} \mathbf{n}|_{\partial\Omega} = \mathbf{0}, \int_{\Omega} \boldsymbol{\sigma} \cdot \boldsymbol{\sigma} dA < \infty, \int_{\Omega} \nabla \boldsymbol{\sigma} \cdot \nabla \boldsymbol{\sigma} dA < \infty \right\}.$$

subject to the normalization constraint

$$\int_{\Omega} w_2 \boldsymbol{\sigma} \cdot \boldsymbol{\sigma} dA = 1.$$

We denote the set of $\boldsymbol{\sigma}$ that belong to \mathcal{S} and satisfy the above constraint as \mathcal{P} .

We assumed that w_1 and w_2 are smooth functions which are positive everywhere.

This time we see that the set over which the stationary points of the functional are sought is the same as that in Section 7.1, however the functional itself includes an extra weighting function. Moreover, we saw that the stationary points satisfy a different orthogonality property (Eq. 5.29):

$$\int_{\Omega} w_1 \nabla \boldsymbol{\varphi}_i \cdot \nabla \boldsymbol{\varphi}_j dA = \int_{\Omega} w_2 \boldsymbol{\varphi}_i \cdot \boldsymbol{\varphi}_j dA = (\boldsymbol{\varphi}_i, \boldsymbol{\varphi}_j)_w = 0.$$

We now look at steps 1a through 2e of the proof template of Section 7.1, and point out the modifications required.

Step 1a: Since the functions $\boldsymbol{\varphi}$ are orthogonal in a different inner product (than the L^2 inner product that we have been using), the algebra involved in proving that there are infinitely many eigenfunctions is slightly more involved, but we will see below that the principles remain the same.

We argue by contradiction.

Let us assume that only a finite number N of eigenvalue-eigenfunction pairs $(\lambda_p, \boldsymbol{\varphi}_p, \boldsymbol{\mu}_p)$ exist.

Let \mathcal{S}_N be the subspace of \mathcal{S} spanned by the finite sequence $(\boldsymbol{\varphi}_p)$, $p = 1, 2, \dots, N$. Let $\mathcal{S}_{N\perp}$ be the orthogonal complement (in the weighted inner product) of \mathcal{S}_N in \mathcal{S} . Let us now extremize J_0 within $\mathcal{S}_{N\perp}$. To the extremizer $\boldsymbol{\sigma}$, restriction to $\mathcal{S}_{N\perp}$ adds N integral constraints to the previous extremization problem, namely

$$\int_{\Omega} w_2 \boldsymbol{\varphi}_p \cdot \boldsymbol{\sigma} dA = 0, \quad p = 1, 2, \dots, N, \quad (7.6)$$

for which we introduce N new scalar Lagrange multipliers, $\nu_1, \nu_2, \dots, \nu_N$, and find that the extremizer $\boldsymbol{\sigma}$ satisfies the following eigenvalue problem:

$$\begin{aligned} -w_1 \Delta \boldsymbol{\sigma} - \nabla \boldsymbol{\sigma} \odot \nabla w_1 + \nabla_s \boldsymbol{\mu} &= \lambda w_2 \boldsymbol{\sigma} + \sum_{p=1}^N \nu_p w_2 \boldsymbol{\varphi}_p & \text{and} & \quad \text{div } \boldsymbol{\sigma} = \mathbf{0} & \text{in } \Omega, \\ \nabla_n \boldsymbol{\sigma} \cdot (\mathbf{t} \otimes \mathbf{t}) &= 0 & \text{and} & \quad \boldsymbol{\sigma} \mathbf{n} = \mathbf{0} & \text{on } \partial\Omega. \end{aligned} \quad (7.7)$$

Consider the inner product of the first of Eq. 7.7 with any eigenfunction φ_k , $1 \leq k \leq N$, i.e.,

$$\int_{\Omega} (-w_1 \Delta \sigma - \nabla \sigma \odot \nabla w_1 + \nabla_s \mu) \cdot \varphi_k dA = \lambda \int_{\Omega} w_2 \sigma \cdot \varphi_k dA + \sum_{p=1}^N \nu_p \int_{\Omega} w_2 \varphi_p \cdot \varphi_k dA. \quad (7.8)$$

Let us first consider the term $(-w_1 \Delta \sigma - \nabla \sigma \odot \nabla w_1) \cdot \varphi_k$. Using indicial notations, it simplifies to (omitting the index k for clarity):

$$\begin{aligned} (-w_1 \Delta \sigma - \nabla \sigma \odot \nabla w_1) \cdot \varphi &= -w_1 \sigma_{ij, ll} \varphi_{ij} - \sigma_{ij, l} w_{1, l} \varphi_{ij} \\ &= (-w_1 \sigma_{ij, l} \varphi_{ij})_{, l} + w_{1, l} \sigma_{ij, l} \varphi_{ij} + w_1 \sigma_{ij, l} \varphi_{ij, l} - \sigma_{ij, l} w_{1, l} \varphi_{ij} = (-w_1 \sigma_{ij, l} \varphi_{ij})_{, l} + w_1 \sigma_{ij, l} \varphi_{ij, l}. \end{aligned}$$

Thereupon using the divergence theorem, we have

$$\begin{aligned} \int_{\Omega} (-w_1 \Delta \sigma - \nabla \sigma \odot \nabla w_1) \cdot \varphi_k dA &= - \int_{\partial \Omega} w_1 \nabla_n \sigma \cdot \varphi_k ds + \int_{\Omega} w_1 \nabla \sigma \cdot \nabla \varphi_k dA \\ &= \int_{\Omega} w_1 \nabla \sigma \cdot \nabla \varphi_k dA, \end{aligned} \quad (7.9)$$

where the boundary integral drops out because $\varphi_k = \gamma \mathbf{t} \otimes \mathbf{t}$ for some scalar function γ on the boundary, and $\nabla_n \sigma \cdot (\mathbf{t} \otimes \mathbf{t}) = 0$ on the boundary.

Let us now return to Eq. 7.8. By the reasoning in Appendix C, the $\int_{\Omega} \nabla_s \mu \cdot \varphi_k dA$ term drops out. By Eq. 7.6, the $\lambda \int_{\Omega} w_2 \sigma \cdot \varphi_k dA$ term drops out. By orthonormality of the eigenfunctions, $\sum_{p=1}^N \nu_p \int_{\Omega} w_2 \varphi_p \cdot \varphi_k dA$ contributes just ν_k . Thus, we get

$$\int_{\Omega} w_1 \nabla \sigma \cdot \nabla \varphi_k dA = \nu_k. \quad (7.10)$$

However, since σ is an element of \mathcal{S} and also orthogonal to φ_k , Eq. 5.28 shows that

$$\int_{\Omega} \nabla \varphi_k \cdot \nabla \sigma dA = 0.$$

Thus $\nu_k = 0$ for $1 \leq k \leq N$. Inserting these zeros in Eq. 7.7 we obtain exactly Eq. 5.22, which shows that the new solution merely adds another element to the existing sequence.

We conclude that there are infinitely many eigenfunctions.

Step 1b: We use the same ideas above to show that the eigenfunctions span \mathcal{S} .

Step 2a: Since w_1 is assumed to be positive everywhere, the functional $\hat{J} = (2J_0)^{\frac{1}{2}}$ is bounded below by zero on \mathcal{P} . Thus, there exists a minimizing sequence (σ_n) .

Step 2b: The details in this step remain the same as in Section 7.1. We conclude that (σ_n) converges weakly in the H^1 norm and strongly in the L^2 norm to some σ_0 .

Step 2c: In this step, we need to show that σ_0 belongs to \mathcal{P} . For that, we need to show that σ_0 is divergence-free, traction-free, has finite H^1 norm, and has unit norm. The proof of the first three conditions is identical to that of Section 7.1. We prove that σ_0 has unit norm below.

By the Cauchy-Schwartz inequality, and the fact that $\|\sigma_n\|_w = 1$,

$$\begin{aligned} \|\sigma_0 - \sigma_n\|_w^2 &= \|\sigma_0\|_w^2 + \|\sigma_n\|_w^2 - 2 \int_{\Omega} w_2 \sigma_0 \cdot \sigma_n \, dA \\ &\geq \|\sigma_0\|_w^2 + 1 - 2 \|\sigma_0\|_w = (\|\sigma_0\|_w - 1)^2. \end{aligned} \quad (7.11)$$

But,

$$\begin{aligned} \|\sigma_0 - \sigma_n\|_w^2 &= \int_{\Omega} w_2 (\sigma_0 - \sigma_n) \cdot (\sigma_0 - \sigma_n) \, dA \\ &\leq \|w_2\|_{\infty} \int_{\Omega} (\sigma_0 - \sigma_n) \cdot (\sigma_0 - \sigma_n) \, dA = \|w_2\|_{\infty} \|\sigma_0 - \sigma_n\|_{L^2}^2, \end{aligned}$$

which implies that

$$\|\sigma_0 - \sigma_n\|_w^2 \rightarrow 0$$

since (σ_n) converges strongly in the L^2 norm to σ_0 and $\|w_2\|_{\infty}$ is bounded.

So, from Eq. 7.11, we have

$$\|\sigma_0\|_w = 1.$$

Step 2d: Next, we show that \hat{J} is strong lower semi-continuous in the H^1 norm. This is true because, for a given σ ,

$$\begin{aligned} 0 \leq \hat{J}(\sigma) &= \left(\int_{\Omega} w_1 \nabla \sigma \cdot \nabla \sigma \, dA \right)^{\frac{1}{2}} \leq \|w_1\|_{\infty}^{\frac{1}{2}} \left(\int_{\Omega} \nabla \sigma \cdot \nabla \sigma \, dA \right)^{\frac{1}{2}} \\ &\leq \|w_1\|_{\infty}^{\frac{1}{2}} \left(\int_{\Omega} \sigma \cdot \sigma \, dA + \int_{\Omega} \nabla \sigma \cdot \nabla \sigma \, dA \right)^{\frac{1}{2}} = \|w_1\|_{\infty}^{\frac{1}{2}} \|\sigma\|_{H^1}. \end{aligned}$$

Consequently, if a sequence $(\tilde{\sigma}_m)$ converges strongly to some $\tilde{\sigma}_0$ in the H^1 norm, $\hat{J}(\tilde{\sigma}_m) = \hat{J}(\tilde{\sigma}_0)$. Thus, \hat{J} is strong lower semi-continuous in the H^1 norm.

It is straightforward to show that \hat{J} is a norm, and hence convex. Consequently, it is weak lower semi-continuous in the H^1 norm.

We then proceed as in Section 7.1 to conclude that at least one minimizer exists in $\mathcal{P} : \sigma_0$.

Step 2e: Using the above procedure repeatedly, we can show the existence of a minimizer in each $\mathcal{S}_{N\perp}$, $N \in \mathbb{N}$.

7.6 Residual stress eigenfunctions Φ with zero boundary value of Section 6.4

In section 7.6, we obtained an orthogonal sequence (Φ_n) of residual stresses which are zero on the boundary. Those functions are the solutions of the following extremization problem:

Find the stationary points of the functional

$$J_0(\sigma) = \frac{1}{2} \int_{\Omega} \nabla \sigma \cdot \nabla \sigma \, dA$$

over those elements of the set

$$\mathcal{S} = \left\{ \sigma \mid \sigma \in \text{Sym}, \operatorname{div} \sigma = \mathbf{0}, \sigma|_{\partial\Omega} = \mathbf{0}, \int_{\Omega} \sigma \cdot \sigma \, dA < \infty, \int_{\Omega} \nabla \sigma \cdot \nabla \sigma \, dA < \infty \right\},$$

which satisfy

$$\int_{\Omega} \sigma \cdot \sigma \, dA = 1.$$

As we mentioned in Section 6.4, the only difference between this problem and that of Chapter 2 is that the elements of the set \mathcal{S} are zero at the boundary. We have seen in the previous sections of this chapter that this difference has a bearing only on Step 2d of the proof template of Section 7.1, wherein we now need to show that the limit of the minimizing sequence σ_0 will be zero at the boundary. This is straightforward because the minimizing sequence is bounded in the Sobolev space H_0^1 , and the weak limit of a subsequence σ_0 also belongs to H_0^1 . As a result, σ_0 is zero at the boundary.

Finally, since any residual stress of interest (even with non-zero boundary value) is arbitrarily close in the L^2 norm to a residual stress which is zero on the boundary, Φ span the set of *all* residual stresses with finite L^2 norm.

7.7 Summary of the chapter

In this chapter, we saw how the proof of Chapter 2 may be modified for the extremization problems considered in the subsequent chapters, if similar formal proofs are to be attempted. We saw that most of the proof remains unaltered in spirit in each of these cases, with only the algebraic details varying from case to case.

Chapter 8

Conclusions and future work

8.1 Conclusions

In this thesis, we obtained a sequence of second-order tensors that span all continuous residual stress fields in the L^2 and the H^1 norms, and residual stress fields with simple discontinuities in the L^2 norm. We demonstrated that the basis functions ϕ_i can be used for fitting given but arbitrary residual stress fields (Chapter 4), interpolating residual stresses (Chapter 5), and representing residual stress fields in forward problems (Chapter 6). There is no comparable deliberate construction of such a basis in the mechanics literature, to the best of our knowledge.

We used an indirect approach to develop these basis functions by considering the extremization of a quadratic functional involving the gradient of an input stress field. We obtained a linear eigenvalue problem, and we showed that the eigenfunctions span all residual stress fields with sufficient regularity. The main portion of our proof of the eigenfunctions forming a basis uses simple ideas accessible to an audience with no background in functional analysis.

We computed the basis functions using the FEM for arbitrarily shaped bodies, and we also developed semi-numerical methods for some special geometries. In particular, to develop the semi-numerical methods for a rectangle and an annular prism, we used ideas that are new to the best of our knowledge. For each of these geometries, we used a sequence of 1D functions with zero mean and zero boundary values to develop a complete representation of all residual stress fields in that geometry. We used these representations to convert the foregoing eigenvalue problem, which is a PDE system, into a system of algebraic equations.

We presented ample evidence that ϕ_i form a basis for residual stresses irrespective of the material properties or the deformation history of the stressed component. We successfully fitted hypothetical residual stresses, elastic stresses from shrink fitting and non-uniform heating, and stresses obtained from metal forming of elasto-plastic workpieces with different strain-hardening models. Moreover, since ϕ_i form a basis in the H^1 norm, we noted that for smooth fields the fitted stresses converge rapidly to the actual fields.

We demonstrated that our theoretical formulation is amenable to some useful modifications. We modified our formulation by introducing three different normalization constraints to obtain a basis for residual stress fields in infinitely long prismatic geometries. We illustrated that this basis gives better convergence than other standard bases such as the Laplace operator eigenfunctions and the Stokes operator eigenfunctions. We also modified our theoretical formulation by weighting the functional J_0 and the normalization constraint to obtain spatially localized eigenfunctions.

We also demonstrated direct use of the residual stress basis functions ϕ_i in solving a forward problem using the weighted residual method. There is no comparable published solution in the mechanics literature to the best of our knowledge. Along the way, we noted some interesting new results concerning planar residual stresses. We found that a function in 2D is harmonic if and only if it is orthogonal to all residual stress traces. We showed that the inner product of any two planar residual stress fields is equal to the inner product of their traces, and that the mean of the determinant of a planar residual stress is zero. We also offered some useful insights into the workings of approximation methods like the Galerkin method and the least squares method. We hope that these insights will be useful for an engineering audience in avoiding some potential pitfalls while using such methods.

The importance of our work is two-fold. The first is academic: this work presents a new framework to discuss residual stresses without tying them to deformation history or constitutive behaviour. The second is practical: this work opens the door to useful new computations in industrial settings, for interpolation and representation of residual stresses.

We now discuss some ideas for future work.

8.2 Future work

We list below some work that could perhaps be undertaken in future.

Modification of our formulation to obtain other bases: We have demonstrated in Chapter 5 that our theoretical formulation is quite amenable to modifications. We believe that our framework is general enough to obtain bases for other constrained vector/tensor spaces. For instance, if we wish to develop a basis for irrotational fluids (which are not necessarily incompressible), we might include those vector fields \mathbf{v} in the set \mathcal{S} that satisfy the constraint

$$\operatorname{curl} \mathbf{v} = \mathbf{0} \quad \text{in } \Omega.$$

It remains to be seen if the resulting eigenvalue problem (with the same, or perhaps a different, J_0) yields a basis, but our framework offers a fresh possibility that uses only basic calculus of variations for the actual computations.

Capturing residual stresses with point singularities: Since our basis functions (including the spatially localized eigenfunctions developed in Chapter 5) have high regularity, they give slow convergence for residual stress fields in L^2 with point singularities, such as those due to dislocations or cracks. We do not know if our formulation can be adapted to cover such cases.

Infinite domains: In this work, we have assumed the domain of interest Ω to be finite. However, there are many problems in mechanics where an infinite domain is of interest. We do not presently know how to develop general descriptions of stresses in infinite domains.

Theoretical stability of our FEM formulation: In our FEM formulation (Section 3.1), we used the 8-noded serendipity elements for the interpolation of the stress components, while the Lagrange multipliers were assumed to be piecewise constant. Although we did not theoretically prove the stability of our FEM formulation, we gave ample evidence of it. In addition to providing numerical support, we noted the similarity of our eigenvalue problem with the Stokes operator used in fluid mechanics. It is established for the Stokes operator FEM formulation that the 8-noded serendipity elements (with piecewise constant pressure) satisfy the inf-sup condition guaranteeing stability [53]. Extending this result to our framework might be attempted in future work.

Theoretical estimates of convergence rate: In Chapter 4, we observed from the log-log plots of the fitting errors E_N and \tilde{E}_N that they follow a power law decay for large N . For smooth fields, these decay rates were like N^{-3} and N^{-1} , respectively. In future work, formal proof of such convergence rates could be attempted.

Removal of Gibbs oscillations: In the shrink fitting example in Chapter 4, we saw Gibbs oscillations in the fit for $\sigma_{\theta\theta}$ since the candidate hoop stress was discontinuous (Figure 4.7). The Fourier series also exhibits such oscillations when used to fit discontinuous functions. There are ways of quenching those oscillations without affecting the convergence, one of them being the ‘sigma approximation’ [69]. In future work, ways to remove these Gibbs oscillations could be studied.

Appendix A

Proof that the stationary points are sufficiently regular

We restrict attention to the set of smooth compactly supported ζ in Eq. 2.6 of Chapter 2 (note that the infinitesimal variations ζ belong to the set \mathcal{R} defined in Eq. 2.5). Denoting the distribution $\Delta\sigma - \nabla\mu + \lambda\sigma$ as \mathcal{D} , we have that for such ζ ,

$$\mathcal{D}(\zeta) = 0. \tag{A.1}$$

Since \mathcal{D} acts linearly on ζ , we can scale ζ arbitrarily to conclude from the above equation that

$$\mathcal{D}(\Phi) = 0 \tag{A.2}$$

for all Φ that are symmetric, smooth and supported compactly in Ω . This means that \mathcal{D} is a skew-symmetric distribution. Adding \mathcal{D} to its transpose, we obtain, in a distributional sense,

$$\Delta\sigma = \nabla_s\mu - \lambda\sigma, \tag{A.3}$$

where

$$\nabla_s\mu = \frac{\nabla\mu + (\nabla\mu)^T}{2}.$$

The function $\lambda\sigma$ is square integrable. The Lagrange multiplier μ is a construct, and can be assumed to have a square integrable gradient. Then, from Eq. A.3, $\Delta\sigma$ is a square integrable function.

Finally, for functions with square integrable gradient and square integrable Laplacian, the normal gradient at the boundary $\nabla_n\sigma$ ($= \sigma_{ij,k}n_k$ in indicial notation) makes sense through

the following relation:

$$\int_{\partial\Omega} \nabla_n \boldsymbol{\sigma} \cdot \boldsymbol{\sigma} \, ds = \int_{\Omega} \Delta \boldsymbol{\sigma} \cdot \boldsymbol{\sigma} \, dA + \int_{\Omega} \nabla \boldsymbol{\sigma} \cdot \nabla \boldsymbol{\sigma} \, dA. \quad (\text{A.4})$$

Technically, the left hand side in the above equation is a duality product between $\nabla_n \boldsymbol{\sigma}$ and $\boldsymbol{\sigma}$, considered as elements of Sobolev spaces $H^{-1/2}(\partial\Omega)$ and $H^{1/2}(\partial\Omega)$, respectively (e.g., see Eq. IV.10, Page 248 of [45]).

Hence, although the elements of set \mathcal{S} do not in general have the required regularity for us to proceed from Eq. 2.6 to Eq. 2.7, we have concluded in this section that a stationary point $\boldsymbol{\sigma}$ possesses enough regularity enabling us to carry out the analysis in Chapter 2.

Appendix B

Sufficient conditions for a stationary point

In this section, we show that if a unit-normed $\boldsymbol{\sigma}$ satisfies Eqs. 2.12, it must be a stationary point of J_0 on the unit ball of \mathcal{S} .

If $\boldsymbol{\sigma}$ is perturbed infinitesimally to a unit-normed element $\boldsymbol{\sigma} + \boldsymbol{\zeta} \in \mathcal{S}$, it is clear that $\text{div } \boldsymbol{\zeta} = \mathbf{0}$ and $\boldsymbol{\zeta} \mathbf{n} = \mathbf{0}$. Moreover, up to first order,

$$1 = \int_{\Omega} (\boldsymbol{\sigma} + \boldsymbol{\zeta}) \cdot (\boldsymbol{\sigma} + \boldsymbol{\zeta}) dA = \int_{\Omega} \boldsymbol{\sigma} \cdot \boldsymbol{\sigma} dA + 2 \int_{\Omega} \boldsymbol{\sigma} \cdot \boldsymbol{\zeta} dA = 1 + 2 \int_{\Omega} \boldsymbol{\sigma} \cdot \boldsymbol{\zeta} dA,$$

and hence,

$$\int_{\Omega} \boldsymbol{\sigma} \cdot \boldsymbol{\zeta} dA = 0. \quad (\text{B.1})$$

We will need this result below.

Let us now evaluate J_0 at $\boldsymbol{\sigma} + \boldsymbol{\zeta}$:

$$J_0(\boldsymbol{\sigma} + \boldsymbol{\zeta}) = \frac{1}{2} \int_{\Omega} \nabla(\boldsymbol{\sigma} + \boldsymbol{\zeta}) \cdot \nabla(\boldsymbol{\sigma} + \boldsymbol{\zeta}) dA = J_0(\boldsymbol{\sigma}) + \int_{\Omega} \nabla \boldsymbol{\sigma} \cdot \nabla \boldsymbol{\zeta} dA, \quad (\text{B.2})$$

where we have ignored the second order term. Using integration by parts and the divergence theorem on the term $\int_{\Omega} \nabla \boldsymbol{\sigma} \cdot \nabla \boldsymbol{\zeta} dA$, we obtain

$$\int_{\Omega} \nabla \boldsymbol{\sigma} \cdot \nabla \boldsymbol{\zeta} dA = \int_{\partial\Omega} \nabla_n \boldsymbol{\sigma} \cdot \boldsymbol{\zeta} ds - \int_{\Omega} \Delta \boldsymbol{\sigma} \cdot \boldsymbol{\zeta} dA. \quad (\text{B.3})$$

Since $\boldsymbol{\zeta} \mathbf{n} = \mathbf{0}$ on $\partial\Omega$, by the reasoning given after Eq. 2.10, $\boldsymbol{\zeta} = \kappa(s) \mathbf{t} \otimes \mathbf{t}$ for some boundary function $\kappa(s)$. Substituting this into the boundary integral of Eq. B.3 and using

the natural boundary condition $\nabla_n \boldsymbol{\sigma} \cdot (\mathbf{t} \otimes \mathbf{t}) = 0$, we see that the boundary integral drops out. Using the first of Eqs. 2.12 and Eq. B.1, we can simplify the domain integral in Eq. B.3 as

$$\int_{\Omega} \Delta \boldsymbol{\sigma} \cdot \boldsymbol{\zeta} dA = \int_{\Omega} (\nabla_s \boldsymbol{\mu} - \lambda \boldsymbol{\sigma}) \cdot \boldsymbol{\zeta} dA = \int_{\Omega} \nabla_s \boldsymbol{\mu} \cdot \boldsymbol{\zeta} dA$$

The right-most term in the above equation is the inner product of a gradient function and a divergence free function, and we show in Appendix C that it is zero. Thus,

$$\int_{\Omega} \nabla \boldsymbol{\sigma} \cdot \nabla \boldsymbol{\zeta} dA = 0, \quad (\text{B.4})$$

and we conclude from Eq. B.2 that, up to first order,

$$J_0(\boldsymbol{\sigma}) = J_0(\boldsymbol{\sigma} + \boldsymbol{\zeta})$$

for arbitrary infinitesimal perturbations on the unit ball of \mathcal{S} . Thus, if a unit-normed $\boldsymbol{\sigma}$ satisfies Eqs. 2.12, it must be a stationary point of J_0 on the unit ball of \mathcal{S} .

Appendix C

Proof of Eq. 2.14

First, we show that

$$\int_{\Omega} \nabla_s \boldsymbol{\mu} \cdot \boldsymbol{\sigma} \, dA = 0 \quad (\text{C.1})$$

in Eq. 2.13. Note that

$$\nabla_s \boldsymbol{\mu} \cdot \boldsymbol{\sigma} = \frac{\mu_{i,j} + \mu_{j,i}}{2} \sigma_{ij} = \mu_{i,j} \sigma_{ij} = (\mu_i \sigma_{ij})_{,j} - \mu_i \sigma_{ij,j} = (\mu_i \sigma_{ij})_{,j}$$

where we have used $\sigma_{ij} = \sigma_{ji}$ and $\sigma_{ij,j} = 0$. Using the divergence theorem,

$$\int_{\Omega} (\mu_i \sigma_{ij})_{,j} \, dA = \int_{\partial\Omega} \mu_i \sigma_{ij} n_j \, ds = 0$$

because $\sigma_{ij} n_j = 0$ on $\partial\Omega$. Thus Eq. 2.13 becomes

$$\int_{\Omega} (-\Delta\phi - \lambda\phi) \cdot \boldsymbol{\sigma} \, dA = 0. \quad (\text{C.2})$$

Next, observe that

$$\Delta\phi \cdot \boldsymbol{\sigma} = \phi_{ij,kk} \sigma_{ij} = (\phi_{ij,k} \sigma_{ij})_{,k} - \phi_{ij,k} \sigma_{ij,k}.$$

In the right hand side above,

$$\phi_{ij,k} \sigma_{ij,k} = \nabla\phi \cdot \nabla\boldsymbol{\sigma},$$

while

$$\int_{\Omega} (\phi_{ij,k} \sigma_{ij})_{,k} \, dA = \int_{\partial\Omega} \phi_{ij,k} \sigma_{ij} n_k \, ds.$$

Recalling Eq. 2.11 and the related discussion, symmetry of $\boldsymbol{\sigma}$ means $\sigma_{ij} = \kappa(s)t_it_j$ for some scalar $\kappa(s)$, and so

$$\int_{\partial\Omega} \phi_{ij,k} \sigma_{ij} n_k ds = 0,$$

proving Eq. 2.14.

Appendix D

Proof that complex conjugates of eigenvalues/eigenfunctions are themselves eigenvalues/eigenfunctions

Let (λ, ϕ) be a complex eigenvalue-eigenfunction pair, with μ the corresponding Lagrange multiplier. Let $\lambda = \lambda_r + \iota\lambda_\iota$, $\phi = \phi_r + \iota\phi_\iota$ and $\mu = \mu_r + \iota\mu_\iota$, where the quantities $\lambda_r, \lambda_\iota, \phi_r, \phi_\iota, \mu_r, \mu_\iota$ are real, and ι represents the imaginary number. Substituting these expressions in the first of Eqs. 2.12 (with $\sigma = \phi$), we get

$$\begin{aligned} -\Delta\phi_r - \iota\Delta\phi_\iota + \nabla_s\mu_r + \iota\nabla_s\mu_\iota &= (\lambda_r + \iota\lambda_\iota)(\phi_r + \iota\phi_\iota) \\ &= \lambda_r\phi_r - \lambda_\iota\phi_\iota + \iota(\lambda_r\phi_\iota + \lambda_\iota\phi_r). \end{aligned}$$

Equating the real and the imaginary parts in the above equation, we obtain

$$\begin{aligned} -\Delta\phi_r + \nabla_s\mu_r &= \lambda_r\phi_r - \lambda_\iota\phi_\iota, \\ -\Delta\phi_\iota + \nabla_s\mu_\iota &= \lambda_r\phi_\iota + \lambda_\iota\phi_r. \end{aligned}$$

Now, let us consider the quantity $-\Delta\bar{\phi} + \nabla_s\bar{\mu}$, where overbar represents complex conjugate. Using the above equation, we get

$$\begin{aligned}
 -\Delta\bar{\phi} + \nabla_s\bar{\mu} &= -\Delta\phi_r + \iota\Delta\phi_\iota + \nabla_s\mu_r - \iota\nabla_s\mu_\iota \\
 &= -\Delta\phi_r + \nabla_s\mu_r + \iota(\Delta\phi_\iota - \nabla_s\mu_\iota) \\
 &= \lambda_r\phi_r - \lambda_\iota\phi_\iota - \iota(\lambda_r\phi_\iota + \lambda_\iota\phi_r) \\
 &= (\lambda_r - \iota\lambda_\iota)(\phi_r - \iota\phi_\iota) \\
 &= \bar{\lambda}\bar{\phi}.
 \end{aligned}$$

Similarly, $\bar{\phi}$ satisfies the other three equations in Eq. 2.12.

Thus, $(\bar{\lambda}, \bar{\phi})$ is an eigenvalue-eigenfunction pair, with $\bar{\mu}$ the corresponding Lagrange multiplier.

Appendix E

Proof that the eigenfunctions form a basis for \mathcal{S}

Assume that the span of the infinitely many eigenfunctions is a subspace \mathcal{S}_∞ which is a proper subspace of \mathcal{S} . It is not clear what the dimension of its orthogonal complement $\mathcal{S}_{\infty\perp}$ is.

If the dimension is 2 or more, then it contains infinitely many elements of unit norm, and the arguments used in the first part of Section 2.4 can be applied and the same contradiction is obtained.

If the dimension of $\mathcal{S}_{\infty\perp}$ is 1, then we have a unique (up to a scalar multiple) $\boldsymbol{\tau}$ which lies in $\mathcal{S}_{\infty\perp}$. Normalizing that $\boldsymbol{\tau}$, we find that we cannot take variations of it while keeping it inside $\mathcal{S}_{\infty\perp}$. This precludes variational equations, and a different argument is easier.

The eigenfunctions $\{\phi_k\}$ along with $\boldsymbol{\tau}$ form a basis for \mathcal{S} . The issue is solely whether $\boldsymbol{\tau}$, too, is an eigenfunction.

Let us now consider a different extremization problem, namely: find a $\boldsymbol{\sigma}$ in \mathcal{S} that extremizes $\frac{1}{2} \int_{\Omega} \nabla \boldsymbol{\sigma} \cdot \nabla \boldsymbol{\sigma} dA$ subject to the condition $\int_{\Omega} \boldsymbol{\sigma} \cdot \boldsymbol{\tau} dA = 1$. We make no assumptions about how the extremizing $\boldsymbol{\sigma}$ might be related to the eigenfunctions $\{\phi_k\}$.

We approach this new problem in two ways: (i) using the calculus of variations, and (ii) directly.

Using the calculus of variations, we obtain:

$$\begin{aligned} -\Delta\boldsymbol{\sigma} + \nabla_s\boldsymbol{\mu} = \lambda\boldsymbol{\tau} & \quad \text{and} \quad \operatorname{div}\boldsymbol{\sigma} = \mathbf{0} & \quad \text{in } \Omega, \\ \boldsymbol{\sigma}\mathbf{n} = \mathbf{0} & \quad \text{and} \quad \nabla_n\boldsymbol{\sigma} \cdot (\mathbf{t} \otimes \mathbf{t}) = 0 & \quad \text{on } \partial\Omega. \end{aligned} \tag{E.1}$$

Using a direct approach, we can assume a solution of the form

$$\boldsymbol{\sigma} = a_0\boldsymbol{\tau} + \sum_{k=1}^{\infty} a_k\boldsymbol{\phi}_k.$$

The above representation contains the solution because by assumption we have a basis. Directly substituting into

$$\frac{1}{2} \int_{\Omega} \nabla\boldsymbol{\sigma} \cdot \nabla\boldsymbol{\sigma} \, dA$$

and using orthogonality, we find that we are extremizing

$$\frac{1}{2} \left(a_0^2 \int_{\Omega} \nabla\boldsymbol{\tau} \cdot \nabla\boldsymbol{\tau} \, dA + \sum_{k=1}^{\infty} a_k^2 \lambda_k \right),$$

subject to the constraint

$$\int_{\Omega} \boldsymbol{\sigma} \cdot \boldsymbol{\tau} \, dA = a_0 = 1.$$

In the above, the λ_k 's are the eigenvalues already found. The minimizer is obvious: $a_0 = 1$, and $a_k = 0$ for $k = 1, 2, 3, \dots$. It follows that the extremizing $\boldsymbol{\sigma}$ is exactly $\boldsymbol{\tau}$. Therefore, $\boldsymbol{\sigma} = \boldsymbol{\tau}$ must also satisfy Eqs. E.1, obtained using the calculus of variations. We conclude that $\boldsymbol{\tau}$ is an eigenfunction after all.

Appendix F

Eigenfunctions ϕ form an orthogonal basis to \mathcal{S} in the H^1 norm

The H^1 inner product between stress fields σ_1 and σ_2 is defined as

$$(\sigma_1, \sigma_2)_{H^1} = \int_{\Omega} \sigma_1 \cdot \sigma_2 \, dA + \int_{\Omega} \nabla \sigma_1 \cdot \nabla \sigma_2 \, dA. \quad (\text{F.1})$$

Since the mappings

$$\sigma \rightarrow \operatorname{div} \sigma \quad \text{in } \Omega$$

and

$$\sigma \rightarrow \sigma n \quad \text{on } \partial\Omega$$

are continuous in the H^1 norm [43], \mathcal{S} is a complete space when equipped with the H^1 inner product (and the corresponding norm). Our claim is that the eigenfunctions ϕ_i form an orthogonal basis of \mathcal{S} in the H^1 norm as well.

Orthogonality in H^1 of any two eigenfunctions ϕ_p and ϕ_q follows from Eq. 2.16.

Let us assume that there is an element σ in \mathcal{S} such that

$$(\sigma, \phi_i)_{H^1} = 0 \quad \forall i.$$

Upon using Eqs. F.1 and 2.14, we obtain

$$(\boldsymbol{\sigma}, \phi_i)_{H^1} = \int_{\Omega} \boldsymbol{\sigma} \cdot \phi_i dA + \int_{\Omega} \nabla \boldsymbol{\sigma} \cdot \nabla \phi_i dA = (1 + \lambda_i) \int_{\Omega} \boldsymbol{\sigma} \cdot \phi_i dA = 0 \quad \forall i.$$

Since λ_i are positive, we conclude that

$$\int_{\Omega} \boldsymbol{\sigma} \cdot \phi_i dA = 0 \quad \forall i.$$

However, ϕ_i form a basis of \mathcal{S} in the L^2 norm, and we conclude that $\boldsymbol{\sigma} = \mathbf{0}$. Hence, ϕ_i form an orthogonal basis of \mathcal{S} in the H^1 norm.

Appendix G

Proof that Eq. 5.23 is an inner product and Eq. 5.24 is a norm

We first show that $(\cdot, \cdot)_w$ is an inner product. For any $\boldsymbol{\sigma}_1, \boldsymbol{\sigma}_2, \boldsymbol{\sigma}_3 \in \mathcal{S}$ and $\alpha_1, \alpha_2 \in \mathbb{R}$,

$$\begin{aligned}(\alpha_1 \boldsymbol{\sigma}_1 + \alpha_2 \boldsymbol{\sigma}_2, \boldsymbol{\sigma}_3)_w &= \int_{\Omega} w_2 (\alpha_1 \boldsymbol{\sigma}_1 + \alpha_2 \boldsymbol{\sigma}_2) \cdot \boldsymbol{\sigma}_3 dA \\ &= \alpha_1 \int_{\Omega} w_2 \boldsymbol{\sigma}_1 \cdot \boldsymbol{\sigma}_3 dA + \alpha_2 \int_{\Omega} w_2 \boldsymbol{\sigma}_2 \cdot \boldsymbol{\sigma}_3 dA = \alpha_1 (\boldsymbol{\sigma}_1, \boldsymbol{\sigma}_3)_w + \alpha_2 (\boldsymbol{\sigma}_2, \boldsymbol{\sigma}_3)_w, \\ (\boldsymbol{\sigma}_1, \boldsymbol{\sigma}_2)_w &= \int_{\Omega} w_2 \boldsymbol{\sigma}_1 \cdot \boldsymbol{\sigma}_2 dA = \int_{\Omega} w_2 \boldsymbol{\sigma}_2 \cdot \boldsymbol{\sigma}_1 dA = (\boldsymbol{\sigma}_2, \boldsymbol{\sigma}_1)_w, \\ (\boldsymbol{\sigma}_1, \boldsymbol{\sigma}_1)_w &= \int_{\Omega} w_2 \boldsymbol{\sigma}_1 \cdot \boldsymbol{\sigma}_1 dA \geq 0 \quad \text{with equality if and only if } \boldsymbol{\sigma}_1 = \mathbf{0}.\end{aligned}$$

In the third equation above, we have used the assumption that $w_2 > 0$ everywhere in Ω , so that $w_2 \boldsymbol{\sigma}_1 \cdot \boldsymbol{\sigma}_1$ is positive everywhere for non-zero $\boldsymbol{\sigma}_1$.

The operation $\|\cdot\|_w$ is a norm because

$$\begin{aligned}
\|\boldsymbol{\sigma}_1\|_w &= \left(\int_{\Omega} w_2 \boldsymbol{\sigma}_1 \cdot \boldsymbol{\sigma}_1 dA \right)^{\frac{1}{2}} \geq 0 \text{ with equality if and only if } \boldsymbol{\sigma}_1 = \mathbf{0}, \\
\|\alpha \boldsymbol{\sigma}_1\|_w &= \left(\int_{\Omega} w_2 \alpha \boldsymbol{\sigma}_1 \cdot \alpha \boldsymbol{\sigma}_1 dA \right)^{\frac{1}{2}} = \alpha \left(\int_{\Omega} w_2 \boldsymbol{\sigma}_1 \cdot \boldsymbol{\sigma}_1 dA \right)^{\frac{1}{2}} = \alpha \|\boldsymbol{\sigma}_1\|_w, \\
\|\boldsymbol{\sigma}_1 + \boldsymbol{\sigma}_2\|_w &= \left\{ \int_{\Omega} w_2 (\boldsymbol{\sigma}_1 + \boldsymbol{\sigma}_2) \cdot (\boldsymbol{\sigma}_1 + \boldsymbol{\sigma}_2) dA \right\}^{\frac{1}{2}} \\
&= \left\{ \int_{\Omega} w_2 \boldsymbol{\sigma}_1 \cdot \boldsymbol{\sigma}_1 + \int_{\Omega} w_2 \boldsymbol{\sigma}_2 \cdot \boldsymbol{\sigma}_2 + 2 \int_{\Omega} w_2 \boldsymbol{\sigma}_1 \cdot \boldsymbol{\sigma}_2 dA \right\}^{\frac{1}{2}} \\
&= \left\{ \|\boldsymbol{\sigma}_1\|_w^2 + \|\boldsymbol{\sigma}_2\|_w^2 + 2 \int_{\Omega} \sqrt{w_2} \boldsymbol{\sigma}_1 \cdot \sqrt{w_2} \boldsymbol{\sigma}_2 dA \right\}^{\frac{1}{2}} \\
&\leq \left\{ \|\boldsymbol{\sigma}_1\|_w^2 + \|\boldsymbol{\sigma}_2\|_w^2 + 2 \left(\int_{\Omega} \sqrt{w_2} \boldsymbol{\sigma}_1 \cdot \sqrt{w_2} \boldsymbol{\sigma}_1 dA \right)^{\frac{1}{2}} \left(\int_{\Omega} \sqrt{w_2} \boldsymbol{\sigma}_2 \cdot \sqrt{w_2} \boldsymbol{\sigma}_2 dA \right)^{\frac{1}{2}} \right\}^{\frac{1}{2}} \\
&= \left\{ \|\boldsymbol{\sigma}_1\|_w^2 + \|\boldsymbol{\sigma}_2\|_w^2 + 2 \|\boldsymbol{\sigma}_1\|_w \|\boldsymbol{\sigma}_2\|_w \right\}^{\frac{1}{2}} = \|\boldsymbol{\sigma}_1\|_w + \|\boldsymbol{\sigma}_2\|_w.
\end{aligned}$$

Note that in the third equation above, the inequality follows from the Cauchy-Schwarz inequality.

Bibliography

- [1] G S Schajer. *Practical residual stress measurement methods*. John Wiley & Sons, UK, 2013.
- [2] S Tiwari and A Chatterjee. Basis functions for residual stresses. *Applied Mathematics and Computation*, 386:125468, 2020.
- [3] Lord Rayleigh. *The theory of sound*. Macmillan, London, UK, 1877.
- [4] R J Knops and L E Payne. *Uniqueness theorems in linear elasticity*. Springer-Verlag, Berlin, 1971.
- [5] P J Withers and H Bhadeshia. Residual stress. Part 1- Measurement techniques. *Material Science and Technology*, 17:355–365, 2001.
- [6] P J Withers and H Bhadeshia. Residual stress. Part 2- Nature and origins. *Material Science and Technology*, 17:366–375, 2001.
- [7] B A Boley and J H Weiner. *Theory of thermal stresses*. John Wiley & Sons, New York, 1960.
- [8] M R Eslami, R B Hetnarski, J Ignaczak, N Noda, N Sumi, and Y Tanigawa. *Theory of elasticity and thermal stresses*, volume 197. Springer, Dordrecht, 2013.
- [9] J D Eshelby. The determination of the elastic field of an ellipsoidal inclusion, and related problems. *Proceedings of the Royal Society of London A*, 241:376–396, 1957.
- [10] J D Eshelby. The elastic field outside an ellipsoidal inclusion. *Proceedings of Royal Society of London A*, 252:561–569, 1959.
- [11] J D Eshelby. The elastic model of lattice defects. *Annalen der Physik*, 1:116–121, 1958.
- [12] J D Eshelby. A simple derivation of the elastic field of an edge dislocation. *British Journal of Applied Physics*, 17:1131–1135, 1966.

-
- [13] E Kröner et al. Continuum theory of defects. *Physics of defects*, 35:217–315, 1981.
- [14] T Mura. *Micromechanics of defects in solids*. Martinus Nijhoff Publishers, Dordrecht, 1987.
- [15] A Goriely. *The mathematics and mechanics of biological growth*. Springer, New York, NY, 2017.
- [16] L Truskinovsky G Zurlo. Printing non-Euclidean solids. *Physical review letters*, 119:48001, 2017.
- [17] D Swain and A Gupta. Biological growth in bodies with incoherent interfaces. *Proceedings of the Royal Society of London A*, 474:20170716, 2018.
- [18] M Epstein. *The elements of continuum biomechanics*. John Wiley & Sons, Chichester, UK, 2012.
- [19] A Hoger. On the determination of residual stress in an elastic body. *Journal of Elasticity*, 16:303–324, 1986.
- [20] A Hoger. On the residual stress possible in an elastic body with material symmetry. *Archive for Rational Mechanics and Analysis*, 88:271–290, 1985.
- [21] M Shams, M Destrade, and R W Ogden. Initial stresses in elastic solids: constitutive laws and acoustoelasticity. *Wave Motion*, 48:552–567, 2011.
- [22] A L Gower, T Shearer, and P Ciarletta. A new restriction for initial stressed elastic solids. *The Quarterly Journal of Mechanics and Applied Mathematics*, 70.4:455–478, 2017.
- [23] A L Gower, P Ciarletta, and M Destrade. Initial stress symmetry and its applications in elasticity. *Proceedings of the Royal Society of London A*, 471:20150448, 2015.
- [24] M H B M Shariff, R Bustamante, and J Merodio. On the spectral analysis of residual stress in finite elasticity. *IMA Journal of Applied Mathematics*, 82:656–680, 2017.
- [25] C S Man. Hartig’s law and linear elasticity with initial stress. *Inverse Problems*, 14:313–319, 1998.
- [26] M Destrade and R W Ogden. On stress dependent elastic moduli and wave speeds. *IMA Journal of Applied Mathematics*, 78.5:965–997, 2013.

-
- [27] P Ciarletta, M Destrade, A L Gower, and M Taffetani. Morphology of residually stressed tubular tissues: beyond the elastic multiplicative decomposition. *Journal of Mechanics and Physics of Solids*, 90:242–253, 2016.
- [28] M B Prime. Residual stress measurement by successive extension of a slot: the crack compliance method. *Applied Mechanics Reviews*, 52:75–96, 1999.
- [29] G S Schajer and M B Prime. Residual stress solution extrapolation for the slitting method using equilibrium constraints. *Journal of Engineering Materials and Technology*, 129:226–232, 2007.
- [30] S Akbari, F Taheri-Behrooz, and M M Shokrieh. Slitting measurement of residual hoop stresses through the wall-thickness of a filament wound composite ring. *Experimental Mechanics*, 53:1509–1518, 2013.
- [31] M Beghini, L Bertini, L F Mori, and W Rosellini. Genetic algorithm optimization of the hole-drilling method for non-uniform residual stress fields. *The Journal of Strain Analysis for Engineering Design*, 44:105–115, 2009.
- [32] P Ballard and A Constantinescu. On the inversion of subsurface residual stresses from surface stress measurements. *Journal of Mechanics and Physics of Solids*, 42:1767–1787, 1994.
- [33] R Robertson. Determining residual stress from boundary measurements: a linearized approach. *Journal of Elasticity*, 52:63–73, 1998.
- [34] R Nedin and A Vatulyan. Inverse problem of non-homogeneous residual stress identification in thin plates. *International Journal of Solids and Structures*, 50:2107–2114, 2013.
- [35] Z Gao and T Mura. On the inversion of residual stresses from surface displacements. *Journal of Applied Mechanics*, 56(3):508–513, 1989.
- [36] G Schajer and M B Prime. Use of inverse solutions for residual stress measurements. *Journal of Engineering Materials and Technology*, 128(3):375–382, 2006.
- [37] S A Faghidian. A smoothed inverse eigenstrain method for reconstruction of the regularized residual fields. *International Journal of Solids and Structures*, 51:4427–4434, 2014.
- [38] B E Pobedrja. Problems in terms of a stress tensor. *Doklady Akademii Nauk SSSR*, 240:564–567, 1978.

-
- [39] B E Pobedrja. A new formulation of the problem in mechanics of a deformable solid body under stress. *Soviet Mathematics - Doklady*, 22:88–91, 1980.
- [40] S Li, A Gupta, and X Markenscoff. Conservation laws of linear elasticity in stress formulations. *Proceedings of the Royal Society of London A*, 461:99–116, 2005.
- [41] X Markenscoff and A Gupta. Configurational balance laws for incompatibility in stress space. *Proceedings of the Royal Society of London A*, 463:1379–1392, 2007.
- [42] M E Gurtin. The linear theory of elasticity. In *Linear theories of elasticity and thermoelasticity*, pages 1–295. Springer, 1973.
- [43] R Témam. *Navier-Stokes equations - Theory and numerical analysis*. North-Holland Publishing Company, New York, NY, 1977.
- [44] P R Halmos. What does the spectral theorem say? *The American Mathematical Monthly*, 70:241–247, 1963.
- [45] F Boyer and P Fabrie. *Mathematical tools for the study of the incompressible Navier-Stokes equations and related models*, volume 183. Springer Science & Business Media, 2012.
- [46] R Courant and D Hilbert. *Methods of mathematical physics, volume 1*. Interscience Publishers, New York, NY, 1966.
- [47] J K Seo and H Zorgati. Compactness and Dirichlet’s principle. *Journal of the Korean Society for Industrial and Applied Mathematics*, 18(2):193–207, 2014.
- [48] A F Monna. *Dirichlet’s principle: a mathematical comedy of errors and its influence on the development of analysis*. Oosthoek, Scheltema & Holkema, Utrecht, 1975.
- [49] L Giovanni. *A first course in Sobolev spaces*. American Mathematical Society, Providence, Rhode Island, 2009.
- [50] H Brezis. *Functional analysis, Sobolev spaces and partial differential equations*. Springer, New York, NY, 2011.
- [51] A Bossavit. *Computational electromagnetism*. Academic Press, Boston, 1998.
- [52] I Ekeland and R Témam. *Convex analysis and variational problems*. Society for Industrial and Applied Mathematics, Philadelphia, 1999.
- [53] K J Bathe. *Finite element procedures*. Prentice-Hall, New Jersey, 1996.

-
- [54] K J Bathe. The inf-sup condition and its evaluation for mixed finite element methods. *Computers and Structures*, 79:243–252, 2001.
- [55] W Bao, X Wang, and K J Bathe. On the inf-sup condition of mixed finite-element formulations for acoustic fluids. *Mathematical Models and Methods in Applied Sciences*, 11(5):883–901, 2001.
- [56] R S Falk. *Finite element methods for linear elasticity. In Mixed finite elements, compatibility conditions, and applications.* Springer, New York, NY, 2008.
- [57] R R Archer, N H Cook, S H Crandall, N C Dahl, F A McClintock, E Rabinowicz, and G S Reichenbach. *An introduction to mechanics of solids.* McGraw-Hill, New York, NY, 1959.
- [58] S Timoshkeno and J N Goodier. *Theory of elasticity.* McGraw Hill, New York, NY, 1951.
- [59] E Hewitt and R E Hewitt. The Gibbs-Wilbraham phenomenon: an episode in Fourier analysis. *Archive for History of Exact Sciences*, 21:129–160, 1979.
- [60] J R Barber. *Elasticity.* Springer, Dordrecht, 1992.
- [61] M Murugesan and D W Jung. Johnson-Cook material and failure model parameters estimation of AISI-1045 medium carbon steel for metal forming applications. *Materials*, 12(4):609, 2019.
- [62] A Ray. *Spatial oscillations in residual stresses in angular extrusion.* PhD thesis, Indian Institute of Technology Kanpur, 2018.
- [63] O Orringer, J Orkisz, and Z Swiderski (eds.). *Residual stress in rails: effects on rail integrity and railroad economics. Volume 2: theoretical and numerical analyses.* Kluwer, Boston, 1992.
- [64] O Lablée. *Spectral theory in Riemannian geometry.* EMS Publishing House, Zurich, 2015.
- [65] C O Horgan and K L Miller. Antiplane shear deformations for homogeneous and inhomogeneous anisotropic linearly elastic solids. *Journal of Applied Mechanics*, 61(1):23–29, 1994.
- [66] B Dasgupta. *Applied mathematical methods.* Pearson Education, India, 2006.
- [67] J Boyd. *Chebyshev and Fourier spectral methods*, volume 2. Dover Publications, New York, NY, 2000.

- [68] P Hagedorn and A Dasgupta. *Vibrations and waves in continuous mechanical systems*. Wiley, Chichester, 2007.
- [69] C Lanczos. *Applied analysis*. Prentice Hall, Englewood Cliffs, 1988.
- [70] E Nelson. A proof of Liouville's theorem. *Proceedings of the American Mathematical Society*, 12:995, 1961.